



Universiteit
Leiden
The Netherlands

Multidimensional evaluation of cardiac hemodynamics and electrophysiology in patients with congenital and acquired heart disease
Kamphuis, V.P.

Citation

Kamphuis, V. P. (2019, January 31). *Multidimensional evaluation of cardiac hemodynamics and electrophysiology in patients with congenital and acquired heart disease*. Retrieved from <https://hdl.handle.net/1887/68280>

Version: Not Applicable (or Unknown)

License: [Licence agreement concerning inclusion of doctoral thesis in the Institutional Repository of the University of Leiden](#)

Downloaded from: <https://hdl.handle.net/1887/68280>

Note: To cite this publication please use the final published version (if applicable).

Cover Page



Universiteit Leiden



The following handle holds various files of this Leiden University dissertation:

<http://hdl.handle.net/1887/68280>

Author: Kamphuis, V.P.

Title: Multidimensional evaluation of cardiac hemodynamics and electrophysiology in patients with congenital and acquired heart disease

Issue Date: 2019-01-31

Multidimensional evaluation of cardiac hemodynamics
and electrophysiology in patients with congenital
and acquired heart disease

Vivian Paola Kamphuis

© 2018 V.P. Kamphuis, Leiden, The Netherlands

All rights reserved. No part of this thesis may be reproduced, stored or transmitted in any form or by any means, electronic or mechanical, including photocopy, recording or any information storage or retrieval system, without permission of the copyright owner.

ISBN: 978-94-6323-462-7

The research described in this thesis was supported by a grant of the Dutch Heart Foundation (DHF grant number 2013T091).

Financial support by the Dutch Heart Foundation for the publication of this thesis is gratefully acknowledged.

The printing of this thesis was financially supported by Willem-Alexander kindziekenhuis Leiden, Medis medical imaging systems B.V., Fysiologic ECG services B.V., Pie Medical Imaging B.V.

Cover image: Intracardiac 4D flow MRI, made with LAVA (with thanks to Patrick de Koning), cover model: Daan Kamphuis

Back cover: Hook's hut beach, Curaçao

Printed by: Gildeprint, Enschede

Multidimensional evaluation of cardiac hemodynamics and electrophysiology in patients with congenital and acquired heart disease

Proefschrift

Ter verkrijging van
de graad van Doctor aan de Universiteit Leiden,
op gezag van Rector Magnificus prof.mr. C.J.J.M. Stolker,
volgens besluit van het College voor Promoties
te verdedigen op donderdag 31 januari 2019
klokke 16:15 uur

door

Vivian Paola Kamphuis
geboren te Willemstad, Curaçao
in 1990

Promotores:

Prof. dr. N.A. Blom

Prof. dr. W.A. Helbing

Co-promotor:

Dr. A.A.W. Roest

Promotiecommissie:

Prof. dr. M.J. Schalijs

Prof. dr. A. de Roos

Prof. dr. B.J.M. Mulder-van der Wall (Universiteit van Amsterdam)

Dr. M. Carlsson (University of Lund, Sweden)

Dr. R.N. Planken (Universiteit van Amsterdam)

Aan mijn ouders

Table of contents

Chapter 1	General introduction and thesis outline	9
Part I	Electrocardiographic variables reflecting cardiac function	17
Chapter 2	Electrocardiographic characteristics before and after correction of right-sided congenital heart defects and its relation to prognosis. <i>J Electrocardiol.</i> 2018. doi: 10.1016/j.jelectrocard.2018.10.001. [Epub ahead of print]	19
Chapter 3	Normal values of the ventricular gradient and QRS-T angle, derived from the pediatric electrocardiogram. <i>J Electrocardiol.</i> 2018 May - Jun;51(3):490-495	31
Chapter 4	Electrical remodeling after percutaneous atrial septal defect closure in pediatric and adult patients. <i>Submitted for publication</i>	45
Chapter 5	Electrocardiographic detection of right ventricular pressure overload in patients with suspected pulmonary hypertension. <i>J Electrocardiol.</i> 2014 Mar-Apr;47(2):175-82.	63
Part II	4D flow MRI-derived cardiac flow and function: validation and clinical utility	81
Chapter 6	Unravelling cardiovascular disease using four dimensional flow cardiovascular magnetic resonance. <i>Int J Cardiovasc Imaging.</i> 2017 Jul;33(7):1069-1081. Direct assessment of tricuspid regurgitation by 4D flow CMR in a patient with Ebstein's anomaly. <i>Eur Heart J Cardiovasc Imaging.</i> 2018 May;19(5): 587-588 Bi-ventricular vortex ring formation corresponds to regions of highest intra-ventricular viscous energy loss in a Fontan patient: analysis by 4D flow MRI. <i>Int J Cardiovasc Imaging.</i> 2018 Mar;34(3):441-442.	83
Chapter 7	In-scan and scan-rescan assessment of LV in- and outflow volumes by 4D flow MRI versus 2D planimetry. <i>J Magn Reson Imaging.</i> 2018 Feb;47(2):511-522	111
Chapter 8	Automated cardiac valve tracking for flow quantification with four-dimensional flow MRI <i>Radiology.</i> 2018. doi: 10.1148/radiol.2018180807. [Epub ahead of print]	133

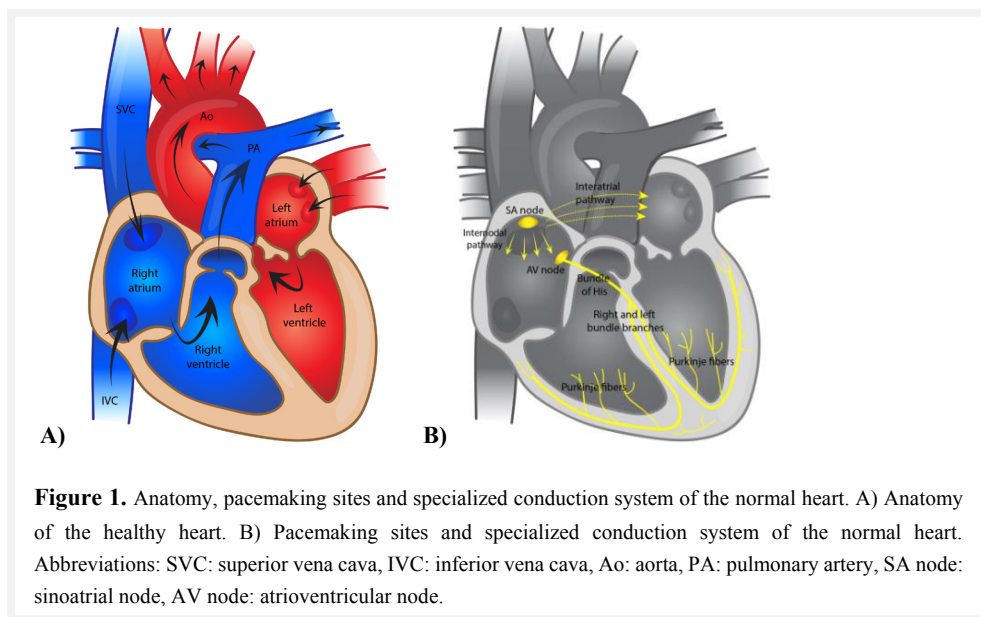
Part III	4D flow MRI-derived novel determinants of intraventricular hemodynamics	161
Chapter 9	Scan-rescan reproducibility of diastolic left ventricular kinetic energy, viscous energy loss and vorticity assessment using 4D flow MRI: analysis in healthy subjects. <i>Int J Cardiovasc Imaging. 2018 Jun;34(6):905-920.</i>	163
Chapter 10	Disproportionate intraventricular viscous energy loss in Fontan patients: analysis by 4D flow MRI. <i>Eur Heart J Cardiovasc Imaging 2018 doi: 10.1093/ehjci/jez096. [Epub ahead of print]</i>	191
Chapter 11	Intraventricular vorticity is associated with viscous energy loss and kinetic energy from 4D flow MRI in healthy subjects and Fontan patients. <i>Submitted for publication</i>	221
Chapter 12	Dobutamine-induced increase in intracardiac kinetic energy, energy loss and vorticity is inversely related to VO ₂ max in Fontan patients. <i>Submitted for publication</i>	239
Chapter 13	General discussion and conclusions	257
Chapter 14	Nederlandse samenvatting (Dutch summary)	267
Appendices	Co-authors affiliations	274
	List of publications	275
	Curriculum vitae	276
	Dankwoord	277

Chapter 1

General introduction

Background

The heart is a muscular organ that pumps blood through the circulatory system. *Figure 1A* shows the anatomy and flow directions of the normal heart. The pacemaking sites and specialized conduction system of the normal heart are shown in *Figure 1B*.



Cardiovascular diseases are the number one cause of death globally and form a major health burden with an estimated 422.7 million cases of cardiovascular disease and 17.92 million cardiovascular deaths worldwide in 2015 [1]. In the Netherlands alone, 18.130 men and 20.483 women died due to cardiovascular disease in 2016 [2]. Cardiovascular diseases encompass both acquired and congenital heart diseases. Acquired heart diseases are cardiovascular diseases that develop after birth, in contrast to congenital heart diseases, that are present at birth and caused by abnormal prenatal formation of the heart and/or the major blood vessels. Congenital heart diseases are the most common birth defects, affecting 8 out of 1000 live births worldwide [3]. Because of advances in interventions and medication, most patients with congenital heart diseases can currently survive with few problems for many years, despite abnormal loading conditions. However, the development of heart failure, arrhythmias and pulmonary hypertension still forms a problem in these patients, for which regular follow-up is generally needed. Nevertheless, the pathophysiological mechanisms behind this late attrition still remain largely unknown [4].

This thesis is part of the multicenter study titled: ‘COBRA³: Congenital heart defects: Bridging the gap between Growth, Maturation, Regeneration, Adaptation, late Attrition and Ageing’. The objectives of this multicenter study are:

1. To gain mechanistic insight into the impact of congenital heart disease on growth, renewal and homeostasis of the heart, especially the right ventricle.
2. To improve identification of patients at risk for attrition of heart function in congenital heart disease.
3. To establish the context to develop therapies to prevent or reverse heart failure or arrhythmias in congenital heart disease patients.

This thesis focuses on the multidimensional evaluation of acquired and congenital heart diseases by electrocardiography and magnetic resonance imaging (MRI) before and after intervention (*Objective 1*). Insight in the impact of congenital and acquired heart diseases on electrophysiology and hemodynamics in the heart can help understand the often complex nature of cardiovascular diseases and might aid in the early detection of patients prone to cardiovascular deterioration (*Objective 2*).

Electrocardiography

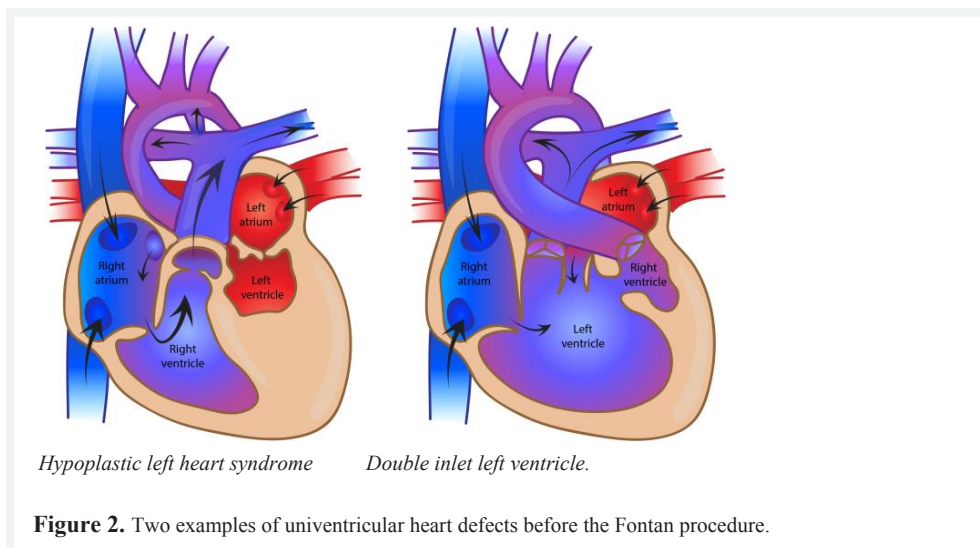
The electrocardiogram (ECG) is an indispensable non-invasive diagnostic tool that has been used for more than a century to measure the electrical currents produced by the heart at the body surface. However, the standard 12-lead ECG only gives a one-dimensional scalar representation of these electrical currents, while vectorcardiography contains three-dimensional (3D) information that is not directly accessible in the standard 12-lead ECG [5]. The spatial vectorcardiographic approach is based on the concept that the electrical forces from the heart can be represented at any point in time by a single vector originating at the center of the heart, the heart vector. The course of the heart vector can be visualized as a loop in 3D space over time [6], as such it could be seen as four-dimensional (4D). Around 1950-1980, when the vectorcardiogram (VCG) was used in clinical practice, it was recorded with special lead systems, of which the Frank lead system [7] became the most pervasive. Nowadays, the VCG is usually mathematically synthesized from the 12-lead ECG by multiplying it by a conversion matrix (initially the inverse Dower matrix [8], currently the Kors matrix [9]). Two vectorcardiographic variables in particular, namely the spatial QRS-T angle and the ventricular gradient (VG), have shown to be of diagnostic and prognostic value. An increased spatial QRS-T angle improves prediction of sudden cardiac death after acute coronary syndrome [10] and overall mortality in the general population [11-13]. The VG has been used, amongst others, in the detection of right ventricular pressure overload [14, 15].

Magnetic resonance imaging

Magnetic resonance imaging can be used to assess volume, flow and function of the heart. Four-dimensional (3D + time) flow MRI, i.e. phase contrast MRI with velocity encoding in all directions and spatial regions of the acquired volume, is a novel tool that can be used for comprehensive evaluation of the flow pattern inside the heart and great vessels [16]. Quantification of valvular flow is the main application of 4D flow MRI [17]. Flow quantification by 4D flow MRI has several advantages over 2D phase contrast MRI with velocity encoding in a single direction and a static imaging plane. Firstly, with the use of 4D flow MRI-derived streamline visualization [16], measurement planes can be placed in every time frame and adjusted dynamically to the orientation of the flow direction or the position of the valve. Moreover, flow volumes over all four valves can be measured in a single acquisition which eliminates the chance of heart variability between acquisitions. These advantages make 4D flow MRI more accurate than 2D MRI for quantification of valvular flow volumes and regurgitation [18, 19] in healthy subjects and patients with acquired or congenital heart diseases.

Furthermore, 4D flow MRI offers the unique and novel ability to quantify *in vivo* intraventricular hemodynamic parameters such as kinetic energy, viscous energy loss (the kinetic energy that is lost due to viscosity induced flow-structure interaction) and vorticity (the magnitude of vortical flow) [16]. These 4D flow MRI-derived novel parameters can give comprehensive insight in intraventricular flow, which can be of great value in patients with congenital or acquired cardiac diseases.

Patients who have had a Fontan procedure [20], a palliative approach for patients with complex congenital intracardiac deformations in whom a biventricular circulation cannot be created (*Figure 2*) form an important patient group in congenital cardiology with a significant morbidity and mortality. The heterogeneous abnormal underlying cardiac anatomy causes alterations in intracardiac flow patterns and 4D flow MRI is ideally suited to visualize these complex flow patterns [21]. Assessment of the effects of such abnormal intracardiac flow patterns on viscous energy loss might aid in the early detection of circulatory failure, the main cause of mortality in these patients [22].



Aim

The aim of this thesis was to gain insight in cardiac hemodynamics and electrophysiology from a multidimensional perspective in patients with congenital and acquired heart disease.

Outline of this thesis

Part I of this thesis focuses on electrocardiographic variables reflecting cardiac function. **Chapter 2** reviews electrocardiographic characteristics of right-sided congenital heart diseases and its relation to prognosis. In **Chapter 3** normal values of the ventricular gradient and QRS-T angle, derived from the pediatric electrocardiogram are assessed. These normal values could be valuable in the serial follow-up of children with congenital heart diseases, such as an atrial septal defect, which is the focus of **Chapter 4**. Lastly, **Chapter 5** describes the use of the ventricular gradient in electrocardiographic detection of right pressure overload in patients with pulmonary hypertension.

Part II of this thesis focuses on validation and clinical utility of 4D flow MRI-derived cardiac flow and function assessment. In **Chapter 6**, the potential use of 4D flow MRI in unravelling cardiovascular disease is reviewed. In this chapter, two case examples of the use of 4D flow MRI in patients with congenital heart diseases are also shown. Because 4D flow MRI is a relatively new MRI tool, reproducibility of the measurements is crucial. **Chapter 7** shows the scan-rescan reproducibility of left ventricular in- and outflow assessment from 4D flow MRI with manual valve tracking. Valvular flow quantification is the main application of 4D flow MRI. However, clinical applicability of flow quantification by 4D flow MRI is hindered

because manual valve tracking can be a time-consuming process. Therefore, in **Chapter 8**, 4D flow MRI with automated valve tracking is introduced and compared to manual valve tracking in patients with acquired and congenital heart disease and healthy volunteers.

Part III of this thesis describes 4D flow MRI-derived novel determinants of intraventricular hemodynamics. First, **Chapter 9** focuses on the scan-rescan reproducibility of left ventricular kinetic energy, viscous energy loss and vorticity in healthy subjects. In **Chapter 10**, intraventricular viscous energy loss and kinetic energy are assessed in patients with a Fontan circulation and compared to healthy subjects. **Chapter 11** focuses on the association between intraventricular vorticity versus kinetic energy and viscous energy loss in healthy subjects and patients with a Fontan circulation. Lastly, **Chapter 12** describes the influence of pharmacological stress on 4D flow MRI-derived viscous energy loss, kinetic energy and vorticity and their relation to maximal oxygen uptake from cardiopulmonary exercise tests.

Chapter 13 summarizes the main findings of the studies presented in this thesis, discusses them in view with present literature and provides future perspectives. In **Chapter 14** a summary in Dutch is provided.

References

1. Roth GA, Johnson C, Abajobir A, Abd-Allah F, Abera SF, Abyu G, Ahmed M, Aksut B, Alam T, Alam K, et al: Global, Regional, and National Burden of Cardiovascular Diseases for 10 Causes, 1990 to 2015. *J Am Coll Cardiol* 2017, 70:1-25.
2. Buddeke J VDI, Visseren FLJ, Vaartjes I, Bots ML: Ziekte en sterfte aan hart- en vaatziekten. In *Hart- en vaatziekten in Nederland 2017, cijfers over leefstijl, risicofactoren, ziekte en sterfte*. Edited by Buddeke J VDI, Visseren FLJ, Vaartjes I, Bots ML. Den Haag: Hartstichting; 2017
3. Hoffman J: The global burden of congenital heart disease. *Cardiovasc J Afr* 2013, 24:141-145.
4. Nieminen HP, Jokinen EV, Sairanen HI: Causes of late deaths after pediatric cardiac surgery: a population-based study. *J Am Coll Cardiol* 2007, 50:1263-1271.
5. Man S, Maan AC, Schaliij MJ, Swenne CA: Vectorcardiographic diagnostic & prognostic information derived from the 12-lead electrocardiogram: Historical review and clinical perspective. *J Electrocardiol* 2015, 48:463-475.
6. Olson CW, Estes EH, Kamphuis VP, Carlsen EA, Strauss DG, Wagner, GS: The three-dimensional electrocardiogram. In *Marriott's practical electrocardiography*. 12 edition. Edited by Wagner GS, Strauss DG. Philadelphia. LIPPINCOTT WILLIAMS & WILKINS; 2014
7. Frank E: An accurate, clinically practical system for spatial vectorcardiography. *Circulation* 1956, 13:737-749.
8. Edenbrandt L, Pahlm O: Vectorcardiogram synthesized from a 12-lead ECG: superiority of the inverse Dower matrix. *J Electrocardiol* 1988, 21:361-367.
9. Kors JA, van Herpen G, Sittig AC, van Bommel JH: Reconstruction of the Frank vectorcardiogram from standard electrocardiographic leads: diagnostic comparison of different methods. *Eur Heart J* 1990, 11:1083-1092.
10. Lingman M, Hartford M, Karlsson T, Herlitz J, Rubulis A, Caidahl K, Bergfeldt L: Value of the QRS-T area angle in improving the prediction of sudden cardiac death after acute coronary syndromes. *Int J Cardiol* 2016, 218:1-11.
11. Kardys I, Kors JA, van der Meer IM, Hofman A, van der Kuip DA, Witteman JC: Spatial QRS-T angle predicts cardiac death in a general population. *Eur Heart J* 2003, 24:1357-1364.
12. Waks JW, Sitlani CM, Soliman EZ, Kabir M, Ghafoori E, Biggs ML, Henrikson CA, Sotoodehnia N, Biering-Sorensen T, Agarwal SK, et al: Global Electric Heterogeneity Risk Score for Prediction of Sudden Cardiac Death in the General Population: The Atherosclerosis Risk in Communities (ARIC) and Cardiovascular Health (CHS) Studies. *Circulation* 2016, 133:2222-2234.
13. Whang W, Shimbo D, Levitan EB, Newman JD, Rautaharju PM, Davidson KW, Muntner P: Relations between QRS/T angle, cardiac risk factors, and mortality in the third National Health and Nutrition Examination Survey (NHANES III). *Am J Cardiol* 2012, 109:981-987.
14. Kamphuis VP, Haecck ML, Wagner GS, Maan AC, Maynard C, Delgado V, Vliegen HW, Swenne CA: Electrocardiographic detection of right ventricular pressure overload in patients with suspected pulmonary hypertension. *J Electrocardiol* 2014, 47:175-182.
15. Scherptong RW, Henkens IR, Kapel GF, Swenne CA, van Kralingen KW, Huisman MV, Schuerwegh AJ, Bax JJ, van der Wall EE, Schaliij MJ, Vliegen HW: Diagnosis and mortality prediction in pulmonary hypertension: the value of the electrocardiogram-derived ventricular gradient. *J Electrocardiol* 2012, 45:312-318.
16. Kamphuis VP, Westenberg JJM, van der Palen RLF, Blom NA, de Roos A, van der Geest R, Elbaz MSM, Roest AAW: Unravelling cardiovascular disease using four dimensional flow cardiovascular magnetic resonance. *Int J Cardiovasc Imaging* 2017, 33:1069-1081.
17. Kathiria NN, Higgins CB, Ordovas KG: Advances in MR imaging assessment of adults with congenital heart disease. *Magn Reson Imaging Clin N Am* 2015, 23:35-40.
18. Roes SD, Hammer S, van der Geest RJ, Marsan NA, Bax JJ, Lamb HJ, Reiber JH, de Roos A, Westenberg JJ: Flow assessment through four heart valves simultaneously using 3-dimensional 3-directional velocity-encoded magnetic resonance imaging with retrospective valve tracking in healthy volunteers and patients with valvular regurgitation. *Invest Radiol* 2009, 44:669-675.
19. Westenberg JJ, Roes SD, Ajmone Marsan N, Binnendijk NM, Doornbos J, Bax JJ, Reiber JH, de Roos A, van der Geest RJ: Mitral valve and tricuspid valve blood flow: accurate quantification

- with 3D velocity-encoded MR imaging with retrospective valve tracking. *Radiology* 2008, 249:792-800.
20. Fontan F, Baudet E: Surgical repair of tricuspid atresia. *Thorax* 1971, 26:240-248.
 21. She HL, Roest AA, Calkoen EE, van den Boogaard PJ, van der Geest RJ, Hazekamp MG, de Roos A, Westenberg JJ: Comparative Evaluation of Flow Quantification across the Atrioventricular Valve in Patients with Functional Univentricular Heart after Fontan's Surgery and Healthy Controls: Measurement by 4D Flow Magnetic Resonance Imaging and Streamline Visualization. *Congenit Heart Dis*. 2017, 12:40-48.
 22. Alsaied T, Bokma JP, Engel ME, Kuijpers JM, Hanke SP, Zuhlke L, Zhang B, Veldtman GR: Factors associated with long-term mortality after Fontan procedures: a systematic review. *Heart* 2017, 103:104-110.

A photograph of a bridge at night, illuminated by warm yellow lights. The bridge's metal truss structure is visible. Below the bridge, the water is dark, reflecting the yellow, green, and red lights from the bridge and surrounding area. The text is centered over the image.

Part I

Electrocardiographic
variables reflecting cardiac
function

Chapter 2

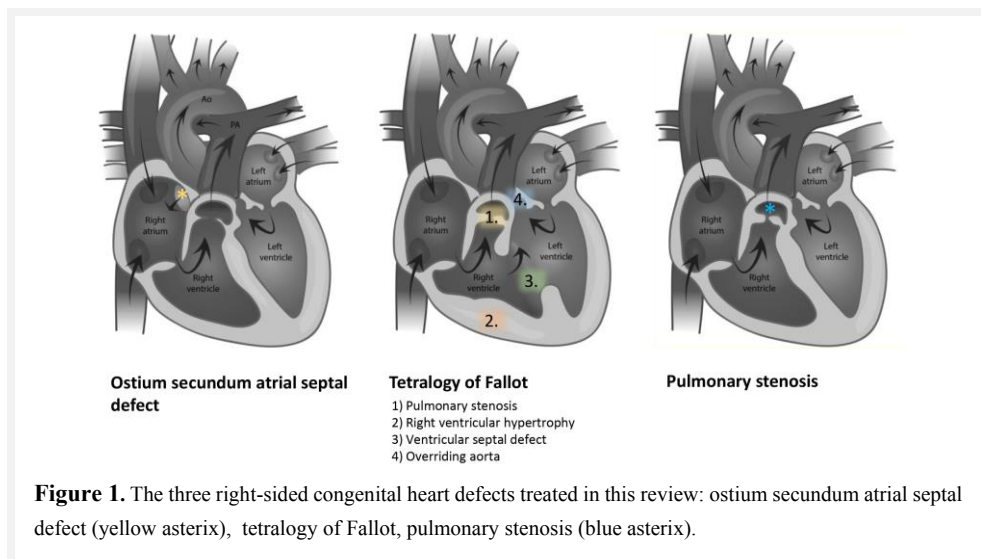
Electrocardiographic characteristics before and after
correction of right-sided congenital heart defects and its
relation to prognosis

Vivian P Kamphuis, Daphne Raad, Martina Nassif, Cees A Swenne, Nico A Blom, Arend DJ
ten Harkel

J Electrocardiol. 2018. doi: 10.1016/j.jelectrocard.2018.10.001. [Epub ahead of print]

Introduction

Congenital heart defects are the most common birth defects and occur in 0.8% of all live births. Nowadays, patients with congenital heart defects usually survive with many event-free years despite abnormal cardiac hemodynamics. However, most patients still need life-long follow-up and main factors for morbidity and mortality in these patients are cardiac failure, arrhythmias or pulmonary hypertension (PH) [1]. The electrocardiogram (ECG) is a noninvasive, widely-used, inexpensive tool that can be used during long-term follow-up of these patients, particularly in order to help predict occurrence of rhythm disorders and sudden cardiac death. From birth to adulthood, several physiological changes influence the cardiac electrical activity. These encompass postnatal circulatory changes and changes due to growth of the body including the heart. Due to the rapid structural and functional changes throughout childhood, interpretation of ECGs in pediatric patients is more challenging than in adults and normal values are always needed for the interpretation of the pediatric ECG. In contrast to adult cardiology, in pediatric cardiology, many congenital heart defects affect the right side of the heart. In this review, we will focus on the ECG of patients with the most frequent right-sided congenital heart defects: ostium secundum atrial septal defect (ASDII), tetralogy of Fallot (ToF) and pulmonary stenosis (PS), as shown in *Figure 1*.



Atrial septal defect

An ASDII generally causes a left-to-right interatrial shunt, which will increase the total blood volume in the pulmonary circulation, resulting in increased volume load of the right side of

the heart causing dilation of the right atrium (RA), right ventricle (RV) and pulmonary arteries. Spontaneous closure of the defect may occur depending on the diameter and age at diagnosis. Percutaneous or surgical closure can be performed for persisting defects depending on hemodynamic significance and/or symptoms. The ASDII, located in the fossa ovalis (remnant of the foramen ovale in the right atrium), is the most common atrial septal defects. In this review we focused on ASDII, however most other ASD types will show similar ECG characteristics, except for the ostium primum defect which often manifests as an atrioventricular septal defect.

Before ASD closure

Figure 2A shows an ECG of a five-month-old patient with a large ASDII, one month before surgical closure. This ECG shows normal sinus rhythm and a heart rate within normal limits for this age (144 bpm) [2]. The P-wave amplitude of 0.35 mV in lead II that can be measured in *Figure 2A* is higher than normal for this age [2]. Increased maximum P-wave amplitudes are common in patients with ASDII, caused by an enlarged right atrium [3]. Also, prolongation of the P-wave duration and P-wave dispersion are frequently described phenomena in these patients, which can be used in the prediction of atrial fibrillation [3]. The ECG in *Figure 2A* shows a P-wave duration of 120 ms, which is prolonged for the age of this child. P-wave dispersion is not evident from this ECG. Furthermore, prolongation of the PR interval is common in ASDII patients and could be an indication of an interrupted or aberrant conduction [4]. The ECG in *Figure 2A* shows a PR interval of 140 ms, which is longer than the mean PR interval at this age but still within the 98th percentile for a five-month-old child [2]. RV volume overload typically causes the QRS-axis to deviate to the right. *Figure 2A* shows extreme QRS-axis deviation.

A prolonged QRS duration and a right bundle branch block (RBBB) are common in the ECG of ASDII patients [5], often as a consequence of RV dilatation [4]. However, since young ASDII patients can already present with a RBBB, impaired interventricular conduction may also play a role. The RSR' complex in lead V1 is common in ASDII patients [5], however this feature is also found in approximately 5% of the normal population [5]. The notable R' described in ASDII patients could be distinguished from the normal variant by a slurred down slope and the association with a slight or moderate widening of the QRS complex [4, 5]. The R'-wave is typically described in lead V1, but can also be visible in V2 and V3 [4]. The RSR' pattern may be the consequence of RV hypertrophy, but considering that it often occurs together with prolonged QRS durations, it is more likely caused by impaired or slow conduction [4, 5]. *Figure 2A* also shows a prolonged QRS duration of 80 ms, however not a typical RSR' pattern. Another common independent ECG sign in patients with an ASDII is

the “crochetage” pattern (a notch near the apex of the R-wave in the inferior limb leads) [6], which is also apparent in the example in *Figure 2A*. The QTc interval in the example in *Figure 2A* is normal (366 ms). Because of RV overload, also a significantly higher mean R/S ratio is seen in patients with an ASDII compared to normal subjects [5]. The ECG in *Figure 2A*, shows tall R waves and deep S waves in V2-V6.

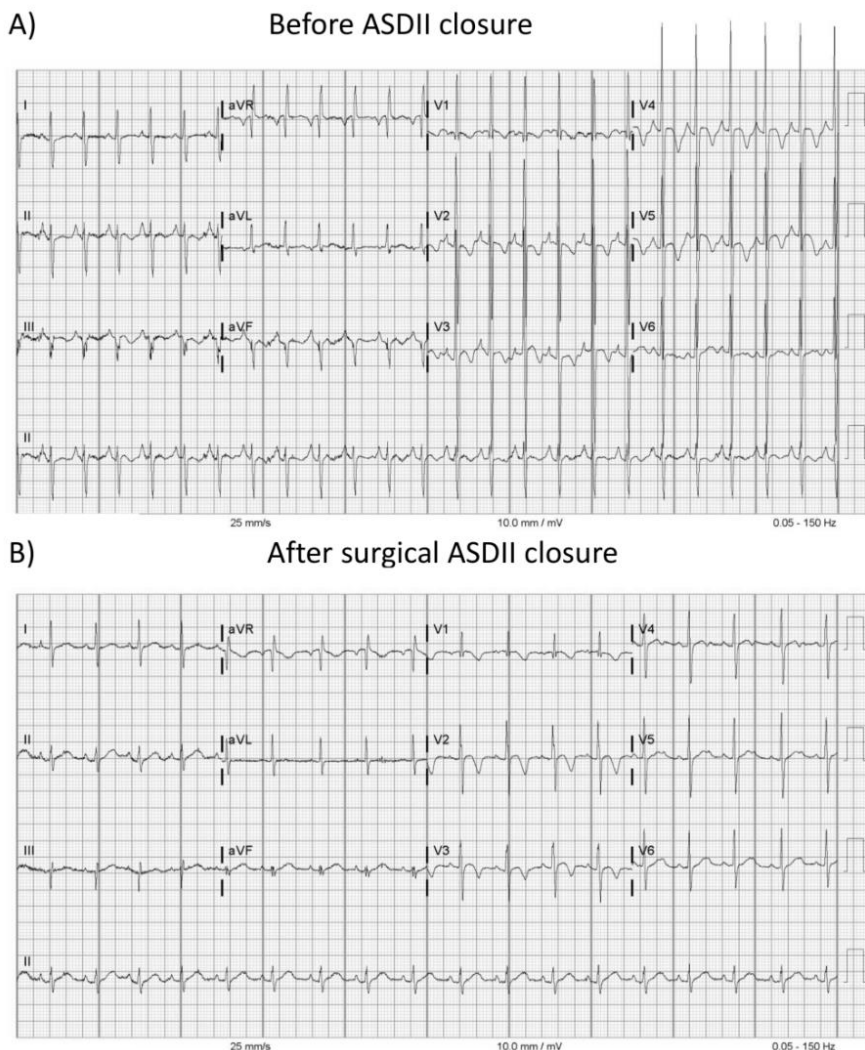


Figure 2. ECGs of a patient with a ostium secundum atrial septal defect (ASDII). A) 1 month before surgical ASDII closure (age: 5 months). B) 1 year and 9 months after surgical ASDII closure (age: 2 years, 3 months).

After ASD closure

Figure 2B shows an ECG of the same patient as *Figure 2A*, 1 year and 9 months after surgical closure of the ASDII (now 2 years and 3 months old). Similar to before closure, this ECG shows normal sinus rhythm and a heart rate of 110 bpm, which is within normal limits for the age of the child [2]. The ECG shows a P-wave amplitude of 0.15 mV in lead II and a P-wave duration of 80 ms, which are both normal for this age [2]. Generally, reduction of P-wave duration and P-wave dispersion can be seen after surgical ASDII closure [7]. In contrast, shortly (around 1 day – 1 week) after percutaneous ASDII closure a prolongation of P-wave duration and P-wave dispersion have been described, which could be related to the incorporation of material used for closing the defect, possibly resulting in atrial tissue stretching and consequent conduction disturbances [3].

In the following months after percutaneous ASDII closure P-wave duration and P-wave dispersion will generally reduce [3]. The PR interval in *Figure 2B* is now 140 ms, which is still longer than the mean PR interval at this age but below the 98th percentile for a 2-year-old [2]. Studies after percutaneous ASD closure have described that PR intervals stayed similar to the values before closure [3], however no studies reported PR interval after surgical closure. In ASDII patients with pronounced PR-interval prolongation or high degree AV block a NKX2-5 gene mutation should be kept in mind [8]. The QRS axis in *Figure 2B* shows an intermediate QRS axis and a QRS duration of 70 ms, which is normal for this age. The QTc interval in *Figure 2B* is still normal (413 ms). It is evident that the tall R waves and deep S waves in V2-V6 that were seen before closure have now reduced to normal. Furthermore, the R/S ratio in V2 is now 1, which is normal for this age.

Prognostic ECG markers

Atrial arrhythmias are a common complication after closure of an ASDII. The frequency of arrhythmias, which are usually of benign nature, increases directly after defect closure, but gradually decreases within a year after closure [9]. Both maximum P-wave amplitude and P-wave dispersion have been described as markers for inter-atrial conduction disturbances and may be used in the prediction of atrial fibrillation [3]. Although these values generally decrease after ASDII closure, a direct increase after percutaneous ASDII closure can occur in some patients [3], which may suggest that the risk of atrial arrhythmias is higher in the first weeks after percutaneous closure. Increasing age is also found to be potentially influencing occurrence of arrhythmias and atrial-ventricular conduction changes in ASDII patients, which is related to more pronounced prolongation of the PR interval [10].

Tetralogy of Fallot

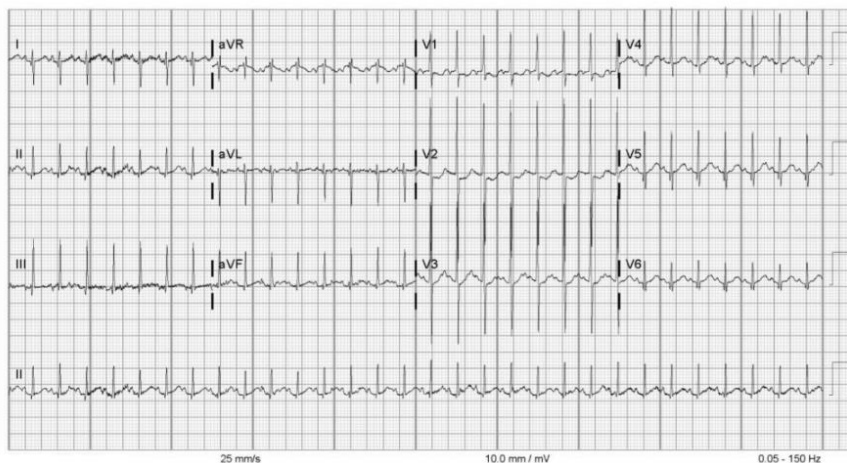
Tetralogy of Fallot (ToF) is a congenital defect that consists of four abnormalities: 1) a large ventricular septal defect (VSD); 2) infundibular pulmonary stenosis (PS); 3) right ventricular hypertrophy (RVH) and 4) an overriding aorta. The basic fault that causes this complex cardiac anomaly is anterior and cephalad deviation of the infundibular septum relative to the septomarginal band, resulting in subvalvar right ventricular outflow tract obstruction and a malaligned VSD. The amount of RVH and the onset of symptoms, such as cyanosis, shortness of breath and poor weight gain, are determined by the severity of obstruction of the RV outflow. ToF patients usually undergo complete intracardiac repair (consisting of VSD repair, infundibulectomy and in most patients insertion of a transannular patch) around the age of 6 months. Insertion of a transannular patch, which is needed to reconstruct the right ventricular outflow tract, causes pulmonary regurgitation and may warrant pulmonary valve replacement (PVR) at a later age.

Before corrective surgery

Figure 3A shows an ECG of a 3-week-old boy with ToF, 2 months before surgical correction. This ECG shows normal sinus rhythm and a heart rate of 180 bpm which is at the upper limit of normal for the age of this child [2]. Before the complete intracardiac repair, the ECG of a ToF patient may exhibit an increased maximum P-wave amplitude and P-wave dispersion. In *Figure 3A*, the P-wave amplitude is 0.20 mV, which is higher than the mean for this age but still within the normal range [2]. P-wave dispersion is not evident from this ECG. PR and QRS duration of ToF patients before correction are usually within normal limits [11]. In this ECG, PR duration is 120 ms and QRS duration is 80 ms which is both higher than the mean for this age but still within the normal range [2]. The QTc interval is 380 ms, which is normal for this age.

In ToF patients, signs of right ventricular hypertrophy are usually present, such as reversal of the R/S ratio (prominent anterior R-waves and posterior S-waves), especially in the right precordial leads (V1-V3). Indeed, in *Figure 3A* the R/S ratio in V1 is 3.5, which is high for this age.

A) Before ToF correction



B) After ToF correction



Figure 3. ECGs of a patient with tetralogy of Fallot (ToF). A) 2 months before ToF correction (age: 3 weeks). B) directly after ToF correction (age: 2 months).

After corrective surgery

Figure 3B shows an ECG of the same patient as Figure 3A, directly after surgical ToF correction (now 2 months old). This ECG shows sinus rhythm of 138 bpm, which is normal for this age. In Figure 3B the P-wave amplitude is 0.15 mV, which is normal for this age, P-wave dispersion is not evident from this ECG. The PR duration is still 120 ms, but the QRS duration is now prolonged (100 ms). Prolongation of the PR and QRS duration is frequently

seen after total ToF correction and is associated with RV outflow tract abnormalities [12]. Furthermore, RBBB is a distinctive feature after ToF correction [13]. In patients who underwent transventricular ToF repair, the origination of this RBBB has been attributed to the interruption of the terminal ramification of the right bundle branch. However, RBBB also occurs in the current transatrial and transpulmonary approaches, which is related to the infundibulectomy causing delayed activation of the RV outflow tract [13]. After ToF correction, a significant increase in mean value of QT dispersion may occur. This ECG feature is possibly amplified by the development of fibrous tissue due to the operation [14] and has been associated with larger RV volume and a larger RV wall mass [15]. Also, JT dispersion is more common among corrected ToF patients compared to healthy controls [16], which has been related to a larger RV volume and decreased RV ejection fraction [15]. Both are not evident in *Figure 3B*.

Because of the insertion of an transannular patch during the ToF correction, pulmonary regurgitation frequently develops at a later age with subsequent right ventricular dysfunction, which may warrant treatment by PVR. *Figure 4A* shows the ECG of a 14- year-old corrected ToF patient, 2 months before PVR. This ECG shows sinus rhythm of 58 bpm. Signs of RV volume and/or pressure overload in this ECG are: right axis deviation, a PR duration of 180 ms and a QRS duration of 140 ms with a RBBB and an increased R amplitude in the right precordial leads (V1-V3).

After PVR, signs of right ventricular volume and/or pressure overload usually normalize. *Figure 4B* shows an ECG of the same patient as *Figure 4A*, 1 year and 4 months after PVR. This ECG shows sinus rhythm of 60 bpm, an intermediate QRS axis, PR duration of 140 ms and QRS duration of 120 ms. The RBBB is still evident. R amplitudes in the right precordial leads have decreased notably.

Prognostic ECG markers

Even though most children with ToF operated today reach adulthood with few problems, arrhythmias and sudden cardiac death still occur. Prolongation of the QRS complex has been associated with ventricular arrhythmias and sudden cardiac death in these patients, even in asymptomatic corrected ToF patients [17]. The predictive value of this phenomenon increases when QRS prolongation is combined with increased dispersions of QT, QRS and JT intervals [18]. Lastly, the presence of a trifascicular block is a risk factor for sudden cardiac death in these patients [19].

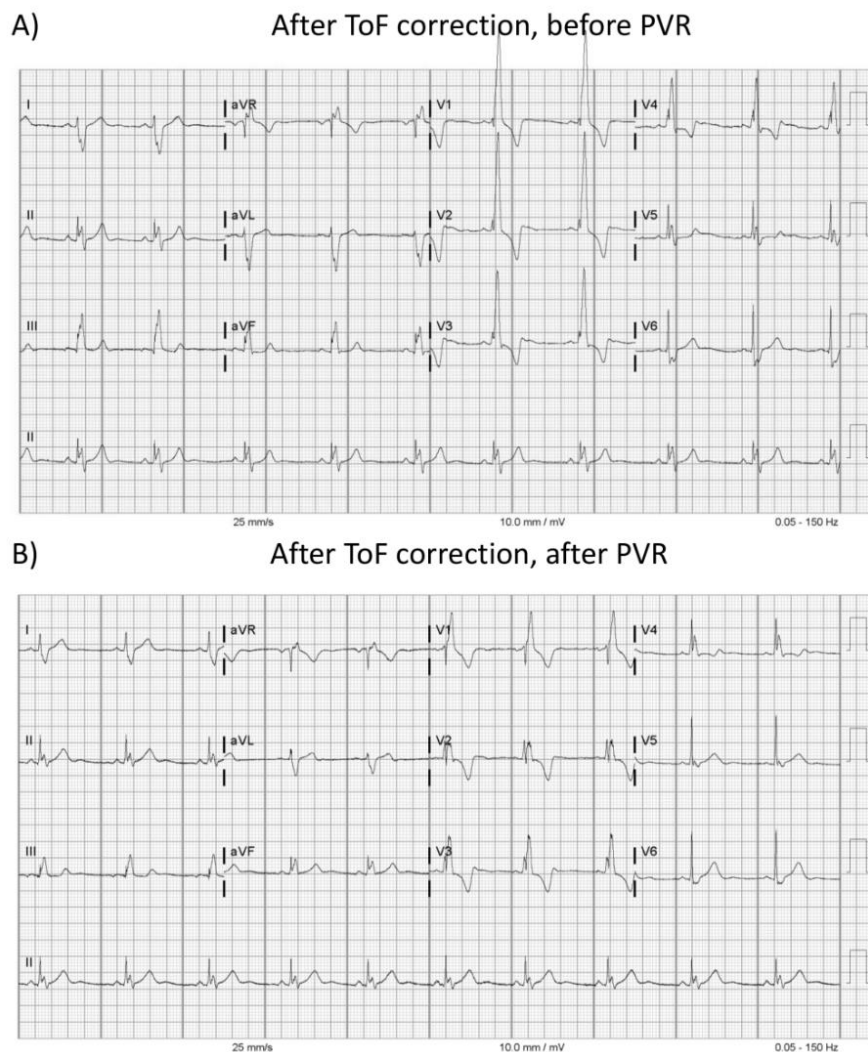


Figure 4. ECGs of a patient with correct tetralogy of Fallot (ToF). A) 2 months before pulmonary valve replacement (PVR) (age: 14 years). B) 1 year and 4 months after PVR (age: 16 years).

Pulmonary stenosis

Pulmonary stenosis (PS) is an obstruction of the right ventricular outflow at the pulmonary valve, which can occur at different levels: valvular, subvalvular (infundibular) or supra-valvular. Valvular pulmonary stenosis is the most common obstruction of the right ventricular outflow. Symptoms will only be present in moderate to severe PS; children with mild PS are usually completely asymptomatic. Symptoms may include exertional dyspnoea and fatigue. In severe PS, heart failure may develop.

Before and after corrective surgery

In mild PS, the ECG will be normal. In moderate to severe pulmonary stenosis the RV outflow tract obstruction will lead to pressure overload of the RV, which will eventually lead to right ventricular hypertrophy which can be visible on the ECG [20]. After successful balloon valvuloplasty it is expected that the ECG will return to normal.

Conclusion

Right-sided congenital heart defects and their correction lead to changes in the electrocardiogram which can be helpful in the follow-up of these patients. Several electrocardiographic parameters together can bring to mind the possibility of a right-sided hemodynamic burden.

Clinical significance

Electrocardiographic characteristics dynamically change after corrective intervention for right-sided congenital heart defects, which can be used for clinical evaluation and follow-up.

References

1. Nieminen HP, Jokinen EV, Sairanen HI: Causes of late deaths after pediatric cardiac surgery: a population-based study. *J Am Coll Cardiol* 2007, 50:1263-1271.
2. Rijnbeek PR, Witsenburg M, Schrama E, Hess J, Kors JA: New normal limits for the paediatric electrocardiogram. *Eur Heart J* 2001, 22:702-711.
3. Grignani RT, Tolentino KM, Rajgor DD, Quek SC: Longitudinal evaluation of P-wave dispersion and P-wave maximum in children after transcatheter device closure of secundum atrial septal defect. *Pediatr Cardiol* 2015, 36:1050-1056.
4. Barber JM, Magidson O, Wood P: Atrial septal defect. *Br Heart J* 1950, 12:277-292.
5. Depasquale NP, Burch GE: Analysis of the Rsr' Complex in Lead V1. *Circulation* 1963, 28:362-367.
6. Heller J, Hagege AA, Besse B, Desnos M, Marie FN, Guerot C: "Crochetage" (notch) on R wave in inferior limb leads: a new independent electrocardiographic sign of atrial septal defect. *J Am Coll Cardiol* 1996, 27:877-882.
7. Yavuz T, Nisli K, Oner N, Dindar A, Aydogan U, Omeroglu RE, Ertugrul T: The effects of surgical repair on P-wave dispersion in children with secundum atrial septal defect. *Adv Ther* 2008, 25:795-800.
8. Pfeufer A, van Noord C, Marcianti KD, Arking DE, Larson MG, Smith AV, Tarasov KV, Muller M, Sotoodehnia N, Sinner MF, et al: Genome-wide association study of PR interval. *Nat Genet* 2010, 42:153-159.
9. Ozyilmaz I, Ozyilmaz S, Tola HT, Saygi M, Kiplapinar N, Tanidir C, Ergul Y, Guzelas A, Odemis E: Holter electrocardiography findings and P-wave dispersion in pediatric patients with transcatheter closure of atrial septal defects. *Ann Noninvasive Electrocardiol* 2014, 19:174-181.
10. Shiku DJ, Stijns M, Lintermans JP, Vliers A: Influence of age on atrioventricular conduction intervals in children with and without atrial septal defect. *J Electrocardiol* 1982, 15:9-13.
11. Woods A: The electrocardiogram in the tetralogy of Fallot. *Br Heart J* 1952, 14:193-203.
12. Uebing A, Gibson DG, Babu-Narayan SV, Diller GP, Dimopoulos K, Goktekin O, Spence MS, Andersen K, Henein MY, Gatzoulis MA, Li W: Right ventricular mechanics and QRS duration in patients with repaired tetralogy of Fallot: implications of infundibular disease. *Circulation* 2007, 116:1532-1539.
13. Horowitz LN, Simson MB, Spear JF, Josephson ME, Moore EN, Alexander JA, Kastor JA, Edmunds LH, Jr.: The mechanism of apparent right bundle branch block after transatrial repair of tetralogy of Fallot. *Circulation* 1979, 59:1241-1252.
14. Balkhi RA, Beghetti M, Friedli B: Time course of appearance of markers of arrhythmia in patients with tetralogy of Fallot before and after surgery. *Cardiol Young* 2004, 14:360-366.
15. van den Berg J, de Bie S, Meijboom FJ, Hop WC, Pattynama PM, Bogers AJ, Helbing WA: Changes during exercise of ECG intervals related to increased risk for ventricular arrhythmia in repaired tetralogy of Fallot and their relationship to right ventricular size and function. *Int J Cardiol* 2008, 124:332-338.
16. Berul CI, Hill SL, Geggel RL, Hijazi ZM, Marx GR, Rhodes J, Walsh KA, Fulton DR: Electrocardiographic markers of late sudden death risk in postoperative tetralogy of Fallot children. *J Cardiovasc Electrophysiol* 1997, 8:1349-1356.
17. Russo G, Folino AF, Mazzotti E, Rebollato L, D'Aliento L: Comparison between QRS duration at standard ECG and signal-averaging ECG for arrhythmic risk stratification after surgical repair of tetralogy of fallot. *J Cardiovasc Electrophysiol* 2005, 16:288-292.
18. Gatzoulis MA, Till JA, Redington AN: Depolarization-repolarization inhomogeneity after repair of tetralogy of Fallot. The substrate for malignant ventricular tachycardia? *Circulation* 1997, 95:401-404.
19. Quattlebaum TG, Varghese J, Neill CA, Donahoo JS: Sudden death among postoperative patients with tetralogy of Fallot: a follow-up study of 243 patients for an average of twelve years. *Circulation* 1976, 54:289-293.
20. Bassingthwaite JB, Parkin TW, Dushane JW, Wood EH, Burchell HB: The Electrocardiographic and Hemodynamic Findings in Pulmonary Stenosis with Intact Ventricular Septum. *Circulation* 1963, 28:893-905

Chapter 3

Normal values of the ventricular gradient and QRS-T angle, derived from the pediatric electrocardiogram

Vivian P Kamphuis, Nico A Blom, Erik W van Zwet, Sum-Che Man, Arend DJ Ten Harkel,
Arie C Maan, Cees A Swenne

J Electrocardiol. 2018 May - Jun;51(3):490-495

Abstract

Objective

Normal values of the mathematically-synthesized vectorcardiogram (VCG) are lacking for children. Therefore, the objective of this study was to assess normal values of the pediatric synthesized VCG (spatial QRS-T angle [SA] and ventricular gradient [VG]).

Methods

Electrocardiograms (ECGs) of 1263 subjects (0-24 years) with a normal heart were retrospectively selected. VCGs were synthesized by the Kors matrix. Normal values (presented as 2nd and 98th percentiles) were assessed by quantile regression with smoothing by splines.

Results

Our results show that heart rate decreased over age, QRS duration increased and QTc interval remained constant. The SA initially decreased and increased again from the age of 8 years. The VG magnitude was relatively stable until the age of 2 years, after which it increased.

Conclusion

Normal values of the pediatric ECG and VCG (VG and SA) were established. These normal values could be important for future studies using VG and SA for risk stratification in heart disease in children.

Introduction

Vectorcardiography, especially the Frank vectorcardiogram (VCG), was a popular form of electrocardiography until it disappeared from the clinical routine in the seventies because it required special equipment and expertise. When computerized synthesis of the VCG from a 12-lead electrocardiogram (ECG) became feasible, it became clear that some vectorcardiographic variables, specifically the angle between the spatial QRS- and T axes (spatial QRS-T angle, [SA]) and the spatial QRS-T integral (ventricular gradient [VG]) [1] contained information that is not explored by standard 12-lead electrocardiography. Thus, the re-introduction of the VCG assumed the form of an add-on to the conventional 12-lead ECG. Both descriptors (VG and SA) have demonstrated additional diagnostic and prognostic value. Projection of the VG in an optimized direction is associated with right ventricular pressure and pulmonary hypertension [2, 3]. An abnormal (i.e., large) SA can improve prediction of sudden cardiac death after acute coronary syndromes [4] and overall mortality in a general population [5-7]. Normal values of the VG and SA in adults have been published [8-10]. Also, pediatric normal values obtained from Frank VCGs have been published [11]. However, up to now, pediatric normal values of SA and VG using a VCG that is synthesized mathematically from a standard 12-lead ECG are still lacking. Therefore, the objective of the current study is to determine pediatric normal values of SA and VG from a synthesized VCG, including their dynamics during growth.

Materials and methods

Study group

Normal subjects were retrospectively selected from the pediatric cardiology outpatient clinics of the Leiden University Medical Centre (LUMC) and the Academic Medical Centre Amsterdam, and from the first year of medical school at the LUMC (ECGs were made for educational purposes). The LUMC Medical Ethics Committee provided a statement of no objection for obtaining and publishing the anonymized data. The ECGs from the first-year medical students are part of a larger database (The Leiden University Einthoven Science Project dataset) that was also used by Rijnbeek et al. [12] and Scherptong et al. [10]. All students gave written informed consent. 1011 children were selected because they visited the pediatric cardiology outpatient clinics and were declared normal after a full diagnostic work-up consisting of evaluation by a pediatric cardiologist, an echocardiogram and ECG. These healthy children were referred to the outpatient clinics because of an additional examination, for instance when a doctor at the consultation clinic heard a functional murmur during a routine check. The age range of interest for our study was 0 days up to 18 years. By including

252 ECGs from first-year medical students (17–24 years), the data covered an age-range between 0 and 24 years, thus allowing for the use of a smoothing algorithm over the full age-range of interest in the statistical analysis. This resulted in a total study group of 1263 normal ECGs. *Table 1* shows the age and sex distribution. Age categories between 0 months and 16 years are conform Rijnbeek et al. [13]. Age categories “16–20 years” and “20–24 years” were added to allow for the application of the smoothing algorithm at the age of 18 years.

Electrocardiogram recording

The 643 ECGs made in the LUMC were recorded with Mortara ELI 250 and 350 electrocardiographs (Mortara Instrument, Milwaukee, WI, USA) with a 1000 samples per second sampling rate; the 368 ECGs made in the AMC were recorded with MAC5500 electrocardiographs (GE Healthcare, Milwaukee, WI, USA) with a 250 samples per second (204 ECGs) or 500 samples per second (164 ECGs) sampling rate. The 252 ECGs of medical students at the LUMC were recorded with MAC5500 electrocardiographs (GE Healthcare, Milwaukee, WI, USA) with 500 samples per second sampling rate. All recordings were converted to ECGs with a 500 samples per second sampling rate.

Vectorcardiogram analysis

All ECGs were processed with the interactive research-oriented MATLAB (The MathWorks, Natick, MA) program LEADS (Leiden University Medical Centre, Leiden, the Netherlands) [14]. VCGs were synthesized by the Kors transformation matrix [15]. In brief, LEADS automatically removes baseline wander, deselects noisy beats, and computes an averaged beat in which it finds default onset of QRS, end of QRS (J point) and end of T landmarks. Subsequently, the LEADS analyst can adjust the beat selection and these landmarks, after which SA (angle between the mean QRS and T vectors) and VG (vectorial sum of the QRS and the T integrals) are automatically computed. All LEADS analyses were done by two analysts independently (VPK, CAS). In case of disagreement, the definite positioning of the landmarks was collectively determined. Additionally to SA and VG, heart rate (HR), QRS duration and QT interval were stored. QTc was calculated with Bazett's formula.

Statistical analysis

Median, 2nd percentile and 98th percentile and their confidence intervals were continuously estimated as a function of age with quantile regression based on smoothing splines [16] with the COBS [17] extension of the statistical program “R” [18]. This smoothing operation allows for influences from younger and older children on the estimated value at a given age. In this respect it is a problem to estimate smoothed values at the end of the age span of interest (18

years): when the collected data ends at the age of 18 years, the smoothing at 18 years is only one-sided, and this creates a border effect in the terminal part of the regression curve. To solve this, we have added data of subjects until the age of 24 years. Adding data until the age of 24 years warrants absence of a border effect at 18 years, and introduces a border effect at 24 years. The latter is, however, not a problem because this is outside the age range of interest in the current study (up to 18 years). Spline knots were chosen at ages 0.08, 1, 5, 10, 15, 16, 17, 18, 19, and 23.6 years. The positions of these knots were determined by the distribution density of the data over the age range: knots were closer together at higher data densities and more distant with sparse data. The knots at ages 0.08 and 23.6 years correspond to the minimal and maximal ages in the data set. Tabulated data were based on the interpolated values in the middle of each of the age classes, at 1 month, 2 months, 4.5 months, 9 months, 2 years, 4 years, 6.5 years, 10 years, 14 years, and 18 years. Data at 22 years (middle of the highest age group) were not included in the table; these data served only to facilitate application of the smoothing algorithm at the age of 18 years.

Results

The total study group consisted of 1263 subjects, 1011 from the pediatric cardiology outpatient clinics and 252 medical students. *Table 1* displays the age and sex distribution of the study group.

Table 1. Age and sex distribution of the study group

Age range	Total (M/F)
0-1 month	20 (12/8)
1-3 months	80 (44/36)
3-6 months	55 (24/31)
6-12 months	57 (24/33)
1-3 years	179 (101/78)
3-5 years	166 (81/85)
5-8 years	172 (99/73)
8-12 years	125 (76/49)
12-16 years	123 (70/53)
16-20 years	192 (91/101)
20-24 years	94 (34/60)
Total	1263 (656/607)

Abbreviations: M = male, F = female

ECG and VCG variables

Figure 1 displays the ECG variables as measured in all subjects of the study group as age-dependent scatter plots. These plots also contain the curves of the estimated medians and 2nd and 98th percentiles with their 95% confidence intervals. *Figure 1a* shows a constantly decreasing median heart rate that stabilizes at higher ages. The larger confidence intervals at lower ages are caused by sparse data; this effect can be seen in all measured variables. The median QRS duration (*Figure 1b*) showed a constant increase that has not yet stabilized at higher ages. The median QT interval (*Figure 1c*) increased constantly and stabilized at higher ages. The median QTc interval (*Figure 1d*) remained rather constant with a slight dip around age 3 years. *Figure 2* displays the VCG variables as measured in all subjects of the study group as age-dependent scatter plots. The median SA (*Figure 2a*) initially decreased and increased again from the age of around 8 years and has not yet stabilized at higher ages. The median VG magnitude (*Figure 2b*) was relatively stable until the age of around 2 years after which it increased without having stabilized at higher ages. Note that the figures display all data including the added normal subjects aged 18–24 years but that the median and the 2nd and 98th percentiles are only valid until the age of 18 years (see the Statistical analysis paragraph in the Methods section). *Table 2* shows the medians and 2nd and 98th percentiles for all ECG and VCG variables at the middle values of the age classes. Values from the highest age category in the study group (20–24 years) have not been included because of the presence of a border effect (see the Statistical analysis paragraph in the Methods section).

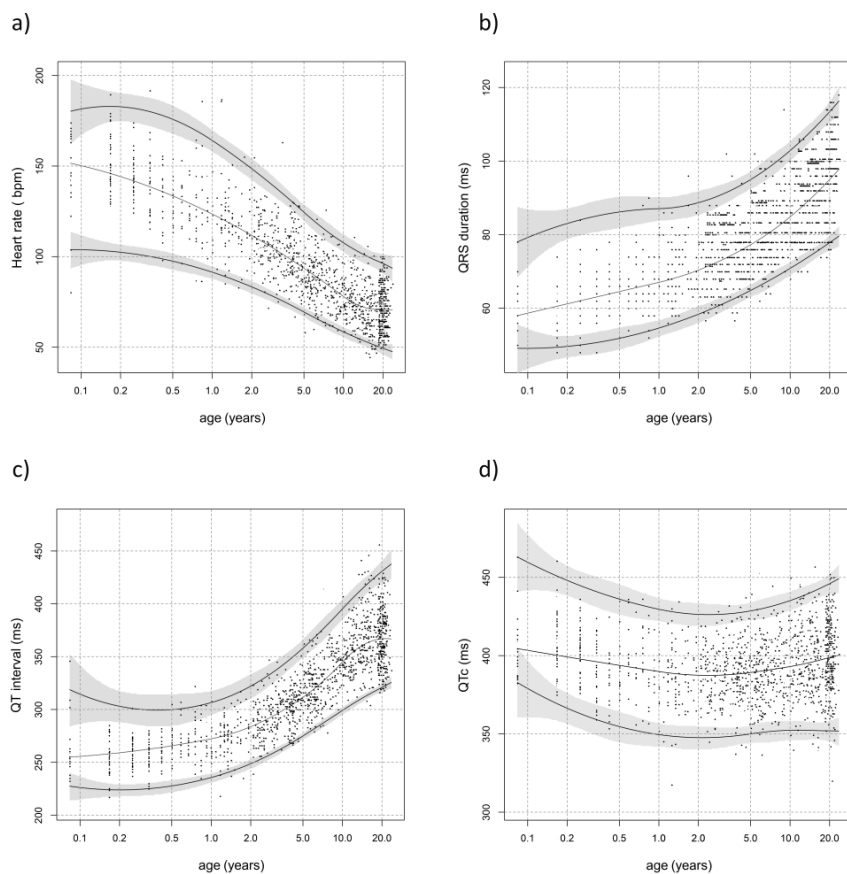


Figure 1. Scatter plots of ECG variables versus age. The black curves show the estimated medians and 2nd and 98th percentiles. The 95% confidence intervals are shown in grey. a) Scatter plot of heart rate versus age. b) Scatter plot of QRS duration versus age. c) Scatter plot of QT interval versus age. d) Scatter plot of QTc versus age. QTc was calculated with Bazett's formula: QT/\sqrt{RR} .

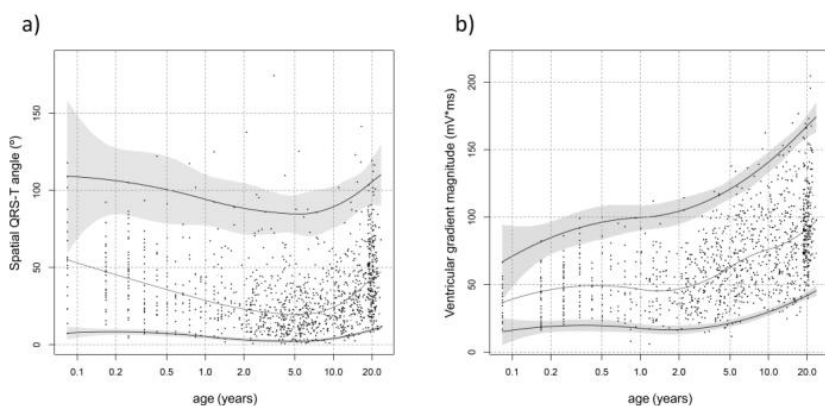


Figure 2. Scatter plots of VCG variables versus age. The black curves show the estimated medians and 2nd and 98th percentiles. The 95% confidence intervals are shown in grey. a) Scatter plot of QRS-T angle versus age. b) Scatter plot of ventricular gradient versus age.

Table 2. ECG and VCG variables

Age	HR	QRS duration	QT interval	QTc*	SA	VG
	<i>bpm</i>	<i>ms</i>	<i>ms</i>	<i>ms</i>	<i>°</i>	<i>mV.ms</i>
1 month	152 (104,180)	58 (49,78)	255 (227,319)	405 (383,463)	55 (8,109)	37 (15,67)
2 months	146 (103,183)	61 (49,82)	258 (224,305)	400 (369,451)	47 (8,107)	45 (18,82)
4.5 months	137 (99,179)	64 (51,85)	263 (226,299)	395 (358,440)	39 (8,103)	49 (20,93)
9 months	128 (94,170)	66 (53,87)	269 (232,303)	392 (351,432)	32 (6,97)	48 (19,99)
2 years	112 (83,149)	70 (58,89)	284 (249,322)	388 (348,426)	23 (3,88)	47 (17,104)
4 years	98 (73,131)	75 (63,93)	303 (268,348)	388 (349,427)	20 (2,85)	57 (20,116)
6.5 years	88 (65,118)	80 (67,98)	323 (284,371)	391 (351,431)	20 (2,85)	69 (24,128)
10 years	78 (59,108)	85 (71,103)	345 (299,395)	393 (352,435)	24 (4,89)	76 (30,141)
14 years	72 (54,101)	89 (74,108)	360 (310,414)	396 (352,440)	32 (6,96)	82 (35,153)
18 years	71 (51,98)	93 (77,112)	366 (318,426)	398 (352,444)	40 (9,102)	88 (40,163)

Data is shown as median (2nd, 98th percentile). Abbreviations: ECG=electrocardiogram, SA=spatial angle, VG=ventricular gradient, VCG=vectorcardiogram. *QTc was calculated with Bazett's formula: $QT/\sqrt{(RR)}$.

Discussion

In the dynamic period between birth and adulthood many structural and functional changes occur, which cause changes in the ECG as a function of age. Several of the dynamic changes in electrocardiographic variables have to be explained by combined changes in the source of the electrocardiogram (the heart) and in the volume conductor between the heart and the body surface (the thorax). Some electrocardiographic variables are independent of the volume

conductor and can be considered as cardiac properties (e.g., heart rate, QRS duration and QT interval). We will discuss these cardiac properties first.

ECG variables

Several studies have been published that determined the normal limits in the pediatric ECG [13, 19-22]. In our study group, heart rate declined with age. Median values in the pediatric age groups correspond well with the median heart rate values as reported by Rijnbeek et al. [13]. Comparison of the 2nd and 98th percentiles show some differences in the lowest age groups; this is likely the consequence of limited sample size and a different statistical method to assess percentiles. The current study showed that the median resting heart rate in our study group stabilized after puberty. This stabilization is not evident from the study by Rijnbeek et al. [13]; our additional inclusion of a group of normal subjects aged 18–24 years allowed for an improved assessment of trends in the highest pediatric age range. The current study showed that median QRS duration constantly increases over all age groups, with no stabilization yet at the age of 18 years. QRS duration and trend roughly correspond to the pediatric normal values described by Rijnbeek et al. [13]. Rijnbeek et al. [13] have shown a significant difference in the 98th percentile of the QRS duration between boys and girls in the age groups “3–6 months” and “6–12 months”. However, this difference was maximally 7 ms and, hence, has limited clinical significance. Note that the trend at higher ages (18–24) cannot be interpreted because of a possible border effect caused by the smoothing algorithm. However, the study by Rijnbeek et al. [12] in subjects until 90 years of age, also showed this trend; in their study it appears that QRS duration only stabilizes at the mid 20's. Compared to the QTc values in the Rijnbeek publication [13] our median values are 10–15 ms shorter and show a U shape with a minimum around the age of 3 years. These differences are likely caused by different methods for determination of the end of the T wave. The LEADS program [14] determines the T wave in the heart-vector magnitude, computing the instant at which the tangent to the steepest slope of the terminal part of the T wave intersects zero. The ECG analysis program used by Rijnbeek et al. uses a template-matching method. Macfarlane et al. report QTc values in a large database of 1784 healthy neonates, infants, and children [23], which are strikingly similar to our values even though QTc in that study was corrected by the Hodges formula.

Spatial QRS-T angle

Several studies have shown, in an adult population, that an abnormal (i.e., large) SA can improve prediction of sudden cardiac death and overall mortality in a general population [6, 7]. Recently, Cortez et al. showed that a smaller SA rules out sustained ventricular

arrhythmias in children with hypertrophic cardiomyopathy [24]. Our data showed that the median SA steadily decreased until the age of 8 years, after which the SA increased without stabilization in the highest age group. This could be caused by changes in the expression of action potential morphology differences between the endocardium and the epicardium over age. Additionally, the RV dominance in the infant heart gradually changes to LV dominance in the adult; which influences the QRS and the T vectors. However, we have to realize that these ECG-derived vectorcardiographic measures do not necessarily have the same physiologic explanation as in adults. The trend in SA as observed by Rautaharju et al. [11] in pediatric Frank VCGs is comparable to our results; in their study the spatial angle between the QRS and STT integral vectors reaches its minimum in the age group 1.5–4.5 years, after which it increases again. Edenbrandt et al. [25] studied the ECGs of 1792 healthy children; however, these ECGs were synthesized with the adjusted Dower matrix. Furthermore, the QRS-T angle was only determined in the transverse plane [25]. Altogether, the results of this study cannot be compared to our results.

Another study by Dilaveris et al. [26] reports about ECGs recorded in 646 children with a mean age of 8.54 ± 1.86 years. Also, in that study the inverse Dower matrix was used to synthesize the VCG. Moreover, the spatial QRS-T angle was computed as the angle between the maximum QRS and T vectors. In our study, we adopted the common definition, and computed the SA as the angle between the mean QRS and T vectors (i.e., the angle between the QRS and T axes). The limited age range and the methodological differences of the study by Dilaveris et al. [26] hamper comparison to our results. Normal values of SA have been published for young adults [10]. However, part of the ECGs used in that study [10] were also used in the current study and in that study the inverse Dower matrix was used to synthesize the VCGs. It has been demonstrated that use of the Kors matrix yields different SA values than the inverse Dower matrix [27]. Nowadays, the Kors matrix is generally accepted as the best VCG synthesis matrix [27, 28]. For this reason, VG and SA results were not compared to the results of current study.

Ventricular gradient

It has been shown in adults, that the VG, a three-dimensional measure of ventricular action potential duration heterogeneity [29], has additional diagnostic value in the electrocardiographic detection of pulmonary hypertension [2, 3]. VG could potentially also be a valuable diagnostic tool in children with a congenital heart defect, especially those at risk of pulmonary hypertension. Our study showed that the median VG magnitude was relatively stable until the age of around 2 years after which it increased without having stabilized at higher ages. Rautaharju et al. [11], who measured the VG in Frank VCGs, report

a different trend. They observed an initial increase in median VG value till around 100 mV·ms at the age of around 6 years, after which a slight decrease was observed till 90 mV·ms at the age of 16 years. In contrast, our data showed a median VG value of 69 mV·ms at age 6.5 years. Results in the highest age group of Rautaharju et al. [11] are comparable to our results. A possible explanation could be that the Kors matrix is less suitable for synthesizing Frank VCGs in children. Even though there is little evidence of clustering of our normal values of the derived VG and SA around the mean, this is not unique for pediatric ECGs and not caused by the use of the Kors transformation. Also in adults, VG and SA do not cluster very well in matrix-derived-VCGs [10] and the same observation was done in the actual Frank VCG [27].

Diagnostic validity

At present, it is not clear to what extent a synthesized pediatric VCG by using the Kors matrix equals a Frank VCG. The Kors matrix has been developed with a database consisting of simultaneously recorded standard 12-lead ECGs and Frank VCGs in adults. It is likely that the Kors matrix will yield less accurate Frank VCGs the more the pediatric thoracic anatomy differs from the average adult's anatomy. This can be verified only when similar simultaneous 12-lead ECGs and Frank VCGs are recorded in children, which warrants further studies. Moreover, in this respect, the question arises as to how well a Frank VCG in children yields valid heart vector components (X, Y, Z). Actually, the Frank VCG rests on a physical model of an adult torso with homogeneous conduction characteristics (without lungs). When doing justice to the dynamic anatomy of human growth, separate models for various age stages should be developed. This would likely lead to different weighting coefficients in the Frank resistor network between the Frank electrodes and the X, Y and Z heart vector components. Corresponding ECG-to-VCG matrices could then be generated by simultaneously recorded 12 lead ECGs and the corrected Frank VCGs for each age group. Following this reasoning, it is not likely that the Kors-VCG-derived metrics in a pediatric population have a diagnostic value that corresponds to the adult measurements. However, a consistently applied algorithm will still produce valid results. After an inventory of normal values as done in the current study, extreme values outside the normal range can be considered pathologic. A study group with various pathologies could reveal how much overlap exists between the normal and the abnormal group. For this purpose, future studies are needed. At this moment, it cannot be predicted if the metrics as provided in this study (SA and VG) will be able to separate normal from abnormal. Though, even when this would not be possible, it is still relevant to study individual trends by serial ECG/VCG analysis because any change in the individual ECG/VCG outside the spontaneous variability should be noted and interpreted within the clinical situation. The current study could be considered as a first step in this process.

Limitations

Our study is limited by the fact that the study data consists of a mix of ECG recordings sampled at 250 samples per second, 500 samples per second and 1000 samples per second. Rijnbeek et al. [30] demonstrated that the maximal positive and negative QRS deflections in pediatric ECGs recorded with a high-frequency bandwidth start to decrease with high-frequency cut-off values below 250 Hz; they conclude that the bandwidth of pediatric ECGs should be increased to 250 Hz. However, at present, not every clinic records ECGs with such high bandwidths and most ECG machines will have a bandwidth of around 0–150 Hz. Also, the average difference in pediatric ECG amplitude measurements with a higher bandwidth was shown by Rijnbeek et al. [30], to be in the order of 50 μ V, which is not clinically relevant. Future studies should assess normal values of different age groups with changing bandwidth. The influence of low bandwidth on SA and VG is unknown. We assume, though, that this influence is limited, because these variables are integrals, and the amount of high-frequency energy content in the ECG is very small. Similar to Rijnbeek et al. [13], age categories “0–1 day”, “1–3 days”, “3–7 days” and “1–4 weeks” as used in the study by Davignon et al. [20] had to be combined into one category “0–1 month” because of the small number of subjects in the lower age groups. Therefore, the reference values that we produced in these groups have to be used carefully. These age groups require further study. Furthermore, because of a small number of subjects in the lower age groups, we were not able to compare male to female values.

Conclusion

Normal values of the ventricular gradient and spatial QRS-T angle, derived from the pediatric electrocardiogram, were established. These normal values could be important for future studies using ventricular gradient and spatial QRS-T angle for risk stratification in heart disease in children.

References

1. Man S, Maan AC, Schalij MJ, Swenne CA: Vectorcardiographic diagnostic & prognostic information derived from the 12-lead electrocardiogram: Historical review and clinical perspective. *J Electrocardiol* 2015, 48:463-475.
2. Kamphuis VP, Haack ML, Wagner GS, Maan AC, Maynard C, Delgado V, Vliegen HW, Swenne CA: Electrocardiographic detection of right ventricular pressure overload in patients with suspected pulmonary hypertension. *J Electrocardiol* 2014, 47:175-182.
3. Scherptong RW, Henkens IR, Kapel GF, Swenne CA, van Kralingen KW, Huisman MV, Schuerwegh AJ, Bax JJ, van der Wall EE, Schalij MJ, Vliegen HW: Diagnosis and mortality prediction in pulmonary hypertension: the value of the electrocardiogram-derived ventricular gradient. *J Electrocardiol* 2012, 45:312-318.
4. Lingman M, Hartford M, Karlsson T, Herlitz J, Rubulis A, Caidahl K, Bergfeldt L: Value of the QRS-T area angle in improving the prediction of sudden cardiac death after acute coronary syndromes. *Int J Cardiol* 2016, 218:1-11.
5. Kardys I, Kors JA, van der Meer IM, Hofman A, van der Kuip DA, Witteman JC: Spatial QRS-T angle predicts cardiac death in a general population. *Eur Heart J* 2003, 24:1357-1364.
6. Waks JW, Sitlani CM, Soliman EZ, Kabir M, Ghafoori E, Biggs ML, Henrikson CA, Sotoodehnia N, Biering-Sorensen T, Agarwal SK, et al: Global Electric Heterogeneity Risk Score for Prediction of Sudden Cardiac Death in the General Population: The Atherosclerosis Risk in Communities (ARIC) and Cardiovascular Health (CHS) Studies. *Circulation* 2016, 133:2222-2234.
7. Whang W, Shimbo D, Levitan EB, Newman JD, Rautaharju PM, Davidson KW, Muntner P: Relations between QRS/T angle, cardiac risk factors, and mortality in the third National Health and Nutrition Examination Survey (NHANES III). *Am J Cardiol* 2012, 109:981-987.
8. Draper HW, Peffer CJ, Stallmann FW, Littmann D, Pipberger HV: The Corrected Orthogonal Electrocardiogram and Vectorcardiogram in 510 Normal Men (Frank Lead System). *Circulation* 1964, 30:853-864.
9. Pipberger HV, Goldman MJ, Littmann D, Murphy GP, Cosma J, Snyder JR: Correlations of the orthogonal electrocardiogram and vectorcardiogram with constitutional variables in 518 normal men. *Circulation* 1967, 35:536-551.
10. Scherptong RW, Henkens IR, Man SC, Le Cessie S, Vliegen HW, Draisma HH, Maan AC, Schalij MJ, Swenne CA: Normal limits of the spatial QRS-T angle and ventricular gradient in 12-lead electrocardiograms of young adults: dependence on sex and heart rate. *J Electrocardiol* 2008, 41:648-655.
11. Rautaharju PM, Davignon A, Soumis F, Boisselle E, Choquette A: Evolution of QRS-T relationship from birth to adolescence in Frank-lead orthogonal electrocardiograms of 1492 normal children. *Circulation* 1979, 60:196-204.
12. Rijnbeek PR, van Herpen G, Bots ML, Man S, Verweij N, Hofman A, Hillege H, Numans ME, Swenne CA, Witteman JC, Kors JA: Normal values of the electrocardiogram for ages 16-90 years. *J Electrocardiol* 2014, 47:914-921.
13. Rijnbeek PR, Witsenburg M, Schrama E, Hess J, Kors JA: New normal limits for the paediatric electrocardiogram. *Eur Heart J* 2001, 22:702-711.
14. Draisma HHMS, Swenne CA, van de Vooren H, Maan AC, Hooft van Huysduynen B, van der Wall EE, Schalij MJ: LEADS: an interactive research oriented ECG/VCG analysis system. *Comput Cardiol* 2005:515-518.
15. Kors JA, van Herpen G, Sittig AC, van Bommel JH: Reconstruction of the Frank vectorcardiogram from standard electrocardiographic leads: diagnostic comparison of different methods. *Eur Heart J* 1990, 11:1083-1092.
16. Pin NG, Maechler M.: A fast and efficient implementation of qualitatively constrained quantile smoothing splines. *Statistical Modelling* 2007, 7:315 - 328.
17. COBS - Constrained B-splines (Sparse matrix based). R package version 1.3-0. [<http://CRAN.R-project.org/package=cobs>]
18. R: A language and environment for statistical computing [<http://www.R-project.org>]
19. Macfarlane PW, van Oosterom, A., Pahlm, O., Kligfield, P., Janse, M., Camm, J. (Eds.): *Comprehensive Electrocardiology*. 2 edn. London: Springer; 2011.

20. Davignon A: Normal ECG standards for infants and children. . *Pediatr Cardiol* 1979;133-152.
21. Macfarlane PW, Coleman EN, Pomphrey EO, McLaughlin S, Houston A, Aitchison T: Normal limits of the high-fidelity pediatric ECG. Preliminary observations. *J Electrocardiol* 1989, 22 Suppl:162-168.
22. Sun K: Normal ECG limits for asian infants and children. *Comput Cardiol* 2005:455-458.
23. Macfarlane PW, McLaughlin SC, Rodger JC: Influence of lead selection and population on automated measurement of QT dispersion. *Circulation* 1998, 98:2160-2167.
24. Cortez D, Sharma N, Cavanaugh J, Tuofo F, Derk G, Lundberg E, Weiner K, Kiciman N, Alejos J, Landeck B, et al: Lower spatial QRS-T angle rules out sustained ventricular arrhythmias in children with hypertrophic cardiomyopathy. *Cardiol Young* 2016:1-5.
25. Edenbrandt L, Houston A, Macfarlane PW: Vectorcardiograms synthesized from 12-lead ECGs: a new method applied in 1792 healthy children. *Pediatr Cardiol* 1994, 15:21-26.
26. Dilaveris P, Roussos D, Giannopoulos G, Katinakis S, Maragiannis D, Raftopoulos L, Arsenos P, Gatzoulis K, Stefanadis C: Clinical determinants of electrocardiographic and spatial vectorcardiographic descriptors of ventricular repolarization in healthy children. *Ann Noninvasive Electrocardiol* 2011, 16:49-55.
27. Schreurs CA, Algra AM, Man SC, Cannegieter SC, van der Wall EE, Schalij MJ, Kors JA, Swenne CA: The spatial QRS-T angle in the Frank vectorcardiogram: accuracy of estimates derived from the 12-lead electrocardiogram. *J Electrocardiol* 2010, 43:294-301.
28. Man S, Algra AM, Schreurs CA, Borleffs CJ, Scherptong RW, van Erven L, van der Wall EE, Cannegieter SC, Schalij MJ, Swenne CA: Influence of the vectorcardiogram synthesis matrix on the power of the electrocardiogram-derived spatial QRS-T angle to predict arrhythmias in patients with ischemic heart disease and systolic left ventricular dysfunction. *J Electrocardiol* 2011, 44:410-415.
29. Draisma HH, Schalij MJ, van der Wall EE, Swenne CA: Elucidation of the spatial ventricular gradient and its link with dispersion of repolarization. *Heart Rhythm* 2006, 3:1092-1099.
30. Rijnbeek PR, Kors JA, Witsenburg M: Minimum bandwidth requirements for recording of pediatric electrocardiograms. *Circulation* 2001, 104:3087-3090

Chapter 4

Electrical remodeling after percutaneous atrial septal defect closure in pediatric and adult patients

Vivian P Kamphuis*, Martina Nassif*, Sum-Che Man, Cees A Swenne, Jan A Kors, A Suzanne Vink, Arend DJ ten Harkel, Arie C Maan, Barbara JM Mulder, Rob J de Winter, Nico A Blom

* equal contribution

Submitted for publication

Abstract

Objective

Several studies have reported changes in electrocardiographic variables after ostium secundum atrial septal defect (ASDII) closure. However no temporal electro-and vectorcardiographic changes have been described from acute to long-term follow-up at different ages. We aimed to study electrical remodeling after percutaneous ASDII closure in pediatric and adult patients.

Methods

ECGs of 69 children and 75 adults (median age 6 [IQR4-11] years and 45 [IQR 33-54] years, respectively) were retrospectively selected before percutaneous ASDII closure and at acute (1-7 days), intermediate (4-14 weeks) and late (6-18 months) follow-up. Apart from electrocardiographic variables, spatial QRS-T angle and ventricular gradient (VG) were derived from mathematically-synthesized vectorcardiograms.

Results

In both pediatric and adult patients, the heart rate decreased immediately post-closure, which persisted to late follow-up. The P-wave amplitude also decreased acutely post-closure, but remained unchanged at later follow-up. The PQ duration shortened immediately in children and at intermediate follow-up in adults. The QRS duration and QTc interval decreased at intermediate-term follow-up in both children and adults. In both groups the spatial QRS-T angle decreased at late follow-up. The VG magnitude increased at intermediate follow-up in children and at late follow-up in adults, after an initial decrease in children.

Conclusion

In both pediatric and adult ASDII patients, electrocardiographic changes mainly occurred directly after ASDII closure except for shortening of QRS duration and QTc interval, which occurred at later follow-up. Adults also showed late changes in PQ duration. At 6-to-18-months post-closure, the spatial QRS-T angle decreased, reflecting increased electrocardiographic concordance. The initial acute decrease in VG in children, which was followed by a significant increase, may be the effect of action potential duration dynamics directly after percutaneous ASDII closure.

Introduction

The ostium secundum atrial septal defect (ASDII) is one of the most common congenital heart diseases and is defined as an interatrial septum defect at the site of the fossa ovalis, causing a left-to-right shunt [1]. A hemodynamically significant shunt causes volume overload of the right atrium (RA), right ventricle (RV) and the pulmonary circulation, and is, therefore, an indication for ASDII closure to prevent further right-sided deterioration such as volume and/or pressure overload and eventually heart failure [2]. Closing an ASD-based left-to-right shunt initiates both geometrical and electrical RA and RV remodeling [3, 4], the extent of which may depend on several factors including the patients' age at closure and closure technique. Percutaneous ASDII closure is currently the first choice of treatment in selected cases, due to the minimal invasiveness, and has proven to reduce morbidity and mortality similar to surgical closure [1].

The electrocardiogram (ECG) is the standard tool to visualize cardiac electrical activation, and after ASDII closure it can show potential complications such as atrial arrhythmias [2] as well as the electrical reverse remodeling at several time points. The latter gives insight into the long-term process of reverse remodeling, in which distinction is made between acute and late effects of ASDII closure. The standard 12-lead ECG only allows for scalar, one-dimensional, visualization of the electrical currents in the heart. The vectorcardiogram (VCG), however, offers several advantages over the 12-lead ECG. Firstly, the lead vectors of the X-, Y- and Z-lead assume the directions of the main anatomical axes of the body. Furthermore, the sensitivities of these X-, Y- and Z-lead are equal. Lastly, by displaying the instantaneous electrical heart activity (represented as the heart vector) in three-dimensional (3D) space, the phase-relationships between the X-, Y- and Z-leads become apparent [5]. Historically, the VCG was recorded directly with the Frank VCG system; currently, conversion of a 12-lead ECG to a VCG by mathematical transformation (using the inverse Dower or Kors matrix [6]) is the standard. Two vectorcardiographic variables in particular have recently gained interest: the ventricular gradient (VG), which has been shown useful in the detection of RV pressure overload [7], and the spatial QRS-T-angle, which has shown prognostic value in the prediction of sudden cardiac death [8].

Several studies have reported changes in ECG variables after ASDII closure [3, 9-12], however no temporal ECG and VCG changes have been described from acute to long-term follow-up at different ages. Hence, the objective of this study was to assess acute, intermediate and late electrical remodeling in terms of ECG and VCG changes after ASDII closure in both children and adults.

Methods

Study design and population

In this multicenter retrospective cohort study, all patients with an ASDII who were referred to the Center for Congenital Heart Disease Amsterdam Leiden (CAHAL) for percutaneous ASDII closure in a period of 13 months (2016-2017) were screened. The study cohort comprised of pediatric (age 0-17 years) and adult patients (age ≥ 18 years) who had a 12-lead ECG in sinus rhythm maximally 14 weeks before successful ASDII closure and at acute (1-7 days) or intermediate (4-14 weeks) follow-up after closure. Additionally, when available in these patients, ECGs that were made late (6-18 months) after closure were also assessed. All the included ECGs were made as part of routine clinical follow-up. Baseline patient characteristics, clinical history and medication were collected from medical records. The Medical Ethics Committee provided a statement of no objection for obtaining and publishing the anonymized data.

ASD closure

Percutaneous ASDII closure was performed conform current guidelines, in which ASD closure is indicated in the presence of hemodynamically significant left-to-right shunting with pulmonary vascular resistance < 5 Woods units (Class I, level B) [2]. Patients underwent general anesthesia and an Amplatzer Septal Occluder (Abbott Vascular Inc., Santa Clara, CA, USA) of appropriate size was implanted under transesophageal echocardiographic guidance.

ECG/VCG processing

All ECGs made in Leiden were recorded with ELI 250 and 350 electrocardiographs (Mortara Instrument, Milwaukee, USA) with a sampling rate of 1000 samples per second. The ECGs made in Amsterdam were recorded with MAC5500 electrocardiographs (GE Healthcare, Milwaukee, USA) with sampling rates of 250 or 500 samples per second. All ECG and VCG measurements were performed with the Modular ECG Analysis System (MEANS) [13], which has been evaluated extensively, both by its' developers and by others [14, 15]. For each lead, MEANS performs baseline correction, removes main interference, and computes a representative averaged beat after excluding ectopic beats. MEANS determines global fiducial points in the averaged beats of all 12 leads together, resulting in an overall P-wave onset, P-wave offset, QRS complex onset and offset, and T-wave offset. The following ECG variables were assessed: heart rate, P-wave amplitude in lead II, P-wave duration, PQ duration, QRS duration and the QT interval, corrected with Bazett's formula (QTc).

The X-, Y- and Z leads of the VCGs were synthesized from the ECGs by the Kors transformation matrix [6]. For the directions of the X-, Y- and Z axes and the spatial vector orientation (azimuth, elevation), the American Heart Association VCG standard was followed [16]. From the VCG, the spatial QRS-T-angle was computed as the spatial angle between the QRS- and T-integral vectors. Also, the azimuth, elevation and magnitude of the VG (vectorial sum of the QRS and the T integrals) were assessed, as well as its components in the X-, Y- and Z-direction (VG-X, VG-Y and VG-Z).

Statistical analysis

Statistical analyses were performed in SPSS v.23 (IBM, Armonk, NY, USA). Quantitative data are presented as median [25th-75th percentile] with minimum and maximum where relevant for continuous variables, and as frequencies (percentages) for categorical variables. Comparisons between ECG- and VCG parameters at different time points (i.e. acute, intermediate and late follow-up) included one ECG/VCG per time interval and were performed using the Wilcoxon signed-rank test. Correlations between ECG/VCG-parameters and patient characteristics were tested using the Spearman correlation. A *P*-value <0.05 was considered statistically significant.

Results

In total, 168 patients were screened (75 children and 93 adults), of which 144 patients met the inclusion criteria (69 children and 75 adults). Baseline characteristics, stratified by pediatric and adult groups, are shown in *Table 1*. Not all patients had an ECG at all four time points, absolute numbers are shown in *Table 1*. Median age of children was 6 years [4-11 years] (range 5 months–17 years), and of adults 45 years [33-54 years] (range 18-79 years). Fourteen adults (19%) had paroxysmal atrial fibrillation.

Table 1. Baseline patient characteristics of the study cohort

	Children N=69	Adults N=75
Demographics		
Age, y	6 [4-11]	45 [33-54]
Male	26 (38%)	24 (32%)
Body mass index, kg/m ²	16.2[14.5-18.3]	26 [23-29]
Number of ECGs		
Number of patients with an ECG before closure	69 (100%)	75 (100%)
Number of patients with an ECG at acute follow-up	69 (100%)	74 (99%)
Number of patients with an ECG at intermediate follow-up	32 (46%)	56 (75%)
Number of patients with an ECG at late follow-up	20 (29%)	49 (65%)
Clinical history		
Chromosomal disorder	4 (6%)	0 (0%)
Down syndrome	1 (1%)	0 (0%)
Turner	1 (1%)	0 (0%)
22q11 deletion	1 (1%)	0 (0%)
Smith-Lemli-Opitz syndrome	1 (1%)	0 (0%)
Paroxysmal atrial fibrillation	0 (0%)	14 (19%)
Medication		
Anti arrhythmica (β-blockers)	0 (0%)	5 (6.7%)
QT-prolongating drugs (Methylphenidate)	1 (1.4%)	0 (0%)
ASDII-related characteristic		
Occluder size	14 [12-18]	22 [17-26]

Data are presented as median [25th-75th percentile] or frequency (%)

ECG changes after ASDII closure in children

ECG variables of the pediatric patients at the different time points are shown in *Table 2*. In children, heart rate significantly decreased acutely after ASDII closure, which became most evident at late follow-up. The P-wave amplitude in lead II showed a significant decrease in the acute period after closure; however, later follow-up showed no significant changes compared to baseline. P-wave duration did not change at post-procedural follow-up. The PQ duration, however, showed a significant decrease from baseline at acute and intermediate follow-up. Compared to the baseline ECG, the QRS duration, as well as the QTc interval, were shorter at intermediate-term follow-up.

ECG changes after ASDII closure in adults

ECG variables of the adult patients are shown in *Table 2* at the different time points. In this age group, the heart rate also decreased significantly acutely after intervention. The P-wave amplitude in lead II showed an acute significant decrease, while late effects of ASDII closure were not observed. P-wave duration did not change at post-procedural follow-up. However, the PQ duration shortened from baseline to intermediate and late follow-up. Compared to the baseline ECG, QRS duration and the QTc-interval shortened significantly at intermediate-term and late follow-up.

VCG changes after ASDII closure in children

The VCG parameters of pediatric patients are shown in *Table 3* at the different time points. The spatial QRS-T-angle remained equal at acute and intermediate post-procedural follow-up, but showed a significant decrease at late follow-up. Compared to baseline, VG magnitude significantly decreased acutely after closure, however significantly increased at intermediate and late follow-up. VG azimuth showed a significant change at intermediate follow-up. VG elevation showed no significant changes at follow-up compared to baseline. *Figure 1* shows the spatial median VG changes and the changes projected in each of the three standard planes in the pediatric patients. The X-, Y- and Z components of the VG in the pediatric group are shown in *Table 3*. The VG-X first showed an acute decrease compared to baseline, after which the VG-X increased at intermediate and late follow-up. Similarly, the VG-Y, also showed an acute decrease compared to baseline, followed by an increase at late follow-up. The VG-Z showed a significant increase at intermediate follow-up and late follow-up.

VCG changes after ASDII closure in adults

The VCG parameters of the adult patients at the different time points are shown in *Table 3*. The spatial QRS-T-angle remained equal at acute and intermediate post-procedural follow-up, but showed a significant decrease at late follow-up. Compared to baseline, VG magnitude significantly increased at late follow-up. VG azimuth showed a significant change at intermediate follow-up. VG elevation showed an acute decrease but no significant change compared to baseline at intermediate and late follow-up. *Figure 2* shows the spatial median VG changes and the changes projected in each of the three standard planes in the adult patients. The X-, Y- and Z-coordinates of the VG in the adult group are also shown in *Table 3*. The VG-X showed an increase at intermediate and late follow-up compared to baseline. The VG-Y first showed an acute decrease compared to baseline, after which the VG-Y increased again at late follow-up. The VG-Z shows a significant increase at intermediate follow-up.

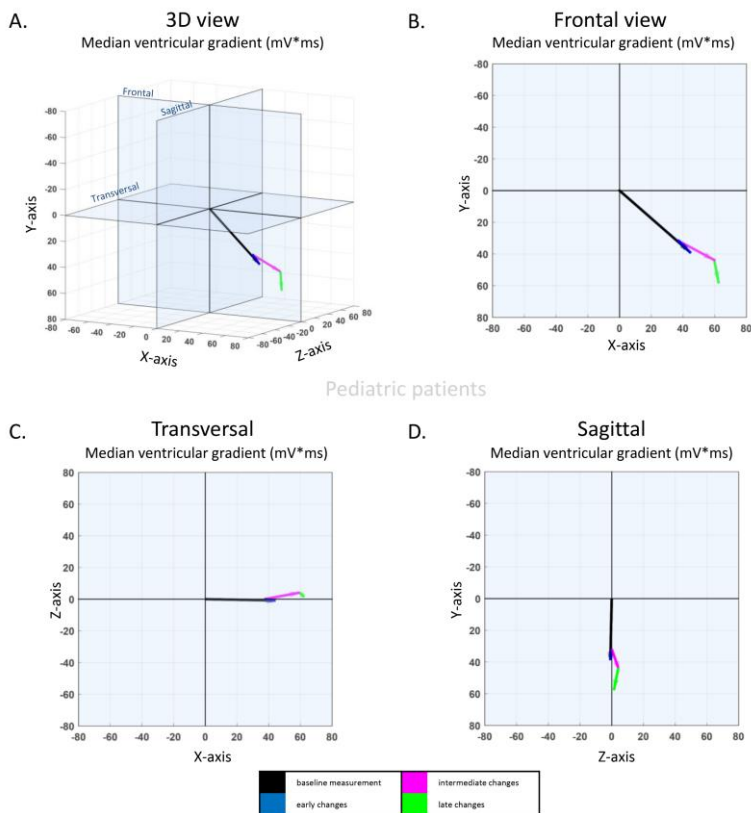


Figure 1. Representation of the spatial changes of the median ventricular gradient in the pediatric patients. A. Three-dimensional (3D) view of the VG changes. B. Frontal view C. transversal view D. Sagittal view. In all images the black line represents the baseline measurement, the blue line represents the early changes, the purple line represents the intermediate changes and the green line represents the late changes.

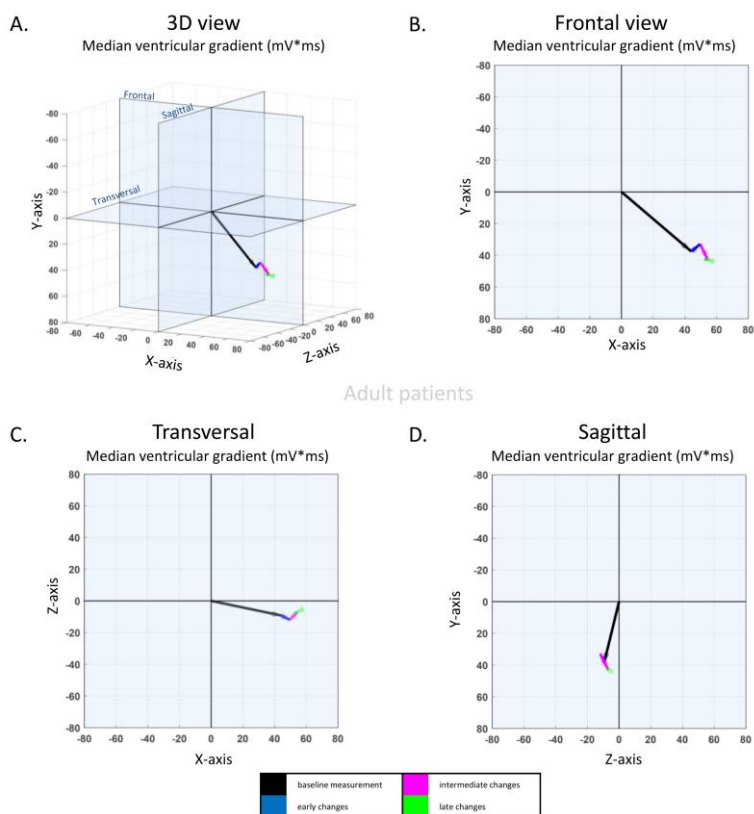


Figure 2. Representation of the spatial changes of the median ventricular gradient in the adult patients. A. Three-dimensional (3D) view of the VG changes. B. Frontal view C. transversal view D. Sagittal view. In all images the black line represents the baseline measurement, the blue line represents the early changes, the purple line represents the intermediate changes and the green line represents the late changes.

Table 2. ECG results at baseline and post ASDII closure

	Baseline	Acute	P-value	Intermediate	P-value	Late	P-value
	Max -14 w	+ 1-7 d	Baseline-acute	+ 4-14 w	Baseline-intermediate	+ 6-18 m	Baseline-late
<i>Children</i>							
Heart rate, bpm	94 [83-109]	91 [82-102]	0.01	92 [75-102]	0.005	82 [71-92]	0.001
P-wave amplitude in lead II, mV	0.13 [0.11-0.18]	0.11 [0.09-0.15]	<0.001	0.14 [0.12-0.19]	0.51	0.12 [0.08-0.18]	0.55
P-wave duration, ms	94 [92-100]	94 [90-100]	0.24	94 [88-99]	0.08	96 [92-106]	0.24
PQ duration, ms	139 [132-152]	134 [128-148]	0.007	132 [124-149]	<0.001	138 [128-160]	0.52
QRS duration, ms	90 [81-100]	88 [81-97]	0.05	89 [77-98]	<0.001	89 [80-96]	0.06
QTc interval, ms	433 [422-449]	431 [422-447]	0.19	429 [420-440]	0.02	424 [410-448]	0.15
<i>Adults</i>							
Heart rate, bpm	72 [61-81]	67 [59-78]	<0.001	65 [58-76]	0.014	65 [56-74]	<0.001
P-wave amplitude in lead II, mV	0.15 [0.10-0.16]	0.11 [0.08-0.14]	<0.001	0.13 [0.10-0.16]	0.07	0.14 [0.11-0.17]	0.63
P-wave duration, ms	115 [106-125]	114 [104-126]	0.63	112 [102-123]	0.20	113 [104-124]	0.11
PQ duration, ms	163 [150-184]	162 [148-185]	0.62	157 [144-172]	0.01	106 [94-116]	0.009
QRS duration, ms	106 [94-116]	108 [94-118]	0.46	101 [91-112]	0.004	102 [92-109]	<0.001
QTc interval, ms	432 [414-451]	433 [416-449]	0.20	418 [407-441]	0.005	417 [404-435]	<0.001

Data are presented as median [25th-75th percentile].
d = days; w = weeks; m = months

Table 3. VCG results at baseline and post ASDII closure

	Baseline Max -14 w	Acute + 1-7 d	P-value* Baseline- acute	Intermediate + 4-14 w	P-value* Baseline- intermediate	Late + 6-18 m	P-value* Baseline-late
Children							
Spatial QRST angle, °	52 [30-84]	58 [26-81]	0.05	38 [24-77]	0.44	39 [19-56]	0.002
VG magnitude, mV.ms	63 [48-76]	55 [42-70]	<0.001	78 [64-103]	0.01	83 [68-107]	0.007
VG azimuth, °	-1 [-17-7]	0 [-21-13]	0.69	5 [-6-18]	0.006	1 [-11-18]	0.16
VG elevation, °	39 [34-45]	37 [32-44]	0.71	38 [30-45]	0.16	39 [33-45]	0.96
VG-X, mV.ms	44 [35-58]	37 [28-52]	<0.001	60 [45-74]	0.001	62 [49-78]	0.048
VG-Y, mV.ms	39 [29-51]	32 [23-44]	0.001	44 [34-63]	0.23	58 [38-75]	0.02
VG-Z, mV.ms	-1 [-15-5]	0 [-15-9]	0.17	4 [-7-17]	0.007	1 [-12-21]	0.03
Adults							
Spatial QRS-T angle, °	42 [21-82]	38 [22-70]	0.79	30 [17-45]	0.39	36 [20-48]	0.001
VG magnitude, mV.ms	66 [45-86]	63 [37-89]	0.32	75 [50-94]	0.08	70 [56-89]	0.001
VG azimuth, °	-12 [-26-0]	-15 [-24 to -3]	0.70	-7 [-17-3]	<0.001	-8 [-24-1]	0.48
VG elevation, °	39 [32-47]	36 [29-41]	<0.001	37 [31-44]	0.07	38 [29-45]	0.65
VG-X, mV.ms	44 [28-60]	50 [22-68]	0.43	55 [38-72]	0.01	52 [38-71]	0.001
VG-Y, mV.ms	38 [24-54]	33 [22-45]	<0.001	43 [26-61]	0.23	42 [27-60]	0.002
VG-Z, mV.ms	-9 [-20-0]	-12 [-24 to -2]	0.90	-7 [-22-3]	0.006	-8 [-26-1]	0.062

Data are presented as median [25th-75th percentile].

d = days; w = weeks; m = months

Discussion

In the present study, the acute, intermediate and late electrical remodeling in terms of ECG and VCG changes after percutaneous ASDII closure in children and adults was assessed. The main findings of the study are: 1) ASDII closure was followed by a sustained numerical decrease in heart rate, QRS duration and QTc interval in both children and adults. Except for the late QRS duration and QTc interval changes, most changes occurred directly after device closure. 2) The spatial QRS-T angle significantly decreased at late follow-up in both children and adults. 3) VG magnitude increased at intermediate follow-up in children and at late follow-up in adults, after an initial decrease in children. 4) VG direction change was most apparent in the less negative azimuth at intermediate follow-up in both groups, VG elevation directly decreased in the adult group but did not change during follow-up in the pediatric group.

Mechanisms of ECG changes after percutaneous ASDII closure

Right-sided volume overload due to atrial left-to-right shunting leads to both atrial and ventricular stretch which may cause changes on the 12-lead ECG [4, 17] due to mechano-electrical coupling. RA dilatation, for example, may result in increased P-wave amplitude as well as prolonged P-wave duration and increased P-wave dispersion due to delayed atrial conduction, which are all useful markers in the prediction of atrial arrhythmias [3, 12]. RV dilatation may result in QRS-duration prolongation, right bundle branch block and crochitage (a notch near the apex of the R-wave in the inferior limb leads [18]). Recently, it has been shown that RV volume overload can cause QTc-interval prolongation in ASDII patients [11]. Successful ASDII-closure should correct the right-sided volume overload within 24 hours, initiating geometric remodeling of the right atrium and ventricle, which continues up to 6-8 weeks following percutaneous ASDII closure [4, 19]. Indeed, multiple studies reported electrical remodeling after percutaneous ASDII closure [3, 9-12]. The present study showed a direct decrease in heart rate after ASDII closure in both children and adults, with a maintained decrease on the long term. We hypothesize that two mechanisms may have contributed to this heart rate decrease: deactivation of the Bainbridge reflex [20] and a decreased stretching of the pacemaking tissue in the sinus node [21]. Heart rate lowering via deactivation of the Bainbridge reflex after ASDII can be expected on the basis of deactivation of the stretch receptors at the junction of the vena cava and the right atrium. This will lead to decreased afferent neural traffic via fibers in the vagus nerve that project on the medulla. As a consequence, the reflex-induced inhibition of parasympathetic outflow to the sinus node will be decreased, and the reflex-induced enhancement of sympathetic outflow to the sinus node will be reduced, thus causing a slowing of the heart rate. Furthermore, RA

dimensions decrease. Since stretching of the sinus node tissue causes an increased intrinsic pacemaking rate, such decrease in RA size will have also contributed to the observed decrease in heart rate. In addition, the present study showed an acute decrease in P-wave amplitude in both groups, which is in line with the findings of a previous study done by Grignani et al. [3] They demonstrated an even further decrease in P-wave amplitude at their long-term follow-up of 45 ± 33 months post-closure, suggesting continuation of atrial remodeling over several years. In contrast to other studies [3, 10], the present study did not show a decrease in P-wave duration. We did find significant PQ-duration decrease directly after intervention in the pediatric group, and at intermediate follow-up in the adult group. The largest change in PQ duration was seen at late follow-up in the adult group, suggesting that even late after ASDII closure atrial remodeling takes place. Similar to previous studies [3, 10, 11], our results support the finding that ventricular electrical remodeling as reflected by QRS duration on the 12-lead ECG does not take place on the short-term after ASDII closure, despite clear RV geometrical remodeling within one-month post-closure reported by Veldtman et al. [19]. Our results showed that QRS duration slightly decreased at intermediate follow-up in both groups. While the presented change is clinically irrelevant, it may reflect ventricular electrical remodeling later after ASDII closure. A recent study by Rucklova et al. [11] suggested that RV volume overload in ASDII is associated with prolonged repolarization. In their study it was shown that QTc-interval was significantly shorter at 6 months after ASDII closure. In the present study we observed that the QTc-interval numerically shortens from the fourth week post-closure onwards, both in adults and children, which may indicate that shortening of the QTc-interval does not occur immediately after the reduction of RV volume overload after ASDII closure.

Mechanisms of VCG changes after percutaneous ASDII closure

In the current study, we have approached the dynamics in the VCG by measuring two general vectorcardiographic properties, the VG and the spatial QRS-T angle. The VG reflects the integrated action potential duration (APD) inhomogeneity in the heart [5, 22]. As such it is subject to cancellation and the magnitude and direction of the VG in a person expresses asymmetric inhomogeneity. Between individuals with normal hearts, the magnitude and direction of the VG varies considerably [23]. For this reason, individual trends in the VG are more informative than the overall VG value. In general, we may expect that any form of electrical remodeling in the heart is reflected in a change in the VG.

In an earlier study, the relation between the VG and RV pressure overload in patients with suspected pulmonary hypertension was shown [7]. VG changes were explained by different APD dynamics between subendocardial and epicardial myocytes as a result of RV pressure

overload [24, 25]. The hearts of ASDII patients are characterized by RV volume overload rather than RV pressure overload. The RV volume overload in ASDII patients results in APD prolongation in the RV epicardium [26]. Because successful ASDII closure eliminates the volume overload [19], we expect normalization of the APD prolongation and therefore a change in the VG. In the current study, median VG magnitude was 63 [48-76] mV.ms in children before ASDII closure, which is similar to the mean normal VG at 6.5 years of 69 mV.ms (2nd and 98th percentile: 24, 128) [27]. In adults, the VG magnitude before ASDII closure was 66 [45-86], which is in the normal range for adults [23]. In children, the VG magnitude showed an acute decrease, after which it increased again at intermediate follow-up. In adults the VG magnitude increased at late follow-up. A change in VG direction was most apparent in the azimuth becoming less negative at intermediate follow-up in both groups, while elevation decreased directly post-closure in the pediatric group but did not change during follow-up in the adult group. In our previous study on RV pressure overload [7], a preferential direction in which the VG changed with increasing pulmonary artery pressure was found. In the current study, however, we were not able to find a preferential direction in which the VG changed with decreasing RV volume overload due to successful ASDII closure.

The spatial QRS-T-angle is the angle between the QRS axis and the T axis [5]. As such it can be considered a measure of concordance/discordance of the ECG: a small QRS-T angle represents a concordant ECG in which the QRS-complex and T-wave polarities assume the same values in most ECG-leads, whereas a large, obtuse, QRS-T angle represents a discordant ECG in which the QRS-complex and T-wave polarities assume opposite values in most ECG leads. Generally, we may expect that changes in the QRS-complex or T-wave morphology always imply a change in the QRS and T axes, and, consequently, a change in the QRS-T angle. In many cases, an increase in the QRS-T angle is expected to represent a worsening condition. A larger spatial QRS-T angle has been linked to sudden cardiac death after acute coronary syndromes [28] and overall mortality in a general population [8]. Our study group included children of different ages with a median of 6 [4-11] years. Before closure of the ASDII, median QRS-T angle was 52 [30-84]° in the children, which is larger than the mean normal QRS-T angle in children of 6.5 years of 20° but still within the normal range (2th and 98th percentile: 2, 85°) [27]. In the adult group the QRS-T angle was 42°, which is in the normal range for adults [23]. In both groups, the spatial QRS-T angle significantly decreased at late follow-up. This most likely reflects ventricular electrical remodeling occurring relatively late after ASDII closure. Thus far, there are no data to suggest that a decrease in QRS-T angle also implies a lower risk of sudden death, arrhythmia or mortality in ASDII patients.

Limitations

This study has several limitations. Not all patients had an ECG at all four time points and the study group consisted of a relatively small number of patients; hence, further studies with larger and more homogeneous patient groups and more complete ECG data are needed to confirm our findings. Also, this study only targeted ECG and VCG measurements and did not focus on accompanying hemodynamic and morphological data to correlate electrical and structural reverse remodeling. Finally, the ECG data in the current study consist of a mix of ECGs with sampling rates of 250, 500 and 1000 samples per second. However, because the studied QRS-T angle and the VG are computed from ECG integrals, it is unlikely that differences in sampling rate have consequences for the VCG findings in this study.

Conclusion

Successful percutaneous atrial septal defect closure was followed by a decrease in heart rate, P-wave amplitude, PQ duration, QRS duration and QTc interval in both children and adults. Changes mostly occurred directly after ASDII closure except for QRS duration and QTc interval changes, which occurred later. Most of these electrocardiographic changes remained limited. The changes in the vectorcardiographic spatial QRS-T angle reflect increasing concordance of the electrocardiogram, which can be interpreted as partly normalization of the electrical properties of the heart. The ventricular gradient showed changes which can be seen as a result of action potential duration dynamics after atrial septal defect closure.

References

1. Lindsey JB, Hillis LD: Clinical update: atrial septal defect in adults. *Lancet* 2007, 369:1244-1246.
2. Baumgartner H, Bonhoeffer P, De Groot NM, de Haan F, Deanfield JE, Galie N, Gatzoulis MA, Gohlke-Baerwolf C, Kaemmerer H, Kilner P, et al: ESC Guidelines for the management of grown-up congenital heart disease (new version 2010). *Eur Heart J* 2010, 31:2915-2957.
3. Grignani RT, Tolentino KM, Rajgor DD, Quek SC: Longitudinal evaluation of P-wave dispersion and P-wave maximum in children after transcatheter device closure of secundum atrial septal defect. *Pediatr Cardiol* 2015, 36:1050-1056.
4. Monfredi O, Luckie M, Mirjafari H, Willard T, Buckley H, Griffiths L, Clarke B, Mahadevan VS: Percutaneous device closure of atrial septal defect results in very early and sustained changes of right and left heart function. *Int J Cardiol* 2013, 167:1578-1584.
5. Man S, Maan AC, Schalij MJ, Swenne CA: Vectorcardiographic diagnostic & prognostic information derived from the 12-lead electrocardiogram: Historical review and clinical perspective. *J Electrocardiol* 2015, 48:463-475.
6. Kamphuis VP, Haeck ML, Wagner GS, Maan AC, Maynard C, Delgado V, Vliegen HW, Swenne CA: Electrocardiographic detection of right ventricular pressure overload in patients with suspected pulmonary hypertension. *J Electrocardiol* 2014, 47:175-182.
7. Waks JW, Sitlani CM, Soliman EZ, Kabir M, Ghafoori E, Biggs ML, Henrikson CA, Sotoodehnia N, Biering-Sorensen T, Agarwal SK, et al: Global Electric Heterogeneity Risk Score for Prediction of Sudden Cardiac Death in the General Population: The Atherosclerosis Risk in Communities (ARIC) and Cardiovascular Health (CHS) Studies. *Circulation* 2016, 133:2222-2234.
8. Kors JA, van Herpen G, Sittig AC, van Bommel JH: Reconstruction of the Frank vectorcardiogram from standard electrocardiographic leads: diagnostic comparison of different methods. *Eur Heart J* 1990, 11:1083-1092.
9. Fang F, Luo XX, Lin QS, Kwong JS, Zhang YC, Jiang X, Yu CM, Lam YY: Characterization of mid-term atrial geometrical and electrical remodeling following device closure of atrial septal defects in adults. *Int J Cardiol* 2013, 168:467-471.
10. Kaya MG, Baykan A, Dogan A, Inanc T, Gunebakmaz O, Dogdu O, Uzum K, Eryol NK, Narin N: Intermediate-term effects of transcatheter secundum atrial septal defect closure on cardiac remodeling in children and adults. *Pediatr Cardiol* 2010, 31:474-482.
11. Rucklova K, Koubsky K, Tomek V, Kubus P, Janousek J: Prolonged repolarization in atrial septal defect: An example of mechanoelectrical feedback due to right ventricular volume overload. *Heart Rhythm* 2016, 13:1303-1308.
12. Thilen U, Carlson J, Platonov PG, Olsson SB: Atrial myocardial pathoelectrophysiology in adults with a secundum atrial septal defect is unaffected by closure of the defect. A study using high resolution signal-averaged orthogonal P-wave technique. *Int J Cardiol* 2009, 132:364-368.
13. van Bommel JH, Kors JA, van Herpen G: Methodology of the modular ECG analysis system MEANS. *Methods Inf Med* 1990, 29:346-353.
14. Willems JL, Arnaud P, van Bommel JH, Bourdillon PJ, Degani R, Denis B, Graham I, Harms FM, Macfarlane PW, Mazzocca G, et al.: A reference data base for multilead electrocardiographic computer measurement programs. *J Am Coll Cardiol* 1987, 10:1313-1321.
15. Morton JB, Sanders P, Vohra JK, Sparks PB, Morgan JG, Spence SJ, Grigg LE, Kalman JM: Effect of chronic right atrial stretch on atrial electrical remodeling in patients with an atrial septal defect. *Circulation* 2003, 107:1775-1782.
16. Heller J, Hagege AA, Besse B, Desnos M, Marie FN, Guerot C: "Crochetage" (notch) on R wave in inferior limb leads: a new independent electrocardiographic sign of atrial septal defect. *J Am Coll Cardiol* 1996, 27:877-882.
17. Veldtman GR, Razack V, Siu S, El-Hajj H, Walker F, Webb GD, Benson LN, McLaughlin PR: Right ventricular form and function after percutaneous atrial septal defect device closure. *J Am Coll Cardiol* 2001, 37:2108-2113.
18. Lingman M, Hartford M, Karlsson T, Herlitz J, Rubulis A, Caidahl K, Bergfeldt L: Value of the QRS-T area angle in improving the prediction of sudden cardiac death after acute coronary syndromes. *Int J Cardiol* 2016, 218:1-11.

19. Kamphuis VP, Blom NA, van Zwet EW, Man S, Ten Harkel ADJ, Maan AC, Swenne CA: Normal values of the ventricular gradient and QRS-T angle, derived from the pediatric electrocardiogram. *J Electrocardiol* 2018 May - Jun;51(3):490-495.
20. Scherptong RW, Henkens IR, Man SC, Le Cessie S, Vliegen HW, Draisma HH, Maan AC, Schalij MJ, Swenne CA: Normal limits of the spatial QRS-T angle and ventricular gradient in 12-lead electrocardiograms of young adults: dependence on sex and heart rate. *J Electrocardiol* 2008, 41:648-6

Chapter 5

Electrocardiographic detection of right ventricular pressure overload in patients with suspected pulmonary hypertension

Vivian P Kamphuis*, Marlieke L Haeck*, Galen S Wagner, Arie C Maan, Charles Maynard, Victoria Delgado, Hubert W Vliegen, Cees A Swenne

* equal contribution

J Electrocardiol. 2014 Mar-Apr;47(2):175-82.

Abstract

Objective

Early, preferably noninvasive, detection of pulmonary hypertension improves prognosis. Our study evaluated the diagnostic accuracy of the electrocardiographically derived Butler–Leggett (BL) score and ventricular gradient (VG) to estimate mean pulmonary artery pressure (PAP).

Methods

In 63 patients with suspected pulmonary hypertension, BL score and VG were calculated. The VG was projected on a direction optimized for detection of right ventricular pressure overload (VG-RVPO). BL score and VG-RVPO were entered in multiple linear regression analysis and the diagnostic performance to detect PH (invasively measured mean PAP ≥ 25 mmHg) was assessed with receiver operating characteristic analysis.

Results

Both BL score and VG-RVPO correlated significantly with mean PAP ($r = 0.45$ and $r = 0.61$, respectively; $P < 0.001$). Combining BL score and VG-RVPO increased the correlation to 0.67 ($P < 0.001$). The diagnostic performance of this combination for the detection of PH was good with an area under the curve of 0.79 ($P < 0.001$).

Conclusion

Combination of the BL score and VG-RVPO allows for accurate detection of increased PAP.

Introduction

Pulmonary hypertension (PH) is a serious condition with an unfavorable prognosis [1]. PH causes pressure overload of the right ventricle (RV) with an increase in RV wall tension and RV hypertrophy and dilatation [2]. Commonly, there is a delay in diagnosis of PH, partly due to the often mild and nonspecific symptoms of the disease and the absence of overt signs of RV dysfunction in the early stage of the disease. Early detection of PH is crucial in order to improve the prognosis [3–5]. Therefore, simple and widely available diagnostic tests to detect PH are needed, especially in patient groups at risk for the development of PH, such as patients with connective tissue disease or portal hypertension. The electrocardiogram (ECG) may provide such a test. However, the standard 12-lead ECG has only limited value to detect PH. The vectorcardiogram (VCG), synthesized from the standard 12-lead ECG, has been recognized as a novel and easy applicable method to detect RV pressure overload (RVPO) due to PH [6–9]. Several applications of the VCG have been described in the evaluation of RVPO in patients with PH, including the Butler Leggett (BL) [6] QRS amplitude criteria and the ventricular gradient (VG), a 3-dimensional measure of ventricular action potential duration (APD) heterogeneity [8]. Both methods were able to distinguish patients with PH from patients without PH. In addition, the VG was also associated with mortality in a heterogeneous group of PH patients [9]. These studies demonstrated that the VCG could be a valuable tool in the screening of patients with suspected PH.

However, it remains unknown if the combination of the ECG-derived BL score and VG would improve detection of PH. Therefore, the aims of the current study were to determine the separate diagnostic accuracies of the ECG-derived BL score and VCG-based VG for estimating mean pulmonary artery pressure (PAP), and to assess the value of combining these two methods to diagnose RVPO in patients with suspected PH.

Methods

A total of 63 patients who were evaluated with right heart catheterization for suspected PH were included in the current study. According to the current recommendations, patients with mean PAP ≥ 25 mmHg were considered to have PH [10]. All patients were screened according to the institutional protocol based on the current guidelines [10] prior to right heart catheterization including a conventional 10-second 12-lead ECG and 2-dimensional transthoracic echocardiography. In addition, the underlying etiology of PH was determined according to the Dana Point classification [10]. All data for the current study were prospectively collected in the departmental Cardiology Information System (EPD-Vision®, Leiden University Medical Center, the Netherlands) and were retrospectively analyzed.

Patients were included if an ECG was available within 40 days of the right heart catheterization. Exclusion criteria were the presence of atrial fibrillation, pacemaker rhythm, prior myocardial infarction, and complex congenital heart disease. Additionally, to reduce the possibility that abnormal electrical activity of the left ventricle (LV) would influence the ECG, patients with increased LV mass index ($> 95 \text{ g/m}^2$ and $> 115 \text{ g/m}^2$ for female and male patients, respectively) or increased relative wall thickness (> 0.42) measured with echocardiography were excluded [11].

Standard 10-s 12-lead ECGs were recorded in the supine position and were processed with the ECG Analysis Program of the University of Glasgow [12]. All ECGs were also processed with the Leiden University interactive research-oriented MATLAB (The MathWorks, Natick, MA) program LEADS (Leiden University Medical Center, Leiden, the Netherlands) [13] that performed the VCG analysis needed for the VG calculation. The VCG was synthesized by multiplying the 8 independent ECG leads I, II and V1–V6 by the Kors ECG-to-VCG transformation matrix [14]. *Figure 1* shows the American Heart Association VCG standard [15], which we adopted for the directions of the X-, Y- and Z-axes and the spatial vector orientation (azimuth, elevation). The magnitude of the ventricular gradient is computed as the vectorial sum of its X-, Y- and Z-components (QRST integrals in the X-, Y-, and Z-leads; *Figure 2*).

In the current study the projection of the VG on the X-axis (VG-X) [8,9,16] was used as the predictor variable, as well as an optimized projection direction that might be advantageous because of a better correspondence to the cardiac anatomy and the position of the heart in the chest.

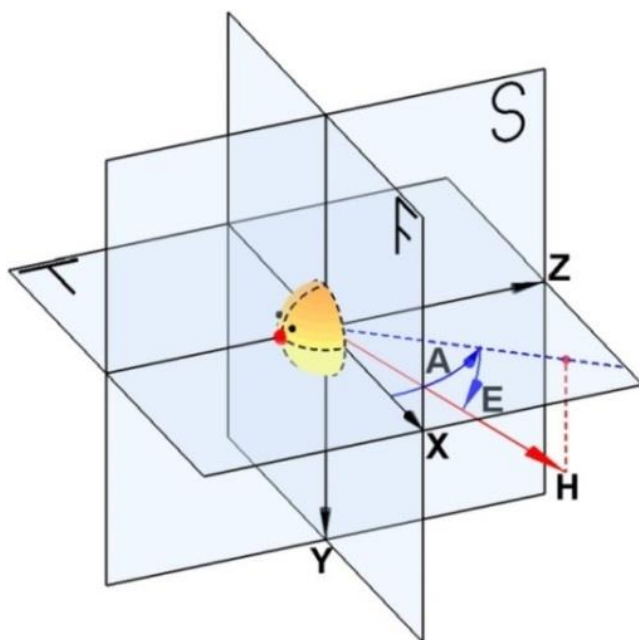
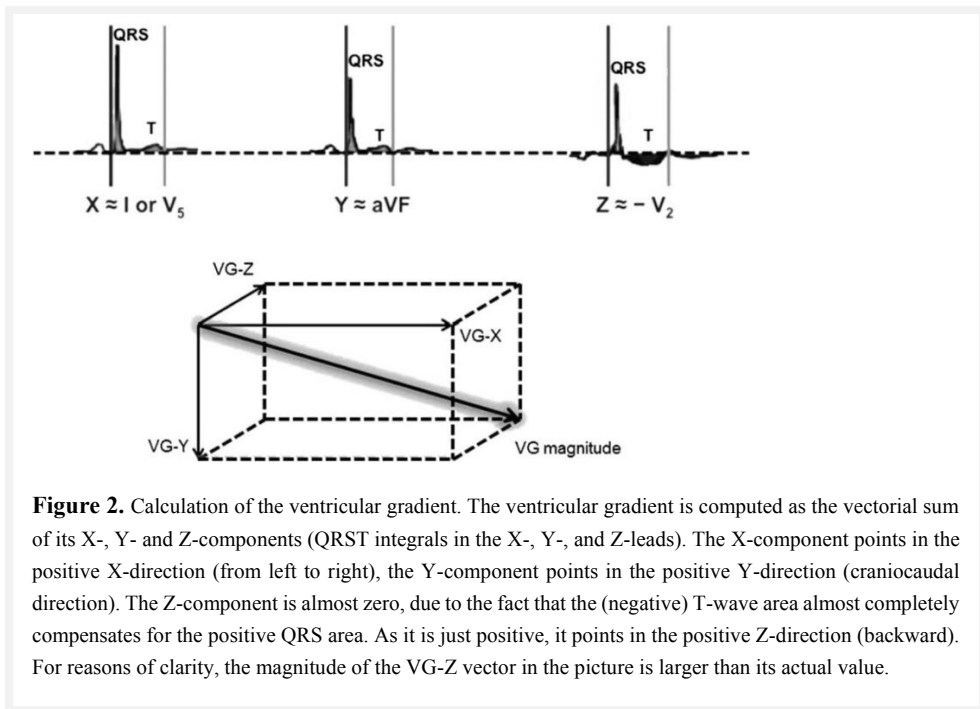


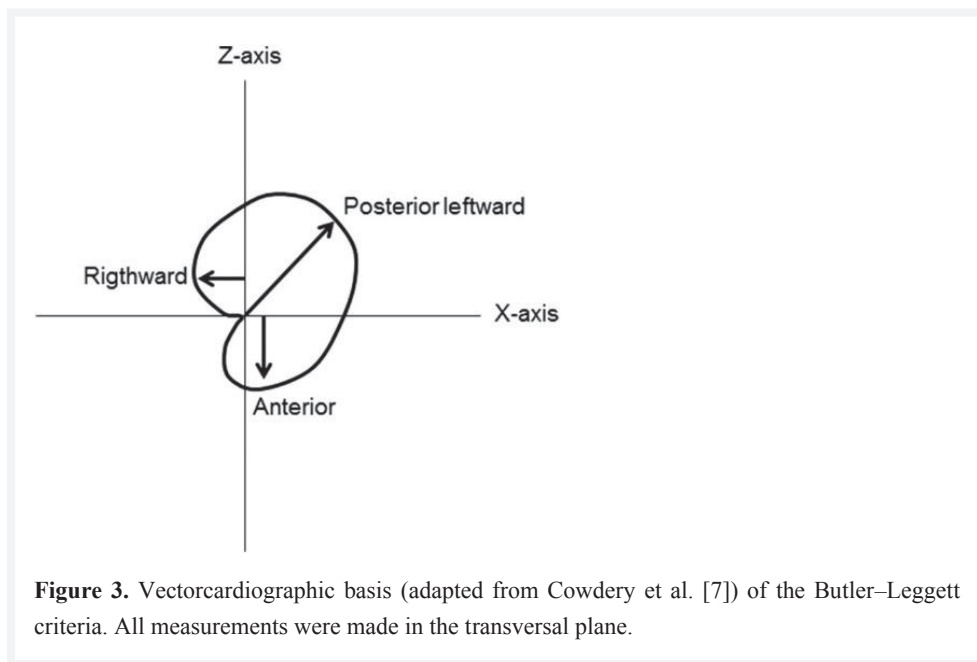
Figure 1. AHA vectorcardiographic conventions. Pictorial representation of the vectorcardiographic conventions as published by the American Heart Association [15]. A = azimuth; E = elevation; H = heart vector; T = transverse plane; F = frontal plane; S = sagittal plane; X, Y, Z = X, Y, Z axes.

For every combination of azimuth and elevation of the projection direction we computed the correlation coefficient between the corresponding VG projections of the study population and their mean PAP values. Azimuth and elevation were varied in steps of 1 degree, either in azimuth, in elevation, or in both. From a given azimuth and elevation combination, the algorithm determined the best possible step by comparing all neighboring correlation values and selecting the largest value (steepest ascent algorithm). In the following, the VG projection in the optimized direction will be referred to as VG projection optimized for detection of RVPO (VG-RVPO).



BL scores were manually calculated in all ECGs according to the formula $A + R - PL$ [6], where A denotes the maximal positive amplitude in the QRS complexes in leads V1 or V2, R the maximal negative amplitude in the QRS complexes in leads I or V6 and PL the maximal negative amplitude of the QRS complex in lead V1. *Figure 3* shows the vectorcardiographic basis of the BL criteria that has led to the current 12-lead based BL criteria [6,7]. Echocardiographic images were obtained with the patient in the left lateral decubitus position using a commercially available system (Vivid 7 and E9, General Electric-Vingmed, Horten, Norway). All images were analyzed offline using EchoPAC version 111.0.0 software (General Electric-Vingmed, Horten, Norway) and included standard 2-dimensional, color, pulsed and continuous wave Doppler acquisitions. Standard linear LV dimensions were measured and LV mass index and relative wall thickness were calculated as recommended [11]. Furthermore, RV wall thickness was measured in the subcostal or the parasternal view at end-diastole [17,18]. RV hypertrophy was defined as RV wall thickness > 5 mm [18].

Right heart catheterization was performed in accordance with the international guidelines for invasive hemodynamic assessment of PH [10]. Data were obtained with the patient in supine position with a Swan–Ganz catheter placed in the pulmonary artery and included the systolic, diastolic and mean PAP and the pulmonary capillary wedge pressure.



Continuous variables are reported as mean \pm SD and categorical data as frequencies or percentages. A P -value of < 0.05 was considered significant. The patient population was categorized according to the presence or absence of PH (mean PAP ≥ 25 mmHg). Patient characteristics were compared using the Student t test or the χ^2 test. Pearson correlation analysis was used to measure the association between each individual predictor variable (BL score, VG-X, VG-RVPO) and the mean PAP. Furthermore, the BL score and VG-RVPO were combined with multiple linear regression analysis to derive a formula that will estimate the PAP. In addition, the contribution of each VCG parameter to the regression formula was evaluated by calculating the change in R square. The BL score and VG-RVPO were introduced stepwise. Pearson correlation analysis was used to measure the association between the expected mean PAP and the observed mean PAP. Finally, the diagnostic accuracy of the combined BL score and VG-RVPO to detect mean PAP ≥ 25 mmHg (PH) was assessed using receiver operating characteristic (ROC) analysis.

Results

The general characteristics of the 63 patients are listed in *Table 1*. According to the guideline's definition [10], 39 patients (62%) had PH. The mean age of the patient population was 57 ± 13 years and 24 (38%) patients were male. Mean LV mass index was 74 ± 17 g/m² and mean RV wall thickness was 4.9 ± 1.5 mm. Fifteen (24%) patients had RV hypertrophy on echocardiography. *Figure 4* shows a scatterplot of RV wall thickness versus mean PAP with a dotted vertical line separating patients with and without PH, and a dotted horizontal line separating patients with and without RV hypertrophy. This figure illustrates that 13 (87%) patients with RV hypertrophy had PH, but that only 13 (33%) patients with PH had RV hypertrophy.

Table 1. General characteristics of the study population

	Total population (N=63)	Mean PAP <25mmHg (N=24)	Mean PAP >25mmHg (N=39)	P-value
Male sex (%)	24 (38)	12 (50)	12 (31)	0.13
Age (years)	57 ± 13	55 ± 13	58 ± 13	0.31
HR (beats/minute)	74 ± 12	73 ± 12	75 ± 12	0.55
BSA (g/m ²)	2 ± 0.3	2 ± 0.3	2 ± 0.3	0.96
LVMI (g/m ²)	74 ± 17	72 ± 18	75 ± 17	0.55
RV wall thickness (mm)	4.9 ± 1.5	4.5 ± 1.1	5.1 ± 1.7	0.11
RV hypertrophy (%)	15 (24)	2 (8)	13 (33)	0.02
Systolic PAP (mmHg)	47 ± 17	30 ± 8	58 ± 12	<0.001
Diastolic PAP (mmHg)	21 ± 10	12 ± 4	26 ± 8	<0.001
Mean PAP (mmHg)	30 ± 11	18 ± 4	37 ± 8	<0.001
<i>Underlying etiology of PH</i>				
Idiopathic (%)			2 (5)	
Connective tissue disease (%)			10 (26)	
Liver disease (%)			2 (5)	
Simple congenital shunt (%)			4 (10)	
Chronic haemolytic anemia (%)			1 (3)	
Left heart disease (%)			10 (26)	
Lung disease (%)			5 (13)	
Pulmonary embolism (%)			4 (10)	
Myeloproliferative (%)			1 (3)	

Abbreviations: BSA, body surface area; HR, heart rate; LVMI, left ventricular mass index; PAP, pulmonary artery pressure; RV, right ventricle.

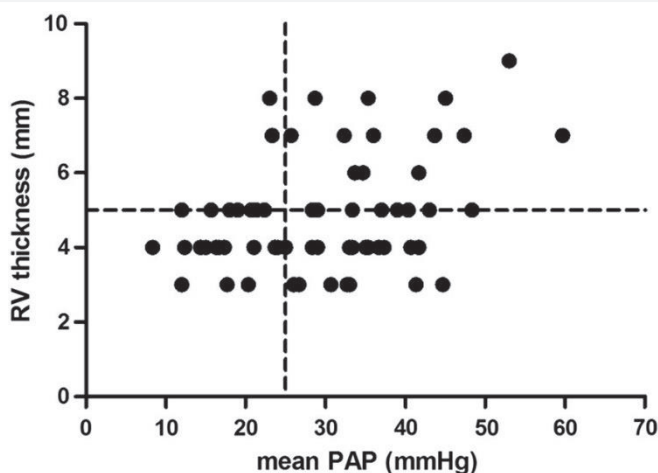


Figure 4. Mean pulmonary artery pressure (PAP) versus right ventricular (RV) wall thickness. Scatterplot of mean PAP versus RV wall thickness. The dotted vertical line shows the cutoff value for the presence of PH (mean PAP ≥ 25 mmHg), and the dotted horizontal line shows the cutoff value for the presence of RV

Patients with and without PH were comparable in terms of age, sex, body surface area and LV mass index. Patients with PH had more RV hypertrophy (33% vs. 8%, $P = 0.02$) compared to patients without PH. *Table 2* summarizes the descriptive statistics of the ECG variables of the total study group. The VG depends strongly on sex [19]; therefore, we divided the groups into male and female. Normal values are presented as mean \pm SD and in the form of the 2nd and 98th percentile [19].

The optimal projection direction of the VG was found at azimuth 155° and elevation 27° . *Table 3* demonstrates the optimization function, which is the value of the correlation between the VG projection and mean PAP. This value was flat over more than $\pm 5^\circ$ in the azimuth and/or elevation direction, and within a change of $\pm 2^\circ$ in azimuth and/or elevation, the correlation coefficient decreased only by 0.001. By definition, projection on the inverse projection direction generates similar correlation coefficient magnitudes, but with negative values. We have chosen for azimuth 155° and elevation 27° as the projection direction instead of the opposite direction (azimuth -25° and elevation -27°), because of the positive sign of the correlation, indicating that increases of the projected VG correspond to increases in mean PAP.

Table 2. ECG/VCG characteristics

ECG characteristic	Mean \pm SD	Range	Normal values Mean \pm SD ^{6,19}	Normal values 2nd and 98th percentiles ¹⁹
BL score (mV)	0.3 \pm 0.7	[-1, 2]	< 0.7	
VG magnitude (mV.ms)				
male	62 \pm 31	[-6, 137]	110 \pm 29	59, 187
female	52 \pm 23	[19, 104]	81 \pm 23	39, 143
VG azimuth (°)				
male	-7 \pm 58	[-162, 98]	-23 \pm 15	-52, 13
female	-6 \pm 38	[-68, 125]	-13 \pm 14	-38, 20
VG elevation (°)				
male	25 \pm 27	[-71, 66]	27 \pm 9	8, 47
female	42 \pm 12	[12, 65]	30 \pm 8	12, 48
VG-X (mV.ms)	33 \pm 24	[-31, 94]		
VG-Y (mV.ms)	31 \pm 21	[-52, 88]		
VG-Z (mV.ms)	-3 \pm 26	[-49, 73]		
VG-RVPO (mV.ms)	-14 \pm 20	[-64, 60]		

Abbreviations: BL, Butler-Leggett; ECG, electrocardiogram; RVPO, right ventricular pressure overload; SD, standard deviation; VG, ventricular gradient

Table 3. Optimal projection direction of the VG

Azimuth	151°	152°	153°	154°	155°	156°	157°	158°
Elevation								
24°	0.610	0.610	0.611	0.611	0.611	0.610	0.610	0.609
25°	0.610	0.611	0.611	0.611	0.611	0.611	0.611	0.610
26°	0.610	0.611	0.611	0.612	0.612	0.611	0.611	0.611
27°	0.610	0.611	0.611	0.612	0.612	0.612	0.611	0.611
28°	0.610	0.611	0.611	0.612	0.612	0.612	0.611	0.611
29°	0.610	0.610	0.611	0.611	0.611	0.611	0.611	0.611
30°	0.609	0.610	0.610	0.610	0.611	0.611	0.610	0.610

Figure 5 shows the linear regressions between BL, VG-X and VG-RVPO and mean PAP; correlations were 0.45, -0.49 and 0.61 , respectively ($P < 0.001$, for all correlations). Pearson correlation analysis was performed to determine the relationship between the BL score and VG-RVPO ($r = 0.33$, $P = 0.009$). Both variables were included in a multiple linear regression analysis to determine their independent contribution to the estimation of PAP. This yielded the following regression formula: $\text{mean PAP} = 32.30 + 0.30 \times \text{VG-RVPO} + 4.67 \times \text{BL score}$ (Table 4). The contribution to the correlation coefficient of the BL score was only 6.9%, although this contribution achieved statistical significance ($P = 0.009$).

Figure 6A shows the correlation coefficient of 0.67 ($P < 0.001$) between the predicted mean PAP using this regression formula and the observed mean PAP. ROC analysis revealed an area under the curve of 0.79 (95% confidence interval $0.67\text{--}0.90$) (Figure 6B). Furthermore, the ROC curve showed that the most sensitive and specific cut-off value of the predicted mean PAP calculated by the regression formula was 28.5 mmHg with a sensitivity of 72% and a specificity of 71%.

Table 4. Predictors of mean PAP

Variable	Coefficient	Standard error	<i>P</i> -value
<i>VG-RVPO</i>	0.30	0.06	<0.001
<i>BL score</i>	4.67	1.72	0.009
<i>Constant</i>	32.30	1.52	<0.001

Abbreviations: BL, Butler-Leggett; PAP, pulmonary artery pressure; RVPO, right ventricular pressure overload; VG, ventricular gradient

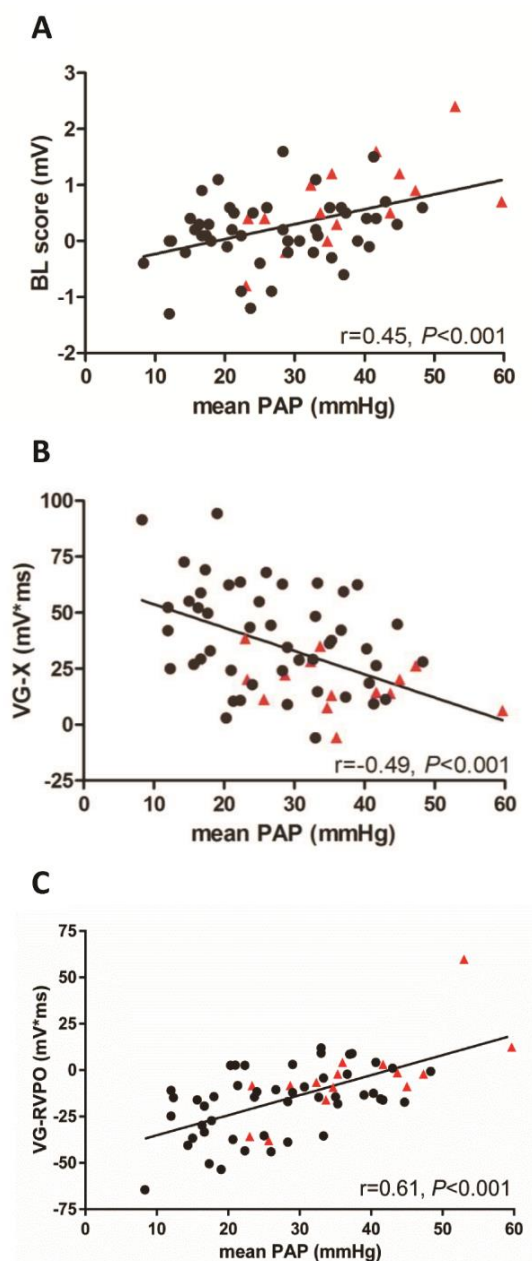


Figure 5. BL score, VG-X and VG-RVPO versus mean PAP. A: The Butler–Leggett score versus mean PAP. B: VG-X versus the mean PAP. C: VG-RVPO versus the mean PAP. The red triangles represent patients with right ventricular hypertrophy (right ventricle wall thickness > 5 mm), the black dots represent patients without right ventricular hypertrophy. Abbreviations: BL, Butler–Leggett; PAP, pulmonary artery pressure; RVPO, right ventricular pressure overload; VG, ventricular gradient

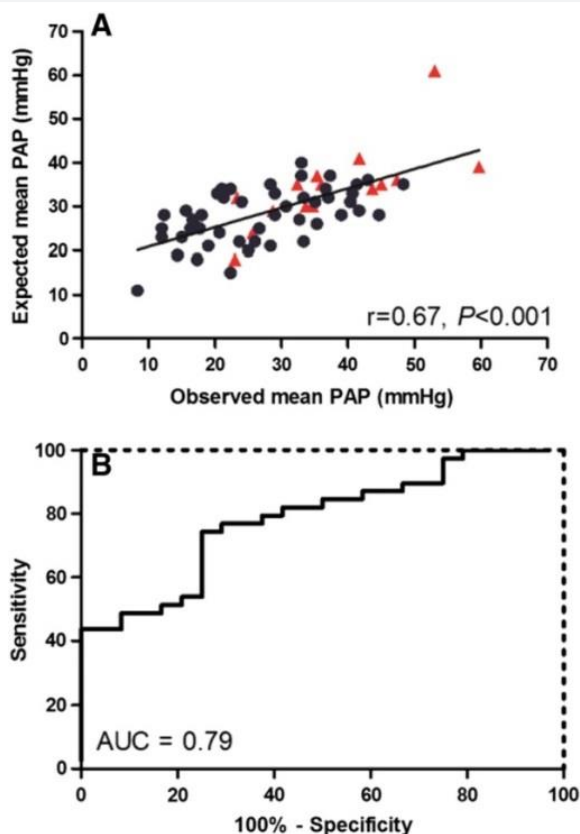


Figure 6. Expected mean pulmonary artery pressure (PAP) versus measured mean PAP and corresponding receiver operating characteristic (ROC) analysis. A: The expected mean PAP, calculated from the regression formula, versus the measured mean PAP. The red triangles represent patients with right ventricular hypertrophy (right ventricle wall thickness > 5 mm), the black dots represent patients without right ventricular hypertrophy. B: ROC for mean PAP \geq 25 mm Hg.

Discussion

In the current study we demonstrated that the combination of the VG (VG-RVPO) and the Butler–Leggett QRS amplitude criteria accurately estimates the mean PAP in patients screened for PH. In this formula, the largest contribution to the discriminatory power of this detection is provided by the VG-RVPO, while the significant contribution of BL score was less.

In a normal heart, the RV is thin-walled and in the ECG most of the RV electrical activity is masked by that of the thicker septum and the LV free wall. In situations where RV hypertrophy may be present, as in PH, the RV electrical forces tend to counterbalance with

the LV forces [20], resulting in a rightward deviation of the QRS loop. Based on this concept, Cowdery et al. [7] developed QRS amplitude VCG criteria to identify patients with RV hypertrophy as a result of increased PAP. The VCGs of 84 patients with mitral stenosis and a high likelihood of RV hypertrophy were compared to 173 young, healthy volunteers and 151 subjects with chest pain who had no mitral stenosis or elevated systolic PAP measured by cardiac catheterization. The authors demonstrated that these newly developed VCG criteria were able to identify 60% of the patients with moderate-to-severe RV hypertrophy (based on the presence of mitral stenosis with systolic PAP values > 40 mmHg measured by right heart catheterization) with a specificity of 96% and a sensitivity of 60%. These VCG criteria were later adapted for the 12-lead ECG into the BL score by Butler [6], who found comparable sensitivity and specificity of 34% and 97%, respectively, in a similar group of patients with mitral stenosis and elevated systolic PAP. Blyth et al. [21] also studied the performance of the BL criteria for the detection of RV hypertrophy defined by either RV mass > 51 g or RV mass/LV mass > 0.582 measured by cardiovascular magnetic resonance imaging (CMR), in 28 patients with PH and 6 controls. The BL criteria diagnosed RV hypertrophy with a specificity of 100% for RV mass and for RV mass index, and a sensitivity of 74% for RV mass and 61% for RV mass index, respectively. The difference in sensitivity between these studies may be attributed to the fact that in the study by Blyth et al. [21] the presence of RV hypertrophy was verified by CMR while in the study of Butler and Leggett, the presence of RV hypertrophy was not directly measured, but assumed by the presence of invasively measured elevated systolic PAP.

In the current study right heart catheterization was used as the reference method for diagnosing PH. In the absence of an RV outflow tract obstruction, it may be assumed that increased mean PAP represents RVPO. RVPO results in increased RV wall stress and consequently in RV remodeling with RV hypertrophy [2]. However, RV hypertrophy is often not present in early stages of PH. Improvement of ECG detection of RVPO would therefore require criteria that are not primarily based on hypertrophy-induced rightward deviation of the QRS loop but rather on the typical electrophysiological changes in APD that are to be expected with elevated pressures. In the current study, the BL score, which was designated to detect RV hypertrophy, had only a limited contribution to the discrimination between patients with and without PH on the basis of their ECG. This may be explained by the absence of RV hypertrophy in a large part of the patient population (*Figure 4*).

Initially, when the VG emerged as a potentially important electrocardiographic variable, it was determined in the frontal plane [22,23]; Burger [24] gave the mathematical proof that, when computed from the VCG, the VG measures the 3-dimensional integral of the gradients

in the ventricular APDs. Because of its 3-dimensionality, and because it measures APD heterogeneity, the spatial (3-dimensional) VG as we have computed it, may reflect the presence of RVPO better. In a study by Henkens et al., patients with idiopathic pulmonary arterial hypertension were matched with healthy controls [8]. It was found that the ECG-derived VG projected on the X axis is highly accurate in detecting chronic increases in RV pressure load as a consequence of PH, and can be used to distinguish between normal, mildly to moderately increased, and severely increased chronic RVPO. In line with this, Scherptong et al. studied the VG projected on the X axis as an indicator of PH in a heterogeneous group of patients and demonstrated that this is a sensitive indicator of elevated systolic PAP measured by echocardiography [9]. These studies demonstrated that the VG-X could be a valuable tool in the detection of RVPO in the screening of patients at risk for PH. The current study also demonstrated a significant relation between mean PAP and the VG-X. Moreover, after optimization of the VG projection direction for detection of RVPO, the correlation with mean PAP improved even further.

Our study shows that, in our patient group, BL and VG-RVPO assess mean PAP by multiple linear regression with a correlation coefficient of 0.67. The contribution of BL to this correlation is significant but limited (0.07). This suggests that VG-RVPO is superior in assessing pressure, and, as the BL score was designed to assess hypertrophy, it is conceivable that BL would be superior to VG-RVPO in assessing RV wall thickness. Multiple linear regression of BL and VG-RVPO on RV wall thickness indeed revealed that only BL contributed significantly ($P = 0.009$).

It has been demonstrated that in acute RVPO sarcomere-length increases during contraction and APD shortens [25]. However, in long standing RVPO, action potentials prolong and action potential dispersion increases [26]: subendocardial and epicardial myocytes show different APD dynamics [27]. In general, changes in APD dispersion are reflected in the VG [28]. It is difficult to predict how these electrophysiological changes precisely work out in the VG, and it is also unknown which regions in the heart contribute to these VG changes. Any involved myocardium will be affected in terms of electrophysiological properties and APD changes, not only in the RV free wall, but also in the interventricular septum. It may be difficult to estimate how much myocardium is involved, but it is reasonable to assume that this is not confined to a relatively small amount of cardiac muscle.

The presented improved ECG/VCG criteria to assess mean PAP could be of potential use in surveillance of diseases that are likely to cause PH, such as connective tissue disease. Measuring the mean PAP with this simple non-invasive diagnostic test may be clinically important because early detection of PH may improve prognosis. Whether this combination

of VG-RVPO and BL scores is useful in regular monitoring of patients with PH deserves further study.

It is difficult to translate our findings to conventional ECG criteria. In PH and/or RV hypertrophy QRS- as well as T-wave changes have been described [20]. The VG is an integral over the QRS complex and the T wave, insensitive to ventricular activation order/conduction disorders [28]. It is possible that patients with a low BL score have a quite normal QRS complex; in such cases the typical changes in the VG will merely be caused by T-wave changes. But this is only part of the patients. In most cases, a mix of QRS- and T-wave changes together causes the VG changes.

The ECG/VCG algorithm developed in this study has not been validated in other groups of patients with RVPO. Hence, our results are restricted to a heterogeneous patient population with suspected PH without LV hypertrophy. The limited size of the patient population prevented to split the population into a derivation and validation group. Hence, the results in terms of the optimal projection direction of the VG, the mean PAP assessment formula on the basis of the projected VG and the BL score, and the diagnostic performance as to the discrimination between patients with and without PH were not verified in a test group. It may be considered a limitation that vectorcardiographic analysis is needed to detect RVPO in PH patients. However, it has to be acknowledged that several ECG analysis systems use VCG techniques to calculate certain ECG variables, e.g., a QRS axis or QRS duration. Electrocardiographs and ECG analyses programs could mostly easily be extended with elementary VCG analysis.

Conclusion

With a combination of BL score and optimized VG projection it is feasible to detect presence or absence of RVPO in a typical population of patients evaluated for PH. Further validation in another comparable patient group is required. Whether this algorithm may be used in the monitoring of development of RVPO in PH by serial ECG-VCG analysis warrants further study.

References

1. M. Humbert, O. Sitbon, A. Chaouat, M. Bertocchi, G. Habib, V. Gressin, *et al.* Survival in patients with idiopathic, familial, and anorexigen-associated pulmonary arterial hypertension in the modern management era. *Circulation*, 122 (2010), pp. 156-163
2. D. Chemla, V. Castelain, P. Herve, Y. Lecarpentier, S. Brimiouille, *et al.* Haemodynamic evaluation of pulmonary hypertension. *Eur Respir J*, 20 (2002), pp. 1314-1331
3. D.B. Badesch, G.E. Raskob, C.G. Elliott, A.M. Krichman, H.W. Farber, A.E. Frost, *et al.* Pulmonary arterial hypertension: baseline characteristics from the REVEAL Registry. *Chest*, 137 (2010), pp. 376-387
4. S.B. Brown, A. Raina, D. Katz, M. Szerlip, S.E. Wiegers, P.R. Forfia, *et al.* Longitudinal shortening accounts for the majority of right ventricular contraction and improves after pulmonary vasodilator therapy in normal subjects and patients with pulmonary arterial hypertension. *Chest*, 140 (2011), pp. 27-33
5. C. Tueller, H. Stricker, P. Soccia, M. Tamm, J.D. Aubert, M. Maggiorini, *et al.* Epidemiology of pulmonary hypertension: new data from the Swiss registry. *Swiss Med Wkly*, 138 (2008), pp. 379-384
6. P.M. Butler, S.I. Leggett, C.M. Howe, C.J. Freye, N.B. Hindman, G.S. Wagner Identification of electrocardiographic criteria for diagnosis of right ventricular hypertrophy due to mitral stenosis. *Am J Cardiol*, 57 (1986), pp. 639-643
7. C.D. Cowdery, G.S. Wagner, J.W. Starr, G. Rogers, J.C. Greenfield Jr. New vectorcardiographic criteria for diagnosing right ventricular hypertrophy in mitral stenosis: comparison with electrocardiographic criteria. *Circulation*, 62 (1980), pp. 1026-1032
8. I.R. Henkens, K.T. Mouchaers, A. Vonk-Noordegraaf, A. Boonstra, C.A. Swenne, A.C. Maan, *et al.* Improved ECG detection of presence and severity of right ventricular pressure load validated with cardiac magnetic resonance imaging. *Am J Physiol Heart Circ Physiol*, 294 (2008), pp. H2150-H2157
9. R.W. Scherptong, I.R. Henkens, G.F. Kapel, C.A. Swenne, K.W. van Kralingen, M.V. Huisman, *et al.* Diagnosis and mortality prediction in pulmonary hypertension: the value of the electrocardiogram-derived ventricular gradient. *J Electrocardiol*, 45 (2012), pp. 312-318
10. N. Galie, M.M. Hoeper, M. Humbert, A. Torbicki, J.L. Vachiery, J.A. Barbera, *et al.* Guidelines for the diagnosis and treatment of pulmonary hypertension: the Task Force for the Diagnosis and Treatment of Pulmonary Hypertension of the European Society of Cardiology (ESC) and the European Respiratory Society (ERS), endorsed by the International Society of Heart and Lung Transplantation (ISHLT). *Eur Heart J*, 30 (2009), pp. 2493-2537
11. R.M. Lang, M. Bierig, R.B. Devereux, F.A. Flachskampf, E. Foster, P.A. Pellikka, *et al.* Recommendations for chamber quantification: a report from the American Society of Echocardiography's Guidelines and Standards Committee and the Chamber Quantification Writing Group, developed in conjunction with the European Association of Echocardiography, a branch of the European Society of Cardiology. *J Am Soc Echocardiogr*, 18 (2005), pp. 1440-1463
12. P.W. Macfarlane, B. Devine, S. Latif, S. McLaughlin, D.B. Shoaib, M.P. Watts, *et al.* Methodology of ECG interpretation in the Glasgow program. *Methods Inf Med*, 29 (1990), pp. 354-361
13. H.H.M. Draaisma, C.A. Swenne, H. Van de Vooren, A.C. Maan, B. Hooft van Huysduynen, E.E. Van der Wall, *et al.* LEADS: an interactive research oriented ECG/VCG analysis program. *Comput Cardiol*, 32 (2005), pp. 515-518
14. J.A. Kors, G. van Herpen, A.C. Sittig, J.H. van Bommel Reconstruction of the Frank vectorcardiogram from standard electrocardiographic leads: diagnostic comparison of different methods. *Eur Heart J*, 11 (1990), pp. 1083-1092
15. C.E. Kossmann, D.A. Brody, G.E. Burch, H.A. Hecht, F.D. Johnston, C. Kay, *et al.* Recommendations for standardization of leads and of specifications for instruments in electrocardiography and vectorcardiography. *Circulation*, 35 (1967), pp. 583-602
16. I.R. Henkens, R.W. Scherptong, K.W. van Kralingen, S.A. Said, H.W. Vliegen. Pulmonary hypertension: the role of the electrocardiogram. *Neth Heart J*, 16 (2008), pp. 250-254

17. R. Prakash, S.A. Umali. Comparison of echocardiographic and necropsy measurements of left ventricular wall thickness in patients with coronary artery disease. *Am J Cardiol*, 53 (1984), pp. 838-841
18. L.G. Rudski, W.W. Lai, J. Afilalo, L. Hua, M.D. Handschumacher, K. Chandrasekaran, *et al.* Guidelines for the echocardiographic assessment of the right heart in adults: a report from the American Society of Echocardiography endorsed by the European Association of Echocardiography, a registered branch of the European Society of Cardiology, and the Canadian Society of Echocardiography. *J Am Soc Echocardiogr*, 23 (2010), pp. 685-713
19. R.W. Scherptong, I.R. Henkens, S.C. Man, S. Le Cessie, H.W. Vliegen, H.H. Draisma, *et al.* Normal limits of the spatial QRS-T angle and ventricular gradient in 12-lead electrocardiograms of young adults: dependence on sex and heart rate. *J Electrocardiol*, 41 (2008), pp. 648-655
20. P.W. Macfarlane, P.M. Okin, T.D.V. Lawrie, J.A. Milliken Enlargement and Hypertrophy. P.W. Macfarlane, A. VanOosterom, O. Pahlm, P. Kligfield, M. Janse, J. Camm (Eds.), *Comprehensive electrocardiology*, Springer Verlag, London (2011), pp. 607-644
21. K.G. Blyth, J. Kinsella, N. Hakacova, L.E. McLure, A.M. Siddiqui, G.S. Wagner, *et al.* Quantitative estimation of right ventricular hypertrophy using ECG criteria in patients with pulmonary hypertension: a comparison with cardiac MRI. *Pulm Circ*, 1 (2011), pp. 470-474
22. R. Ashman, E. Byer. The normal human ventricular gradient. I. Factors which affect its direction and its relation to the mean QRS axis. *Am Heart J*, 25 (1943), pp. 16-35
23. F.N. Wilson, A.G. MacLeod, P.S. Barker, F.D. Johnston. The determination and significance of the areas of the ventricular deflections of the electrocardiogram. *Am Heart J*, 10 (1934), pp. 46-61
24. H.C. Burger. A theoretical elucidation of the notion ventricular gradient. *Am Heart J*, 53 (1957), pp. 240-246
25. G. Greve, M.J. Lab, R. Chen, D. Barron, P.A. White, A.N. Redington, *et al.* Right ventricular distension alters monophasic action potential duration during pulmonary arterial occlusion in anaesthetised lambs: evidence for arrhythmogenic right ventricular mechanoelectrical feedback. *Exp Physiol*, 86 (2001), pp. 651-657
26. Y. Tanaka, B. Takase, T. Yao Right ventricular electrical remodeling and arrhythmogenic substrate in rat pulmonary hypertension. *Am J Respir Cell Mol Biol*, 49 (2013), pp. 426-436
27. C. Shi, X. Wang, F. Dong, Y. Wang, J. Hui, Z. Lin, *et al.* Temporal alterations and cellular mechanisms of transmural repolarization during progression of mouse cardiac hypertrophy and failure. *Acta Physiol (Oxf)*, 208 (2013), pp. 95-110
28. H.H. Draisma, M.J. Schalij, E.E. van der Wall, C.A. Swenne Elucidation of the spatial ventricular gradient and its link with dispersion of repolarization. *Heart Rhythm*, 3 (2006), pp. 1092-1099

A photograph of a bridge at night, with its structure illuminated by warm yellow lights. The bridge spans across a body of water, and the lights from the bridge and surrounding area reflect on the water's surface, creating a shimmering effect. The sky is dark, and the overall scene is atmospheric and serene.

Part II

4D flow MRI-derived cardiac flow
and function: validation and
clinical utility

Chapter 6

Unravelling cardiovascular disease using four dimensional flow MRI

This chapter is adapted from:

- ✚ Kamphuis VP, Westenberg JJM, van der Palen RLF, Blom NA, de Roos A, van der Geest R, Elbaz MSM, Roest AAW. Unravelling cardiovascular disease using four dimensional flow cardiovascular magnetic resonance.
Int J Cardiovasc Imaging. 2017 Jul;33(7):1069-1081.
- ✚ Kamphuis VP, Westenberg JJM, van den Boogaard PJ, Clur SB, Roest AAW. Direct assessment of tricuspid regurgitation by 4D flow CMR in a patient with Ebstein's anomaly.
Eur Heart J Cardiovasc Imaging 2018 May 1;19(5):587-588.
- ✚ Kamphuis VP, Roest AAW, Westenberg JJM, Elbaz MSM. Bi-ventricular vortex ring formation corresponds to regions of highest intra-ventricular viscous energy loss in a Fontan patient: analysis by 4D Flow MRI.
Int J Cardiovasc Imaging. 2018 Mar;34(3):441-442.

Abstract

Knowledge of normal and abnormal flow patterns in the human cardiovascular system increases our understanding of normal physiology and may help unravel the complex pathophysiological mechanisms leading to cardiovascular disease. Four-dimensional (4D) flow magnetic resonance imaging (MRI) has emerged as a suitable technique that enables visualization of *in vivo* blood flow patterns and quantification of parameters that could potentially be of prognostic value in the disease process. In this review, current image processing tools that are used for comprehensive visualization and quantification of blood flow and energy distribution in the heart and great vessels will be discussed. Also, imaging biomarkers extracted from 4D flow MRI will be reviewed that have been shown to distinguish normal and abnormal flow patterns. Furthermore, current applications of 4D flow MRI in the heart and great vessels will be discussed, showing its potential as an additional diagnostic modality which could aid in disease management and timing of surgical intervention.

Introduction

In normal cardiovascular physiology, blood flow in the heart and great vessels shows complex and dynamic three-dimensional (3D) flow patterns, leading to efficient ejection of the blood into the pulmonary and systemic circulation [1]. Congenital or acquired heart disease cause alterations in these blood flow patterns resulting in increased energy loss [2] and reduction of the efficiency of the heart pump by over 10% [1]. Moreover, altered blood flow patterns induce changes to the endothelium, which may increase the risk for cardiovascular incidents later in life [3, 4]. Knowledge of these flow patterns increases our understanding of normal physiology and may help unravel the complex pathophysiological mechanisms leading to cardiovascular disease [1, 5]. However, these complex 3D flow patterns remain challenging to visualize and characterize. Four-dimensional (4D) flow magnetic resonance imaging (MRI) has emerged as a suitable technique for comprehensive visualization and quantification of blood flow and energy distribution in the heart and great vessels in healthy subjects as well as in patients with cardiovascular disease [6].

The influence of altered aortic flow patterns on pathophysiology has been investigated most intensely in patients with a bicuspid aortic valve (BAV) [3, 7, 8] and in patients with Marfan syndrome [9-13]. For example, in patients with Marfan syndrome, flow parameters have been linked to an increased aortic size, as shown by 4D flow MRI [9-13]. Because of the complexity of the heart's atria and ventricles, assessment of intra-cardiac blood flow characteristics is more challenging, but knowledge of such blood flow is of utmost importance in diseases like ischemic heart disease, dilated cardiomyopathy, congenital heart defects (CHD) and pulmonary hypertension.

In this review, the challenges in the application of 4D flow MRI to study hemodynamics in the cardiovascular system are discussed, as well as the visualization and quantification methods. Furthermore, current insights in normal flow patterns, flow disturbances due to cardiovascular disease and its consequences, as assessed with 4D flow MRI, will be addressed.

State of the art

Four-dimensional flow MRI, phase-contrast (PC) MRI with velocity-encoding in all three spatial directions, resolved relative to all dimensions of space and the dimension of time along the cardiac cycle, represents all directions and spatial regions of flow within the boundaries of the defined volume [14, 15].

Acquisition parameters

Recently, a consensus statement was published, stating the clinical and scientific significance of 4D flow MRI and providing recommendations for its use [15]. In this consensus statement, a list of acquisition parameter settings as a baseline 4D flow MRI protocol is proposed against which alternative protocols can be compared. Optimized parameter choices are recommended for special populations (e.g. children) or analysis of advanced flow parameters [15]. An important parameter is the Venc, which represents the maximum flow velocity that can be acquired without having to correct for phase wrapping. If the Venc is set too low, velocity aliasing will occur, however when the Venc is set too high, the level of velocity noise will increase [14]. A Venc that is set 10% higher than the maximal expected velocity is recommended [15].

Evaluation of flow patterns in the cardiac chambers requires a spatial resolution of $<3.0 \times 3.0 \times 3.0 \text{ mm}^3$ and $<2.5 \times 2.5 \times 2.5 \text{ mm}^3$ for the aorta or pulmonary artery. In order to extract feature information (i.e., stroke volume, peak velocity, peak flow rate, etc.) of flow (velocity) curves from the velocity field, a high temporal resolution is required. This resolution is defined by the repetition time, the number of velocity encodings and, in case of segmented acquisition, the number of segments. Since 4D flow MRI is to be applied to these large anatomical regions in the human body with adequate spatial and temporal resolution and potentially with some form of respiratory motion compensation, the acquisition time required to collect all this flow information is typically long (i.e., 10-25 minutes) and may be too demanding on patients or on the clinical workflow.

Three-directional encoding without any acceleration technique would be the most accurate approach, with the best signal-to-noise ratio (SNR) and the least amount of phase offset errors [15]. However, this is generally not feasible in a clinical setting. Therefore, to make 4D flow MRI applicable for clinical use, several methods are available to reduce acquisition time. Such accelerating techniques include parallel imaging using multi-element phased array coils (SENSitivity Encoding, SENSE) [16] or k-t undersampling methods like k-t BLAST (Broad Linear Acquisition Speed-up Technique) [17]. Acquiring read-outs of multiple k-lines per

radiofrequency excitation may accelerate the acquisition as well, however, at the penalty of reducing temporal resolution and/or signal-to-noise. Furthermore, different acquisition strategies apart from the standard Cartesian k-space read-out, like echo planar imaging (EPI) [18], spiral [19] or radial [20] (e.g., PC-VIPR, vastly undersampled isotropic projection reconstruction) read-out methods can further reduce acquisition time.

Another way to accelerate the acquisition is to acquire free-breathing 4D flow MRI with sophisticated respiratory gating or even without any respiratory motion control. Compensation of respiratory motion, which is used to reduce motion artifacts and improve accuracy, is usually difficult to achieve without significantly increasing scan duration. The most commonly used method for this motion suppression is respiratory gating by a navigator, however this increases acquisition duration substantially. Respiratory self-gating methods allow sampling of 4D flow data over the entire cardiac cycle, usually using center K_0 point, center K_0 profiles or low-resolution images to derive the breathing motion and then to adjust the acquisition scheme in real-time to reacquire motion-corrupted data, allowing free breathing while acquiring 4D flow data within clinically acceptable acquisition time [21, 22]. However, recently it was shown that 4D flow MRI without any respiratory gating may be performed while preserving accurate quantitative results from stroke volume assessment in the great vessels [23] and in whole-heart 4D flow [24].

Sources of error

Several sources of errors can affect the 4D flow data and should be corrected for. Major sources of error are: eddy current effects, concomitant gradient field effects, gradient field non-linearity and phase wraps [15]. Inhomogeneities in the magnetic field and eddy current effects in the receive coil will result in background phase distortion [25]. Concomitant gradient fields are a result of Maxwell's equations for the divergence and curl of the magnetic field and lead to background offsets [26]. Furthermore, a non-linear gradient field can induce deviations from the nominal gradient strength and orientation causing deviations in velocity quantification [27]. Some of these errors are partially corrected by reconstruction algorithms implemented on the MRI scanner software. Background phase offset errors are usually corrected by either performing a phantom velocity-encoded scan simulating static tissue and using this data set as a reference for background subtraction, or by the approach of fitting a multi-order polynomial through areas identified as static tissue, for correcting the local phase signal [28].

Finally, velocity aliasing, or phase-wrapping, will occur when blood flow velocities exceed the a priori set V_{enc} value. The use of a phase-unwrapping algorithm is recommended prior

to image analysis. Identification of abrupt phase shifts in the temporal and/or spatial domain is a common way to identify areas with phase wrapping [29]. Aliasing correction should be performed in the original source images of each individual encoding direction.

Visualization and quantification

Several tools are developed to help visualize velocity vector fields of blood flow in the heart and vessels, which makes qualitative assessment of flow patterns possible. Visualization is needed in order to characterize blood flow parameters.

Most common visualization types are the vector glyph representation, or the use of streamlines or pathlines (*Figure 1*). A vector glyph represents the magnitude and direction of the velocity measured from each voxel. However, a cine representation of vector data may be difficult to interpret, as data may quickly become cluttered.

Streamlines are curves which are tangent to the velocity direction at a particular point in time, representing the blood flow direction at an instant of time [30, 31]. Streamline visualization can be used for visualization of inflow and outflow direction, regurgitant jets and circulating flow patterns at specific time points in the cardiac cycle [32, 33]. In the aorta, streamline visualization is often used to show helical flow patterns [34]. Streamline visualization in combination with retrospective valve tracking allows for accurate quantification of net flow volumes through each of the four heart valves (*Figure 2*) [35, 36].

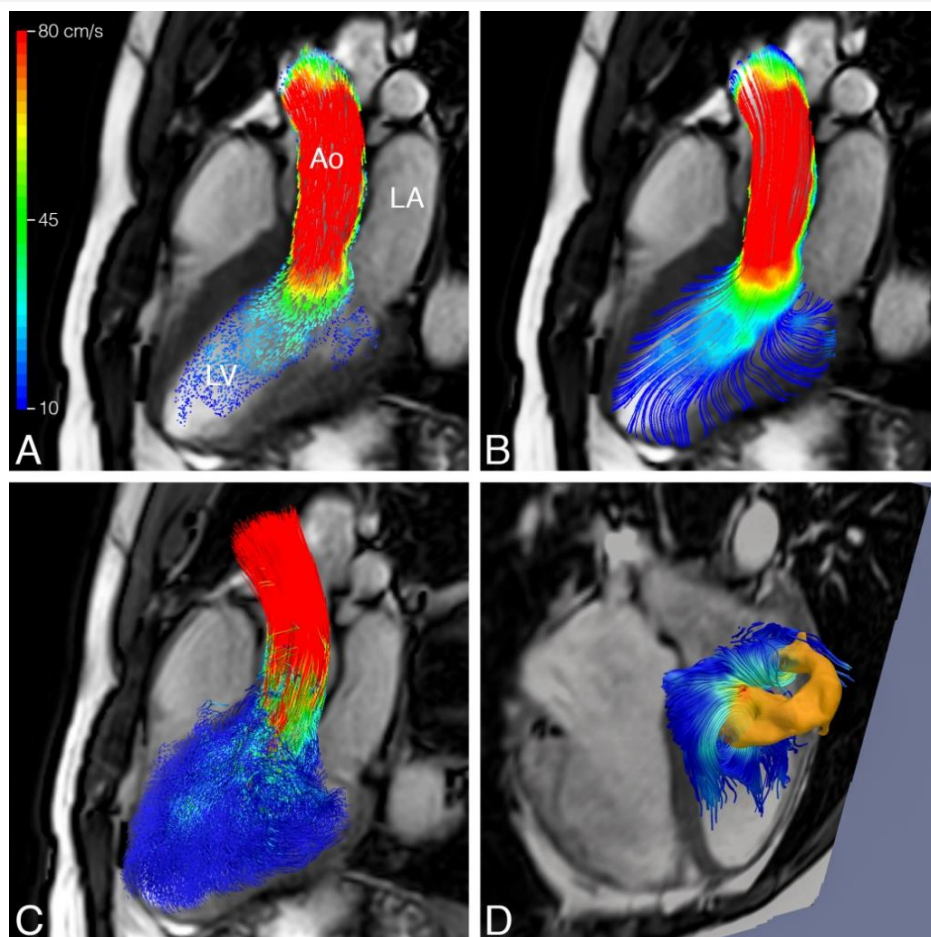


Figure 1. Visualization of left ventricular systolic blood flow using 4D flow MRI in a healthy volunteer (24 year old man). In A, blood flow velocity is displayed by color-coded vector glyph representation. Direction and velocity magnitude are presented by vector size and color. In B, a streamline representation is presented and C shows a pathline representation. Isosurfaces can be used to display flow structures with a common property, such as vorticity. In D, a ring-shape vortex is displayed in late diastolic LV filling in the same volunteer. Vortex extraction is performed using Eulerian vortex core analysis. The vortex ring is displayed with streamlines superimposed. LA: left atrium, LV: left ventricle, Ao: Aorta.

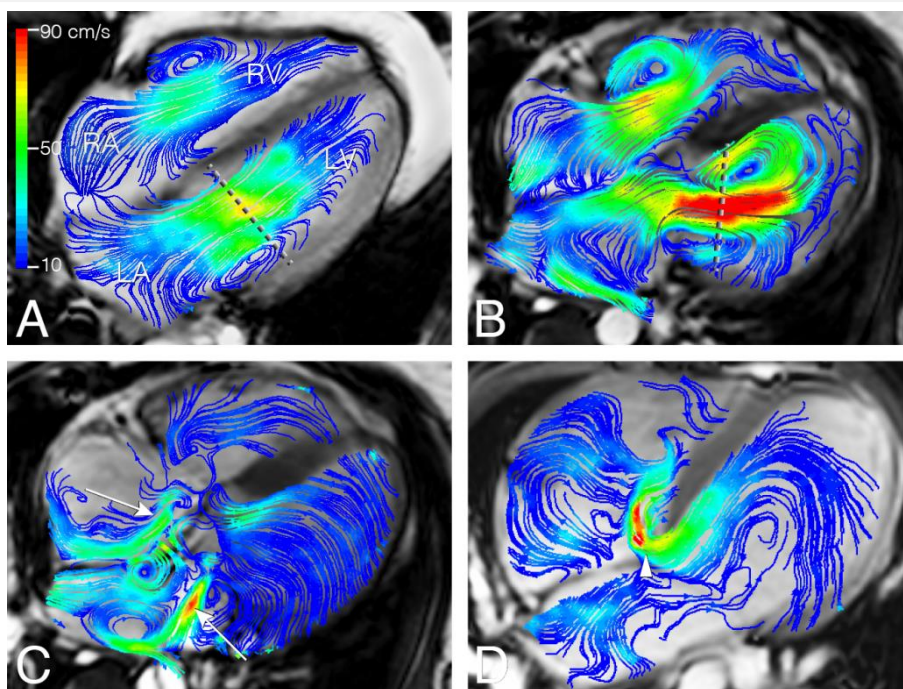


Figure 2. Left ventricular (LV) inflow assessment from 4D flow MRI and retrospective valve tracking. Streamline visualization with color coding of early LV inflow shows central inflow in a healthy volunteer (in A; 53 year old man) and a laterally directed inflow in a patient with corrected atrioventricular septal (AVSD) defect (in B; 26 year old woman). Positioning of the reformat plane is displayed by the dashed line. In C, eccentric regurgitant jets in both atrioventricular valves during systole in the same corrected AVSD patient are displayed (arrows). In D, shunt flow in an uncorrected AVSD is displayed (arrowhead) in a 24 year old male patient. LA: left atrium, LV: left ventricle, RA: right atrium; RV: right ventricle.

Retrospective valve tracking is a method in which the scanned 3D volume is retrospectively reformatted into two-dimensional (2D) measurement planes with through-plane velocity encoding to allow for trans-valvular flow quantification [35, 36]. Measurement planes can be adjusted per individual phase, following the valve position, inflow direction and the dynamically changing regurgitant jets. Optimized positioning of these planes should be based on the direction of the peak velocity visualized by streamlines [37].

Figure 3 shows an example of retrospective valve tracking in patient with Ebstein's Anomaly, a rare congenital heart disease in which the septal and posterior leaflets of the tricuspid valve are located more apically (*Figure 3A*, stylized representation of the tricuspid valve leaflets with the septal leaflet indicated by an arrow) [38]. In this case example validated 4D flow MRI with retrospective valve tracking was used to directly quantify tricuspid regurgitation (TR). Streamline visualization was used to visualize flow patterns and

the dynamic regurgitation jet. A measurement plane was placed on the level of maximum velocity in every timeframe and adjusted perpendicular to the flow direction (*Figure 3B*).

The resulting flow curve (*Figure 3C*) shows a regurgitation fraction of 82%, illustrated by the ratio between the negative versus positive area-under-the-curve. Retrospective valve tracking was done over all valves in a single acquisition (acquisition time 8 minutes, post-processing time 20 minutes). The small differences between the net flow volumes through the four valves of maximally 3 ml indicate conservation of mass (*Figure 3D*). This proof-of-principle case demonstrates the feasibility of direct TR-quantification by 4D flow MRI with retrospective valve tracking in a patient with Ebstein's anomaly and can be a starting point for prospective evaluation of clinical utility of direct TR-quantification in Ebstein patients with various degrees of TR. 4D flow MRI-derived direct quantification of TR may prove to be helpful in the follow-up of patients with Ebstein's anomaly and may have implications for the timing of an intervention.

Different from streamlines, pathlines show the path a particle (i.e., a voxel) has followed over time [30]. Particle paths or pathlines are generated by backward/forward particle tracing using integration methods to calculate displacement from the velocity data [30]. For intra-cardiac blood flow, typically, at end diastole, each voxel inside the LV is considered to represent a seed point (i.e., a particle). Pathlines are then calculated by integration over time: backward tracing over the diastole and forward tracing over systole. Pathlines are also frequently used to evaluate complex flow patterns, such as helical flow patterns in the aorta and pulmonary artery [34, 39].

Another unique feature of particle tracing in intra-cardiac blood flow is the possibility to discriminate different parts of blood flow with some specific functional property based on where the seed points are flowing towards and where they came from. Different components in the blood flow organization in the left ventricle (LV) [40] and the right ventricle (RV) [41] can be discriminated, such as the 4-component evaluation (*Figure 4*) as introduced by Bolger et al. [42].

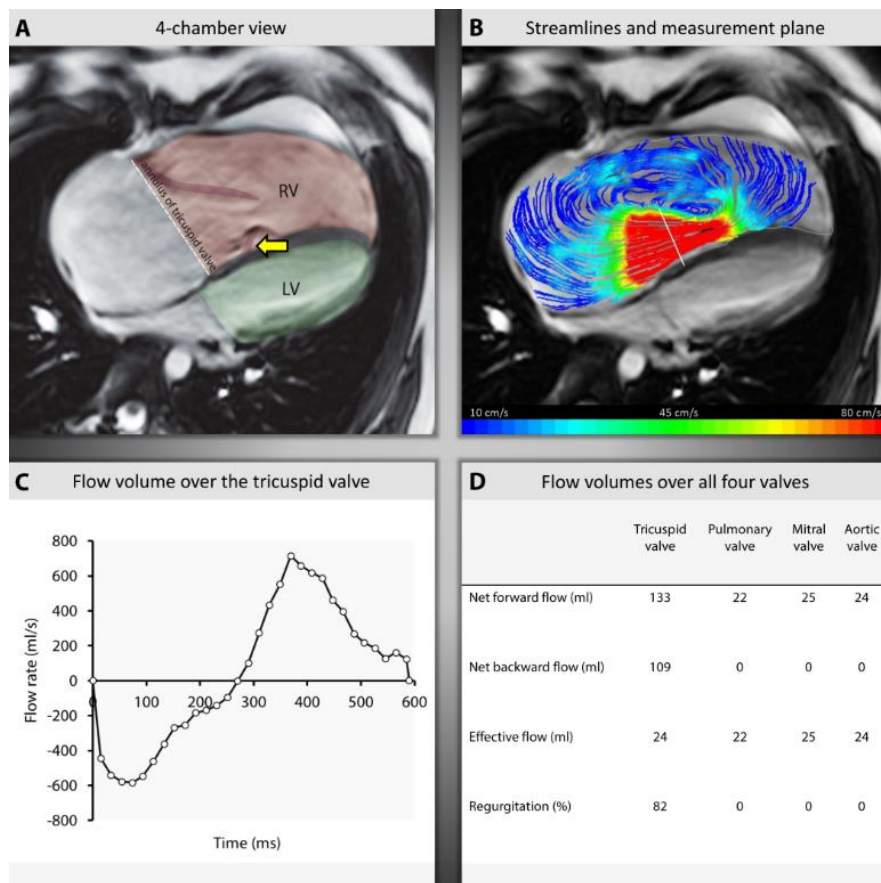


Figure 3. Direct assessment of Tricuspid Regurgitation by 4D flow MRI in a Patient with Ebstein's Anomaly

The following components can be discriminated for the LV:

1. *Direct flow*: Blood that enters the LV through the mitral valve during diastole and is ejected from the LV into the aorta during the subsequent systole in the analysed heartbeat;
2. *Retained inflow*: Blood that enters the LV during diastole but is not ejected during the subsequent systole in the analysed heartbeat;
3. *Delayed ejection flow*: Blood that starts and remains inside the LV during diastole but is ejected during the subsequent systole;
4. *Residual volume*: Blood that remains within the LV for at least two subsequent cardiac cycles.

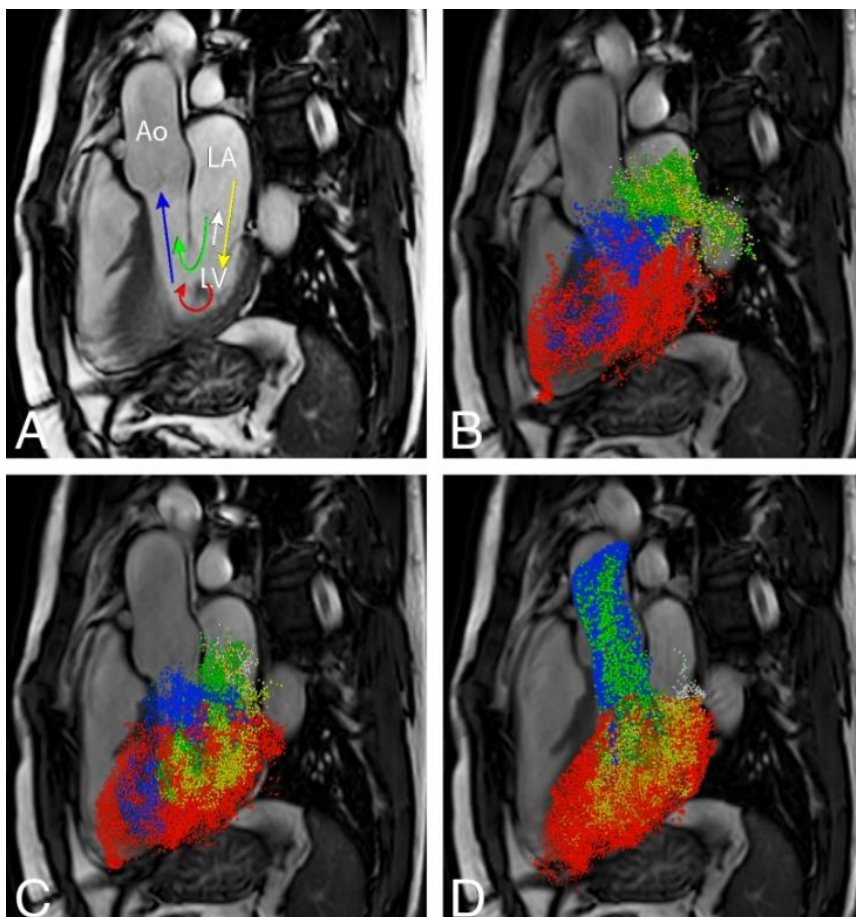


Figure 4. Multi-component particle tracing of left ventricular (LV) blood flow in a healthy volunteer (26 year old man). In A, five components of LV are schematically presented. Green: direct flow; Yellow: retained inflow; Blue: delayed ejection flow; Red: residual volume; White: regurgitation. Three time-points in cardiac cycle are represented: diastole in B, end diastole in C, systole in D. LA: left atrium, LV: left ventricle, Ao: Aorta.

A fifth component can be added, *Regurgitation*: Blood that leaves the LV through the mitral valve into the atrium during systole [43]. It should be taken into account that particle tracing analysis requires high temporal resolution and adequate signal-to-noise, as results coming from an integration procedure on noisy data and over large time steps may not be reliable.

From the 3D flow velocity field, helical and vortical flow patterns can be identified in normal and pathological blood flow. An important intra-cardiac flow pattern is vortex flow: a group

of fluid particles swirling around a common axis. Two methods have been used to analyze and visualize intra-cardiac vortex flow patterns: Lagrangian and Eulerian. Lagrangian coherent structures (LCS) can be used to quantify and visualize the total amount of flow that entrains into vortex ring flow structure over a period of time [44]. Eulerian vortex core analysis allows quantitative characterization of instantaneous 3D vortical flow patterns and its intra-cardiac evolution over time [45]. Altered intra-cardiac 3D vortex flow properties have been identified in the presence of abnormal valvular morphology and were associated with adverse blood flow efficiency [2, 45, 46].

Four-dimensional flow MRI is also used for studying energetics in the blood flow. The kinetic energy (KE) of a moving particle with a certain mass m (particle volume multiplied by the blood density) and velocity v , can be calculated with the formula $\frac{1}{2}mv^2$. The KE at a specific time point can then be calculated by summing the KE of each voxel within a specified anatomical region. Viscous energy loss (EL) is the kinetic energy that is lost due to frictional forces among blood particles and surrounding structures in the ventricle, induced by the blood viscosity. EL can be calculated from the Navier-Stokes energy equations [2]. Turbulent kinetic energy (TKE) is another frequently used energy parameter used to quantify the energy lost due to turbulent flow and is calculated from dedicated reconstructions of the intravoxel distribution of spin velocities [47].

Figure 5 shows an example of a patient with a Fontan circulation because of a complete atrioventricular septal defect (AVSD) and a double outlet right ventricle with pulmonary stenosis [48].

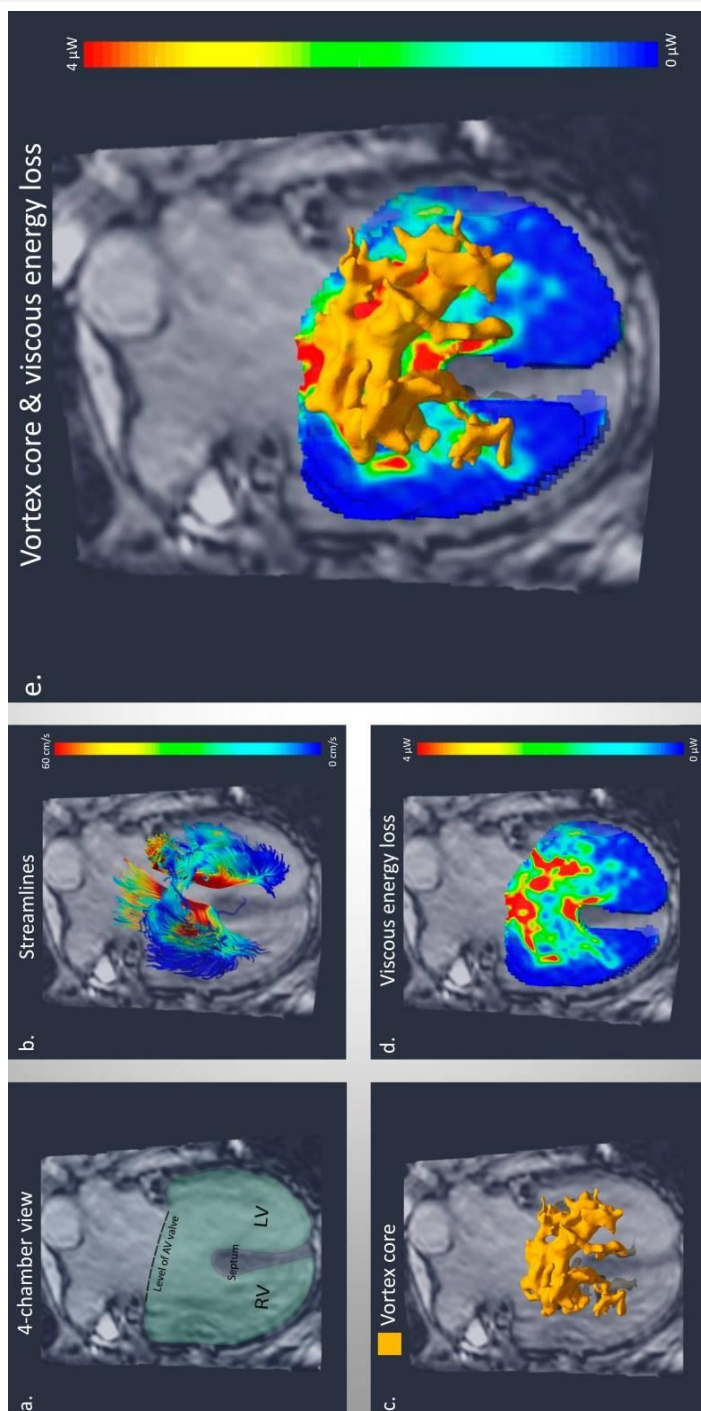


Figure 5. vortex formation and viscous energy loss in an adult Fontan patient

In this case example 4D flow MRI-derived streamline visualization showed a complex 3D inflow pattern from the common atrioventricular valve with the formation of vortical flow around the ventricular part of the septal defect (*Figure 5B*). Mathematical identification of vortex core structures from 4D flow MRI [45] showed a large 3D ring-like vortex formation filling the common biventricular region at the level of the ventricular septal defect, with protrusion in both ventricles (*Figure 5C*). To assess the regions of highest EL in this patient, a map of EL inside the ventricle was made in the cross-sectional four-chamber view (*Figure 5D*). In *Figure 5E*, regions of the identified 3D vortex structure associate with the highest EL levels in the EL map. These high EL levels anatomically correspond to the region of the ventricular septal defect and part of the remaining septum. Knowledge on the consequences of intracardiac deformations on hemodynamic vortex formation and viscous energy loss might be useful in unraveling the pathophysiological mechanisms leading to circulatory failure, one of the main causes of morbidity and mortality in Fontan patients.

Knowledge on the consequences of intracardiac deformations on hemodynamic vortex formation and viscous energy loss might be useful in unraveling the pathophysiological mechanisms leading to circulatory failure, one of the main causes of morbidity and mortality in Fontan patients.

Wall shear stress (WSS) is a quantitative value for the shear forces of the blood flow acting on the vessel wall [49]. It can be used to quantify the impact of flow on the vessel wall and it has been shown to correlate with changes in the extracellular matrix (ECM) and endothelial cells [3]. Higher blood flow velocity will increase WSS [50].

Aortic wall elasticity, an important mechanical property of the vascular wall, can be measured with traditional 2D one-directional velocity-encoded MRI [51], but also by multi-directional velocity-encoding or 4D flow MRI [52], by measuring the propagation speed of the systolic wave front along the course of the aorta. This biomarker for arterial stiffness is called the pulse wave velocity (PWV) [53]. A shorter propagation time, thus higher PWV, is indicative of a stiffer aorta and presence of atherosclerosis [54].

Applications

In the following section normal and abnormal blood flow characteristics as assessed with 4D flow MRI will be reviewed. We will describe the use of 4D flow MRI in assessing normal intra-cardiac and intravascular flow patterns, as well as applications in acquired and congenital cardiovascular disease.

Atrial flow patterns

In the normal human heart, blood flow in the left atrium (LA) follows specific paths from the pulmonary veins to the mitral valve. The occurrence of atrial vortices has been shown, which may be beneficial in avoiding atrial stasis [55]. In the LA, inflow from the right pulmonary veins follows the atrial wall from its inlet near the inter-atrial septum toward the mitral annulus, while inflow from the left pulmonary veins suddenly shifts towards the mitral valve after entry through the lateral left atrial wall, as was shown with particle tracing analysis [55]. In the right atrium (RA), blood flow from the inferior vena cava (IVC) and superior vena cava (SVC) turns anterior after entering the atrium, which causes a forward rotating movement of the anterior part of the right atrial blood volume towards the inlet of the tricuspid valve [56].

Assessment of atrial flow patterns and blood flow velocity is important in patients with atrial fibrillation (AF), since AF is associated with an increased risk of embolic stroke due to thrombus formation in the LA [57]. Patients with AF show global and regional changes in atrial flow dynamics, such as decreased blood flow velocities and increased stasis, which can be evaluated with 4D flow MRI and could be a helpful indicator in risk assessment for thrombogenesis in these patients [58-60].

In patients with mitral regurgitation, severely disturbed flow patterns in the LA with elevated values of TKE develop, related to the severity of regurgitation [61]. These atrial flow effects of mitral regurgitation assessed by 4D flow MRI could potentially be used in risk assessment for the onset of decompensated heart failure in patients with prior asymptomatic mitral regurgitation [61]. The amount and severity of mitral valve regurgitation (i.e., the regurgitant flow volume and the regurgitant flow fraction) can accurately be assessed with the use of 4D flow MRI with retrospective valve tracking [35, 36].

In corrected AVSD patients, regurgitation of the left atrioventricular valve (LAVV) is common [62]. In these patients, the regurgitant jets are dynamic and eccentric (*Figure 2*) and have a non-circular cross-sectional shape, which makes them challenging to quantify with echocardiography [63]. However, the regurgitant fraction and the volume of the complex

regurgitant jets can be quantified accurately with the use of 4D flow MRI with retrospective valve tracking [33]. Furthermore, 4D flow MRI can also be applied to investigate intra-cardiac baffle constructions for leakage and obstruction, for instance after double switch operation for congenitally corrected transposition of the great arteries [64].

Flow patterns in the left ventricle

The complex geometry of the normal LV causes asymmetric blood flow, which promotes efficient ejection of blood in the systemic circulation and minimizes the energy dissipation [1, 56]. In the normal LV, 30-35% of the LV end diastolic volume represents blood flow that enters the LV during diastole and is ejected into the aorta during systole in the subsequent heartbeat (i.e. direct flow) [40, 43]. Using 4D flow MRI, vortical flow patterns have been described that form during diastole, with a close relation to the motion of the anterior mitral leaflet and the shape of mitral inflow [44, 45, 65]. During diastole, a pair of counter rotating vortices has been consistently reported to form distal to the mitral valve. In three-dimensions, this pair of vortices extend to form a ring-like vortex shape. 4D flow MRI has enabled the characterization of the instantaneous time-evolution of 3D vortex ring flow within the LV over the complete diastole [45]. Formation of vortex ring flow has been suggested to help efficient MV closure and diastolic filling, minimize kinetic energy loss and prevent thrombus formation [1, 56, 66, 67]. Vortex flow patterns can change due to age, gender, blood pressure, ventricular geometry and mitral/atrioventricular valve abnormalities [46, 68].

In patients after AVSD correction, the LV inflow over the LAVV is altered (i.e., a more lateral inflow was shown by streamline visualization) (*Figure 2*) [32]. 4D flow MRI with particle tracing showed that this altered inflow after AVSD correction also affected the intra-cardiac flow organization, which presented as reduced direct flow and increased retained inflow in apical and lateral region of the LV cavity [43]. Despite that global cardiac function parameters (including EF, EDV, SV, CO) were within the normal range in these patients, significantly altered vortex ring flow properties were found and associated with a 2-4 fold increase in viscous energy loss levels compared to healthy volunteers [2, 46]. This might indicate that properties of vortex ring flow within LV blood flow could be a subclinical marker of cardiac (dys)function preceding decline in global functional parameters [2].

In patients with systolic or diastolic dysfunction, flow disturbances can be evaluated with 4D flow MRI imaging. LV diastolic dysfunction in patients with normal systolic LV function is a risk factor for mortality [69]. LV diastolic function parameters, such as early (E) and late (A) filling rates, E/A ratio, and E-peak acceleration and deceleration duration, can be assessed accurately with the use of 4D flow MRI with retrospective valve tracking [70]. Furthermore,

a study using 4D flow MRI with color vector visualization showed that in patients with various stages of diastolic dysfunction, LV diastolic flow only extends a short distance in the LV and stops in the middle of the LV cavity due to decreased flow acceleration [71]. Patients with dilated cardiomyopathy showed a smaller direct flow volume and greater end-diastolic KE distribution in the residual volume, despite normal LV stroke volume, as shown by particle tracing analysis with the 4-component model [72]. Whereas, in patients with ischemic dilated cardiomyopathy, altered flow patterns were related to complex and asymmetric vortex rings and decreased vortex volume [44].

Patients who have had a Fontan operation, a palliative treatment for patients with single-ventricle physiology, have complex and heterogeneous underlying ventricular morphologies which makes studying the intra-cardiac blood flow in these patients challenging. However, the dynamic and 3D nature of the blood flow in these patients makes 4D flow MRI particularly suitable for the assessment and quantification of these flow patterns. Recently, various blood flow patterns were shown in these patients with 4D flow MRI with streamline visualization and inflow volumes were quantified with retrospective valve tracking [37]. Assessment of the caval blood flow in these complex patients will be addressed in the section on intravascular blood flow patterns.

Flow patterns in the right ventricle

Visualization of flow in the RV remains challenging because of the complex 3D shape of this ventricular cavity. *In vivo* and *in vitro* studies showed that in the normal RV, blood flow rearranges along the converging outflow tract during systole to form helical circulating flow towards the pulmonary orifice [5, 41, 56]. Particle tracing analysis in the RV showed that 44% of the blood is direct flow, which moves from the RA into the RV during diastole and moves towards the RV outflow tract, rounding the infundibular septum and contributing to vortical formation that extends in the outflow tract [41]. Compared to the other flow components, this direct flow possesses a larger presystolic KE, which may benefit the efficiency of systolic ejection [41].

Extensive knowledge of the RV flow and function is of interest in many types of heart defects, especially in patients with CHD, as lesions affecting the RV are an independent risk factor for early attrition [73]. For example, patients with Tetralogy of Fallot (ToF) have altered RV flow patterns resulting in increased vortical flow patterns in the RA and RV during diastole [74]. Accurate assessment of forward flow and regurgitation fraction over the tricuspid and pulmonary valve in these ToF patients after corrective surgery, which is important in the

assessment of RV diastolic functional impairment, can be performed using 4D flow MRI with retrospective valve tracking [75].

In patients with pulmonary hypertension (PH), RV diastolic dysfunction (RVDD) is an important prognostic factor [76]. Recently, it was shown by 4D flow MRI that patients with RVDD due to PH have altered vorticity in the RV at peak E- and A- diastolic filling. The presence of altered RV vorticity could be a valuable marker to evaluate the risk of RVDD development, as it was shown to have a clear relationship [77]. Furthermore, 4D flow MRI showed that PH is related to altered KE RV work density (i.e., a measure of the amount of work the RV has produce to transport blood from RA to the pulmonary artery) and viscous energy loss in the blood flow in the pulmonary artery [78], which is also shown to be related to increased vorticity in the blood flow in the pulmonary artery [79].

In patients with ischemic heart disease, 4D flow MRI could be used to detect impairment of RV function, as shown by changes in flow distribution and KE, which could potentially have prognostic implications [80].

Flow patterns in the great vessels

Aorta

Normal aortic flow patterns include right-handed helical outflow and late systolic retrograde flow (blood flowing counter to the main forward stream), as shown by 4D flow MRI [34, 81]. This helical and retrograde flow results from the curvature of the arch, the pulsatility of the blood flow and the compliance of the aortic wall [81]. Aging has been shown to influence flow patterns in several ways; direction of the helical flow may change from right-handed to left-handed [82, 83], the aortic velocity distribution may change, resulting in changing WSS maps [84-86] and PWV values along the aorta increase [87, 88]. Therefore, age has to be taken into account when evaluating aortic flow patterns in healthy subjects and patients with cardiovascular disease. The application of 4D flow MRI in patients with aortic disease is promising as it can help gain knowledge of the disease progression, it can aid the prediction of adverse aortic events and can be useful in the optimization of individualized management strategies. Most extensive aortic 4D flow research has been done in patients with BAV [3, 7, 8] and Marfan syndrome [9-13].

Patients with BAV frequently develop aortic valve dysfunction, ascending aortic aneurysms, and aortic dissection. For many years, aortic dilatation in these patients has been attributed to the genetic susceptibility resulting in a concomitant abnormal development of the ascending aorta and BAV. 4D flow MRI shed another light on this hypothesis by identifying

different abnormal outflow patterns in the ascending aorta (*Figure 6*) that might predispose to this aortopathy [7, 8]. Recently, it has been shown that different fusion patterns of the aortic valve will lead to different impingement flow jets on the ascending aortic wall [3, 8]. Fusion of right and left leaflets causes right-handed helical flow and right-anterior flow jets, while right and non-coronary leaflet fusion causes left-handed helical flow with left-posterior flow jets [8]. These regions of altered flow patterns show elevated WSS which correlates well with extracellular matrix changes in that aortic region [3]. This suggests a hemodynamic contribution of the aortopathy.

In patients with Marfan syndrome, an inherited connective tissue disease at risk for thoracic aortic dilatation, local helix flow in the ascending aorta as well as abnormal regional WSS has been linked to increased aortic size [9-11]. Furthermore, in young patients with Marfan syndrome, hemodynamic differences in WSS were found at specific regions along the thoracic aorta that correspond to the locations where aortic dissection and aortic rupture often originate in these patients, i.e., the proximal ascending aorta and proximal descending aorta [13]. These data, together with the report of a single Marfan syndrome case in which prior to an aortic dissection type B, formation of abnormal flow patterns and altered WSS in the proximal descending aorta was observed, suggest that hemodynamic factors may play a predictive role in the onset of adverse events [12].

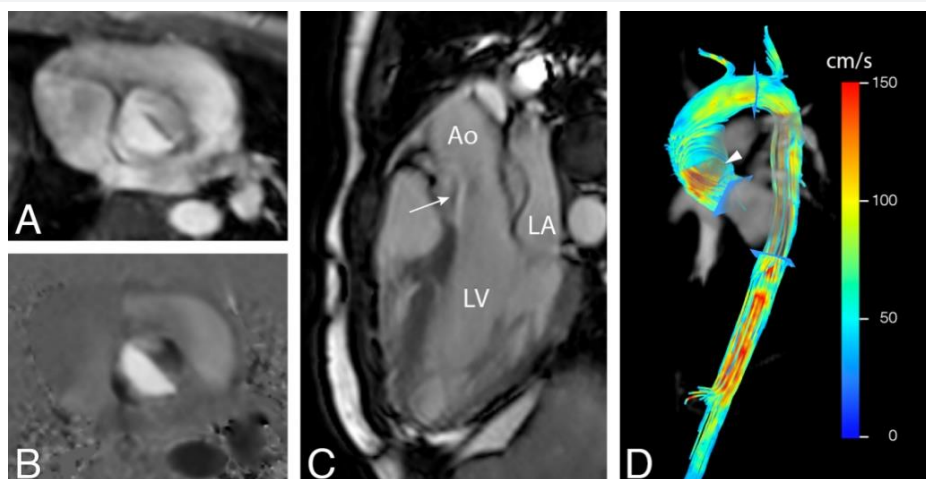
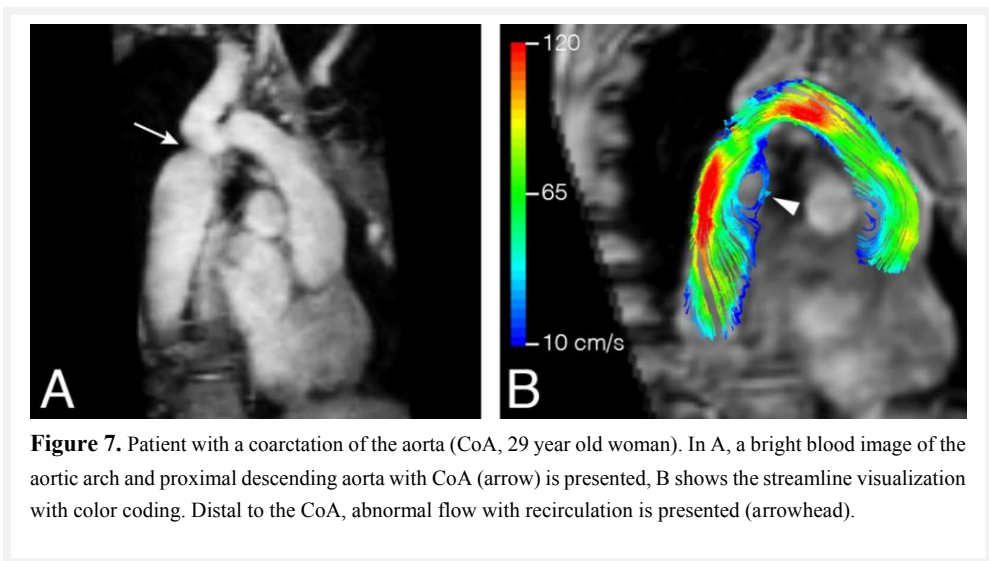


Figure 6. Patient with bicuspid aortic valve (BAV, 28 year old man) and mild dilatation of the ascending aorta. A and B show axial views of through-plane velocity-encoded phase contrast MRI acquisition of the flow velocity through the valve (A: magnitude image, B: phase image). In C, a double-oblique lateral view of the aortic outflow tract with BAV is presented. D shows streamline visualization with color coding of systolic outflow, with abnormal circulating blood flow (arrowhead) and helical flow in the aortic arch.

In patients with coarctation of the aorta (CoA), a short segment of narrowing of the proximal descending aorta just beyond the origin of the arteries that supply the head and arms, 4D flow MRI is an accurate method for the evaluation of collateral flow, which is related to hemodynamic significant coarctation [89]. Also, altered flow patterns and increased WSS can be found in patients with CoA in the entire aorta, before and after repair (*Figure 7*) [90]. Other promising applications of aortic 4D flow MRI are related to noninvasive investigation of trans-stenotic pressure gradients in the presence of stenosis in vascular diseases such as aortic CoA [91, 92]. Today, severity of stenosis in CoA is estimated by ultrasonography but the pressure gradients are often overestimated compared to the actual measurements in vivo per catheter. This potentially leads to unnecessary early interventions, with its risk for the need of more complex and a larger amount of re-interventions per patient. Thus, better predicting the need and timing of intervention for aortic CoA non-invasively can be optimized with 4D flow MRI. Furthermore, energy losses that appears in these turbulent flow conditions can be quantified and maps for dissipation of kinetic energy can be created [93, 94]. These applications make it possible to simulate with advanced post-processing software (by virtual interventions) which intervention preserves the natural thoracic aortic function the most, prior to the intervention [95].



Pulmonary artery

In normal pulmonary physiology, two counter-rotating helical flow structures in the main pulmonary artery (PA) were shown with 4D flow MRI, which both contribute mainly to the flow in the right pulmonary artery (RPA) [96]. In early systole, blood flow from the right

side of the PA is distributed to the RPA and blood flow from the left side of the PA is distributed to the left pulmonary artery (LPA), while later in systole blood flow from the left posterior side of the PA is distributed to the RPA as shown by streamline visualization [96]. Changes in the pulmonary blood flow are age dependent, which may be helpful in future studies in understanding pathological blood flow in patients with pulmonary disease [97].

Patients with PH are currently diagnosed when mean pulmonary artery pressure (mPAP), measured invasively by right heart catheterization, exceeds 25 mmHg [98]. However, 4D flow MRI with streamline visualization showed abnormal vortical flow in the main PA of these patients. The presence, and in particular the duration of vortical flow presence, could become a useful noninvasive diagnostic marker as it has been shown to correlate well with mPAP [79]. Also, a decrease in vorticity in the main PA and RPA as assessed by 4D flow MRI was recently associated with an increase in pulmonary vascular resistance (PVR) in patients with PH [99].

Altered flow patterns have also been described with 4D flow MRI in the PA of patients with repaired ToF [74]. The increase of these abnormal flow patterns, specifically helical and vortical flow, could be related to the size of the pulmonary arteries or increased PVR and elevated PAP [74].

In patients with a Fontan circulation, blood flows passively from the IVC and SVC to the pulmonary arteries without passing through a ventricle. As expected, this results in altered pulmonary and caval blood flow patterns [39]. As these patients require lifelong follow-up, accurate visualization and quantification of flow patterns is crucial. Several 4D flow MRI studies have shown that blood flow from the SVC favors the right pulmonary artery, while most of the IVC blood flows to the left pulmonary artery, as shown by particle tracing analysis [100, 101]. Recently it was shown that the cross-sectional area of the pulmonary arteries in these patients is related to altered flow distribution [101]. The study of caval blood flow distribution could help to identify the patients at risk for Fontan failure or the development of pulmonary arteriovenous malformations, an important complication in these patients leading to systemic oxygen desaturation [102].

Conclusions and future application/advances

In the recent years, 4D flow MRI has emerged as a suitable technique for research use and several studies have shown its clinical value in patients with congenital and acquired heart disease. Shorter acquisition duration has made this application feasible in the clinic. However, dedicated studies investigating the reproducibility and reliability of some of the

4D flow MRI parameters are still warranted before 4D flow MRI can be applied in daily clinical practice. In this review, we showed the different advantages and possibilities of 4D flow MRI intra-cardiac as well as intravascular. Knowledge of normal and abnormal blood flow has increased the understanding of normal physiology and is necessary for the distinction between cardiovascular healthy and diseased. 4D flow MRI is a promising additional diagnostic tool that could aid in management of cardiovascular disease and timing of surgical intervention. Furthermore, 4D flow MRI gives the opportunity to further unravel the influence of different surgical reconstruction methods on the cardiac and vascular function. However, longitudinal follow-up studies are needed to clarify the clinical value of 4D flow MRI derived hemodynamic factors for risk stratification. Other future applications could include the use of 4D flow MRI in the assessment of blood flow patterns in coronary arteries, which is currently still too challenging because of demands regarding the high spatial resolution needed for such small vessels and stringent necessity of cardiac motion correction, but this application might become feasible when further improvements in hardware and imaging at high field strength become available.

References

1. Pedrizzetti G, Domenichini F: Nature optimizes the swirling flow in the human left ventricle. *Phys Rev Lett* 2005, 95:108101.
2. Elbaz MS, van der Geest RJ, Calkoen EE, de Roos A, Lelieveldt BP, Roest AA, Westenberg JJ: Assessment of viscous energy loss and the association with three-dimensional vortex ring formation in left ventricular inflow: In vivo evaluation using four-dimensional flow MRI. *Magn Reson Med* 2017, 77:794-805.
3. Guzzardi DG, Barker AJ, van Ooij P, Malaisrie SC, Puthumana JJ, Belke DD, Mewhort HE, Svystonyuk DA, Kang S, Verma S, et al: Valve-Related Hemodynamics Mediate Human Bicuspid Aortopathy: Insights From Wall Shear Stress Mapping. *J Am Coll Cardiol* 2015, 66:892-900.
4. Shyy YJ, Hsieh HJ, Usami S, Chien S: Fluid shear stress induces a biphasic response of human monocyte chemotactic protein 1 gene expression in vascular endothelium. *Proc Natl Acad Sci U S A* 1994, 91:4678-4682.
5. Mangual JO, Domenichini F, Pedrizzetti G: Describing the highly three dimensional Right Ventricle flow. *Ann Biomed Eng* 2012, 40:1790-1801.
6. Markl M, Chan FP, Alley MT, Wedding KL, Draney MT, Elkins CJ, Parker DW, Wicker R, Taylor CA, Herfkens RJ, Pelc NJ: Time-resolved three-dimensional phase-contrast MRI. *J Magn Reson Imaging* 2003, 17:499-506.
7. Barker AJ, Markl M, Burk J, Lorenz R, Bock J, Bauer S, Schulz-Menger J, von Knobelsdorff-Brenkenhoff F: Bicuspid aortic valve is associated with altered wall shear stress in the ascending aorta. *Circ Cardiovasc Imaging* 2012, 5:457-466.
8. Hope MD, Hope TA, Meadows AK, Ordoas KG, Urbana TH, Alley MT, Higgins CB: Bicuspid aortic valve: four-dimensional MR evaluation of ascending aortic systolic flow patterns. *Radiology* 2010, 255:53-61.
9. Geiger J, Markl M, Herzer L, Hirtler D, Loeffelbein F, Stiller B, Langer M, Arnold R: Aortic flow patterns in patients with Marfan syndrome assessed by flow-sensitive four-dimensional MRI. *J Magn Reson Imaging* 2012, 35:594-600.
10. Kroner ES, Scholte AJ, de Koning PJ, van den Boogaard PJ, Kroft LJ, van der Geest RJ, Hilhorst-Hofstee Y, Lamb HJ, Siebelink HM, Mulder BJ, et al: MRI-assessed regional pulse wave velocity for predicting absence of regional aorta luminal growth in marfan syndrome. *Int J Cardiol* 2013, 167:2977-2982.
11. Wang HH, Chiu HH, Tseng WY, Peng HH: Does altered aortic flow in marfan syndrome relate to aortic root dilatation? *J Magn Reson Imaging* 2016, 44:500-508.
12. Hope TA, Kvitting JP, Hope MD, Miller DC, Markl M, Herfkens RJ: Evaluation of Marfan patients status post valve-sparing aortic root replacement with 4D flow. *Magn Reson Imaging* 2013, 31:1479-1484.
13. Geiger J, Arnold R, Herzer L, Hirtler D, Stankovic Z, Russe M, Langer M, Markl M: Aortic wall shear stress in Marfan syndrome. *Magn Reson Med* 2013, 70:1137-1144.
14. Pelc NJ, Herfkens RJ, Shimakawa A, Enzmann DR: Phase contrast cine magnetic resonance imaging. *Magn Reson Q* 1991, 7:229-254.
15. Dyverfeldt P, Bissell M, Barker AJ, Bolger AF, Carlhall CJ, Ebbers T, Francios CJ, Frydrychowicz A, Geiger J, Giese D, et al: 4D flow cardiovascular magnetic resonance consensus statement. *J Cardiovasc Magn Reson* 2015, 17:72.
16. Thunberg P, Karlsson M, Wigstrom L: Accuracy and reproducibility in phase contrast imaging using SENSE. *Magn Reson Med* 2003, 50:1061-1068.
17. Baltes C, Kozerke S, Hansen MS, Pruessmann KP, Tsao J, Boesiger P: Accelerating cine phase-contrast flow measurements using k-t BLAST and k-t SENSE. *Magn Reson Med* 2005, 54:1430-1438.
18. Firmin DN, Klipstein RH, Hounsfield GL, Paley MP, Longmore DB: Echo-planar high-resolution flow velocity mapping. *Magn Reson Med* 1989, 12:316-327.
19. Sigfridsson A, Petersson S, Carlhall CJ, Ebbers T: Four-dimensional flow MRI using spiral acquisition. *Magn Reson Med* 2012, 68:1065-1073.
20. Gu T, Korosec FR, Block WF, Fain SB, Turk Q, Lum D, Zhou Y, Grist TM, Haughton V, Mistretta CA: PC VIPR: a high-speed 3D phase-contrast method for flow quantification and high-resolution angiography. *AJNR Am J Neuroradiol* 2005, 26:743-749.

21. Uribe S, Beerbaum P, Sorensen TS, Rasmusson A, Razavi R, Schaeffter T: Four-dimensional (4D) flow of the whole heart and great vessels using real-time respiratory self-gating. *Magn Reson Med* 2009, 62:984-992.
22. Uribe S, Muthurangu V, Boubertakh R, Schaeffter T, Razavi R, Hill DL, Hansen MS: Whole-heart cine MRI using real-time respiratory self-gating. *Magn Reson Med* 2007, 57:606-613.
23. Nordmeyer S, Riesenkampff E, Crelier G, Khasheei A, Schnackenburg B, Berger F, Kuehne T: Flow-sensitive four-dimensional cine magnetic resonance imaging for offline blood flow quantification in multiple vessels: a validation study. *J Magn Reson Imaging* 2010, 32:677-683.
24. Kanski M, Toger J, Steding-Ehrenborg K, Xanthis C, Bloch KM, Heiberg E, Carlsson M, Arheden H: Whole-heart four-dimensional flow can be acquired with preserved quality without respiratory gating, facilitating clinical use: a head-to-head comparison. *BMC Med Imaging* 2015, 15:20.
25. Walker PG, Cranney GB, Scheidegger MB, Waseleski G, Pohost GM, Yoganathan AP: Semiautomated method for noise reduction and background phase error correction in MR phase velocity data. *J Magn Reson Imaging* 1993, 3:521-530.
26. Bernstein MA, Zhou XJ, Polzin JA, King KF, Ganin A, Pelc NJ, Glover GH: Concomitant gradient terms in phase contrast MR: analysis and correction. *Magn Reson Med* 1998, 39:300-308.
27. Markl M, Bammer R, Alley MT, Elkins CJ, Draney MT, Barnett A, Moseley ME, Glover GH, Pelc NJ: Generalized reconstruction of phase contrast MRI: analysis and correction of the effect of gradient field distortions. *Magn Reson Med* 2003, 50:791-801.
28. Gatehouse PD, Rolf MP, Graves MJ, Hofman MB, Totman J, Werner B, Quest RA, Liu Y, von Spiczak J, Dieringer M, et al: Flow measurement by cardiovascular magnetic resonance: a multi-centre multi-vendor study of background phase offset errors that can compromise the accuracy of derived regurgitant or shunt flow measurements. *J Cardiovasc Magn Reson* 2010, 12:5.
29. Lotz J, Meier C, Leppert A, Galanski M: Cardiovascular flow measurement with phase-contrast MR imaging: basic facts and implementation. *Radiographics* 2002, 22:651-671.
30. Buonocore MH: Visualizing blood flow patterns using streamlines, arrows, and particle paths. *Magn Reson Med* 1998, 40:210-226.
31. Napel S, Lee DH, Frayne R, Rutt BK: Visualizing three-dimensional flow with simulated streamlines and three-dimensional phase-contrast MR imaging. *J Magn Reson Imaging* 1992, 2:143-153.
32. Calkoen EE, Roest AA, Kroft LJ, van der Geest RJ, Jongbloed MR, van den Boogaard PJ, Blom NA, Hazekamp MG, de Roos A, Westenberg JJ: Characterization and improved quantification of left ventricular inflow using streamline visualization with 4DFlow MRI in healthy controls and patients after atrioventricular septal defect correction. *J Magn Reson Imaging* 2015, 41:1512-1520.
33. Calkoen EE, Westenberg JJ, Kroft LJ, Blom NA, Hazekamp MG, Rijlaarsdam ME, Jongbloed MR, de Roos A, Roest AA: Characterization and quantification of dynamic eccentric regurgitation of the left atrioventricular valve after atrioventricular septal defect correction with 4D Flow cardiovascular magnetic resonance and retrospective valve tracking. *J Cardiovasc Magn Reson* 2015, 17:18.
34. Markl M, Draney MT, Hope MD, Levin JM, Chan FP, Alley MT, Pelc NJ, Herfkens RJ: Time-resolved 3-dimensional velocity mapping in the thoracic aorta: visualization of 3-directional blood flow patterns in healthy volunteers and patients. *J Comput Assist Tomogr* 2004, 28:459-468.
35. Roes SD, Hammer S, van der Geest RJ, Marsan NA, Bax JJ, Lamb HJ, Reiber JH, de Roos A, Westenberg JJ: Flow assessment through four heart valves simultaneously using 3-dimensional 3-directional velocity-encoded magnetic resonance imaging with retrospective valve tracking in healthy volunteers and patients with valvular regurgitation. *Invest Radiol* 2009, 44:669-675.
36. Westenberg JJ, Roes SD, Ajmone Marsan N, Binnendijk NM, Doornbos J, Bax JJ, Reiber JH, de Roos A, van der Geest RJ: Mitral valve and tricuspid valve blood flow: accurate quantification with 3D velocity-encoded MR imaging with retrospective valve tracking. *Radiology* 2008, 249:792-800.
37. She HL, Roest AA, Calkoen EE, van den Boogaard PJ, van der Geest RJ, Hazekamp MG, de Roos A, Westenberg JJ: Comparative Evaluation of Flow Quantification across the Atrioventricular Valve in Patients with Functional Univentricular Heart after Fontan's Surgery and Healthy Controls: Measurement by 4D Flow Magnetic Resonance Imaging and Streamline Visualization. *Congenit Heart Dis*. 2017, 12:40-48.

38. Kamphuis VP, Westenberg JJM, van den Boogaard PJ, Clur SB, Roest AAW: Direct assessment of tricuspid regurgitation by 4D flow cardiovascular magnetic resonance in a patient with Ebstein's anomaly. *Eur Heart J Cardiovasc Imaging* 2018, 5:587-588.
39. Houtzager JH, Westenberg JJ, de Koning PJ, Hazekamp MG, Roest AA: Helical flow pattern in the right pulmonary artery after Fontan palliation. *Eur Heart J Cardiovasc Imaging* 2014, 15:1183.
40. Eriksson J, Carlhall CJ, Dyverfeldt P, Engvall J, Bolger AF, Ebberts T: Semi-automatic quantification of 4D left ventricular blood flow. *J Cardiovasc Magn Reson* 2010, 12:9.
41. Fredriksson AG, Zajac J, Eriksson J, Dyverfeldt P, Bolger AF, Ebberts T, Carlhall CJ: 4-D blood flow in the human right ventricle. *Am J Physiol Heart Circ Physiol* 2011, 301:H2344-2350.
42. Bolger AF, Heiberg E, Karlsson M, Wigstrom L, Engvall J, Sigfridsson A, Ebberts T, Kvitting JP, Carlhall CJ, Wranne B: Transit of blood flow through the human left ventricle mapped by cardiovascular magnetic resonance. *J Cardiovasc Magn Reson* 2007, 9:741-747.
43. Calkoen EE, de Koning PJ, Blom NA, Kroft LJ, de Roos A, Wolterbeek R, Roest AA, Westenberg JJ: Disturbed Intracardiac Flow Organization After Atrioventricular Septal Defect Correction as Assessed With 4D Flow Magnetic Resonance Imaging and Quantitative Particle Tracing. *Invest Radiol* 2015, 50:850-857.
44. Toger J, Kanski M, Carlsson M, Kovacs SJ, Soderlind G, Arheden H, Heiberg E: Vortex ring formation in the left ventricle of the heart: analysis by 4D flow MRI and Lagrangian coherent structures. *Ann Biomed Eng* 2012, 40:2652-2662.
45. Elbaz MS, Calkoen EE, Westenberg JJ, Lelieveldt BP, Roest AA, van der Geest RJ: Vortex flow during early and late left ventricular filling in normal subjects: quantitative characterization using retrospectively-gated 4D flow cardiovascular magnetic resonance and three-dimensional vortex core analysis. *J Cardiovasc Magn Reson* 2014, 16:78.
46. Calkoen EE, Elbaz MS, Westenberg JJ, Kroft LJ, Hazekamp MG, Roest AA, van der Geest RJ: Altered left ventricular vortex ring formation by 4-dimensional flow magnetic resonance imaging after repair of atrioventricular septal defects. *J Thorac Cardiovasc Surg* 2015, 150:1233-1240 e1231.
47. Dyverfeldt P, Kvitting JP, Sigfridsson A, Engvall J, Bolger AF, Ebberts T: Assessment of fluctuating velocities in disturbed cardiovascular blood flow: in vivo feasibility of generalized phase-contrast MRI. *J Magn Reson Imaging* 2008, 28:655-663.
48. Kamphuis VP, Roest AAW, Westenberg JJM, Elbaz MSM: Biventricular vortex ring formation corresponds to regions of highest intraventricular viscous energy loss in a Fontan patient: analysis by 4D Flow MRI. *Int J Cardiovasc Imaging* 2018, 34:441-442.
49. Frydrychowicz A, Stalder AF, Russe MF, Bock J, Bauer S, Harloff A, Berger A, Langer M, Hennig J, Markl M: Three-dimensional analysis of segmental wall shear stress in the aorta by flow-sensitive four-dimensional-MRI. *J Magn Reson Imaging* 2009, 30:77-84.
50. Burk J, Blanke P, Stankovic Z, Barker A, Russe M, Geiger J, Frydrychowicz A, Langer M, Markl M: Evaluation of 3D blood flow patterns and wall shear stress in the normal and dilated thoracic aorta using flow-sensitive 4D CMR. *J Cardiovasc Magn Reson* 2012, 14:84.
51. Grotenhuis HB, Westenberg JJ, Steendijk P, van der Geest RJ, Ottenkamp J, Bax JJ, Jukema JW, de Roos A: Validation and reproducibility of aortic pulse wave velocity as assessed with velocity-encoded MRI. *J Magn Reson Imaging* 2009, 30:521-526.
52. Westenberg JJ, de Roos A, Grotenhuis HB, Steendijk P, Hendriksen D, van den Boogaard PJ, van der Geest RJ, Bax JJ, Jukema JW, Reiber JH: Improved aortic pulse wave velocity assessment from multislice two-directional in-plane velocity-encoded magnetic resonance imaging. *J Magn Reson Imaging* 2010, 32:1086-1094.
53. Markl M, Wallis W, Brendecke S, Simon J, Frydrychowicz A, Harloff A: Estimation of global aortic pulse wave velocity by flow-sensitive 4D MRI. *Magn Reson Med* 2010, 63:1575-1582.
54. Blacher J, Asmar R, Djane S, London GM, Safar ME: Aortic pulse wave velocity as a marker of cardiovascular risk in hypertensive patients. *Hypertension* 1999, 33:1111-1117.
55. Fyrenius A, Wigstrom L, Ebberts T, Karlsson M, Engvall J, Bolger AF: Three dimensional flow in the human left atrium. *Heart* 2001, 86:448-455.
56. Kilner PJ, Yang GZ, Wilkes AJ, Mohiaddin RH, Firmin DN, Yacoub MH: Asymmetric redirection of flow through the heart. *Nature* 2000, 404:759-761.
57. Bernhardt P, Schmidt H, Hammerstingl C, Luderitz B, Omran H: Patients with atrial fibrillation and dense spontaneous echo contrast at high risk a prospective and serial follow-up over 12 months

- with transesophageal echocardiography and cerebral magnetic resonance imaging. *J Am Coll Cardiol* 2005, 45:1807-1812.
58. Lee DC, Markl M, Ng J, Carr M, Benefield B, Carr JC, Goldberger JJ: Three-dimensional left atrial blood flow characteristics in patients with atrial fibrillation assessed by 4D flow CMR. *Eur Heart J Cardiovasc Imaging* 2015.
 59. Markl M, Carr M, Ng J, Lee DC, Jarvis K, Carr J, Goldberger JJ: Assessment of left and right atrial 3D hemodynamics in patients with atrial fibrillation: a 4D flow MRI study. *Int J Cardiovasc Imaging* 2016, 32:807-815.
 60. Markl M, Lee DC, Ng J, Carr M, Carr J, Goldberger JJ: Left Atrial 4-Dimensional Flow Magnetic Resonance Imaging: Stasis and Velocity Mapping in Patients With Atrial Fibrillation. *Invest Radiol* 2016, 51:147-154.
 61. Dyverfeldt P, Kvitting JP, Carlhall CJ, Boano G, Sigfridsson A, Hermansson U, Bolger AF, Engvall J, Ebbers T: Hemodynamic aspects of mitral regurgitation assessed by generalized phase-contrast MRI. *J Magn Reson Imaging* 2011, 33:582-588.
 62. Hohenkerk GJ, Bruggemans EF, Rijlaarsdam M, Schoof PH, Koolbergen DR, Hazekamp MG: More than 30 years' experience with surgical correction of atrioventricular septal defects. *Ann Thorac Surg* 2010, 90:1554-1561.
 63. Lancellotti P, Moura L, Pierard LA, Agricola E, Popescu BA, Tribouilloy C, Hagendorff A, Monin JL, Badano L, Zamorano JL, European Association of E: European Association of Echocardiography recommendations for the assessment of valvular regurgitation. Part 2: mitral and tricuspid regurgitation (native valve disease). *Eur J Echocardiogr* 2010, 11:307-332.
 64. van der Palen RL, Westenberg JJ, Hazekamp MG, Kuipers IM, Roest AA: Four-dimensional flow cardiovascular magnetic resonance for the evaluation of the atrial baffle after Mustard repair. *Eur Heart J Cardiovasc Imaging* 2016, 17:353.
 65. Kim WY, Walker PG, Pedersen EM, Poulsen JK, Oyre S, Houliand K, Yoganathan AP: Left ventricular blood flow patterns in normal subjects: a quantitative analysis by three-dimensional magnetic resonance velocity mapping. *J Am Coll Cardiol* 1995, 26:224-238.
 66. Bellhouse BJ: Fluid mechanics of a model mitral valve and left ventricle. *Cardiovasc Res* 1972, 6:199-210.
 67. Ghosh E, Shmuylovich L, Kovacs SJ: Vortex formation time-to-left ventricular early rapid filling relation: model-based prediction with echocardiographic validation. *J Appl Physiol (1985)* 2010, 109:1812-1819.
 68. Foll D, Taeger S, Bode C, Jung B, Markl M: Age, gender, blood pressure, and ventricular geometry influence normal 3D blood flow characteristics in the left heart. *Eur Heart J Cardiovasc Imaging* 2013, 14:366-373.
 69. Bhatia RS, Tu JV, Lee DS, Austin PC, Fang J, Haouzi A, Gong Y, Liu PP: Outcome of heart failure with preserved ejection fraction in a population-based study. *N Engl J Med* 2006, 355:260-269.
 70. Brandts A, Bertini M, van Dijk EJ, Delgado V, Marsan NA, van der Geest RJ, Siebelink HM, de Roos A, Bax JJ, Westenberg JJ: Left ventricular diastolic function assessment from three-dimensional three-directional velocity-encoded MRI with retrospective valve tracking. *J Magn Reson Imaging* 2011, 33:312-319.
 71. Kumar R, Charonko J, Hundley WG, Hamilton CA, Stewart KC, McNeal GR, Vlachos PP, Little WC: Assessment of left ventricular diastolic function using 4-dimensional phase-contrast cardiac magnetic resonance. *J Comput Assist Tomogr* 2011, 35:108-112.
 72. Eriksson J, Bolger AF, Ebbers T, Carlhall CJ: Four-dimensional blood flow-specific markers of LV dysfunction in dilated cardiomyopathy. *Eur Heart J Cardiovasc Imaging* 2013, 14:417-424.
 73. Norozi K, Wessel A, Alpers V, Arnhold JO, Geyer S, Zoege M, Buchhorn R: Incidence and risk distribution of heart failure in adolescents and adults with congenital heart disease after cardiac surgery. *Am J Cardiol* 2006, 97:1238-1243.
 74. Francois CJ, Srinivasan S, Schiebler ML, Reeder SB, Niespodzany E, Landgraf BR, Wieben O, Frydrychowicz A: 4D cardiovascular magnetic resonance velocity mapping of alterations of right heart flow patterns and main pulmonary artery hemodynamics in tetralogy of Fallot. *J Cardiovasc Magn Reson* 2012, 14:16.
 75. van der Hulst AE, Westenberg JJ, Kroft LJ, Bax JJ, Blom NA, de Roos A, Roest AA: Tetralogy of fallot: 3D velocity-encoded MR imaging for evaluation of right ventricular valve flow and diastolic function in patients after correction. *Radiology* 2010, 256:724-734.

76. D'Alonzo GE, Barst RJ, Ayres SM, Bergofsky EH, Brundage BH, Detre KM, Fishman AP, Goldring RM, Groves BM, Kernis JT, et al.: Survival in patients with primary pulmonary hypertension. Results from a national prospective registry. *Ann Intern Med* 1991, 115:343-349.
77. Fenster BE, Browning J, Schroeder JD, Schafer M, Podgorski CA, Smyser J, Silveira LJ, Buckner JK, Hertzberg JR: Vorticity is a marker of right ventricular diastolic dysfunction. *Am J Physiol Heart Circ Physiol* 2015, 309:H1087-1093.
78. Han QJ, Witschey WR, Fang-Yen CM, Arkles JS, Barker AJ, Forfia PR, Han Y: Altered Right Ventricular Kinetic Energy Work Density and Viscous Energy Dissipation in Patients with Pulmonary Arterial Hypertension: A Pilot Study Using 4D Flow MRI. *PLoS One* 2015, 10:e0138365.
79. Reiter G, Reiter U, Kovacs G, Kainz B, Schmidt K, Maier R, Olschewski H, Rienmueller R: Magnetic resonance-derived 3-dimensional blood flow patterns in the main pulmonary artery as a marker of pulmonary hypertension and a measure of elevated mean pulmonary arterial pressure. *Circ Cardiovasc Imaging* 2008, 1:23-30.
80. Fredriksson AG, Svalbring E, Eriksson J, Dyverfeldt P, Alehagen U, Engvall J, Ebbers T, Carlhall CJ: 4D flow MRI can detect subtle right ventricular dysfunction in primary left ventricular disease. *J Magn Reson Imaging* 2016, 43:558-565.
81. Kilner PJ, Yang GZ, Mohiaddin RH, Firmin DN, Longmore DB: Helical and retrograde secondary flow patterns in the aortic arch studied by three-directional magnetic resonance velocity mapping. *Circulation* 1993, 88:2235-2247.
82. Frydrychowicz A, Berger A, Munoz Del Rio A, Russe MF, Bock J, Harloff A, Markl M: Interdependencies of aortic arch secondary flow patterns, geometry, and age analysed by 4-dimensional phase contrast magnetic resonance imaging at 3 Tesla. *Eur Radiol* 2012, 22:1122-1130.
83. Bogren HG, Buonocore MH: 4D magnetic resonance velocity mapping of blood flow patterns in the aorta in young vs. elderly normal subjects. *J Magn Reson Imaging* 1999, 10:861-869.
84. Mohiaddin RH, Firmin DN, Longmore DB: Age-related changes of human aortic flow wave velocity measured noninvasively by magnetic resonance imaging. *J Appl Physiol* (1985) 1993, 74:492-497.
85. van Ooij P, Garcia J, Potters WV, Malaisrie SC, Collins JD, Carr JC, Markl M, Barker AJ: Age-related changes in aortic 3D blood flow velocities and wall shear stress: Implications for the identification of altered hemodynamics in patients with aortic valve disease. *J Magn Reson Imaging* 2016, 43:1239-1249.
86. Voges I, Jerosch-Herold M, Hedderich J, Pardun E, Hart C, Gabbert DD, Hansen JH, Petko C, Kramer HH, Rickers C: Normal values of aortic dimensions, distensibility, and pulse wave velocity in children and young adults: a cross-sectional study. *J Cardiovasc Magn Reson* 2012, 14:77.
87. Segers P, Rietzschel ER, De Buyzere ML, Vermeersch SJ, De Bacquer D, Van Bortel LM, De Backer G, Gillebert TC, Verdonck PR, Asklepios i: Noninvasive (input) impedance, pulse wave velocity, and wave reflection in healthy middle-aged men and women. *Hypertension* 2007, 49:1248-1255.
88. Smulyan H, Asmar RG, Rudnicki A, London GM, Safar ME: Comparative effects of aging in men and women on the properties of the arterial tree. *J Am Coll Cardiol* 2001, 37:1374-1380.
89. Hope MD, Meadows AK, Hope TA, Ordovas KG, Saloner D, Reddy GP, Alley MT, Higgins CB: Clinical evaluation of aortic coarctation with 4D flow MR imaging. *J Magn Reson Imaging* 2010, 31:711-718.
90. Frydrychowicz A, Markl M, Hirtler D, Harloff A, Schlensak C, Geiger J, Stiller B, Arnold R: Aortic hemodynamics in patients with and without repair of aortic coarctation: in vivo analysis by 4D flow-sensitive magnetic resonance imaging. *Invest Radiol* 2011, 46:317-325.
91. Rengier F, Delles M, Eichhorn J, Azad YJ, von Tengg-Kobligh H, Ley-Zaporozhan J, Dillmann R, Kauczor HU, Unterhinninghofen R, Ley S: Noninvasive 4D pressure difference mapping derived from 4D flow MRI in patients with repaired aortic coarctation: comparison with young healthy volunteers. *Int J Cardiovasc Imaging* 2015, 31:823-830.
92. Rengier F, Delles M, Eichhorn J, Azad YJ, von Tengg-Kobligh H, Ley-Zaporozhan J, Dillmann R, Kauczor HU, Unterhinninghofen R, Ley S: Noninvasive pressure difference mapping derived from 4D flow MRI in patients with unrepaired and repaired aortic coarctation. *Cardiovasc Diagn Ther* 2014, 4:97-103.

93. Dyverfeldt P, Hope MD, Tseng EE, Saloner D: Magnetic resonance measurement of turbulent kinetic energy for the estimation of irreversible pressure loss in aortic stenosis. *JACC Cardiovasc Imaging* 2013, 6:64-71.
94. Lantz J, Ebbers T, Engvall J, Karlsson M: Numerical and experimental assessment of turbulent kinetic energy in an aortic coarctation. *J Biomech* 2013, 46:1851-1858.
95. Andersson M, Lantz J, Ebbers T, Karlsson M: Quantitative Assessment of Turbulence and Flow Eccentricity in an Aortic Coarctation: Impact of Virtual Interventions. *Cardiovasc Eng Technol* 2015, 6:281-293.
96. Bachler P, Pinochet N, Sotelo J, Crelier G, Irrazaval P, Tejos C, Uribe S: Assessment of normal flow patterns in the pulmonary circulation by using 4D magnetic resonance velocity mapping. *Magn Reson Imaging* 2013, 31:178-188.
97. Wehrum T, Hagenlocher P, Lodemann T, Vach W, Dragonu I, Hennemuth A, von Zur Muhlen C, Stuplich J, Ngo BT, Harloff A: Age dependence of pulmonary artery blood flow measured by 4D flow cardiovascular magnetic resonance: results of a population-based study. *J Cardiovasc Magn Reson* 2016, 18:31.
98. Galie N, Torbicki A, Barst R, Darteville P, Haworth S, Higenbottam T, Olschewski H, Peacock A, Pietra G, Rubin LJ, et al: Guidelines on diagnosis and treatment of pulmonary arterial hypertension. The Task Force on Diagnosis and Treatment of Pulmonary Arterial Hypertension of the European Society of Cardiology. *Eur Heart J* 2004, 25:2243-2278.
99. Kheifets VO, Schafer M, Podgorski CA, Schroeder JD, Browning J, Hertzberg J, Buckner JK, Hunter KS, Shandas R, Fenster BE: 4D magnetic resonance flow imaging for estimating pulmonary vascular resistance in pulmonary hypertension. *J Magn Reson Imaging* 2016.
100. Bachler P, Valverde I, Pinochet N, Nordmeyer S, Kuehne T, Crelier G, Tejos C, Irrazaval P, Beerbaum P, Uribe S: Caval blood flow distribution in patients with Fontan circulation: quantification by using particle traces from 4D flow MR imaging. *Radiology* 2013, 267:67-75.
101. Jarvis K, Schnell S, Barker AJ, Garcia J, Lorenz R, Rose M, Chowdhary V, Carr J, Robinson JD, Rigsby CK, Markl M: Evaluation of blood flow distribution asymmetry and vascular geometry in patients with Fontan circulation using 4-D flow MRI. *Pediatr Radiol* 2016, 46:1507-19.
102. Dasi LP, Whitehead K, Pekkan K, de Zelicourt D, Sundareswaran K, Kanter K, Fogel MA, Yoganathan AP: Pulmonary hepatic flow distribution in total cavopulmonary connections: extracardiac versus intracardiac. *J Thorac Cardiovasc Surg* 2011, 141:207-214.

Chapter 7

In-scan and scan-rescan assessment of LV in- and outflow volumes by 4D flow MRI versus 2D planimetry

Vivian P Kamphuis, Roel LF van der Palen, Patrick JH de Koning, Mohammed SM Elbaz,
Rob J van der Geest, Albert de Roos, Arno AW Roest, Jos JM Westenberg

J Magn Reson Imaging 2018 Feb; 47 (2): 511-522

Abstract

Objective

To evaluate the in-scan and scan-rescan consistency of left ventricular (LV) in- and outflow assessment from 1) 2D planimetry; 2) 4D flow magnetic resonance imaging (MRI) with retrospective valve tracking and 3) 4D flow MRI with particle tracing.

Methods

Ten healthy volunteers (age 27 ± 3 years) underwent multi-slice cine short-axis planimetry and whole-heart 4D flow MRI on a 3T MRI scanner twice with repositioning between the scans. LV in- and outflow was compared from 1) 2D planimetry; 2) 4D flow MRI with retrospective valve tracking over the mitral valve (MV) and aortic valve (AV) and 3) 4D flow MRI with particle tracing through forward and backward integration of velocity data.

Results

In-scan consistency between MV and AV flow volumes is excellent for both 4D flow MRI methods with $r \geq 0.95$ ($P \leq 0.001$). In-scan AV and MV flow by retrospective valve tracking shows good to excellent correlations versus AV and MV flow by particle tracing ($r \geq 0.81$, $P \leq 0.004$). Scan-rescan SV assessment by 2D planimetry shows excellent reproducibility (ICC=0.98, $P < 0.001$, CV=7%). Scan-rescan MV and AV flow volume assessment by retrospective valve tracking shows strong reproducibility (ICCs ≥ 0.89 , $P \leq 0.05$, CVs $\leq 12\%$), as well as by forward and backward particle tracing (ICCs ≥ 0.90 , $P \leq 0.001$, CVs $\leq 11\%$). Multi-component particle tracing shows good scan-rescan reproducibility (ICCs ≥ 0.81 , $P \leq 0.007$, CVs $\leq 16\%$).

Conclusion

LV in- and outflow assessment by 2D planimetry and 4D flow MRI with retrospective valve tracking and particle tracing show good in-scan consistency and strong scan-rescan reproducibility, which indicates that both 4D flow MRI methods are reliable and can be used clinically.

Introduction

Accurate assessment of left ventricular (LV) in- and outflow volumes is crucial for the evaluation of cardiovascular disease and the distinction between health and disease. The most commonly used approach for assessing LV dimensions and stroke volume is multi-slice planimetry from cine short-axis slices. However, this approach has important limitations for direct quantitation of in- and outflow volumes in the presence of (multi-valve) regurgitation or intracardiac shunts. In such cases, a direct flow assessment at the LV inlet and outlet will resolve these limitations [1, 2].

Four-dimensional (4D) flow MRI (three-dimensional cine phase-contrast (PC) MRI with three-directional velocity-encoding) represents all directions and spatial regions of blood flow velocity and has emerged as a suitable technique for comprehensive visualization and quantification of blood flow volumes over the valves [1-11]. 4D flow MRI with retrospective valve tracking enables accurate direct flow volume quantification through all four valves within a single acquisition, even in patients with valve regurgitation [1, 2] and allows for assessment of diastolic function in the presence of aortic or pulmonary valve regurgitation [7]. 4D flow MRI can also be used in combination with particle tracing to evaluate the intracardiac blood flow distribution and ventricular in- and outflow volumes [5, 8-11].

This approach allows unprecedented insights into normal intracardiac physiology and the way it changes due to congenital or acquired heart disease and may eventually lead to new parameters for early detection of cardiovascular disease [9, 10]. Four functional flow components can be discriminated in a multi-component particle tracing approach as introduced by Bolger et al. [8]. This approach has been used to show ventricular in- and outflow in the healthy LV [5] and right ventricle (RV) [11], as well as for identification of changed ventricular flow in patients with various cardiovascular diseases [9, 10, 12]. Validation of this method and comparison with other techniques for LV volumetry is currently lacking, as particle tracing was only compared to echocardiography and 2D phase-contrast MRI [5] and it was never tested against 2D planimetry or 4D flow MRI with retrospective valve tracking. Both retrospective valve tracking as well as particle tracing have shown good accuracy in LV in- and outflow assessment and low intra- and interobserver variation from repeated analysis [1, 2, 5]. However, scan-rescan reproducibility of LV in- and outflow assessment by valve tracking and particle tracing remains unknown. Scan-rescan reproducibility is important in the clinical workflow since patients often undergo several MRI examinations during their life as follow-up. Furthermore, scan-rescan reproducibility is essential to differentiate an abnormal stress response with prognostic importance from a normal response during a stress MRI-examination [13].

Therefore, the purpose of this study is to compare LV in- and outflow from 1) 2D planimetry; 2) 4D flow MRI with retrospective valve tracking and 3) 4D flow MRI with particle tracing and to assess the scan-rescan reproducibility of these three methods.

Methods

Study population

The study protocol was approved by the Medical Ethical Committee of the Leiden University Medical Center and informed consent was obtained from all participants. Ten healthy volunteers with no history of cardiac disease were included. All subjects underwent an MRI scan including whole-heart 4D flow MRI between July 2015 and March 2016. The same scanning protocol was performed twice in the same session with a 10-minute break between the scans and repositioning and replanning for every volunteer.

MRI acquisition

Whole-heart 4D flow MRI was obtained on a 3 Tesla MRI scanner (Ingenia, Philips Medical Systems, with Software Stream 4.1.3.0) with maximal amplitude of 45 mT/m for each axis, slew rate of 200 T/m/sec and a combination of FlexCoverage Posterior coil in the table top with a dStream Torso coil, providing up to 32 coil elements for signal reception. The orientation of the acquisition of 4D flow data was identical to the four-chamber orientation (usually double-oblique axial or coronal). Velocity-encoding of 150 cm/s in all three directions was used in a standard four-point encoding scheme, spatial resolution $3.0 \times 3.0 \times 3.0 \text{ mm}^3$, flip angle 10° , echo time (TE) 3.7 ms, repetition time (TR) 10 ms, true temporal resolution 40 ms, SENSitivity Encoding (SENSE) factor 2 in anterior-posterior direction and Echo Planar Imaging (EPI) readout with a factor 5 for acceleration. No contrast agent was used. Concomitant gradient correction and local phase correction were performed from standard available scanner software and the heart was scanned in the isocenter of the magnet to minimize phase offset. For the 4D flow MRI acquisition, whole-body Specific Absorption Rate (SAR) was $< 0.3 \text{ W/kg}$ and Specific Energy Dose (SED) was $< 0.2 \text{ kJ/kg}$. Cine 2D left two-chamber, four-chamber, coronal and sagittal aorta views and a cine multi-2D short-axis stack of slices were acquired, using steady-state free-precession sequences with TE/TR 1.5/3.0, 350 mm field-of-view, 45° flip angle, acquisition resolution $1.9 \times 2.0 \times 8.0 \text{ mm}^3$. Retrospective gating was used with 30 phases reconstructed to represent one cardiac cycle. Free breathing was allowed without using motion suppression, three signal averages were taken to minimize effects of breathing motion. For the 2D cine acquisition, whole-body SAR was $< 2.6 \text{ W/kg}$ and SED was $< 0.5 \text{ kJ/kg}$.

MRI analysis

Image analysis was performed by one observer with two years of experience in MRI (VPK) and verified by one observer with over 15 years of experience in MRI (JJMW). Ventricular volume segmentation was done based on multi-slice 2D cine short-axis images using in-house developed *MASS* software (Leiden University Medical Center, Leiden, the Netherlands). The endocardial border was manually traced in all slices and phases and ventricular volume was calculated at the end-diastolic (ED) and end-systolic (ES) phases. Papillary muscles were disregarded and assumed to be included in the ventricular volume. Stroke volume (SV) was calculated as left ventricular end-diastolic volume (LVEDV) - left ventricular end-systolic volume (LVESV).

Phase wrapping artefacts in the 4D flow data were corrected in the source images [14]. Retrospective valve tracking over the mitral valve (MV) and aortic valve (AV) was done using in-house developed *MASS* software (Leiden University Medical Center, Leiden, the Netherlands) following previously published methods [1, 2]. In short, streamlines of LV in- and outflow were visualized and multi-planar reformatting planes (MPR) were obtained perpendicular to these streamlines in all phases at the location of peak flow velocity. Through-plane velocity-encoded MPR images for all phases were reconstructed (typically in sets of 5 parallel slices with 5 mm interslice distance) on which borders of the MV or AV and myocardial wall (for through-plane motion and velocity offset error correction, not necessarily in the same slice as the transvalvular flow velocity) were manually segmented. Correct positioning of the MV and AV and background contours was verified using the resulting velocity-time curves. LV in- and outflow per heart beat were obtained as area under the curve from resulting flow rate-time curves. For internal validation, the net LV inflow volume per heartbeat measured over the MV (MV flow) was compared with the net LV outflow volume per heartbeat measured over the AV (AV flow). Cardiac output (CO) was computed from the 4D flow data as: LV outflow volume per heartbeat \times Heart Rate (HR).

For segmenting the LV cavity in the 4D flow MRI data, the available segmentation of the 2D cine short-axis acquisition was used. To correct for patient motion-related misalignment between the two acquisitions, automated image-based 3D rigid registration was performed using the phase with optimal depiction of the LV cavity in both scans with the Elastix image registration toolbox [15]. In addition to the concomitant gradient correction as provided by the scanner software, prior to particle tracing, the residual velocity offset errors were further minimized by subtracting the median velocity within the myocardial region at the moment of end-systole for all voxels and at every time phase. The 4D velocity data was then used for the particle tracing algorithm, using fourth-order Runge-Kutta numerical integration with a

time-step of one fifth of the actual temporal resolution (~8 ms) to create pathlines. At end-diastole, each voxel inside the LV was considered to represent one seed point (i.e., one particle). Pathlines of the particles were calculated by integration of velocity data over time: backward tracing over the diastole and forward tracing over systole. In- and outflow was allowed over the MV and AV only; particles exiting the LV other than into the aorta (i.e., aortic outflow) or the left atrium (i.e., mitral regurgitation) were calculated and excluded from analysis. Using particle tracing, LV in- and outflow volumes (i.e., flow volume over MV and AV, respectively) can be calculated in two ways. The first method is by performing a direct calculation by forward tracing to calculate AV flow and by backward tracing to calculate MV flow. The second method is by using the multi-component particle tracing evaluation (i.e., discriminating *direct flow*, *delayed ejection flow*, *retained inflow and residual volume*) as introduced by Bolger et al. [8] and then summing direct flow and delayed ejection flow components to calculate the AV flow volume and summing direct flow and retained inflow components to calculate MV flow.

In-scan comparison of MRI methods

To evaluate in-scan agreement (i.e. measurements within one scan), SV by short-axis 2D planimetry was compared to AV flow assessment from retrospective valve tracking and from particle tracing analysis. Furthermore, to evaluate agreement between the two 4D flow MRI methods, MV and AV flow values from retrospective valve tracking were compared to MV and AV flow values from particle tracing analysis. *Figure 1* shows the three methods for LV in- and outflow assessment that were used.

Scan-rescan analysis

For the scan-rescan analysis, all data were presented blinded to the observer and all scans were analyzed in a random order. Scan-rescan analysis was performed to test the reproducibility of 1) SV assessment by 2D planimetry; 2) MV and AV flow volume assessment by 4D flow MRI with retrospective valve tracking and 3) MV and AV flow volume assessment by 4D flow MRI with backward and forward particle tracing only and multi-component particle tracing.

Statistical analysis

Data analysis was performed using SPSS Statistics software (v. 23.0 IBM SPSS, Chicago, IL). Variables were tested for normal distribution using the Shapiro-Wilk test. Continuous data was expressed as mean \pm standard deviation (SD) or as median with inter-quartile range (IQR), in case of non-normality of the data. Mean differences were determined for in-scan and scan-rescan comparison and for comparison of different methods. Significance was

tested by a paired samples t-test or, in case of non-normality, the Wilcoxon signed-rank test. Correlation between two methods or measurements done in repeated scans was tested by the Pearson correlation coefficient (r), or the Spearman correlation coefficient (ρ) in case of non-normality of the data. The approach described by Bland and Altman [16] was used to study systematic differences between the two scans. To detect a possible trend in bias in the Bland-Altman plots, linear regression was performed for the differences versus the means. Agreement between scans was assessed by determining the intra-class correlation (ICC) coefficient and coefficient of variation (CV). The CV was defined as the SD of the differences between two series of measurements divided by the mean of both measurements. Correlation and agreement were classified as follows for both r and ICC: >0.95 : excellent, $0.95-0.85$: strong, $0.85-0.70$: good, $0.70-0.5$: moderate, <0.5 : poor. A P -value <0.05 was considered statistically significant.

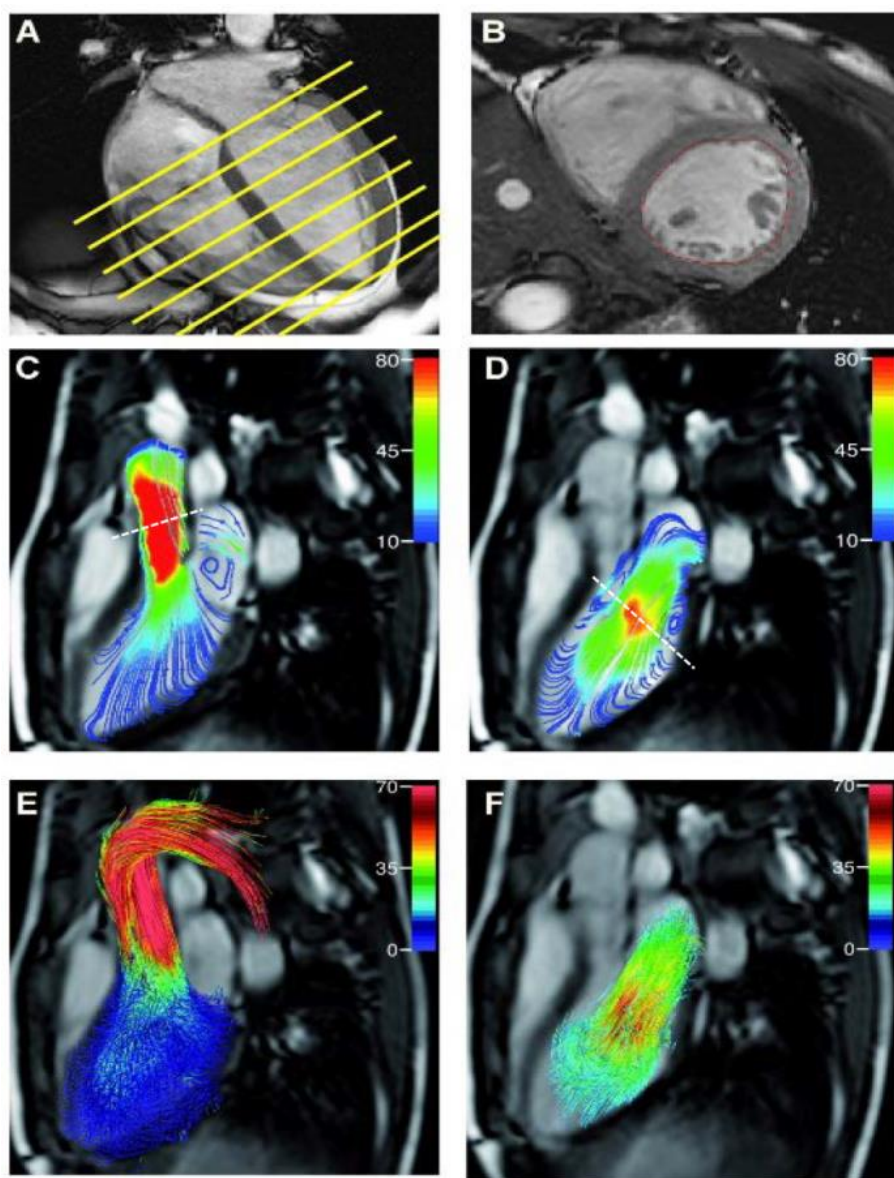


Figure 1. Three methods illustrating the assessment of LV in- and outflow volumes. Short-axis planimetry (in a, planning for multislice 2D short-axis is illustrated on four-chamber view and in b, mid-ventricular short-axis slice is presented). Streamline representation of 4D flow MRI shows mid-systolic aortic outflow (c) and early diastolic mitral (d) inflow volume with the positioning of the retrospective valve tracking indicated by a dashed line. Outflow assessment over the aortic valve by forward particle tracing (e) and inflow assessment over the mitral valve by backward particle tracing (f)

Results

Volunteer characteristics are shown in *Table 1*. Fifty percent of the study group were male (5/10), mean age was 27 ± 3 years. HR was marginally significantly different between the two scans (scan 1: 62.3 ± 7.3 ; scan 2: 59.8 ± 7.6 bpm, $P=0.047$). CO was not significantly different between the two scans (scan 1: 5.7 ± 0.8 ; scan 2: 5.7 ± 1.4 l/min, $P=0.88$). 4D flow MRI data acquisition was successful in all volunteers. Mean acquisition time of the whole-heart 4D flow MRI scan was 9.6 ± 1.4 minutes in scan 1 and 9.5 ± 1.7 minutes in scan 2. In two cases phase wrapping occurred. This was mathematically unwrapped in the source images of the respective velocity directions which presented the phase wrap.

Table 1. Characteristics of the volunteers

Total population			
N	10		
Male %	50 (5)		
Age (years)	27 ± 3		
Height (cm)	176 ± 7		
Weight (kg)	69 ± 13		
BSA (m ²)	1.8 ± 0.2		
BMI (kg/m ²)	22 ± 3		
	Scan 1	Scan 2	P-value
HR (bpm)	62.3 ± 7.3	59.8 ± 7.6	0.047
CO (l/min)	5.7 ± 0.8	5.7 ± 1.4	0.88

Data are presented as mean \pm standard deviation. Abbreviations: BMI = Body Mass Index, BSA = Body surface area, HR = Heart rate, bpm: beats per minute.

In-scan comparison of MV versus AV flow for both 4D flow MRI methods

Table 2 shows the in-scan comparison of flow volume assessment through the MV and AV by retrospective valve tracking and by particle tracing. When using retrospective valve tracking, both scans show excellent correlation between MV and AV flow volumes (scan 1: $r=0.95$, $P<0.001$; scan 2: $r=0.98$, $P<0.001$). The mean difference between MV and AV flow was -2.7 ± 5.5 mL ($P=0.15$) in scan 1 and -2.3 ± 5.7 mL ($P=0.23$) in scan 2. The ICC is excellent (scan 1: 0.97 , $P<0.001$; scan 2: 0.98 , $P<0.001$) and the CV of MV and AV flow assessment by retrospective valve tracking is small in both scans (6%). Also when using particle tracing analysis to determine LV in- and outflow, excellent in-scan correlation between MV versus AV flow volumes is observed in both scans (scan 1: $r=0.95$, $P<0.001$; scan 2: $r=0.99$, $P<0.001$). The mean difference between MV and AV flow in scan 1 was -0.04 ± 11.3 mL ($P=0.99$) and -5.9 ± 6.8 mL ($P=0.02$) in scan 2. The ICC is strong (scan 1:

0.92, $P=0.001$; scan 2: 0.93, $P<0.001$). The CV of MV and AV flow assessment by particle tracing shows more variation (8-12%) than assessment by retrospective valve tracking.

In-scan comparison of MV and AV flow between MRI methods

Figure 2 shows the in-scan comparison between SV assessment by short-axis 2D planimetry versus AV flow assessment by retrospective valve tracking (*Figure 2a*) and SV assessment by short-axis 2D planimetry versus AV flow assessment by particle tracing analysis (*Figure 2b*). AV flow assessment by retrospective valve tracking shows strong to excellent correlation with 2D planimetry (scan 1: $r=0.88$, $P=0.001$; scan 2: $r=0.95$, $P<0.001$). AV flow assessment by particle tracing shows excellent correlation with 2D planimetry (scan 1: $r=0.95$, $P<0.001$; scan 2: $r=0.95$, $P<0.001$). The Bland-Altman plots, also shown in *Figure 2*, display small limits of agreements. However, SV by 2D planimetry versus AV flow assessment by retrospective valve tracking shows a significant trend in scan 1 ($r=-0.64$, $P=0.05$), but not in scan 2 ($r=-0.17$, $P=0.64$), as shown in *Figure 2a*. This trend in scan 1 means that the differences between 2D planimetry and retrospective valve tracking increase with an increasing mean from both methods. A significant trend is also present in the measurement of SV by 2D planimetry versus AV flow assessment by particle tracing in both scans. The linear regression lines are plotted in *Figure 2b* (scan 1: $r=-0.85$, $P=0.002$; scan 2: $r=-0.84$, $P=0.002$). This trend in both scans means that the differences between 2D planimetry and particle tracing increase with an increasing mean from both methods.

Table 2. Internal consistency of assessment of flow volumes through the mitral (MV) and aortic valve (AV) by retrospective valve tracking and particle tracing analysis

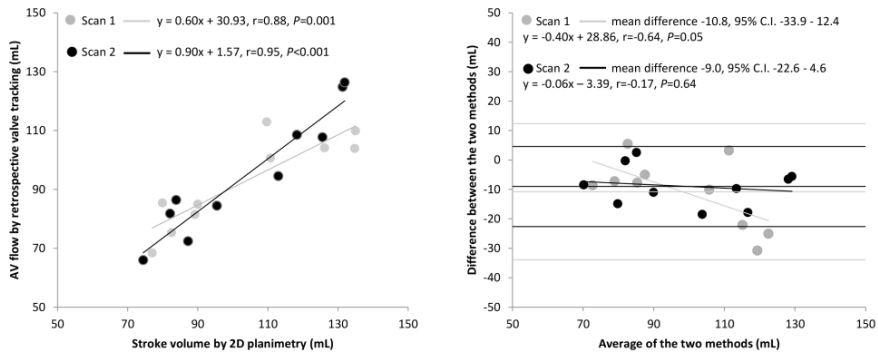
	MV flow (mL)	AV flow (mL)	Difference (AV-MV) (mL) ^a	Pearson correlation coefficient	ICC (95% C.I.)	COV (%)
	Mean ± SD (min - max)	Mean ± SD (min - max)	Mean ± SD (min-max)			
Retrospective valve tracking scan 1	95.4 ± 17.0 (71.4-121.2)	92.7 ± 15.5 (68.4-112.9)	-2.7 ± 5.5 (-11.2-7.1)	0.95 ^b	0.97 (0.87-0.99) ^b	6
Retrospective valve tracking scan 2	97.6 ± 24.0 (62.3-135.0)	95.3 ± 20.9 (66.0-126.4)	-2.3 ± 5.7 (-11.7-6.8)	0.98 ^b	0.98 (0.93-1.00) ^b	6
Particle tracing scan 1	91.7 ± 23.6 (57.5-133.1)	91.6 ± 14.0 (71.5-112.1)	-0.04 ± 11.3 (-22.7-14.0)	0.95 ^b	0.92 (0.65-0.98) ^c	12
Particle tracing scan 2	94.1 ± 20.0 (63.3-121.8)	88.1 ± 13.6 (68.2-105.2)	-5.9 ± 6.8 (-16.6-5.0) ^c	0.99 ^b	0.93 (0.56-0.99) ^b	8

^aDifferences were calculated with the paired samples t-test

^bIndicates $P < 0.001$, ^cIndicates $P < 0.05$

Abbreviations: AV=aortic valve, MV=mitral valve, ICC=intra-class correlation coefficient, COV=coefficient of variation

a. 2D planimetry versus retrospective valve tracking



b. 2D planimetry versus particle tracing

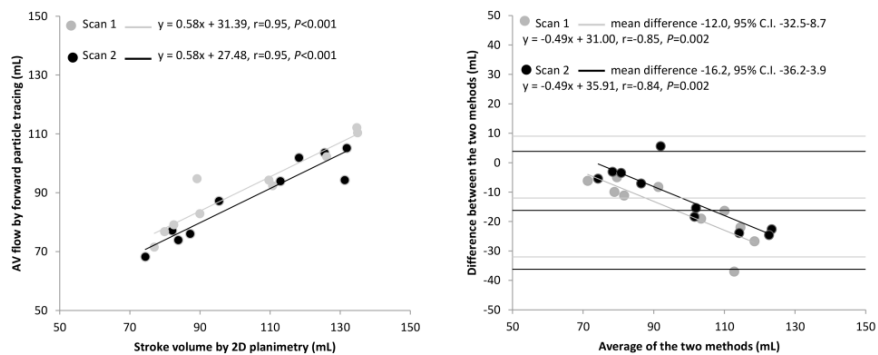


Figure 2. Scatterplots and Bland–Altman plots for comparison of left ventricular in- and outflow by 2D planimetry and 4D flow MRI with retrospective valve tracking and particle tracing. (a) left: scatter plot depicting the correlation between SV measured by 2D planimetry versus AV flow measured by retrospective valve tracking in scan 1 and scan 2, right: Bland–Altman plot depicting the agreement between SV measured by 2D planimetry versus AV flow measured by retrospective valve tracking in scan 1 and scan 2. (b) left: scatter plot depicting the correlation between SV measured by 2D planimetry versus AV flow measured by forward particle tracing in scan 1 and scan 2, right: Bland–Altman plot depicting the agreement between SV measured by 2D planimetry versus AV flow measured by forward particle tracing in scan 1 and scan 2. The linear regression lines are plotted in the Bland–Altman plots.

Table 3 shows the in-scan comparison of MV flow assessment by retrospective valve tracking versus MV flow assessment by particle tracing and the in-scan comparison of AV flow assessment by retrospective valve tracking versus AV flow assessment by particle tracing. MV flow from retrospective valve tracking versus MV flow from particle tracing shows strong correlation in both scans (scan 1: $r=0.95$, $P<0.001$; scan 2: $r=0.88$, $P=0.001$). There is no significant difference between MV flow values from retrospective valve tracking and MV flow values from particle tracing (scan 1: 3.7 ± 9.1 mL, $P=0.23$; scan 2: 3.6 ± 11.5 mL, $P=0.35$). Also, AV flow from retrospective valve tracking versus AV flow from particle tracing shows good correlation in both scans (scan 1: $r=0.81$, $P=0.004$; scan 2: $r=0.87$, $P=0.001$) and no significant difference between AV flow values from retrospective valve tracking and AV flow values from particle tracing (scan 1: 1.1 ± 9.2 mL, $P=0.72$; scan 2: 7.2 ± 11.2 mL, $P=0.07$).

Table 3. Comparison between retrospective valve tracking and particle tracing for MV and AV flow quantification

Statistics	MV retrospective valve tracking versus MV particle tracing	AV retrospective valve tracking versus AV particle tracing
Scan 1		
Mean difference (mL)	3.7 ± 9.1	1.1 ± 9.2
<i>P</i> -value*	0.23	0.72
Pearson correlation coefficient	0.95	0.81
<i>P</i> -value	<0.001	0.004
Scan 2		
Mean difference (mL)	3.6 ± 11.5	7.2 ± 11.2
<i>P</i> -value*	0.35	0.07
Pearson correlation coefficient	0.88	0.87
<i>P</i> -value	0.001	0.001

**P*-values were calculated with the paired samples t-test

Abbreviations: AV= aortic valve, MV= mitral valve

Scan-rescan analysis of MRI methods

Results of the scan-rescan analysis for flow assessment by all three methods (2D planimetry, 4D flow MRI with retrospective valve tracking and particle tracing) are presented in Table 4. Scan-rescan assessment of SV by 2D planimetry shows excellent correlation between both scans ($r=0.95$, $P<0.001$) with an excellent ICC (0.98, $P<0.001$) and low CV (7%) indicating excellent reproducibility. Also, scan-rescan assessment of MV and AV flow volumes by retrospective valve tracking from 4D flow MRI shows good reproducibility with good to strong Pearson correlation coefficients (MV: $r=0.90$, $P<0.001$; AV: $r=0.83$, $P<0.003$) and a

strong ICC (MV: 0.92, $P<0.001$; AV: 0.89, $P=0.002$). CVs for both MV and AV flow assessment by retrospective valve tracking are low (MV: 12%; AV: 12%). MV and AV flow assessment by particle tracing from backward (MV) and forward (AV) particle tracing only shows good to strong correlation between both scans (MV: $r=0.89$, $P=0.001$; AV: $r=0.83$, $P=0.003$), non-significant differences (MV: 2.4 ± 10.7 mL, $P=0.50$; AV: -3.5 ± 8.2 mL, $P=0.21$) and strong ICCs (MV: 0.94, $P=0.001$; AV: 0.90, $P=0.001$). CVs for both MV and AV flow assessment by backward and forward particle tracing only are low (MV: 11%; AV: 9%).

MV and AV flow assessment by particle tracing using the multi-component analysis shows good correlation between the values from both scans (MV: $r=0.76$, $P=0.01$; AV: $r=0.72$, $P=0.02$), a non-significant difference (MV: 0.8 ± 13.6 mL; AV: -5.8 ± 10.7 mL) and good to strong ICCs (MV: 0.88, $P=0.003$; AV: 0.81, $P=0.007$). CVs for both MV and AV flow assessment by multi-component particle tracing are acceptable (MV: 16%; AV: 12%).

Scatter plots and Bland-Altman plots for flow assessment by 2D planimetry and 4D flow MRI with retrospective valve tracking and particle tracing are shown in *Figure 3*. No trend is present in the Bland-Altman plot for the assessment of SV in scan 1 versus SV in scan 2 ($r=-0.10$, $P=0.80$), as shown in *Figure 3a*. The Bland-Altman plot for the assessment of AV and MV flow from retrospective valve tracking (*Figure 3b*) shows a significant trend for the scan- rescan assessment of MV flow, but not for AV flow (MV: $r=0.63$, $P=0.05$; AV: $r=0.48$, $P=0.16$). This trend in MV flow assessment by retrospective valve tracking means that the differences between MV flow assessment by retrospective valve tracking in scan 1 and scan 2 increase with an increasing mean from both scans. The Bland-Altman plot for the assessment of AV and MV flow from particle tracing (*Figure 3c*) shows no significant trend for the scan-rescan assessment of MV and AV flow (MV: $r=-0.34$, $P=0.34$; AV: $r=-0.05$, $P=0.89$).

Table 4. Scan-rescan comparison of 2D stroke volume (SV) and flow through the mitral (MV) and aortic valve (AV)

	Scan 1	Scan 2	Difference (mL) ^a	Pearson correlation coefficient	ICC (95% C.I.)	COV (%)
2D planimetry						
	Mean ± SD (min - max)	Mean ± SD (min - max)	Mean ± SD (min-max)			
SV (mL)	103.5 ± 22.8 (77.0-135)	104.3 ± 22.1 (74.4-131.9)	0.8 ± 7.0 (-9.2-12.9)	0.95 ^b	0.98 (0.91-0.99) ^b	7
Retrospective valve tracking						
MV flow (mL)	95.4 ± 17.0 (71.4-121.2)	97.6 ± 24.0 (62.3-135.0)	2.2 ± 11.3 (-16.7-17.6)	0.90 ^b	0.92 (0.70-0.98) ^b	12
AV flow (mL)	92.7 ± 15.5 (68.4-112.9)	95.3 ± 20.9 (66.0-95.3)	2.6 ± 11.7 (-18.4-20.7)	0.83 ^c	0.89 (0.58-0.97) ^c	12
Backward and forward particle tracing for LV in- and outflow						
MV flow (Backward only) (mL)	91.7 ± 23.6 (57.5-133.1)	94.1 ± 20.0 (63.3-121.8)	2.4 ± 10.7 (-11.3-18.2)	0.89 ^c	0.94 (0.77-0.99) ^b	11
AV flow (Forward only) (mL)	91.6 ± 14.0 (71.5-112.1)	88.1 ± 13.6 (68.2-105.2)	-3.5 ± 8.2 (-18.7-9.5)	0.83 ^c	0.90 (0.61-0.97) ^c	9
Multi-component particle tracing for LV in- and outflow						
MV flow (Direct flow + retained inflow) (mL)	82.9 ± 20.1 (56.0-113.5)	83.7 ± 19.2 (57.1-109.6)	0.8 ± 13.6 (-12.7-26.5)	0.76 ^c	0.88 (0.48-0.97) ^c	16
AV flow (Direct flow + delayed ejection flow) (mL)	89.9 ± 13.8 (71.2-109.5)	84.1 ± 14.5 (59.2-103.3)	-5.8 ± 10.7 (-22.7-13.3)	0.72 ^c	0.81 (0.29-0.95) ^c	12

^aDifferences were calculated with the paired samples t-test

^bIndicates $P < 0.001$, ^cIndicates $P < 0.05$

Abbreviations: AV = aortic valve, MV= mitral valve, SV= stroke volume, ICC=intraclass correlation coefficient, COV=coefficient of variation

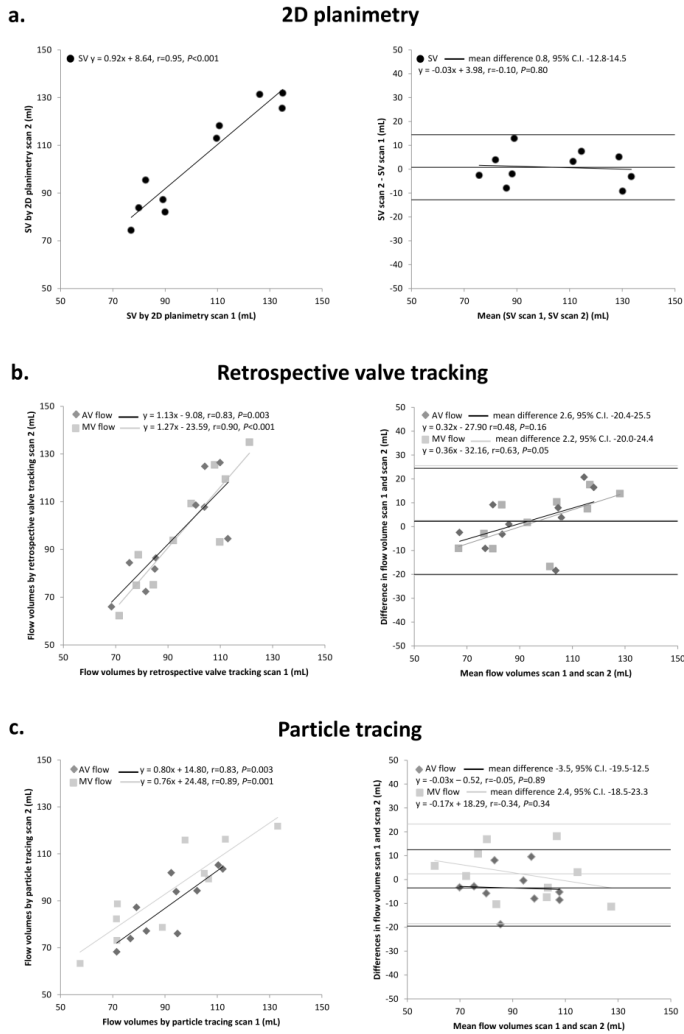


Figure 3. Scatter plots and Bland-Altman plots for comparison of left ventricular in- and outflow by 2D planimetry and 4D flow MRI with retrospective valve tracking and 4D flow MRI with backward and forward particle tracing. (a) left: scatter plot depicting the correlation between SV measured by 2D planimetry in scan 1 and scan 2, right: Bland-Altman plot depicting the agreement between SV measured by 2D planimetry in scan 1 and scan 2. (b) left: scatter plot depicting the correlation between MV flow measured by retrospective valve tracking with 4D flow MRI in scan 1 and scan 2 and the correlation between AV flow measured by retrospective valve tracking with 4D flow MRI in scan 1 and scan 2, right: Bland-Altman plot depicting the agreement between MV flow measured by retrospective valve tracking with 4D flow MRI in scan 1 and scan 2 and the agreement between AV flow measured by retrospective valve tracking with 4D flow MRI in scan 1 and scan 2. (c) left: scatter plot depicting the correlation between MV flow measured by 4D flow MRI with backward particle tracing in scan 1 and scan 2 and the correlation between AV flow measured by 4D flow MRI with backward particle tracing in scan 1 and scan 2, right: Bland-Altman plot depicting the agreement between MV flow measured by 4D flow MRI with backward particle tracing in scan 1 and scan 2 and the agreement between AV flow measured by 4D flow MRI with backward particle tracing in scan 1 and scan 2. The linear regression lines are plotted in the Bland-Altman plots.

Percentages of the multi-component particle tracing analysis are: $40.1 [36.6-41.9]$ % direct flow, 20.4 ± 4.5 % delayed ejection flow, 14.8 ± 4.3 % retained inflow and 24.1 ± 4.6 % residual volume in scan 1 and 40.4 ± 5.2 % direct flow, 18.4 ± 3.5 % delayed ejection flow, 17.6 ± 4.1 % retained inflow and 23.6 ± 3.3 % residual volume in scan 2. In scan 1, 13 ± 5 % of the particles was excluded as this portion of the total particles entered or exited the LV other than through the MV or AV, and in scan 2, 15 ± 5 % of the particles was excluded. Scan-rescan analysis of the four components of 4D flow MRI with multi-component particle tracing analysis shows non-significant mean differences between the components of less than 3% ($-0.1 [-5.9-5.7]$ % ($P=0.80$) for direct flow, -2.0 ± 5.8 % ($P=0.30$) for delayed ejection flow, 2.8 ± 4.3 % ($P=0.07$) for retained inflow and -0.5 ± 4.8 % ($P=0.75$) for residual volume).

Discussion

4D flow MRI allows unprecedented assessment of intracardiac flow volumes and provides new insights into normal physiology and the way this is altered by congenital or acquired heart disease. Furthermore, 4D flow MRI allows improved quantification of LV in- and outflow [1-3, 5] and may provide new parameters to assess cardiac dysfunction [9, 10].

In the current study, LV in- and outflow was assessed by 4D flow MRI with retrospective valve tracking and by particle tracing and both were compared to 2D planimetry. Scan-rescan reproducibility of all these methods was tested. Main findings of the study are: 1) In-scan consistency between flow volumes over the MV and the AV is excellent for both 4D flow MRI methods; 2) In-scan AV flow assessment by both retrospective valve tracking and particle tracing correlates strongly with 2D planimetry SV assessment; 3) In-scan comparison between MV and AV flow assessed by retrospective valve tracking and MV and AV flow assessed by particle tracing shows good to strong correlations with no significant differences; 4) scan-rescan reproducibility of SV assessment by 2D planimetry is excellent and reproducibility of MV and AV flow by both retrospective valve tracking and particle tracing analysis is good to strong, however, retrospective valve tracking and particle tracing analysis show a higher coefficient of variation than 2D planimetry.

Excellent reproducibility of SV assessment by 2D planimetry has already been shown in an earlier study by Grotenhues et al. [17]. The current study, with an updated scan protocol, shows similar results with respect to scan-rescan reproducibility of SV assessment by 2D planimetry. However, in case of multiple valve lesions or intracardiac shunting, SV assessment from 2D planimetry can be insufficient. In such cases 4D flow MRI with retrospective valve tracking will be beneficial as it will provide a direct assessment of flow

at the inlet and outlet of the LV (MV and AV) and valve regurgitation can be directly quantified [1, 2]. Currently, the most common clinical MRI flow assessment technique is 2D cine PC MRI with a static imaging plane and velocity encoding in a single (i.e., through-plane) direction [18]. However, several studies have already shown that 4D flow MRI with retrospective valve tracking is more accurate than 2D cine PC MRI for transvalvular flow volume assessment [1, 3, 6]. 4D flow MRI has multiple advantages over 2D cine PC MRI. First of all, 4D flow MRI represents all directions and spatial regions of flow [19]. Secondly, when using 4D flow MRI with retrospective valve tracking, positioning of measurement planes can be changed dynamically in every time frame and adjusted to the orientation of the flow direction, while with 2D cine PC MRI, the measurement plane cannot adapt to the motion of the heart and the flow direction during the cardiac cycle [1, 2, 4, 6]. Furthermore, with 4D flow MRI multiple measurement planes can be defined from a single acquisition, while 2D cine PC MRI requires a repeated acquisition when assessing flow over multiple valves, which increases the chance of inconsistencies because of heart rate variation between the acquisitions. Also, planning of a 3D volume acquisition is more straightforward than planning 2D acquisition planes. A further clinical benefit of 4D flow MRI with retrospective valve tracking is that diastolic function can be assessed, especially in the presence of aortic or pulmonary valve regurgitation leading to two sources of diastolic ventricular inflow [7].

Roes et al. [1] showed excellent intra- and interobserver agreement for flow volume measurements by retrospective valve tracking over all four valves. The current study confirms the excellent in-scan consistency for MV and AV flow. Also, in the current study AV flow assessment by 4D flow MRI with retrospective valve tracking is compared to SV assessment using 2D planimetry, which shows strong agreement. Furthermore, our study extends these findings by demonstrating excellent scan-rescan reproducibility with good to strong correlations (MV flow: $r=0.90$, $P<0.001$, AV flow: $r=0.83$, $P=0.003$) and strong ICCs. The CV is small, but shows more variation than SV assessment by 2D planimetry (CV 12% versus 7%). These results indicate that 4D flow MRI with retrospective valve tracking is a reliable method that can be used clinically to assess flow volumes, also over repeated examinations.

LV in- and outflow can also be assessed by using particle tracking derived from 4D flow MRI. Bolger et al. [8] introduced the use of multi-component particle tracing to quantify four different functional components of blood flow distribution in the left ventricle (*direct flow*, *retained inflow*, *delayed ejection*, *residual volume*). This comprehensive assessment of intracardiac flow provided unique insights into normal intracardiac flow and how this is affected by congenital and acquired heart disease. Although the clinical usefulness needs to

be established, potentially new parameters for early detection of cardiac dysfunction can be derived from this approach [9, 10]. Furthermore, several studies [5, 8] have used particle tracing in the evaluation of LV in- and outflow. However, a validation of in-scan and scan-rescan consistency and reproducibility and comparison with other techniques for LV volumetry is currently lacking. The current study presents this necessary validation, which is necessary for a full interpretation of quantified differences in LV stroke volume in a follow-up study or in a rest-stress evaluation. Eriksson et al. [5] introduced a semi-automated analysis approach based on the method by Bolger et al. [8] in order to reduce user-dependency and enhance reproducibility. They have shown that multi-component particle tracing can be used to evaluate ventricular flow patterns in healthy subjects as well as patients with dilated cardiomyopathy [10]. In their study, in-scan comparison of MV flow (*direct flow + retained inflow*) and AV flow (*direct flow + delayed ejection flow*) assessed with particle tracing did not show significant differences [5]. Furthermore, low intra- and interobserver variability was shown for the assessment of the flow volumes by particle tracing [5]. A recent 3T MRI study by Calkoen et al. [9] using multi-component particle tracing analysis to assess transvalvular flow in 32 patients with corrected atrioventricular septal defect, showed a statistically significant in-scan difference between MV and AV flow volumes assessed with multi-component particle tracing. In the current study, MV flow and AV flow were not only calculated from the multi-component analysis over the full cardiac cycle as was done in the previous studies. Here, also forward particle tracing over systole for AV flow and backward particle tracing over diastole for MV flow were performed. Using this last approach, in-scan as well as scan-rescan consistency was strong. The possible explanation for this may be that for multi-component particle tracing, numerical integration over the full cardiac cycle is required, while forward and backward particle tracing only requires integration over systole and diastole, respectively. Adding more time steps in the integration procedure will accumulate more error over the full cardiac cycle.

Based on the Bland-Altman analyses, some significant trends in bias were seen when the differences between measurements were correlated with the mean of the measurements. This should be taken into account when comparing the different methods for SV assessment. However, in the evaluation of serial scans (during follow-up or in case of a rest-stress protocol), generally one specific method will be used to detect changes in the SV. In that perspective, CV and ICC are of more importance for reproducibility of the method of choice.

A limitation of the current study is the low number of samples (i.e., 10 volunteers). Nevertheless, our findings show good in-scan and scan-rescan reproducibility of both 4D flow MRI derived measurements of LV in- and out-flow. Additionally, no patient data was

used in this study as it would be unethical to repeat the long 4D flow MRI acquisition in a scan/rescan study in a routine clinical evaluation of patients. Still, scan-rescan analysis of transvalvular flow assessment should also be tested in the presence of valve lesions, shunt flow and decreased cardiac function. Another important limitation is the lack of gold standard. We compared LV outflow to 2D planimetry. This method is currently considered as the reference method for LV volume assessment when image analysis is performed in a standardized manner [20]. However, planimetry from multi-slice short-axis acquisitions is also subject to variability, as images are acquired using multiple breath-holds. In-scan consistency, however, which was used in the current study to compare flow volumes through MV and AV, may be considered as an internal reference standard. 3D cine data might perform better than multi-slice 2D cine. However, this is a novel approach that is not available on all MRI platforms, and was not available for our study. Also, image segmentation for such approach also requires a 3D algorithm instead of the current algorithm that was used for 2D planimetry. Such a 3D approach first requires validation in order to use it in a comparison study as was presented here. Another limitation is the fact that retrospective valve tracking is semi-automatic, as in previous studies, since manual interaction was required to position measurement planes. However, retrospective valve tracking can be performed with low intra- and interobserver variation, as has been previously published [1, 2]. Compared to 2D cine PC MRI with velocity encoding in a single direction, the adjustment of measurements planes requires more processing time (1-2 minutes per valve). Therefore, an automatic valve tracking procedure could further improve reproducibility and reduce analysis time.

Conclusion

In conclusion, SV assessment by 2D planimetry, and MV and AV flow assessment by 4D flow MRI with retrospective valve tracking and particle tracing show strong to excellent in-scan consistency and good to strong scan-rescan reproducibility and correlation, which indicates that 4D flow MRI with retrospective valve tracking and 4D flow MRI with particle tracing analysis are reliable methods to assess LV in- and outflow to be used clinically.

References

1. Roes SD, Hammer S, van der Geest RJ, Marsan NA, Bax JJ, Lamb HJ, Reiber JH, de Roos A, Westenberg JJ: Flow assessment through four heart valves simultaneously using 3-dimensional 3-directional velocity-encoded magnetic resonance imaging with retrospective valve tracking in healthy volunteers and patients with valvular regurgitation. *Invest Radiol* 2009, 44:669-675.
2. Westenberg JJ, Roes SD, Ajmone Marsan N, Binnendijk NM, Doornbos J, Bax JJ, Reiber JH, de Roos A, van der Geest RJ: Mitral valve and tricuspid valve blood flow: accurate quantification with 3D velocity-encoded MR imaging with retrospective valve tracking. *Radiology* 2008, 249:792-800.
3. Calkoen EE, Roest AA, Kroft LJ, van der Geest RJ, Jongbloed MR, van den Boogaard PJ, Blom NA, Hazekamp MG, de Roos A, Westenberg JJ: Characterization and improved quantification of left ventricular inflow using streamline visualization with 4DFlow MRI in healthy controls and patients after atrioventricular septal defect correction. *J Magn Reson Imaging* 2015, 41:1512-1520.
4. Calkoen EE, Westenberg JJ, Kroft LJ, Blom NA, Hazekamp MG, Rijlaarsdam ME, Jongbloed MR, de Roos A, Roest AA: Characterization and quantification of dynamic eccentric regurgitation of the left atrioventricular valve after atrioventricular septal defect correction with 4D Flow cardiovascular magnetic resonance and retrospective valve tracking. *J Cardiovasc Magn Reson* 2015, 17:18.
5. Eriksson J, Carlhall CJ, Dyverfeldt P, Engvall J, Bolger AF, Ebbers T: Semi-automatic quantification of 4D left ventricular blood flow. *J Cardiovasc Magn Reson* 2010, 12:9.
6. She HL, Roest AA, Calkoen EE, van den Boogaard PJ, van der Geest RJ, Hazekamp MG, de Roos A, Westenberg JJ: Comparative Evaluation of Flow Quantification across the Atrioventricular Valve in Patients with Functional Univentricular Heart after Fontan's Surgery and Healthy Controls: Measurement by 4D Flow Magnetic Resonance Imaging and Streamline Visualization. *Congenit Heart Dis* 2017, 12:40-48.
7. van der Hulst AE, Westenberg JJ, Kroft LJ, Bax JJ, Blom NA, de Roos A, Roest AA: Tetralogy of fallot: 3D velocity-encoded MR imaging for evaluation of right ventricular valve flow and diastolic function in patients after correction. *Radiology* 2010, 256:724-734.
8. Bolger AF, Heiberg E, Karlsson M, Wigstrom L, Engvall J, Sigfridsson A, Ebbers T, Kvitting JP, Carlhall CJ, Wranne B: Transit of blood flow through the human left ventricle mapped by cardiovascular magnetic resonance. *J Cardiovasc Magn Reson* 2007, 9:741-747.
9. Calkoen EE, de Koning PJ, Blom NA, Kroft LJ, de Roos A, Wolterbeek R, Roest AA, Westenberg JJ: Disturbed Intracardiac Flow Organization After Atrioventricular Septal Defect Correction as Assessed With 4D Flow Magnetic Resonance Imaging and Quantitative Particle Tracing. *Invest Radiol* 2015, 50:850-857.
10. Eriksson J, Bolger AF, Ebbers T, Carlhall CJ: Four-dimensional blood flow-specific markers of LV dysfunction in dilated cardiomyopathy. *Eur Heart J Cardiovasc Imaging* 2013, 14:417-424.
11. Fredriksson AG, Zajac J, Eriksson J, Dyverfeldt P, Bolger AF, Ebbers T, Carlhall CJ: 4-D blood flow in the human right ventricle. *Am J Physiol Heart Circ Physiol* 2011, 301:H2344-2350.
12. Fredriksson AG, Svalbring E, Eriksson J, Dyverfeldt P, Alehagen U, Engvall J, Ebbers T, Carlhall CJ: 4D flow MRI can detect subtle right ventricular dysfunction in primary left ventricular disease. *J Magn Reson Imaging* 2016, 43:558-565.
13. Luijnenburg SE, Mekic S, van den Berg J, van der Geest RJ, Moelker A, Roos-Hesselink JW, Bogers AJ, de Rijke YB, Strengers JL, Mulder BJ, et al: Ventricular response to dobutamine stress relates to the change in peak oxygen uptake during the 5-year follow-up in young patients with repaired tetralogy of Fallot. *Eur Heart J Cardiovasc Imaging* 2014, 15:189-194.
14. Lotz J, Meier C, Leppert A, Galanski M: Cardiovascular flow measurement with phase-contrast MR imaging: basic facts and implementation. *Radiographics* 2002, 22:651-671.
15. Klein S, Staring M, Murphy K, Viergever MA, Pluim JP: elastix: a toolbox for intensity-based medical image registration. *IEEE Trans Med Imaging* 2010, 29:196-205.
16. Bland JM, Altman DG: Statistical methods for assessing agreement between two methods of clinical measurement. *Lancet* 1986, 1:307-310.
17. Grothues F, Smith GC, Moon JC, Bellenger NG, Collins P, Klein HU, Pennell DJ: Comparison of interstudy reproducibility of cardiovascular magnetic resonance with two-dimensional

- echocardiography in normal subjects and in patients with heart failure or left ventricular hypertrophy. *Am J Cardiol* 2002, 90:29-34.
18. Pelc NJ, Herfkens RJ, Shimakawa A, Enzmann DR: Phase contrast cine magnetic resonance imaging. *Magn Reson Q* 1991, 7:229-254.
 19. Markl M, Chan FP, Alley MT, Wedding KL, Draney MT, Elkins CJ, Parker DW, Wicker R, Taylor CA, Herfkens RJ, Pelc NJ: Time-resolved three-dimensional phase-contrast MRI. *J Magn Reson Imaging* 2003, 17:499-506.
 20. Schulz-Menger J, Bluemke DA, Bremerich J, Flamm SD, Fogel MA, Friedrich MG, Kim RJ, von Knobelsdorff-Brenkenhoff F, Kramer CM, Pennell DJ, et al: Standardized image interpretation and post processing in cardiovascular magnetic resonance: Society for Cardiovascular Magnetic Resonance (SCMR) board of trustees task force on standardized post processing. *J Cardiovasc Magn Reson* 2013, 15:35.

Chapter 8

Automated cardiac valve tracking for flow quantification with four-dimensional flow MRI

Vivian P Kamphuis, Arno AW Roest, Nina Ajmone Marsan, Pieter J van den Boogaard, Lucia JM Kroft, Jean-Paul Aben, Jeroen J Bax, Albert de Roos, Hildo J Lamb, Jos JM Westenberg

Radiology. 2018. doi: 10.1148/radiol.2018180807. [Epub ahead of print]

Abstract

Objective

To compare 4D flow MRI with automated valve tracking to manual valve tracking in patients and healthy volunteers.

Methods

Data of 114 patients (33 acquired heart disease; 81 congenital heart disease; median age 17 years, 55% male) and 46 healthy volunteers (median age 28 years, 59% male) who underwent a 4D flow MRI scan between 2006-2017 at 1.5T or 3.0T MRI was retrospectively evaluated. Two orthogonal cine steady-state free-precession views of each valve were used for manual and automated valve tracking. Wilcoxon signed-rank test was used to compare time needed for analysis and differences and variation in net forward volume (NFV) and valvular regurgitant fraction. Intra- and inter-observer variability was tested by the intra-class correlation coefficient (ICC).

Results

Time needed for analysis was significantly shorter for automated versus manual tracking (patients: 14 [12-15] versus 25 [20-25] minutes, $P<0.001$). Although overall differences in NFV and regurgitant fraction were comparable between automated and manual tracking, NFV variation over four valves was significantly smaller for automated versus manual tracking (patients: 4.9 [3.3-6.7]% versus 9.8 [5.1-14.7]%, $P<0.001$). This resulted in significant reclassification of regurgitation severity. Intra- and inter-observer agreement for automated tracking was excellent for NFV (intra- and inter-observer: $ICC\geq 0.99$) and strong-to-excellent for regurgitant fraction assessment (intra-observer: $ICC\geq 0.94$; inter-observer: $ICC\geq 0.89$).

Conclusion

Automated valve tracking reduces analysis time and improves reliability of valvular flow quantification by 4D flow MRI in patients with acquired or congenital heart disease and in healthy volunteers.

Introduction

In patients with acquired or congenital valvular heart diseases, accurate quantification of blood flow volumes over the heart valves is essential for overall patient management: from diagnosis to follow-up and optimal treatment planning (conservative or surgical) [1-3]. Valvular flow quantification by cardiac magnetic resonance imaging (MRI) with velocity-encoding is considered an important diagnostic tool in addition to conventional imaging modalities, such as (Doppler) echocardiography [4]. In particular for valvular regurgitation assessment, it has been suggested that MRI can overcome some limitations that characterize echocardiography, such as requirements for the acoustic window, operator experience, and the use of geometric modelling assumptions [5, 6].

Time-resolved, three-dimensional, three-directional velocity-encoded MRI, also termed four-dimensional (4D) flow MRI allows for direct quantification of blood flow volumes through all four valves derived from one acquisition and showed superior accuracy over conventional two-dimensional phase-contrast MRI [7-13], in particular for quantification of regurgitant volumes and severity of cardiac shunts [4]. Still, widespread use of this approach into clinical practice is hindered because manual placement and tracking of multi-planar reformatting planes in every cardiac phase for each valve is a time-consuming procedure with observer-dependent variation.

We hypothesize that automated valve tracking will reduce analysis time and improve accuracy of quantification of blood flow volumes by 4D flow MRI post-processing. The purpose of this study was to compare 4D flow MRI post-processing with automated valve tracking to manual tracking in patients and healthy volunteers, and to explore potential differences related to MRI field strength and acquisition protocols.

Materials and Methods

Data in this study were collected as part of several prospective research studies except for two patients who were scanned for clinical evaluation. Institutional medical ethical approval was obtained for all prospective research studies and written informed consent was obtained from all these patients and healthy volunteers. Regarding the two clinical cases, at the time of the study no ethics approval was required for anonymized studies with patient data that were collected as part of standard care in the Netherlands.

Study population

The total study group consisted of 114 patients and 46 healthy volunteers. Patient data was retrospectively retrieved from several prospective research studies and included patients with ischemic cardiomyopathy (IschCMP) and mitral valve regurgitation [9], corrected tetralogy of Fallot (ToF) [10], corrected coarctation of the aorta (CoA) [14] and corrected atrioventricular septal defect (AVSD) [8]. From the same MRI research database, 46 healthy volunteers without history of cardiac disease were randomly retrieved. All studies were performed as clinical research at the Leiden University Medical Center, Leiden, The Netherlands, from 2006-2017. All included studies contained 4D flow MRI data accessible for the post-processing-tools, with all heart valves inside the acquired volume-of-interest. Patients with shunt flow were excluded since the net forward flow volume (NFV) over the four valves was used as internal reference. Since patient data was obtained using either 1.5T or 3.0T field strength and different acquisition protocols, the effect of these variables was tested using data from the healthy volunteers. Some patient and volunteer data has been reported in previous work: 32 of the 33 patients with IschCMP [9, 12], 29 of the 29 patients with AVSD [7, 8], 23 of the 24 patients with ToF [10] and 46 of the 46 volunteers [7, 9, 13]. These previous studies reported on manual valve tracking in these separate patient groups, but current results on automated valve tracking have not been reported.

MRI acquisition

MRI data has been acquired by PJvdB and JJMW (both 20 years' experience in cardiac MRI) using 1.5T or 3.0T MRI systems (Philips Healthcare, Best, The Netherlands). Two validated 4D flow MRI acquisition approaches were followed: a whole-heart protocol covering all four chambers of the heart [15] or a cardiac basal volume acquisition (planned parallel to the basal plane of the heart, encompassing all heart valves) [9, 12]. 4D flow MRI was supplemented with 2D steady-state free-precession cine acquisitions of left and right ventricular two- and four-chamber views and left and right ventricular outflow tract in such way that for each valve, two orthogonal cine views were available for valve tracking during post-processing. Acquisition details are presented in *Supplementary data 1*. Reported acquisition times for basal 4D flow protocol were typically between 4 and 5 minutes (depending on the patient's heart rate). Reported acquisition times for whole-heart 4D flow were between 5 and 12 minutes (depending on the patient's heart rate and cardiac size).

Ventricular volume segmentation by 2D Planimetry

Ventricular volume segmentation was performed based on multi-slice multi-phase 2D cine images using *CAAS MR Solutions 5.0* (Pie Medical Imaging, Maastricht, The Netherlands) by two observers (JJMW with >20 years of cardiac MRI experience and VPK with >3 years of cardiac MRI experience). Ventricular volumes were calculated at the end-diastolic and end-systolic phases. Papillary muscle were assumed to be included in the ventricular volume. Stroke volumes (SV) were calculated as end-diastolic volume (EDV) – end-systolic volume (ESV) for both LV and RV. Ejection fraction (EF) was calculated as $(SV/EDV) \times 100$ (%) for the LV and RV. Stroke volumes and EDV were indexed by body surface area (BSA). Comparison between stroke volumes from 2D cine images and automated valve tracking are presented in *Supplementary data 2*.

Automated versus manual valve tracking

Manual retrospective valve tracking over the aortic valve (AV), pulmonary valve (PV), mitral valve (MV) and tricuspid valve (TV) was done using in-house-developed software *MASS* (version 5.1, Leiden University Medical Center, Leiden, The Netherlands; software available per request), following previously published methods [7-13, 16] by one observer (JJMW). Automated valve tracking was performed with the commercially available *CAAS* software (4D Flow version 2.0, Pie Medical Imaging, Maastricht, The Netherlands) by one observer (JJMW) as shown in *Figure 1*. The excursion of the AV and PV was identified on the left and right ventricular outflow tract cine acquisitions, respectively. MV and TV excursion was identified on the left and right ventricular two- and four-chamber cine acquisitions. Using the valve tracking algorithms, measurement planes, corrected for aliasing, velocity offset and through-plane motion, were obtained for each valve by multi-planar reformatting. *Figure 2* shows automated valve tracking in a ischemic cardiomyopathy patient with mitral regurgitation (regurgitant fraction:17%). *Figure 3* shows automated valve tracking in patients with corrected congenital heart defects and various degrees of valvular regurgitation. Details on valve tracking algorithms, unwrapping of aliased velocity and correction for phase offset and through-plane motion are presented in *Supplementary data 3*. Time needed for complete analysis (valve tracking plus contouring in velocity mapping for all four valves combined) was recorded. For each patient and healthy volunteer, the difference between NFV over the respective valve versus the mean NFV over the three other valves is defined as “NFV difference”. The NFV variation among the four valves (calculated as the standard deviation of differences among all four valves divided by the mean NFV of all four valves) and the NFV differences were used for internal validation of NFV consistency. Regurgitation

severity was categorized into four groups by regurgitant fraction as none-mild (<15%), mild-moderate (15-25%), moderate-severe (26-48%), and severe (>48%) [6].

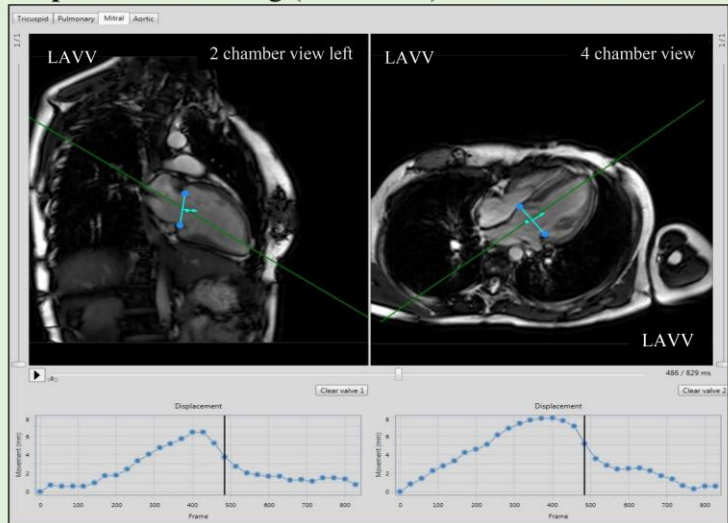
Intra- and inter-observer analysis

To assess intra- and inter-observer variability of NFV difference and regurgitation quantification by automated valve tracking, a randomly selected group of 22 patients and 6 volunteers (representing all patient groups, MRI field strengths and acquisition protocols) was blinded and analyzed twice by **observer 1** JJMW with > 4 weeks between analyses and > 1 week later by **observer 2** (VPK).

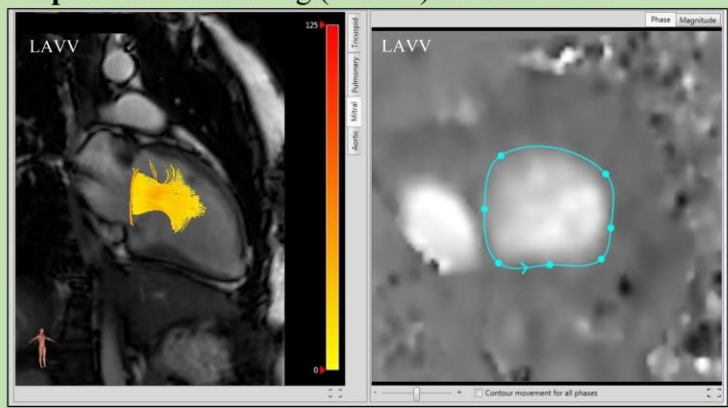
Statistical analysis

Data analysis was performed using SPSS Statistics (v.23.0 IBM SPSS, Chicago, IL). Continuous data was expressed as median [inter-quartile range]. Automated versus manual tracking results were compared with the Wilcoxon signed-rank test for analysis time, NFV difference, NFV variation and regurgitant fractions. For these tests the Holm method was used to correct for multiple testing [17]. Agreement between methods for regurgitation severity categorization was tested by Fleiss-Cohen's kappa. Systematic differences between methods and intra- and inter-observer analyses were tested with Bland-Altman analyses [18]. Median differences (with 95% confidence intervals) between measurements were determined and significance was tested with the Wilcoxon signed-rank test. Agreement between repeated analyses was assessed by the intra-class correlation coefficient (ICC). Variation was tested by the coefficient of variation (COV), calculated as the standard deviation of the differences between measurements divided by the mean of the measurements. Correlation and agreement were categorized as follows: >0.95: excellent; 0.95–0.85: strong; 0.85–0.70: good; 0.70–0.5: moderate; <0.5: poor. A *P* value less than .05 was considered to indicate a statistically significant difference.

Step 1: valve tracking (automated) for each valve



Step 2: contour drawing (manual) for each valve



Result: complete flow data over all four valves

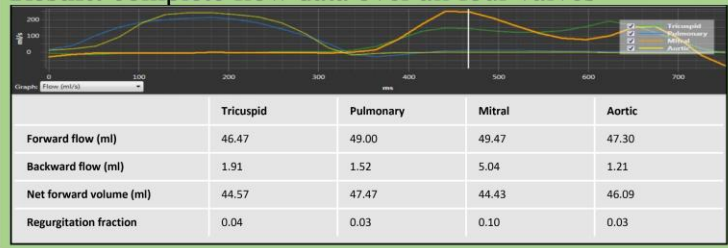


Figure 1. Schematic workflow of automated valve tracking. Example evaluation of one valve (left atrioventricular valve) in a patient with corrected atrioventricular septal defect. Abbreviations: LAVV, left atrioventricular valve.

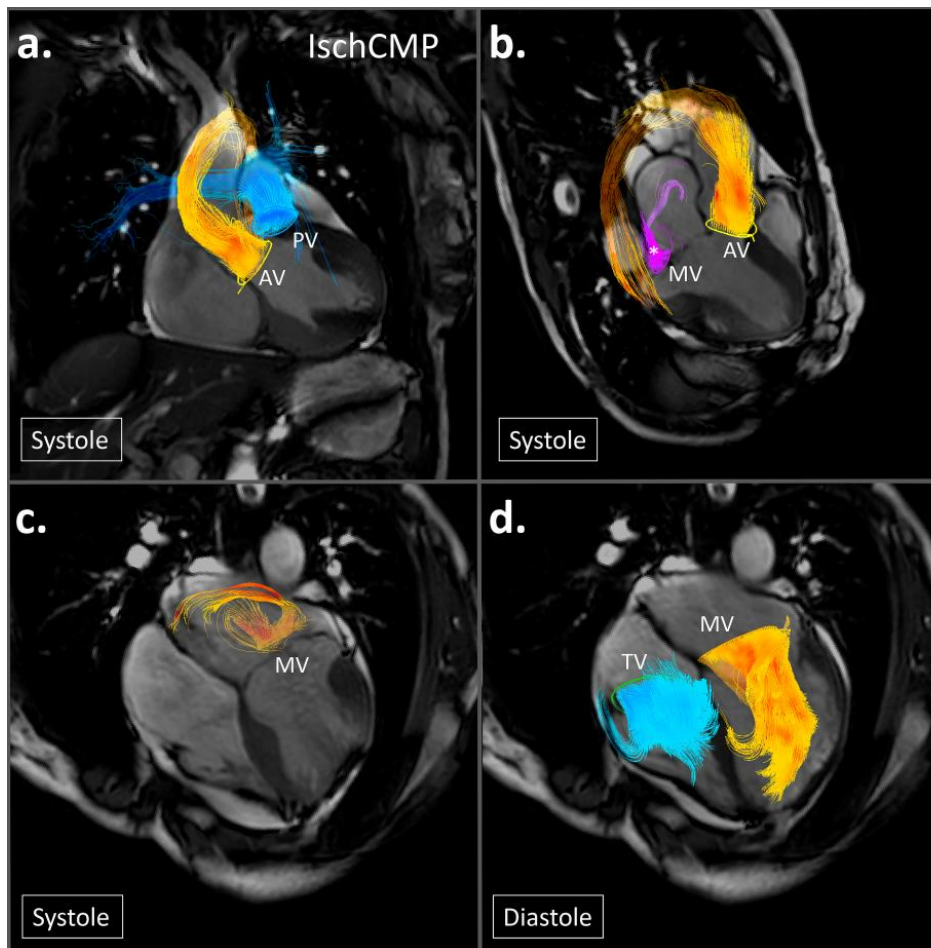


Figure 2. Automated valve tracking in a patient with ischemic cardiomyopathy (IschCMP) with streamlines projected on cine MRI views. (a) Aortic and pulmonary outflow during systole, (b) aortic outflow and mitral regurgitation during systole. * Mitral regurgitation is shown in purple instead of yellow/orange (i.e. the setting of post processing software) because of the overlap with aortic outflow. (c) mitral regurgitation during systole on a standard four-chamber cross-sectional view, (d) mitral and tricuspid inflow on the same four-chamber view.

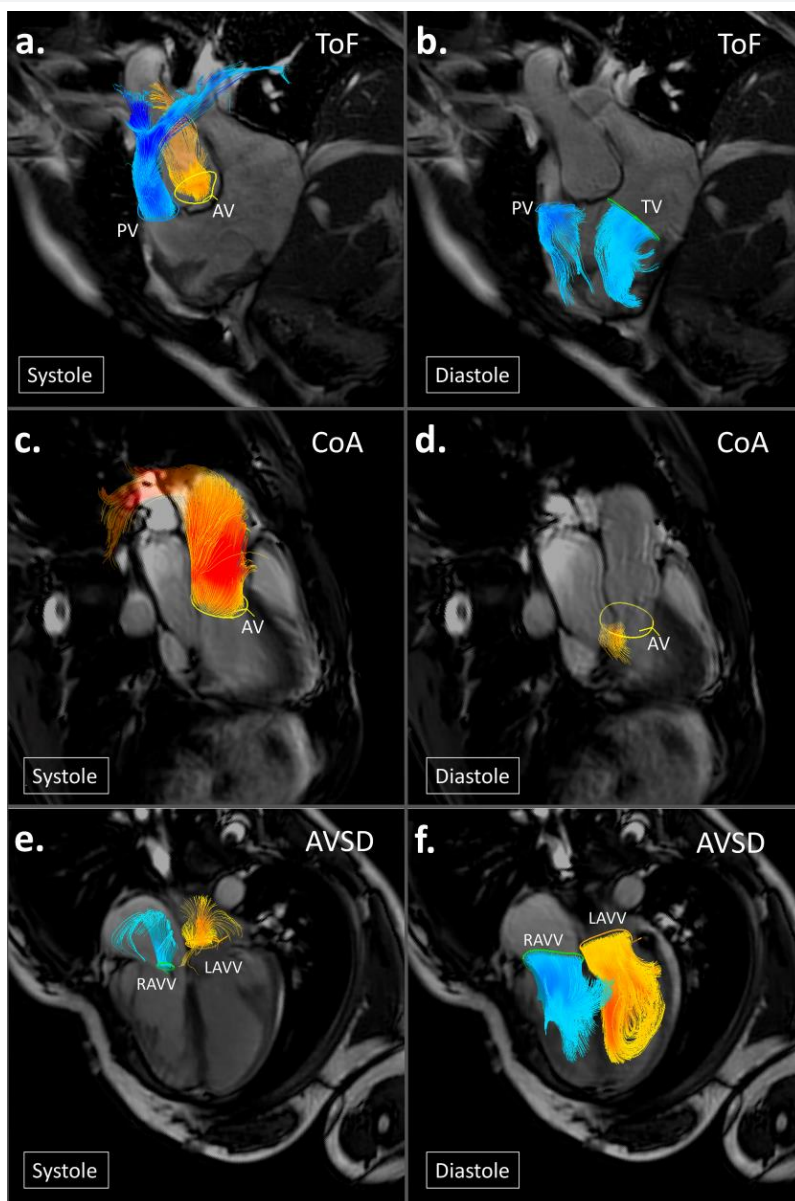


Figure 3. Automated valve tracking in patients with congenital heart defects with streamlines projected on the cine views. (a) Aortic and pulmonary outflow during systole in patient with corrected tetralogy of Fallot (ToF); (b) inflow over the tricuspid valve and pulmonary regurgitation during diastole; (c) aortic outflow during systole in a patient with corrected coarctation of the aorta (CoA); (d) aortic regurgitation during diastole; (e) left and right atrioventricular valve (LAVV, RAVV, respectively) regurgitation during systole in a patient with corrected atrioventricular septal defect (AVSD); (f) inflow over the LAVV and RAVV during diastole.

Results

Characteristics of the 114 patients and 46 healthy volunteers are shown in *Table 1*. Median age [IQR] at the time of MRI acquisition of the total patient group was 17 [13-49] years: 48% (55/114) of the patients was ≥ 18 years of age and 55% (63/114) was male. Median age of the volunteers was 28 [22-36] years. 85% (39/46) of the volunteers was ≥ 18 years of age and 59% (27/46) was male. Patients with IschCMP had the highest median LV end-diastolic volume/BSA (138.4 [109.2-161.0] mL/m²) and the lowest LV ejection fraction (28.7 [20.0-36.7] %). As shown in *Supplementary data 2*, valvular flow mapping and cine planimetry showed significant differences in LV SV of the patients with corrected coarctation of the aorta (CoA) (7.1 [1.4-11.6] mL, $P<0.001$) and volunteers (5.2 [-0.2-9.3] mL, $P<0.001$) and significant differences in RV SV of the patients with corrected tetralogy of Fallot (ToF) (-5.4 [-10.9 to -2.8] mL, $P=0.001$), CoA (-4.3 [-11.3 to -1.5] mL, $P=0.001$), corrected atrioventricular septal defect (AVSD) (-2.8 [-8.0-0.5] mL, $P=0.01$) and volunteers (-3.9 [-10.7-0.2] mL, $P=0.001$). LV and RV stroke volumes assessed from planimetry in healthy volunteers without valve regurgitation showed a median difference of 3.3[-1.4-10.2] mL ($P=0.015$), which is in the same order of magnitude as the differences between valvular flow mapping and 2D planimetry for the patients and volunteers.

Automated versus manual valve tracking

Comprehensive results of valvular flow assessment with automated versus manual valve tracking are shown in *Table 2*. Time needed to quantify flow over all valves was shorter for automated versus manual valve tracking in all groups (patients: median and IQR: 14 [12-15] versus 25 [20-25] minutes; volunteers: 12 [10-15] versus 22 [22-22] minutes, $P<0.001$).

NFV variation was less (i.e. better) for automated valve tracking in all patient groups ($P<0.001$), except for patients with AVSD, in whom the range was not different ($P=0.39$). For all patients combined, NFV variation over four valves was smaller for automated versus manual tracking (4.9 [3.3-6.7]% versus 9.8 [5.1-14.7]%, $P<0.001$). Also in volunteers, automated valve tracking showed significantly less NFV variation ($P<0.001$).

To evaluate whether automated valve tracking resulted in a significantly different assessment of NFV per valve by manual tracking, the magnitude of NFV difference per valve was compared for both tracking techniques. In patients with IschCMP, NFV differences were not statistically significantly different after Holm's correction for multiple testing for automated versus manual valve tracking ($P\geq 0.06$). Also, in patients with ToF, NFV differences were not significantly different for automated versus manual valve tracking ($P\geq 0.004$). In patients

with CoA, NFV difference was less for automated versus manual valve tracking over the AV ($P=0.002$), the MV ($P<0.001$) and the TV ($P<0.001$). NFV differences over all valves in patients with AVSD were not different for automated versus manual valve tracking ($P\geq 0.05$). In volunteers, NFV differences were not different for automated versus manual valve tracking ($P\geq 0.20$).

In patients with IschCMP and patients with ToF, median regurgitant fraction over each valve was not statistically significantly different after Holm's correction for multiple testing for automated versus manual valve tracking ($P\geq 0.03$). In patients with CoA, median regurgitant fraction differed for automated versus manual valve tracking of the AV ($P=0.001$) and the TV ($P<0.001$). In patients with AVSD, median regurgitant fraction differed for automated versus manual valve tracking of the left atrioventricular valve ($P<0.001$), but not for the other valves ($P\geq 0.01$). In the volunteers, the regurgitant fraction was different for automated versus manual valve tracking of the MV ($P<0.001$) and the TV ($P=0.002$), but not for the other valves ($P\geq 0.12$).

To evaluate whether these differences resulted in regurgitation reclassification, the agreement in classification between methods was evaluated and shown in *Table 3*. Classification of aortic regurgitation could not be assessed because there were no patients with more than mild-moderate aortic valve regurgitation in this study. Classification of pulmonary regurgitation, with 6 mild-moderate, 10 moderate-severe cases and 2 severe cases for automated tracking, showed good agreement (κ 0.80, SE 0.06) between both methods, with only seven discordant cases. Classification of mitral regurgitation (i.e., 12 mild-moderate, 5 moderate-severe cases and 0 severe cases for automated tracking) and tricuspid regurgitation (i.e., 15 mild-moderate, 2 moderate-severe cases and 0 severe cases for automated tracking) both showed poor agreement between both methods (MV: κ 0.38, SE 0.10, TV: κ 0.28, SE 0.11), with 22 discordant cases for mitral regurgitation and 21 discordant cases for tricuspid regurgitation, respectively.

Table 1. Patient and volunteer characteristics

	IschCMP	ToF	CoA	AVSD	Volunteers
N	33	24	28	29	46
Median age [IQR] (min, max) in years					
Male	60 [52-71] (41-83)	13 [10-16] (9-33)	14 [10-16] (8-18)	22 [15-35] (11-39)	30 [24-44] (10-72)
Female	65 [52-74 (40-77)]	12 [11-14] (9-17)	13 [11-15] (9-17)	26 [16-33] (9-54)	27 [20-29] (11-50)
Total	63 [52-72] (40-83)	12 [10-14] (9-33)	14 [11-16] (8-18)	24 [16-33] (9-54)	28 [22-36] (10-72)
≥ 18 years (%)	33 (100)	2 (8)	0 (0)	20 (70)	39 (85)
Male (%)	21 (64)	16 (67)	18 (64)	8 (28)	27 (59)
BSA (m ²)*	2.0 [1.8-2.1]	1.4 [1.2-1.7]	1.5 [1.1-1.6]	1.8 [1.5-1.9]	1.9 [1.7-2.0]
NYHA functional class I/II/III/IV	7/11/14/1	24/0/0/0	28/0/0/0	28/1/0/0	46/0/0/0
LV end-diastolic volume/BSA (mL/m ²)	138.4 [109.2-161.0]	81.8 [61.1-87.6]	86.5 [75.5-98.0]	77.5 [69.4-92.5]	84.6 [77.1-93.8]
LV stroke volume/BSA (mL/m ²)	37.5 [32.1-43.3]	49.9 [39.7-58.8]	54.2 [51.5-58.7]	46.2 [40.7-53.3]	52.1 [46.3-57.8]
LV ejection fraction (%)	28.7 [20.0-36.7]	64.2 [57.4-70.3]	66.1 [60.1-70.6]	61.1 [55.1-65.2]	61.3 [58.4-64.8]
RV end-diastolic volume/BSA (mL/m ²)	66.4 [54.5-81.6]	103.6 [87.7-125.6]	92.8 [78.1-105.6]	70.9 [62.0-78.0]	89.0 [76.7-94.8]
RV stroke volume/BSA (mL/m ²)	36.2 [29.8-40.2]	63.6 [54.5-72.0]	48.4 [43.4-54.3]	44.3 [33.7-48.0]	49.2 [44.3-56.8]
RV ejection fraction (%)	58.4 [47.7-63.3]	62.4 [54.8-67.6]	53.5 [48.4-58.9]	59.9 [53.9-66.5]	57.0 [52.5-62.2]
% DCE	30 [13-37]	not applicable	not applicable	minimal enhancement, not further quantified	not applicable

Abbreviations: ToF = tetralogy of Fallot; CoA = coarctation of the aorta; AVSD = atrioventricular septal defect; IschCMP = ischemic cardiomyopathy; IQR = interquartile range; BSA = body surface area; LV = left ventricle; RV = right ventricle; DCE = Delayed contrast-enhancement
 *according to the Mosteller Method: BSA (m²) = square root of (height (cm) × weight (kg)/3600)

Table 2. Automated versus manual valve tracking for valvular flow assessment

	IschCMP	ToF	CoA	AVSD	Volunteers
Analysis time (min)					
Automated	12 [12-15]	15 [10-20]	15 [11-15]	12 [11-15]	12 [10-15]
Manual	25 [20-25]	30 [25-30]	25 [20-25]	25 [20-25]	22 [22-22]
P-value	<0.001	<0.001	<0.001	<0.001	<0.001
NFV variation (%)*					
Automated	5.6 [4.6-8.0]	5.4 [3.7-7.1]	3.6 [2.9-5.9]	3.9 [2.5-6.7]	4.1 [3.2-5.8]
Manual	10.6 [8.3-15.9]	10.9 [5.0-14.8]	12.1 [9.4-18.2]	4.3 [2.7-5.7]	6.7 [4.7-10.0]
P-value	<0.001	0.004	<0.001	0.39	<0.001
NFV difference (mL)**					
Aortic valve					
Automated	-1.2 [-4.9-0.0]	-1.0 [-3.1-3.6]	-1.3 [-2.6-0.2]	-1.5 [-2.8-0.3]	0.4 [-2.8-4.0]
Manual	-1.9 [-7.9-2.5]	2.0 [-0.2-6.0]	-5.0 [-10.8- -0.6]	-0.5 [-3.1-1.2]	-3.1 [-7.2-5.1]
P-value	0.91	0.13	0.002	0.69	0.21
Pulmonary valve					
Automated	1.3 [-3.6-5.6]	-1.1 [-4.7-2.5]	0.1 [-2.2-1.5]	-1.3 [-4.2-0.9]	-1.3 [-4.8-2.2]
Manual	-3.0 [-7.5-7.3]	0.6 [-4.6-5.2]	-1.4 [-6.8-4.1]	-0.6 [-2.2-1.7]	-1.0 [-6.2-5.5]
P-value	0.33	0.21	0.51	0.05	0.91
Mitral valve†					
Automated	-0.1 [-4.0-2.8]	3.4 [-1.2-5.4]	-0.5 [-2.5-2.9]	1.1 [-0.9-6.2]	0.0 [-2.0-3.1]
Manual	2.3 [-4.6-7.7]	3.8 [-1.0-8.1]	-8.0 [-13.7- -1.8]	-0.3 [-3.6-2.1]	1.2 [-2.8-6.0]
P-value	0.06	0.51	<0.001	0.006	0.20
Tricuspid valve†					
Automated	1.6 [-1.3-3.9]	-1.3 [-3.5-1.3]	3.2 [-0.7-5.2]	1.2 [-1.8-3.4]	1.1 [-3.2-4.2]
Manual	-1.6 [-9.5-8.8]	-6.2 [-14.1-1.2]	15.2 [6.5-26.7]	1.6 [-1.0-4.2]	1.9 [-7.7-7.5]
P-value	0.60	0.004	<0.001	0.28	0.97
Regurgitant fraction (%)					
Aortic valve					
Automated	2.2 [0.8-4.8]	1.9 [0.2-4.0]	0.9 [0.1-1.7]	0.6 [0.4-1.2]	1.4 [0.7-2.3]
Manual	2.9 [1.1-4.2]	1.2 [0.1-3.7]	2.1 [1.0-3.5]	0.1 [0.0-0.9]	1.0 [0.4-1.8]
P-value	0.90	0.09	0.001	0.01	0.12
Pulmonary valve					
Automated	1.7 [0.5-3.6]	26.3 [10.2-38.6]	0.9 [0.2-1.3]	1.5 [0.3-2.2]	1.3 [0.5-2.0]
Manual	2.2 [1.0-5.9]	26.5 [15.4-40.7]	1.2 [0.6-2.5]	0.3 [0.1-1.1]	1.3 [0.2-3.5]
P-value	0.03	0.65	0.11	0.01	0.62
Mitral valve†					
Automated	13.4 [6.1-20.7]	4.3 [3.1-6.0]	2.1 [1.7-3.8]	6.5 [4.3-10.0]	3.4 [2.5-5.0]
Manual	9.2 [4.8-18.1]	3.4 [2.0-5.1]	2.5 [1.7-3.2]	11.9 [7.1-19.4]	2.4 [0.9-3.7]
P-value	0.21	0.25	0.63	<0.001	<0.001
Tricuspid valve†					
Automated	10.1 [6.7-13.4]	7.9 [4.3-10.4]	8.3 [5.3-12.2]	4.4 [2.9-7.3]	9.5 [7.1-11.2]
Manual	10.6 [7.0-14.3]	6.6 [3.0-10.7]	4.3 [2.8-6.7]	3.9 [2.2-5.7]	7.2 [4.3-9.8]
P-value	0.91	0.20	<0.001	0.55	0.002

All data are presented as median [IQR], for analysis times minimum-maximum values are also provided

Results were compared with the Wilcoxon signed-rank test for analysis and the Holm method was used to correct for multiple testing [17], which resulted in a multiple testing corrected threshold for significance of $0.05/1 = 0.05$ for analysis time, $0.05/1 = 0.05$ for NFV variation, $0.05/17 = 0.003$ for NFV difference and $0.05/15 = 0.003$ for regurgitant fraction.

* NFV variation = the standard deviation of the differences among all four valves divided by the mean NFV among all four valves

** NFV difference = the difference between the net forward flow volume (NFV) over the respective valve versus mean NFV over the three other valves

† = in the patients with corrected AVSD, mitral valve = left atrioventricular valve; tricuspid valve = right atrioventricular valve

Abbreviations: ToF = tetralogy of Fallot; CoA = coarctation of the aorta; AVSD = atrioventricular septal defect; IschCMP = ischemic cardiomyopathy; NFV = net forward volume; MV = mitral valve; AV = aortic valve; TV = tricuspid valve; PV = pulmonary valve

Table 3. Cross tables for kappa agreement in valvular regurgitation classification

Pulmonary valve regurgitation						
automated	Manual	<15%	15-25%	26-48%	>48%	Total
	<15%	141	1	0	0	142
	15-25%	0	4	2	0	6
	26-48%	0	2	8	0	10
	>48%	0	0	2	0	2
	Total	141	7	12	0	160
κ : 0.80, SE: 0.06 , $P<0.001$						
Mitral valve regurgitation						
automated	Manual	<15%	15-25%	26-48%	>48%	Total
	<15%	131	11	1	0	143
	15-25%	5	5	2	0	12
	26-48%	2	1	2	0	5
	>48%	0	0	0	0	0
	Total	138	17	5	0	160
κ : 0.38, SE: 0.10, $P<0.001$						
Tricuspid valve regurgitation						
automated	Manual	<15%	15-25%	26-48%	>48%	Total
	<15%	134	9	0	0	143
	15-25%	11	4	0	0	15
	26-48%	0	1	1	0	2
	>48%	0	0	0	0	0
	Total	145	14	1	0	160
κ : 0.28, SE: 0.11 , $P<0.001$						

Acquisition differences

Patient data was collected over 10 years, using two different scanning approaches and two different field strengths. In order to rule out possible effects from these variables, healthy volunteer data was evaluated with both tracking techniques. Of the 25 volunteers who were scanned at 1.5T, 14 were scanned with a whole-heart protocol and 11 volunteers with a basal volume protocol. For these volunteers, there was no difference in NFV variation between volunteers scanned with a whole-heart protocol versus a basal volume protocol (automated tracking: 3.6 [2.6-4.5] % versus 3.8 [2.8-4.8] %, $P=0.98$; manual tracking 8.2 [5.8-13.0] % versus 7.3 [5.5-12.5] %, $P=0.65$). Of the 35 volunteers that were scanned with a whole-heart protocol, 21 were scanned at 3.0T and 14 at 1.5T. For automated tracking, the volunteers who were scanned at 3.0T showed a smaller difference in NFV variation compared to those scanned at 1.5T (5.2 [4.1-7.9] % versus 3.6 [2.6-4.5] %, $P=0.005$) but not for manual tracking (5.9 [3.2-9.4] % versus 8.2 [5.8-13.0] %, $P=0.07$).

In order to understand whether differences between automated and manual valve tracking were influenced by the type of heart disease, acquired (ischemic) versus congenital heart disease patients were compared. NFV variation was less in patients with congenital heart disease compared to patients with acquired heart disease when using automated valve tracking (congenital: 4.3 [3.0-6.5] %; acquired: 5.6 [4.6-8.0] %, $P=0.002$) or manual valve tracking (congenital: 8.8 [4.4-13.8] %; acquired: 10.6 [8.3-15.9] %, $P=0.001$). In order to understand whether results in children would be different from adults, NFV variation was compared in pediatric (<18 years) versus adult (≥ 18 years) patients. NFV variation was not different when using manual valve tracking (<18 years: 10.9 [5.8-16.6] %; ≥ 18 years: 8.3 [4.4-12.2] %, $P=0.05$), or automated valve tracking (<18 years: 4.3 [3.2-6.3] %; ≥ 18 years: 5.5 [3.3-7.3] %, $P=0.05$).

Intra- and inter-observer analysis

Results of the intra- and inter-observer analysis with automated valve tracking are shown in *Table 4* and *Figure 4*. Intra-observer analysis showed excellent ICCs for NFV assessment of all valves with $COV \leq 5.2\%$. Mean differences between intra-observer measurements of NFV were ≤ 1.8 mL (*Figure 4a*). ICCs for regurgitant fraction assessment were strong-excellent with mean differences between intra-observer measurements of regurgitant fraction $\leq 1.3\%$ (*Figure 4b*).

Also, inter-observer analysis showed excellent ICCs for NFV assessment of all valves with $COV \leq 5.6\%$. Mean differences between inter-observer measurements of NFV were ≤ 1.5 mL (*Figure 4c*). Furthermore, inter-observer analysis showed strong-excellent ICCs for regurgitant fraction assessment with mean differences between inter-observer measurements of $\leq 1.3\%$ (*Figure 4d*).

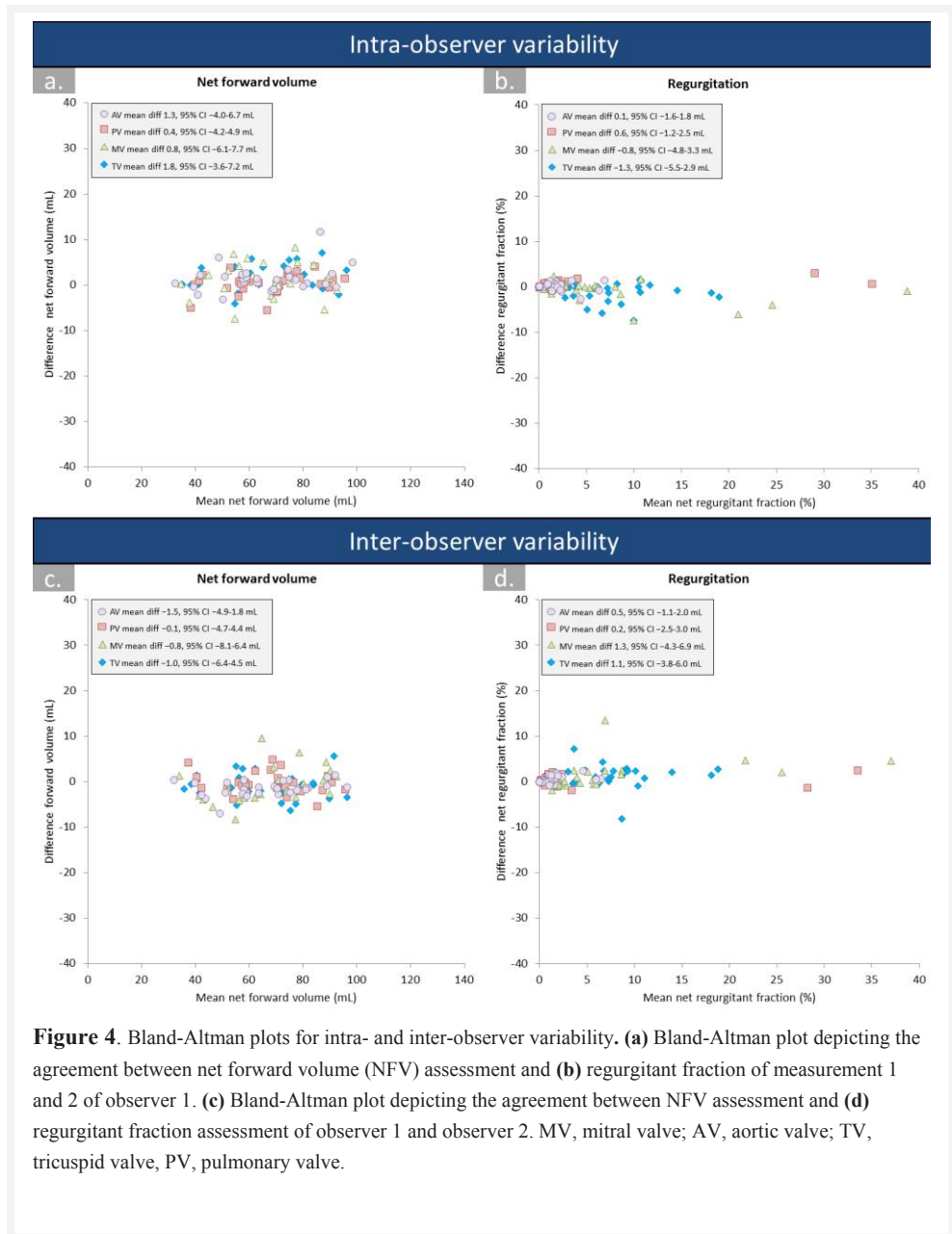


Figure 4. Bland-Altman plots for intra- and inter-observer variability. **(a)** Bland-Altman plot depicting the agreement between net forward volume (NFV) assessment and **(b)** regurgitant fraction of measurement 1 and 2 of observer 1. **(c)** Bland-Altman plot depicting the agreement between NFV assessment and **(d)** regurgitant fraction assessment of observer 1 and observer 2. MV, mitral valve; AV, aortic valve; TV, tricuspid valve, PV, pulmonary valve.

Table 4. Intra- and inter-observer analysis

	Intra-observer			Inter-observer		
	Observer 1 Measurement 1 Median [IQR]	Observer 1 Measurement 2 Median [IQR]	Intra-observer ICC ICC (95% CI)	Intra-observer COV %	Observer 2 Median [IQR]	Inter-observer ICC ICC (95% CI)
AV NFV	66.0 [53.1-79.4]	65.7 [53.6-79.5]	0.99 (0.98-1.00) ^a	4.1	67.5 [54.1-81.2]	1.00 (0.97-1.00) ^a
AV regurgitation (%)	1.2 [0.2-2.0]	1.7 [0.2-2.3]	0.94 (0.88-0.98) ^a		0.8 [0.3-1.3]	0.93 (0.80-0.97) ^a
PV NFV	70.2 [56.3-75.8]	66.8 [55.4-78.6]	0.99 (0.99-1.00) ^a	3.4	66.6 [56.6-76.5]	0.99 (0.99-1.00) ^a
PV regurgitation (%)	1.3 [0.5-2.5]	1.7 [0.8-3.4]	1.00 (0.99-1.00) ^a		0.8 [0.1-2.3]	1.00 (0.99-1.00) ^a
MV NFV	66.3 [52.0-79.1]	67.5 [54.9-81.2]	0.99 (0.97-0.99) ^a	5.2	64.9 [58.1-78.2]	0.99 (0.97-0.99) ^a
MV regurgitation (%)	4.2 [2.2-7.6]	3.3 [2.4-6.3]	0.98 (0.96-0.99) ^a		2.9 [2.0-6.0]	0.97 (0.91-0.99) ^a
TV NFV	63.6 [56.9-78.6]	65.6 [56.7-81.5]	0.99 (0.97-1.00) ^a	4.1	63.1 [56.1-80.0]	0.99 (0.98-1.00) ^a
TV regurgitation (%)	7.7 [6.0-10.4]	6.6 [3.9-10.4]	0.94 (0.83-0.98) ^a		6.8 [4.0-8.8]	0.89 0.75-0.95 ^b

^a P<0.001

^b P<0.05

Abbreviations: IQR = interquartile range; ICC = intraclass correlation coefficient; COV = coefficient of variation; MV = mitral valve; NFV = net forward volume; AV = aortic valve; TV = tricuspid valve; PV = pulmonary valve

Discussion

In this study the clinical applicability of 4D flow MRI with automated valve tracking was evaluated. The main findings are: 1) time needed for analysis was shorter for automated versus manual valve tracking; 2) automated tracking showed less NFV variation compared to manual tracking; 3) automated tracking resulted in reclassification of regurgitation severity for 7 pulmonary valves, 22 mitral valves and 21 tricuspid valves; 4) intra- and inter-observer agreement for automated tracking was excellent for NFV and strong-to-excellent for regurgitant fraction.

Diagnosis and follow-up in valvular heart disease is usually performed with echocardiography. According to current guidelines, additional testing by MRI is appropriate when echocardiographic images are suboptimal, regurgitation severity might be underestimated or better characterization of the regurgitant jet is needed [5]. Clinically, 2D phase-contrast MRI with static imaging planes and through-plane velocity encoding is the most commonly used MRI valvular flow quantification technique. However, several studies have shown that 4D flow MRI with manual retrospective valve tracking is more accurate than 2D phase-contrast MRI when quantifying valvular flow volumes and regurgitation [7-13]. However, manual placement and tracking of measurement planes in every cardiac phase for each valve is time-consuming and may introduce observer-dependent variation. The time needed for analysis for automated tracking was approximately half of that of manual tracking. Of note, the automated tracking procedure itself was a matter of seconds and analysis time was mostly dedicated to manual contouring for velocity mapping.

Four patient groups with valve regurgitation were studied: IschCMP and corrected ToF, corrected CoA and corrected AVSD. In patients with IschCMP, accurate regurgitation quantification, especially of the MV, is important for patient management (surgery versus conservative management) [3] and progressing MV regurgitation is recognized as an independent predictor of adverse events [1]. In patients with corrected ToF, PV regurgitation is a common complication, which can eventually lead to right ventricular dilatation and dysfunction, arrhythmias and sudden cardiac death [19, 20]. Severity of PV regurgitation may warrant replacement [19]. In patients with corrected AVSD, left atrioventricular valve regurgitation is a frequent complication and the main indication for late reoperation [18]. Therefore, in these patients, accurate quantification of regurgitation severity is crucial since mild versus moderate regurgitation has an impact on treatment [19].

Significant differences in NFV variation, difference and regurgitant fraction between automated and manual valve tracking were found in all patient groups, also resulting in

different classification of regurgitation severity. Significant NFV differences were mostly smaller for automated compared to manual valve tracking. Smaller differences and less variation indicate better NFV consistency among the four valves. Only in patients with corrected AVSD, NFV variation was not significantly different between automated and manual tracking and NFV differences were not significantly different for automated versus manual tracking. These findings in patients with corrected AVSD, that are in discrepancy with our findings in other patient groups, probably relate to the fact that automated tracking does not allow for plane alignment perpendicular to the flow direction, which leads to greater accuracy for manual valve tracking in these patients [7, 8].

No independent reference standard is available for NFV or regurgitant fraction assessment, however, automated tracking showed stronger internal consistency in NFV than manual tracking, thus better agreement with conservation of mass, therefore these results imply a better assessment of forward and of regurgitant volumes by automated valve tracking. Stroke volumes from 2D planimetry were compared to valvular flow mapping from automated valve tracking. Of note, LV and RV stroke volumes assessed from planimetry in healthy volunteers without valve regurgitation showed a median difference of 3.3 [-1.4-10.2] mL, ($P=0.015$), which is in the same order of magnitude as the differences between valvular flow mapping and 2D planimetry for the patients and volunteers. When using planimetry as a reference standard against valvular flow mapping, planimetry has some notable limitations as well. Over- or underestimation of the blood pool volume may occur in the basal slice due to the relatively high slice thickness. Also, when using breath holding, translation between slices from different expiration levels can occur. Furthermore, some patients, especially with cardiac disease, may have difficulty performing breath holding. Additionally, breath holding may have an effect on cardiac output, which may be different for assessment of 4D flow data with free breathing. On the other hand, free breathing protocols for planimetry as well as 4D flow MRI result in inferior image quality which may lead to variation in contour definition.

Since this was a retrospective study, the findings did not change patient management at this moment. However, if diagnosis would have been based only on MRI results, automated valve tracking would have reclassified 6 patients with at least mild-to-moderate valve regurgitation at the pulmonary valve (6/114, 5%), 10 patients with at least mild-to-moderate mitral valve regurgitation (10/114, 9%) and 12 patients with at least mild-to-moderate tricuspid valve regurgitation (12/114, 11%). This may have significant impact on clinical decision making regarding follow-up regime. Two patients with severe pulmonary valve regurgitation with automated valve tracking were misclassified with manual valve tracking, which could have impacted a recommendation for surgery.

Roes et al. [9] reported intra- and inter-observer variability for manual tracking for all four valves (intra-observer ICC \geq 0.93%, COV \leq 7%; inter-observer ICC \geq 0.91, COV \leq 8%). In the current study, intra- and inter-observer agreement for automated valve tracking was stronger and variability was smaller (intra-observer ICC \geq 0.99, COV \leq 5.2%; inter-observer ICC \geq 0.99, COV \leq 5.6%).

Fifty-nine patients with congenital heart diseases in this study were children, which could cause more variation because children might be less cooperative during scanning. However, on the contrary, the current study showed significant, but limited, smaller NFV variation in patients with congenital versus acquired heart disease. Also, NFV variation was not significantly different for pediatric versus adult patients.

Furthermore, volunteer data from different acquisition protocols was analyzed to rule out effects of protocol differences. Only volunteers scanned with a whole-heart protocol at 3.0T showed slightly higher NFV variation compared to volunteers scanned at 1.5T (5.2 vs. 3.6%, P=0.005), however, 5.2% variation might still be considered clinically irrelevant.

One of the limitations of this study is the retrospective design of the study, however data were collected as part of several prospective studies. Another limitation is that patients with aortic valve regurgitation or stenosis were not part of the study population. Furthermore, the number of patients with severe valvular regurgitation was limited. However, clinically, distinction between mild versus moderate regurgitation is important since it may impact patient management. Finally, automated and manual valve tracking approaches handled phase offset correction and phase unwrapping differently, which could have introduced additional variation.

Conclusion

In conclusion, automated cardiac valve tracking reduces analysis time and improves reliability of valvular flow quantification by 4D flow MRI in patients with acquired or congenital heart disease and in healthy volunteers, possibly allowing for a wider application of this imaging technique in the clinical setting.

References

1. Kwon DH, Kusunose K, Obuchowski NA, Cavalcante JL, Popovic ZB, Thomas JD, Desai MY, Flamm SD, Griffin BP: Predictors and Prognostic Impact of Progressive Ischemic Mitral Regurgitation in Patients With Advanced Ischemic Cardiomyopathy: A Multimodality Study. *Circ Cardiovasc Imaging* 2016, 9.
2. Nishimura RA, Otto CM, Bonow RO, Carabello BA, Erwin JP, 3rd, Fleisher LA, Jneid H, Mack MJ, McLeod CJ, O'Gara PT, et al: 2017 AHA/ACC Focused Update of the 2014 AHA/ACC Guideline for the Management of Patients With Valvular Heart Disease: A Report of the American College of Cardiology/American Heart Association Task Force on Clinical Practice Guidelines. *J Am Coll Cardiol* 2017, 70:252-289.
3. O'Gara PT, Grayburn PA, Badhwar V, Afonso LC, Carroll JD, Elmariah S, Kithcart AP, Nishimura RA, Ryan TJ, Schwartz A, Stevenson LW: 2017 ACC Expert Consensus Decision Pathway on the Management of Mitral Regurgitation: A Report of the American College of Cardiology Task Force on Expert Consensus Decision Pathways. *J Am Coll Cardiol* 2017, 70:2421-2449.
4. Kathiria NN, Higgins CB, Ordovas KG: Advances in MR imaging assessment of adults with congenital heart disease. *Magn Reson Imaging Clin N Am* 2015, 23:35-40.
5. Doherty JU, Kort S, Mehran R, Schoenhagen P, Soman P: ACC/AATS/AHA/ASE/ASNC/HRS/SCAI/SCCT/SCMR/STS 2017 Appropriate Use Criteria for Multimodality Imaging in Valvular Heart Disease: A Report of the American College of Cardiology Appropriate Use Criteria Task Force, American Association for Thoracic Surgery, American Heart Association, American Society of Echocardiography, American Society of Nuclear Cardiology, Heart Rhythm Society, Society for Cardiovascular Angiography and Interventions, Society of Cardiovascular Computed Tomography, Society for Cardiovascular Magnetic Resonance, and Society of Thoracic Surgeons. *J Am Coll Cardiol* 2017, 70:1647-1672.
6. Zoghbi WA, Enriquez-Sarano M, Foster E, Grayburn PA, Kraft CD, Levine RA, Nihoyannopoulos P, Otto CM, Quinones MA, Rakowski H, et al: Recommendations for evaluation of the severity of native valvular regurgitation with two-dimensional and Doppler echocardiography. *J Am Soc Echocardiogr* 2003, 16:777-802.
7. Calkoen EE, Roest AA, Kroft LJ, van der Geest RJ, Jongbloed MR, van den Boogaard PJ, Blom NA, Hazekamp MG, de Roos A, Westenberg JJ: Characterization and improved quantification of left ventricular inflow using streamline visualization with 4DFlow MRI in healthy controls and patients after atrioventricular septal defect correction. *J Magn Reson Imaging* 2015, 41:1512-1520.
8. Calkoen EE, Westenberg JJ, Kroft LJ, Blom NA, Hazekamp MG, Rijlaarsdam ME, Jongbloed MR, de Roos A, Roest AA: Characterization and quantification of dynamic eccentric regurgitation of the left atrioventricular valve after atrioventricular septal defect correction with 4D Flow cardiovascular magnetic resonance and retrospective valve tracking. *J Cardiovasc Magn Reson* 2015, 17:18.
9. Roes SD, Hammer S, van der Geest RJ, Marsan NA, Bax JJ, Lamb HJ, Reiber JH, de Roos A, Westenberg JJ: Flow assessment through four heart valves simultaneously using 3-dimensional 3-directional velocity-encoded magnetic resonance imaging with retrospective valve tracking in healthy volunteers and patients with valvular regurgitation. *Invest Radiol* 2009, 44:669-675.
10. van der Hulst AE, Westenberg JJ, Kroft LJ, Bax JJ, Blom NA, de Roos A, Roest AA: Tetralogy of fallot: 3D velocity-encoded MR imaging for evaluation of right ventricular valve flow and diastolic function in patients after correction. *Radiology* 2010, 256:724-734.
11. Westenberg JJ, Doornbos J, Versteegh MI, Bax JJ, van der Geest RJ, de Roos A, Dion RA, Reiber JH: Accurate quantitation of regurgitant volume with MRI in patients selected for mitral valve repair. *Eur J Cardiothorac Surg* 2005, 27:462-466; discussion 467.
12. Westenberg JJ, Roes SD, Ajmone Marsan N, Binnendijk NM, Doornbos J, Bax JJ, Reiber JH, de Roos A, van der Geest RJ: Mitral valve and tricuspid valve blood flow: accurate quantification with 3D velocity-encoded MR imaging with retrospective valve tracking. *Radiology* 2008, 249:792-800.
13. Kamphuis VP, van der Palen RLF, de Koning PJH, Elbaz MSM, van der Geest RJ, de Roos A, Roest AAW, Westenberg JJM: In-scan and scan-rescan assessment of LV in- and outflow volumes by 4D flow MRI versus 2D planimetry. *J Magn Reson Imaging* 2018, 47:511-522.

14. Nederend I, de Geus EJC, Kroft LJM, Westenberg JJM, Blom NA, Ten Harkel ADJ: Cardiac Autonomic Nervous System Activity and Cardiac Function in Children After Coarctation Repair. *Ann Thorac Surg* 2018, 105:1803-1808.
15. Garg P, Westenberg JJM, van den Boogaard PJ, Swoboda PP, Aziz R, Foley JRJ, Fent GJ, Tyl FGJ, Coratella L, ElBaz MSM, et al: Comparison of fast acquisition strategies in whole-heart four-dimensional flow cardiac MR: Two-center, 1.5 Tesla, phantom and in vivo validation study. *J Magn Reson Imaging* 2018, 47:272-281.
16. She HL, Roest AA, Calkoen EE, van den Boogaard PJ, van der Geest RJ, Hazekamp MG, de Roos A, Westenberg JJ: Comparative Evaluation of Flow Quantification across the Atrioventricular Valve in Patients with Functional Univentricular Heart after Fontan's Surgery and Healthy Controls: Measurement by 4D Flow Magnetic Resonance Imaging and Streamline Visualization. *Congenit Heart Dis* 2017, 12:40-48.
17. Holm S: A simple sequentially rejective multiple test procedure. *Scandinavian Journal of Statistics* 1979, 6:65-70.
18. Bland JM, Altman DG: Statistical methods for assessing agreement between two methods of clinical measurement. *Lancet* 1986, 1:307-310.
19. Baumgartner H, Bonhoeffer P, De Groot NM, de Haan F, Deanfield JE, Galie N, Gatzoulis MA, Gohlke-Baerwolf C, Kaemmerer H, Kilner P, et al: ESC Guidelines for the management of grown-up congenital heart disease (new version 2010). *Eur Heart J* 2010, 31:2915-2957.
20. Gatzoulis MA, Balaji S, Webber SA, Siu SC, Hokanson JS, Poile C, Rosenthal M, Nakazawa M, Moller JH, Gillette PC, et al: Risk factors for arrhythmia and sudden cardiac death late after repair of tetralogy of Fallot: a multicentre study. *Lancet* 2000, 356:975-981.

Supplementary data 1.

MRI acquisition

MRI data has been acquired using 1.5T (Intera release 11 and 12 and Ingenia release 5) and 3.0T (Ingenia release 4 and 5) MRI systems (Philips Healthcare, Best, the Netherlands). The 1.5T Intera MRI system makes use of a five-element surface cardiac coil for signal reception. The 1.5T and 3.0T Ingenia MRI systems make use of the combination of dStream Torso coil and FlexCoverage Posterior coil in the table top, providing up to 32 coil elements for signal reception. Two different validated acquisition approaches were followed for 4D flow MRI: a whole-heart 4D flow MRI protocol on 1.5T [1] and 3.0T [2] Ingenia MRI systems and a cardiac basal volume acquisition (planned parallel to the basal plane of the heart, encompassing all four heart valves) on a 1.5T Intera MRI system [3,4]. Both sequences used standard four-point three-directional velocity encoding with Venc between 150 cm/s and 350 cm/s per anticipated maximal velocity, retrospective gating with 30 phases reconstructed, non-compensated free breathing and echo planar imaging with echo-planar imaging factor of 5 for accelerated read-out. Commercially available concomitant gradient correction was performed by scanner software. Furthermore, the whole-heart protocol used parallel imaging with sensitivity encoding factor 2 in anterior-posterior direction and a 300-370 mm field-of-view with 105-135mm slab thickness covering the whole heart, reconstructed into 35-41 slices of 3mm thickness. Acquired spatial resolution was 2.3-3.0×2.3-3.0×3.0 mm³. Flip angle was 10°, echo time/repetition time was 3.2/7.7 resulting in 31ms temporal resolution. The basal protocol used a 370 mm field-of-view with 48 mm slab thickness reconstructed in 12 slices of 4mm thickness resulting in an acquired spatial resolution of 2.9×3.8×4.0 mm³. Flip angle was 10°, echo time/repetition time was 3.3/14 to 4.3/7.5 resulting in 30-56ms temporal resolution.

4D flow MRI was supplemented with 2D steady-state free-precession cine acquisitions of left and right ventricular two- and four-chamber views and left and right ventricular outflow tract in such way that for each of the four valves, two orthogonal cine views were available for valve tracking during post-processing. For the whole-heart protocol, these acquisitions were obtained with free breathing and 3 signal averages were taken to suppress breathing motion artifacts and for the basal protocol, breath-holding and 1 signal average was performed. These orthogonal cine acquisitions were obtained with retrospective gating and 30 cardiac phases were reconstructed.

All patients and volunteers were scanned without the use of contrast agent, except for the patients with ischemic cardiomyopathy (IschCMP) and the patients with corrected

atrioventricular septal defect (AVSD). For these patients, contrast was used as part of a clinical myocardial viability evaluation by late gadolinium enhancement, and 4D flow MRI was performed directly after the administration of gadolinium contrast (Dotarem, Guerbet, Aulnay-sous-Bois, France or Magnevist, Schering/Berlex, Berlin, Germany prior to 2008) at a dose of 0.015 mmol/kg body weight.

Supplementary data 2.

Comparison between stroke volumes from 2D cine planimetry and automated valve tracking

Multi-slice multi-phase 2D cine images were available for all patients and volunteers. For patients with corrected tetralogy of Fallot, the left ventricle (LV) and right ventricle (RV) were imaged with a multi-slice multi-phase cine 2D stack in transverse orientation using a steady-state free-precession gradient echo sequence [5]. For all other patients and healthy volunteers, LV and RV were imaged with a multi-slice multi-phase cine 2D stack in short-axis orientation [2, 6-8]. For patients with corrected AVSD and corrected coarctation and healthy volunteers <18 years old, data were acquired using a free breathing protocol and 3 signal averages to compensate for respiration artifacts. Acquisition for other patients and volunteers were performed with breath-holding after expiration. End diastolic and end systolic volumes of LV and RV were assessed from planimetry with semi-automated contouring using CAAS MR Solutions 5.0 (Pie Medical Imaging, Maastricht, The Netherlands). LV and RV stroke volumes (SV) were compared with valvular flow mapping from automated valve tracking: LV SV versus aortic forward flow plus mitral valve regurgitation and RV SV versus pulmonary forward flow plus tricuspid valve regurgitation. Stroke volumes from 2D cine images and automated valve tracking and differences between these methods are shown in *Table S1*.

Table S1. Comparison between stroke volumes from 2D cine planimetry and automated valve tracking

	IschCMP	ToF	CoA	AVSD	Volunteers
LV SV (mL)	70.0 [58.8-84.3]	64.6 [58.1-90.4]	78.9 [65.3-91.9]	83.2 [66.3-91.0]	94.5 [80.8-109.9]
AV _{forward} + MV _{regurgitation} (mL)	69.4 [57.8-81.1]	67.8 [55.4-97.4]	71.1 [55.3-85.4]	78.1 [64.0-90.1]	91.6 [77.2-102.9]
Difference (mL)	-0.2 [-3.3-6.4]	-0.3 [-6.6-4.7]	7.1 [1.4-11.6]	3.0 [-1.9-7.9]	5.2 [-0.2-9.3]
P-value	0.24	0.65	<0.001	0.10	< 0.001
RV SV (mL)	70.1 [50.8-79.5]	91.8 [65.0-113.7]	70.9 [54.4-84.6]	77.5 [58.5-84.5]	89.0 [77.4-106.8]
PV _{forward} + TV _{regurgitation} (mL)	69.6 [57.4-82.3]	93.5 [72.6-121.3]	79.3 [62.2-92.1]	78.9 [62.4-87.7]	96.5 [83.3-111.5]
Difference (mL)	-1.3 [-8.7-3.8]	-5.4 [-10.9 to -2.8]	-4.3 [-11.3 to -1.5]	-2.8 [-8.0-0.5]	-3.9 [-10.7-0.2]
P-value	0.13	0.001	<0.001	0.01	0.001

Data is shown as median [interquartile range]. Abbreviations: IschCMP = ischemic cardiomyopathy; ToF = tetralogy of Fallot; CoA = coarctation of the aorta; AVSD = atrioventricular septal defect; LV = left ventricle; SV = stroke volume MV = mitral valve; AV = aortic valve; RV = right ventricle; TV = tricuspid valve; PV = pulmonary valve

Supplementary data 3. Manual and automated valve tracking

Manual valve tracking

Manual retrospective valve tracking over the aortic valve (AV), pulmonary valve (PV), mitral valve (MV) and tricuspid valve (TV) was done using in-house developed software (MASS), following previously published methods (3,4). The excursion of the AV and PV was identified on the left and right ventricular outflow tract cine acquisitions, respectively. MV and TV excursion was identified on the left and right ventricular two- and four-chamber cine acquisitions. Streamlines were visualized on these cine views to aid positioning and angulation of the multi-planar reformatting measurement planes, as these measurement planes were positioned perpendicular to the streamlines in all phases at the location of peak flow velocity [5]. For all phases, through-plane velocity-encoded images were reconstructed by multi-planar reformatting (typically in sets of 5 parallel slices with 5 mm interslice distance) on which borders of the valvular and myocardial wall were manually segmented (for through-plane motion and velocity offset error correction, not necessarily in the same slice as the transvalvular flow velocity measurement). Analysis times (valve tracking and velocity mapping combined) were recorded. For each patient and healthy volunteer, the difference between NFV over the respective valve versus mean NFV over the three other valves is defined as NFV difference. The NFV variation among the four valves (calculated as the standard deviation of differences among all four valves divided by the mean NFV of

all four valves) and the NFV differences were used for internal validation of NFV consistency. In case aliasing occurred, phase unwrapping was performed prior to the valve tracking in the source images of the three velocity components, using a sliding scale for the velocity sensitivity between minimal encoded velocity ($-V_{enc}$) and maximal encoded velocity ($+V_{enc}$).

Automated valve tracking

The automated valve tracking was performed using CAAS MR 4D Flow v2.0 (Pie Medical Imaging, Maastricht, The Netherlands). Tracking was initiated in each long-axis cine acquisition (within an arbitrary phase) by manually indicating two points at the valve annulus at the selected cardiac phase. Next, the movement of the valve was automatically tracked throughout the cardiac cycle with a multiple template matching using normalized cross-correlation strategy to identify the valve position in every phase of the long-axis cine acquisition. Visual feedback on the valve motion was presented and if required, minimal correction for the tracking was performed by repeating the automated tracking starting from a different cardiac phase. Minimal correction consisted of only choosing another cardiac phase as initiation phase for valve tracking. This manual adaptation was needed in approximately 50% of the tracked pulmonary valves and in less than 5% of the other valves. After changing the initiation phase as starting point for valve tracking, the tracking procedure was fully automatic. Once the valve plane was tracked in the two orthogonal long-axis cine acquisitions (e.g. 2-chamber 4-chamber views), a 3D plane was constructed. These 3D planes were mapped to the 4D flow MRI volume and used for multi-planar reformatting. Initial valve contours were provided for the reformatted velocity image based on the tracked valve landmarks, which were then manually corrected by the user when necessary. Through-plane velocity of the valve plane movement was calculated based on the tracked valve and used for through-plane motion correction. 3D visualization of time-resolved streamlines enabled visual assessment of valvular blood flow, aiding contour delineation.

Automatic velocity aliasing correction was performed for each of the three velocity components independent in an iterative process. During each iteration, the first step was to determine the likelihood of aliasing of each voxel by comparing the local velocity component with that of the two temporal and the six spatial neighbouring voxels. In the next step, those voxels marked as being aliased were unwrapped and marked as being processed. During the next iteration, only the unprocessed voxels were checked again against the already partly unwrapped data.

Furthermore, automatic velocity offset correction was performed for each of the three velocity components independently. Velocity offset correction was based on the method as described by Lankhaar et al. [9] Stationary (i.e., non-moving) tissue was identified by evaluating the behavior of the velocity component of each voxel over time. Per image, a surface was fitted through the time-averaged velocity of only those voxels corresponding with the identified stationary tissue. The obtained fitted velocity image represented the velocity offset per component and was subtracted from each corresponding image over time.

References belonging to the supplementary data

1. Garg P, Westenberg JJM, van den Boogaard PJ et al. Comparison of fast acquisition strategies in whole-heart four-dimensional flow cardiac MR: Two-center, 1.5 Tesla, phantom and in vivo validation study. *J Magn Reson Imaging*. 2018; 47:272-281.
2. Calkoen EE, Westenberg JJ, Kroft LJ et al. Characterization and quantification of dynamic eccentric regurgitation of the left atrioventricular valve after atrioventricular septal defect correction with 4D Flow cardiovascular magnetic resonance and retrospective valve tracking. *J Cardiovasc Magn Reson*. 2015;17:18.
3. Roes SD, Hammer S, van der Geest RJ et al. Flow assessment through four heart valves simultaneously using 3-dimensional 3-directional velocity-encoded magnetic resonance imaging with retrospective valve tracking in healthy volunteers and patients with valvular regurgitation. *Invest Radiol*. 2009;44:669-75.
4. Westenberg JJ, Roes SD, Ajmone Marsan N et al. Mitral valve and tricuspid valve blood flow: accurate quantification with 3D velocity-encoded MR imaging with retrospective valve tracking. *Radiology*. 2008;249:792-800.
5. Calkoen EE, Roest AA, Kroft LJ et al. Characterization and improved quantification of left ventricular inflow using streamline visualization with 4DFlow MRI in healthy controls and patients after atrioventricular septal defect correction. *J Magn Reson Imaging* 2015;41:1512-20.
6. van der Hulst AE, Westenberg JJ, Kroft LJ, et al. Tetralogy of fallot: 3D velocity-encoded MR imaging for evaluation of right ventricular valve flow and diastolic function in patients after correction. *Radiology*. 2010;256:724-34.
7. Marsan NA, Westenberg JJ, Roes SD, et al. Three-dimensional echocardiography for the preoperative assessment of patients with left ventricular aneurysm. *Ann Thorac Surg*. 2011;91:113-21.
8. Nederend I, de Geus EJC, Kroft LJM, Westenberg JJM, Blom NA, Ten Harkel ADJ. Cardiac Autonomic Nervous System Activity and Cardiac Function in Children After Coarctation Repair. *Ann Thorac Surg*. 2018;105:1803-8.
9. Lankhaar JW, Hofman MB, Marcus JT, Zwanenburg JJ, Faes TJ, Vonk-Noordegraaf A. Correction of phase offset errors in main pulmonary artery flow quantification. *J Magn Reson Imaging* 2005;22:73-9

A photograph of a bridge at night, with its structure illuminated by warm yellow lights. The bridge spans across a body of water, and the lights from the bridge and surrounding area are reflected on the rippling surface of the water. The scene is dark, with the primary light sources being the bridge's lights and a few distant, colorful lights (red, green, blue) visible in the background.

Part III

4D flow MRI-derived novel
determinants of intraventricular
hemodynamics

Chapter 9

Scan-rescan reproducibility of diastolic left ventricular kinetic energy, viscous energy loss and vorticity assessment using 4D flow MRI: analysis in healthy subjects.

Vivian P Kamphuis, Jos JM Westenberg, Roel LF van der Palen, Pieter J van den Boogaard, Rob J van der Geest, Albert de Roos, Nico A Blom, Arno AW Roest, Mohammed SM Elbaz

Int J Cardiovasc Imaging 2018 Jun;34(6):905-920

Abstract

Objective

To assess the scan–rescan reproducibility of left ventricular (LV) kinetic energy (KE), viscous energy loss (EL) and vorticity during diastole from four-dimensional (4D) flow magnetic resonance imaging (MRI) in healthy subjects.

Methods

Twelve volunteers (age 27 ± 3 years) underwent whole-heart 4D flow MRI twice in one session. In-scan consistency was evaluated by correlation between KE and EL. EL_{index} was computed to measure the amount of EL relative to KE over diastole. Scan–rescan analysis was performed to test reproducibility of volumetric measurements of KE, EL, EL_{index} and vorticity in the LV over early (E) and late (A) diastolic filling.

Results

In-scan consistency between KE and EL was strong–excellent (E-filling scan 1: $r = 0.92$, $P < 0.001$; scan 2: $\rho = 0.96$, $P < 0.001$ and A-filling scan 1: $\rho = 0.87$, $P < 0.001$; scan 2: $r = 0.99$, $P < 0.001$). For the majority of subjects (10 out of 12), KE and EL measures showed good to strong reproducibility. However, with a wide range of agreement [intraclass correlation (ICC): 0.64–0.95] and coefficients of variation (CV) $\leq 25\%$. EL_{index} showed strong reproducibility for all 12 subjects with a strong ICC (0.94, $P < 0.001$) and a CV of 9%. Scan rescan reproducibility of volumetric vorticity showed good–excellent ICCs (0.83–0.95) with CVs $\leq 11\%$.

Conclusion

The current study shows strong–excellent in-scan consistency and overall good agreement between scans for 4D flow MRI assessment of left ventricular kinetic energy, energy loss and vorticity over diastole. However, substantial differences between the scans were also found in some parameters in two out of twelve subjects. Strong reproducibility was found in the dimensionless EL_{index} , which measures the amount of viscous energy loss relative to the average kinetic energy over diastole.

Introduction

Congenital and acquired heart diseases affect the efficacy of intracardiac flow patterns and energy distribution [1,2]. Given the three-dimensional (3D) time-varying nature of these flow patterns and energetics, specialized *in vivo* imaging and analysis techniques are needed to evaluate volumetric changes in such complex hemodynamic parameters. Four-dimensional (4D) flow magnetic resonance imaging (MRI) allows for comprehensive non-invasive assessment of 3D time-varying blood flow properties in the heart and great vessels in all three velocity encoding directions and spatial dimensions over the cardiac cycle [3].

4D flow MRI has recently emerged as a novel tool for *in vivo* quantification of intracardiac flow energetics, associated energy losses and vortical flow patterns by means of kinetic energy (KE) [4–7], viscous energy loss (EL) [1] and vorticity [8, 9]. KE is the energy contained in the flow of the bloodstream due to motion and EL is the KE that is irreversibly lost due to viscosity-induced frictional forces within the blood flow [1]. In acquired heart disease, remodelling occurs which can lead to alterations in intracardiac hemodynamics [4]. Alteration in intraventricular KE derived from 4D flow MRI has been used to assess left ventricular (LV) and right ventricular (RV) (dys) function in patients with different stages of heart failure (HF) [4–7]. This is also the case in various congenital heart diseases. Even after correction, patients may develop systolic and/or diastolic dysfunction, leading to changes in intracardiac flow energetics [1]. In addition, intracardiac anatomy may not be restored. In corrected atrioventricular septal defect patients, elevated EL was associated with altered 3D vortex ring formation in the LV filling pattern [1]. Vorticity, the curl of velocity, is a fundamental quantity in fluid mechanics that describes the local spinning rate of fluid particles and can characterize vortex flow [10]. Quantitative vortex parameters, such as vorticity, have been used to assess diastolic (dys) function in several patient groups [8, 9, 11, 12]. Furthermore, in patients with complex congenital intracardiac deformations such as after the Fontan operation, flow collision with remaining septal structures and stagnation of flow through a ventricular septal defect may result in altered EL and vortex formation [13].

Recently, good reproducibility of inflow- and outflow assessment from 4D flow MRI was shown [14]. However, there is a lack of studies validating the reproducibility of intracardiac energy and quantitative vorticity parameters from 4D flow MRI in a scan–rescan setting. Scan–rescan reproducibility is important for clinical applicability as it expresses the reliability in repeated quantitation, for example during serial follow-up or in case of a rest–stress protocol. Therefore, the aim of this study was to assess the scan–rescan reproducibility

of 4D flow MRI measurements of kinetic energy, viscous energy loss and vorticity within the LV during diastolic filling in healthy subjects.

Methods

Study population

The study protocol was approved by the local Medical Ethical Committee of the Leiden University Medical Center and informed consent was obtained from all participants. Twelve healthy volunteers with no history of cardiac disease were included. All subjects underwent an MRI scan including whole-heart 4D flow MRI between July 2015 and April 2017. The same scanning protocol was performed twice in the same session with 10-min breaks between the scans and repositioning and replanning for every volunteer. Ten of these volunteers were included in a recent study [14]. That study did not report assessment of KE, EL or vorticity.

Cardiovascular magnetic resonance acquisition and data preparation

Whole-heart 4D flow MRI was obtained on a 3 T scanner (Ingenia, Philips Medical Systems, The Netherlands) with maximal amplitude of 45 mT/m for each axis, slew rate of 200 T/m/s and a combination of FlexCoverage Posterior coil in the table top with a dStream Torso coil, providing up to 32 coil elements for signal reception. The orientation of the acquisition of 4D flow data was identical to the 4-chamber orientation (usually double-oblique axial or coronal). Velocity-encoding of 150 cm/s in all three directions was used in a standard four-point encoding scheme, spatial resolution $3.0 \times 3.0 \times 3.0$ mm³, field-of-view 400 mm, flip angle 10°, echo time (TE) 3.7 ms, repetition time (TR) 10 ms, true temporal resolution 40 ms, SENSitivity Encoding (SENSE) factor 2 in anterior–posterior direction and Echo Planar Imaging (EPI) readout with a factor 5. Free breathing was allowed and no respiratory motion compensation was performed. Retrospective gating was used with 30 phases reconstructed to represent one cardiac cycle. Expected scan-time for the 4D flow MRI acquisition for a patient with a heart rate of 60 bpm and 39 slices would be 9 minutes and 11 seconds. This 4D flow MRI sequence with EPI readout has been validated *in vivo* and *in vitro* [15] and compared to other 4D flow MRI sequences [16]. Concomitant gradient correction was performed from standard available scanner software. Cine two-dimensional (2D) left 2-chamber, 4-chamber, coronal and sagittal aorta views and a cine multi-2D short-axis stack of slices were acquired, using steady-state free-precession (SSFP) sequences with TE/TR 1.5/3.0, 350 mm field-of-view, 45° flip angle, acquisition resolution $1.9 \times 2.0 \times 8.0$ mm³. Retrospective gating was used with 30 phases reconstructed to represent one cardiac cycle. Expected scan-time for the cine multi-2D short-axis acquisition for a patient with a heart rate

of 60 bpm and 12 slices would be 1 minute. Free breathing was allowed without using motion suppression, three signal averages were taken to minimize effects of breathing motion, which makes the expected scan-time 3 minutes. Image analysis was performed by one observer (VPK) with over 2 years of experience in MRI and verified by one observer (JJMW) with over 15 years of experience in MRI. The endocardial border was manually traced in all slices and phases in the multislice 2D cine short-axis images and ventricular volume was calculated at the end-diastolic and end-systolic phases using in-house developed *MASS* software. Papillary muscles were disregarded and assumed to be included in the ventricular volume. LV in- and outflow was assessed using the 4D flow MRI data with retrospective valve tracking of the mitral and aortic valve, as shown in a recent study [14]. Cardiac output (CO) was computed from the 4D flow data as LV outflow \times heart rate (HR). Beginning and ending of diastolic phases [early diastolic filling (E-filling) and late diastolic filling (A-filling)] were derived from the mitral valve flow-time curves that resulted from retrospective valve tracking. Segmentation of the LV cavity in the 4D flow MRI acquisition, that is required for the energy analysis, was obtained by transforming the available time-varying segmentation of multi-slice cine short-axis acquisition to the 4D flow MRI data. To correct for patient motion related misalignment between the two acquisitions, automated image-based 3D rigid registration was performed using the phase with optimal depiction of the LV cavity in both scans with the Elastix image registration toolbox [17]. Kinetic energy, viscous energy loss and vorticity analysis of segmented LV volumes was done by one investigator (MSME) using in-house developed software.

KE analysis over LV diastole

The amount of KE during diastolic filling was computed following previously published methods [1]. KE for each voxel within the LV was computed as $1/2 mv^2$, with (m) as the mass representing the voxel volume multiplied by the density of blood (1.025 g/mL) and (v) as the 3-directional velocity from 4D flow MRI. For each acquired time phase, volumetric KE was then computed by integrating (by cumulative sum) the computed KE over the segmented 3D LV volume. In order to quantify KE during diastolic filling, the time-averaged KE during diastolic phases (KE_{E-avg} and KE_{A-avg}) and peak KE (KE_{E-peak} and KE_{A-peak}), in Joule, were assessed.

Viscous EL analysis over LV diastole

Following recently published methods [1], we have computed EL from 4D flow MRI using the dissipation terms from the Navier–Stokes energy equations, assuming blood as a

Newtonian fluid. The formulae that were used to calculate EL are summarized in *Appendix 1*. The time-averaged viscous energy loss rate [$\dot{E}L$, in Watt (W)] during E-filling ($\dot{E}L_{E\text{-avg}}$) and A-filling ($\dot{E}L_{A\text{-avg}}$) and $\dot{E}L$ peaks ($\dot{E}L_{E\text{-peak}}$ and $\dot{E}L_{A\text{-peak}}$) were assessed. We have used the previously reported correlation between KE and $\dot{E}L$ [1] as a measure of in-scan consistency. Furthermore, EL over the total diastole ($EL_{\text{total diastole}}$) in Joule (J) was computed. Given that the amount of viscous energy lost is proportional to the amount of kinetic energy, we computed a dimensionless energy loss parameter, EL_{index} , that reflects the amount of viscous energy loss indexed for the average kinetic energy over diastole. EL_{index} is a dimensionless index that was used in an earlier echo particle image velocimetry study by Agati et al. [18] to indicate the relative amount of kinetic energy lost to that available over cardiac cycle. In this study, EL_{index} was computed over diastole as $EL_{\text{total diastole}}/KE_{\text{average diastole}}$, with $KE_{\text{average diastole}}$ being the average KE during total diastole. In order to compare our results with a previous study reporting EL values normalized by stroke volume (SV) [1], we also report EL values in the current study as normalized by SV (reported as $\text{norm_}\dot{E}L_{E\text{-avg}}$, $\text{norm_}\dot{E}L_{E\text{-peak}}$, $\text{norm_}\dot{E}L_{A\text{-avg}}$, $\text{norm_}\dot{E}L_{A\text{-peak}}$ and $\text{norm_}EL_{\text{total diastole}}$). To be consistent with the previous study SV was derived from cine SSFP short-axis slices.

Integral vorticity magnitude over LV diastole (vorticity_LV)

The formulae that were used to calculate the integral vorticity magnitude are shown in *Appendix 1*. In short, following previously published work [8, 9], for each acquired time-phase, voxel-wise vorticity magnitude (1/s) was first computed over the segmented LV volume. Then, the instantaneous integral vorticity magnitude was computed as the cumulative sum of voxel-wise vorticity and multiplied by voxel volume to give the integral in (milliliter \times 1/second) i.e. (mL/s). Note that the computed vorticity integral parameter is a scalar quantity and therefore does not take the vorticity direction into account. We will refer to this vorticity integral over the LV as vorticity_LV throughout the text, to differentiate it from voxel-wise vorticity. In order to quantify the integral vorticity_LV over diastolic filling, the time-average and peak vorticity_LV during E-filling ($\text{vorticity_LV}_{E\text{-avg}}$, $\text{vorticity_LV}_{E\text{-peak}}$, respectively) and A-filling ($\text{vorticity_LV}_{A\text{-avg}}$, $\text{vorticity_LV}_{A\text{-peak}}$, respectively) were computed.

Scan-rescan analysis

For the scan-rescan analysis, all data was blinded by one observer (VPK) and presented in a random order to the observer (MSME) that performed the energy and vorticity analysis. Scan-rescan analysis was performed to test the reproducibility of (1) KE over E-filling and

A-filling; (2) EL over E-filling, A-filling and total diastolic filling and (3) vorticity_LV over E-filling and A-filling.

Statistical analysis

Data analysis was performed using SPSS Statistics software (v. 23.0 IBM SPSS, Chicago, IL). Variables were tested for normal distribution using the Shapiro–Wilk test. Continuous data was expressed as mean \pm standard deviation (SD) with minimum and maximum values or as median [interquartile range] where suitable. Mean differences were determined for inter-scan comparison and significance was tested by a paired samples *t* test or, in case of non-normality, the Wilcoxon signed-rank test. Differences were computed as: measurement in scan 2—measurement in scan 1. The coefficient of variation (CV) was calculated with the root mean square method [19]. Correlation between the in-scan and inter-scan measurements done in repeated scans was tested by the Pearson correlation coefficient (*r*), or the Spearman correlation coefficient (ρ) in case of non-normality of the data. The approach described by Bland and Altman [20] was used to study systematic differences between measurements obtained from the two scans. Agreement between these measurements was assessed by determining the intra-class correlation (ICC) coefficient. Correlation and agreement were classified as follows: *r*/ ρ and ICC > 0.95: excellent, 0.95–0.85: strong, 0.85–0.70: good, 0.70–0.5: moderate, < 0.5: poor. A *P* value < 0.05 was considered statistically significant.

Results

Volunteer characteristics are shown in *Table 1*. Heart rate and cardiac output were not significantly different between the two scans (HR: 60.8 ± 7.8 vs. 59.9 ± 6.9 bpm, *P* = 0.52 and CO: 5.5 ± 0.9 vs. 5.6 ± 1.3 L/min, *P* = 0.75). 4D flow MRI data acquisition was successful in all volunteers. *Figure 1a–c* shows cross-sectional mapping of the volumetric measurements of KE, EL and vorticity inside the LV at peak E-filling in a standard 4-chambers view. An example of the temporal evolution of KE and EL over LV diastole is shown in one subject in *Figure 1d*.

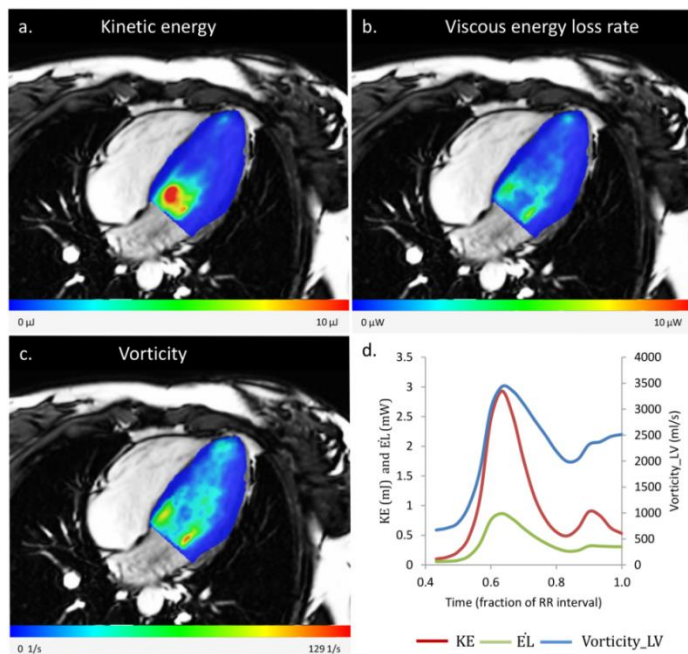


Figure 1. Maps of left ventricular kinetic energy (KE), viscous energy loss rate (\dot{E}_L) and vorticity over the LV of a healthy female subject (age 20 years) in a standard four-chambers MRI cross-sectional view. **(a)** left ventricular kinetic energy at peak early diastolic filling, **(b)** left ventricular viscous energy loss rate at peak early diastolic filling, **(c)** left ventricular voxel-wise vorticity at peak early diastolic filling, **(d)** temporal evolution of volumetric kinetic energy, viscous energy loss rate and vorticity over LV diastole

Table 1. Baseline characteristics

Scan-independent characteristics			
N	12		
Male (%)	6/12 (50%)		
Age (years)	27 ± 3		
Height (cm)	175 ± 7		
Weight (kg)	69 ± 12		
BSA (m²)	1.8 ± 0.2		
BMI (kg/m²)	22 ± 3		
Characteristics per scan			
	Scan 1	Scan 2	<i>P</i> -value
HR (bpm)	60.8 ± 7.8	59.9 ± 6.9	0.52
End-diastolic volume (mL)	143.8 [132.4-183.8]	158.6 ± 30.3	0.64
End-systolic volume (mL)	64.4 ± 16.9	56.2 ± 12.9	0.15
Stroke volume (mL)	100.8 ± 21.8	102.4 ± 21.0	0.44
Ejection fraction (%)	62.8 ± 3.6	63.0 [61.6-65.4]	0.22
CO (l/min)	5.5 ± 0.9	5.6 ± 1.3	0.75

Abbreviations: bpm: beat per minute, BMI = Body Mass Index, BSA = Body surface area, CO = cardiac output, HR = Heart rate, LV = left ventricular

Intra-scan comparison of energetics (KE vs. $\dot{E}L$)

Figure 2 shows the in-scan comparison of KE versus EL. Comparison of KE_{E-avg} to $\dot{E}L_{E-avg}$ showed strong–excellent correlation (scan 1: $r = 0.92$, $P < 0.001$; scan 2: $\rho = 0.96$, $P < 0.001$). Also, correlation between KE_{A-avg} and $\dot{E}L_{A-avg}$ was strong–excellent in both scans (scan 1: $\rho = 0.87$, $P < 0.001$; scan 2: $r = 0.99$, $P < 0.001$).

Scan–rescan analysis of kinetic energy and viscous energy loss rate over early diastolic filling

Detailed results of the scan–rescan tests of KE and EL assessment over early diastolic filling are shown in Tables 2 and 3 and Figure 3. Scan–rescan assessment showed poor results for early diastolic filling, as shown in Table 2. Of note, Figure 3 shows that for KE and $\dot{E}L$ assessment over early diastolic filling two subjects showed more distinct differences. Throughout the text we will refer to these two subjects as “Subject 1” and “Subject 2”. Detailed scan–rescan information of these two subjects is provided in Appendix 2. In Figure 3a, Subject 1 and 2 are indicated as dark (KE_{E-avg}) and light red triangles (KE_{E-peak}) and in Figure 3b, as dark ($\dot{E}L_{E-avg}$) and light red triangles ($\dot{E}L_{E-peak}$). Possibly some factors related to the 4D flow MRI acquisition or physiological factors have resulted in these marked differences, therefore we performed an evaluation for a subcohort without Subject 1 and 2. Scan–rescan correlations were much stronger and variation was less for this sub-cohort, as shown in Table 3. KE_{E-avg} and $\dot{E}L_{E-avg}$ assessment showed non-significant differences between the two scans, strong ICCs (KE_{E-avg} : 0.95, $P < 0.001$ and $\dot{E}L_{E-avg}$: 0.91, $P = 0.03$) and CVs $\leq 11\%$ (KE_{E-avg} : 10% and $\dot{E}L_{E-avg}$: 11%). $norm_ \dot{E}L_{E-avg}$ showed a strong ICC (0.90, $P = 0.001$) and a CV of 12%. Scan–rescan assessment of KE_{E-peak} and $\dot{E}L_{E-peak}$ showed nonsignificant differences. The ICC of KE_{E-peak} was good (0.82, $P = 0.01$) with a CV of 15%. Similarly the ICC of $\dot{E}L_{E-peak}$ was good (0.76, $P = 0.03$) with a CV of 17%. Furthermore, $norm_ \dot{E}L_{E-peak}$ showed a strong ICC (0.86, $P = 0.005$) and a CV of 16%.

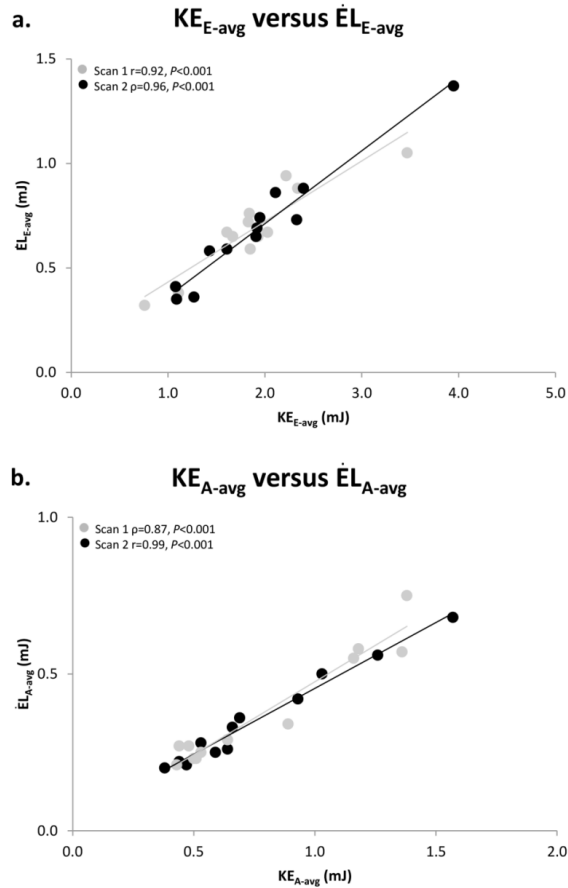


Figure 2. Scatter plots of kinetic energy (KE) versus viscous energy loss rate ($\dot{E}L$) during early diastolic filling and KE versus $\dot{E}L$ during late diastolic filling. a) scatter plot depicting the correlation between KE_{E-avg} and $\dot{E}L_{E-avg}$ measured in scan 1 (grey) and scan 2 (black), in all 12 subjects, b) scatter plot depicting the correlation between KE_{A-avg} and $\dot{E}L_{A-avg}$ measured in scan 1 (grey) and scan 2 (black), in all 12 subjects.

Scan–rescan analysis of kinetic energy and viscous energy loss rate over late diastolic filling

Detailed results of the scan–rescan tests of KE and $\dot{E}L$ assessment over late diastolic filling are shown in *Tables 2 and 3* and *Figure 3*. Scan–rescan assessment showed good results for late diastolic filling, as shown in *Table 2*. Subject 1 and 2 are now within the same range as the other values [*Figure 3c*, indicated as dark (KE_{A-avg}) or light red triangles (KE_{A-peak})]. The same was observed when assessing $\dot{E}L_{A-avg}$ and $\dot{E}L_{A-peak}$ [*Fig. 3d*, indicated as dark ($\dot{E}L_{A-avg}$) or light red triangles ($\dot{E}L_{A-peak}$)]. However, to be consistent we repeated the evaluation in the sub-cohort without Subject 1 and Subject 2. Scan–rescan correlations and variation were

similar for the sub-cohort without Subject 1 and Subject 2, as shown in *Table 3*. Reproducibility of KE_{A-avg} and $\dot{E}L_{A-avg}$ assessment showed non-significant differences, good ICCs (KE_{A-avg} : 0.77, $P = 0.02$ and $\dot{E}L_{A-avg}$: 0.75, $P = 0.03$) and CVs up to 24% (KE_{A-avg} : 23% and $\dot{E}L_{A-avg}$: 24%). $norm_E\dot{L}_{A-avg}$ showed a non-significant difference between the scans, a good ICC (0.70, $P = 0.048$) and a CV of 22%. Scan–rescan assessment of KE_{A-peak} and $\dot{E}L_{A-peak}$ showed non-significant differences, good ICCs (KE_{A-peak} : 0.83, $P = 0.01$ and $\dot{E}L_{A-peak}$: 0.79, $P = 0.02$) and CVs up to 25% (KE_{A-peak} : 23% and $\dot{E}L_{A-peak}$: 25%). Lastly, scan–rescan assessment of $norm_E\dot{L}_{A-peak}$ showed a non-significant difference between the scans, a moderate ICC (0.64, $P = 0.08$) and a CV of 24%.

Scan–rescan analysis of kinetic energy and viscous energy loss over total diastole

Detailed results of the scan–rescan tests of KE and EL assessment over total diastole ($EL_{total\ diastole}$ and $norm_EL_{total\ diastole}$) and EL_{index} are shown in *Tables 2* and *3* and *Fig. 3*. Scan–rescan assessment showed poor results for total diastole, but strong results for EL_{index} , as shown in *Table 2*. Scan–rescan correlations were much stronger and variation was less for the sub-cohort without Subject 1 and Subject 2 (*Table 3*). Scan–rescan assessment of $EL_{total\ diastole}$ showed a non-significant difference between the scans, a strong ICC of 0.91 ($P = 0.001$) and a CV of 11%. $norm_EL_{total\ diastole}$ showed a non-significant difference between the scans, a good ICC (0.81, $P = 0.01$) and a CV of 12%. *Figure 3f* shows the Bland–Altman plot of EL_{index} . For all subjects, scan–rescan assessment of EL_{index} showed excellent reproducibility with a small non-significant difference between the scans, a strong ICC of 0.94 ($P < 0.001$) and a CV of 9%. When evaluating the sub-cohort without Subject 1 and 2 the results remained similar (ICC: 0.95, $P < 0.001$ and CV: 8%).

Table 2. Scan-rescan comparison of energy variables for the cohort with all subjects (N=12)

	Scan 1	Scan 2	Difference (scan 2 – scan 1)	Pearson r	ICC	CV(%)
	Mean ± SD (min -max) or median [IQR] (min-max)	Mean ± SD (min -max) or median [IQR] (min-max)	Mean ± SD (min -max) or median [IQR] (min-max)		ICC (95% C.I.)	
Early filling						
KE _{E-peak} (mJ)	4.9 ± 1.9 (2.6-9.6)	4.8 ± 1.4 (2.0-7.6)	0.1 ± 2.3 (-4.8-5.0)	0.06	0.12 (-2.8-0.8)	28
KE _{E-avg} (mJ)	1.9 ± 0.7 (0.8-3.5)	1.9 [1.3-2.3] (1.1-4.0) ^c	-0.01 [-0.1-0.3] (-2.2-2.1) ^c	0.52	0.31 (-1.8-0.8)	26
EL _{E-peak} (mW)	1.5 ± 0.4 (0.8-2.1)	1.5 ± 0.6 (0.7-2.9)	0.04 ± 0.7 (-1.4-1.7)	0.02	0.04 (-3.2-0.7)	31
norm_ EL _{E-peak} (W/m ³)	15.2 ± 5.1 (9.4-24.9)	14.9 ± 5.1 (6.0-21.8)	-0.2 ± 6.2 (-12.6-12.3)	0.27	0.45 (-1.2-0.85)	30
EL _{E-avg} (mW)	0.7 ± 0.2 (0.3-1.1)	0.7 ± 0.3 (0.4-1.4)	-0.01 [-0.1-0.3] (-0.7-0.8) ^c	0.11	0.21 (-2.4-0.8)	28
norm_ EL _{E-avg} (W/m ³)	7.0 ± 2.3 (4.2-11.4)	6.6 ± 2.1 (3.2-10.4)	-0.4 ± 2.8 (-6.4-5.8)	0.20	0.35 (-1.6-0.8)	28
Late filling						
KE _{A-peak} (mJ)	0.9 [0.7-2.0] (0.7-2.5) ^c	1.0 [0.9-1.6] (0.6-2.6) ^c	0.1 [-0.15-0.26] (-1.2-0.5) ^c	0.62 ^b	0.87 (0.55-0.96) ^b	23
KE _{A-avg} (mJ)	0.6 [0.5-1.2] (0.4-1.4) ^c	0.8 ± 0.4 (0.4-1.6)	-0.03 ± 0.3 (-0.7-0.4)	0.68 ^b	0.84 (0.42-0.95) ^b	23
EL _{A-peak} (mW)	0.5 ± 0.3 (0.3-1.1)	0.5 ± 0.2 (0.3-1.0)	-0.007 ± 0.2 (0.0-0.5-0.3)	0.67 ^b	0.81 (0.33-0.95) ^b	24
norm_ EL _{A-peak} (W/m ³)	5.3 ± 1.8 (2.5-8.3)	5.1 ± 1.5 (3.3-7.9)	-0.2 ± 1.7 (-3.2-2.2)	0.50	0.68 (-0.19-0.91) ^b	22
EL _{A-avg} (mW)	0.3 [0.2-0.6] (0.2-0.7) ^c	0.4 ± 0.2 (0.2-0.8)	-0.02 ± 0.1 (-0.4-0.2)	0.50	0.80 (0.29-0.94) ^b	23
norm_ EL _{A-avg} (W/m ³)	3.7 ± 1.3 (2.1-6.6)	3.4 ± 1.1 (2.2-5.2)	-0.3 ± 1.1 (-2.8-1.5)	0.58 ^b	0.73 (0.07-0.92) ^b	21
Total diastole						
EL _{total diastole} (mJ)	0.5 ± 0.2 (0.3-1.0)	0.5 [0.4-0.6] (0.3-1.3) ^c	-0.006 [-0.07-0.06] (-0.4-0.7) ^c	0.81 ^b	0.58 (-0.60-0.88)	22
norm_ EL _{total diastole} (J/m ³)	5.3 ± 1.5 (3.4-8.1)	4.8 [4.2-5.3] (3.1-9.8) ^c	-0.1 ± 2.2 (-3.9-5.3)	0.30	0.17 (-2.5-0.77)	23
EL _{index}	0.3 ± 0.07 (0.2-0.4)	0.3 ± 0.06 (0.2-0.4)	-0.0008 ± 0.03 (-0.04-0.06)	0.89 ^a	0.94 (0.80-0.98) ^a	9

^a P<0.001, ^b P<0.05, ^c P<0.05 for non-normality (Shapiro-Wilk test).

Abbreviations: KE= kinetic energy, E=early diastolic filling, A=late diastolic filling, EL=viscous energy loss

Table 3. Scan-rescan comparison of energy variables for the sub-cohort without Subject 1 and 2 (N=10)

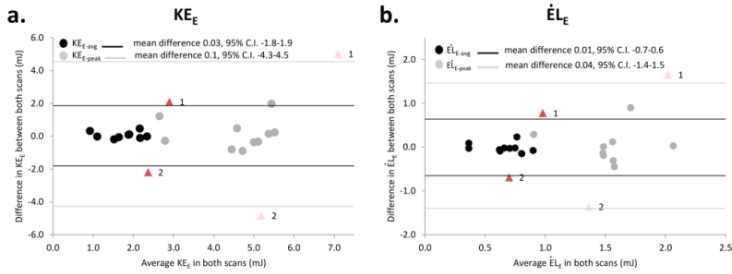
	Scan 1	Scan 2	Difference (scan 2 – scan 1)	Pearson r	ICC	CV(%)
	Mean ± SD (min -max) or median [IQR] (min-max)	Mean ± SD (min -max) or median [IQR] (min-max)	Mean ± SD (min -max) or median [IQR] (min-max)		ICC (95% C.I.)	
Early filling						
KE _{E-peak} (mJ)	5.0 [4.0-5.3] (2.0-5.4) ^c	4.6 ± 1.1 (2.6-6.4)	0.1 ± 0.9 (-0.9-2.0)	0.62	0.82 (0.27-0.96) ^b	14
KE _{E-avg} (mJ)	1.7 ± 0.5 (0.8-2.3)	1.8 ± 0.5 (1.1-2.4)	0.05 ± 0.2 (-0.2-0.5)	0.91 ^a	0.95 (0.82-0.99) ^a	9
EL _{E-peak} (mW)	1.5 ± 0.4 (0.8-2.1)	1.5 ± 0.4 (0.7-2.2)	0.01 ± 0.4 (-0.5-0.9)	0.58	0.76 (-0.07-0.94) ^b	15
norm_ EL _{E-peak} (W/m ³)	15.4 ± 5.2 (9.6-24.9)	15.2 ± 4.2 (8.9 -21.8)	-0.3 ± 3.5 (-4.7-6.9)	0.75 ^b	0.86 (0.40-0.97) ^b	14
EL _{E-avg} (mW)	0.7 ± 0.2 (0.3-0.9)	0.6 ± 0.2 (0.4-0.9)	-0.02 ± 0.1 (-0.2-0.2)	0.83 ^b	0.91 (0.64-0.98) ^b	10
norm_ EL _{E-avg} (W/m ³)	7.0 ± 2.3 (4.2-11.4)	6.6 ± 1.6 (4.2-9.0)	-0.4 ± 1.2 (-2.4-1.6)	0.87 ^b	0.90 (0.60-0.97) ^b	11
Late filling						
KE _{A-peak} (mJ)	0.9 [0.7-1.7] (0.7-2.5) ^c	1.2 ± 0.5 (0.6-2.4)	0.2 [-0.1-0.3] (-1.2-0.5) ^e	0.59	0.83 (0.25-0.96) ^b	21
KE _{A-avg} (mJ)	0.5 [0.5-1.2] (0.4-1.4) ^c	0.7 ± 0.3 (0.4-1.3)	-0.02 ± 0.3 (-0.7-0.4)	0.65 ^b	0.77 (0.02-0.94) ^b	21
EL _{A-peak} (mW)	0.4 [0.3-0.7] (0.3-1.1) ^c	0.5 ± 0.2 (0.3-0.9)	-0.03 ± 0.2 (-0.5-0.3)	0.50	0.79 (0.11-0.95) ^b	23
norm_ EL _{A-peak} (W/m ³)	5.3 ± 2.0 (2.5-8.3)	5.0 ± 1.3 (3.3-7.0)	-0.3 ± 1.7 (-3.2-2.2)	0.49	0.64 (-0.56-0.91)	21
EL _{A-avg} (mW)	0.3 [0.2-0.6] (0.2-0.8) ^c	0.3 ± 0.1 (0.2-0.6)	-0.03 ± 0.1 (-0.4-0.2)	0.42	0.75 (-0.05-0.94) ^b	21
norm_ EL _{A-avg} (W/m ³)	3.6 ± 1.4 (2.1-6.6)	3.4 ± 1.0 (2.3-5.2)	-0.3 ± 1.2 (-2.8-1.5)	0.57	0.70 (-0.21-0.93) ^b	20
Total diastole						
EL _{total diastole} (mJ)	0.5 ± 0.2 (0.3-1.0)	0.5 ± 0.1 (0.3-0.7)	-0.01 [-0.05-0.03] (-0.3-0.08) ^c	0.88 ^b	0.91 (0.64-0.98) ^b	10
norm_ EL _{total diastole} (J/m ³)	5.1 ± 1.3 (3.4-7.0)	4.8 ± 0.9 (3.1-6.4)	-0.3 ± 0.9 (-2.0-1.2)	0.73 ^b	0.81 (0.27-0.95) ^b	11
EL _{index}	0.3 ± 0.06 (0.2-0.4)	0.3 ± 0.07 (0.2-0.4)	-0.01 ± 0.03 (-0.04-0.06)	0.89 ^a	0.95 (0.79-0.99) ^a	8

* Subjects with measurements outside the 95% confidence interval of the respective Bland-Altman plots

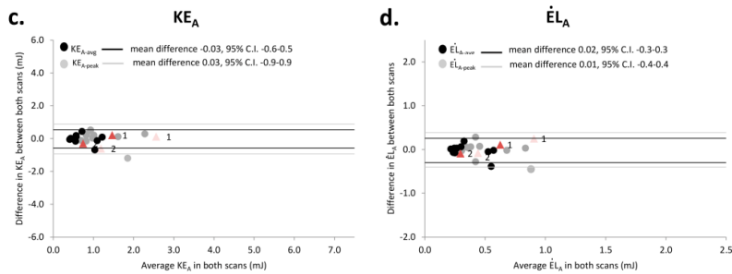
^a P<0.001, ^b P<0.05, ^c P<0.05 for non-normality (Shapiro-Wilk test).

Abbreviations: KE= kinetic energy, E=early diastolic filling, A=late diastolic filling, EL=viscous energy loss.

KE and EL over early diastolic filling



KE and EL over late diastolic filling



EL over total diastole and EL index

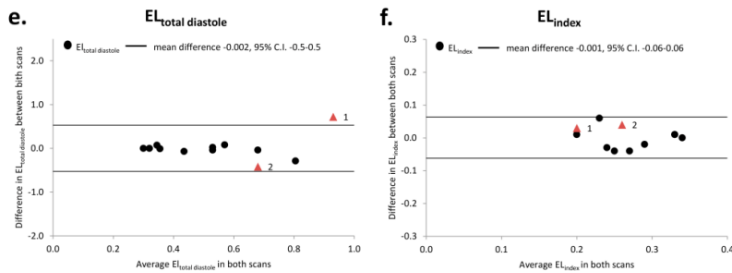


Figure 3. Bland-Altman plots of kinetic energy (KE) and viscous energy loss rate (EL) at peak early diastolic filling (KE_{E-peak} and EL_{E-peak}) and peak late diastolic filling (KE_{A-peak} and EL_{A-peak}) and EL_{index} . (a) Bland-Altman plot depicting the agreement between KE_{E-avg} (black) and KE_{E-peak} (grey) in scan 1 and scan 2. The subjects with distinct higher differences between scan and rescan measurements (Subject 1 and 2) are depicted as red triangles (KE_{E-avg} dark red; KE_{E-peak} light red). (b) Bland-Altman plot depicting the agreement between EL_{E-avg} (black) and EL_{E-peak} (grey) in scan 1 and scan 2. Subject 1 and 2 are depicted as red triangles (KE_{E-avg} dark red; KE_{E-peak} light red). (c) Bland-Altman plot depicting the agreement between KE_{A-avg} (black) and KE_{A-peak} (grey) in scan 1 and scan 2. Subject 1 and 2 are depicted as red triangles (KE_{A-avg} dark red; KE_{A-peak} light red). (d) Bland-Altman plot depicting the agreement between EL_{A-avg} (black) and EL_{A-peak} (grey) in scan 1 and scan 2. Subject 1 and 2 are depicted as red triangles (EL_{A-avg} dark red; EL_{A-peak} light red). (e) Bland-Altman plot depicting the agreement between $EL_{total\ diastole}$ in scan 1 and scan 2. Subject 1 and 2 are depicted as red triangles. (f) Bland-Altman plot

Scan–rescan analysis of volumetric vorticity_LV over early diastolic filling

Detailed results of the scan–rescan tests of vorticity_LV assessment over early diastolic filling are shown in *Tables 4* and *5* and *Figure 4*. Scan–rescan assessment showed moderate results for early diastolic filling as shown in *Table 4*. The Bland–Altman plots of the assessment of vorticity_LV_{E-avg} and vorticity_LV_{E-peak} showed higher differences between scan and rescan measurements for Subject 1 and 2 (*Figure 4a*, indicated as dark (vorticity_LV_{E-avg}) or light red triangles (vorticity_LV_{E-peak})). Scan–rescan correlations were much stronger and variation was less for the sub-cohort without Subject 1 and 2 (*Table 5*). Scan–rescan assessment of vorticity_LV_{E-peak} and vorticity_LV_{E-avg} showed a non-significant difference between the scans, good-strong ICCs (vorticity_LV_{E-peak}: 0.83, $P = 0.01$ and vorticity_LV_{E-avg}: 0.95, $P < 0.001$) and CVs up to 11% (vorticity_LV_{E-peak}: 11% and vorticity_LV_{E-avg}: 7%).

Scan–rescan analysis of volumetric vorticity_LV over late diastolic filling

Detailed results of the scan–rescan tests of vorticity_LV assessment over late diastolic filling are shown in *Tables 4* and *5* and *Figure 4*. Scan–rescan assessment showed good results for late diastolic filling as shown in *Table 4*. Subject 1 and 2 are now within the same range as the other values (*Figure 4b*, indicated as dark (vorticity_LV_{A-avg}) and light red triangles (vorticity_LV_{A-peak})). Scan–rescan variation was similar for the sub-cohort without Subject 1 and 2 (*Table 5*). Scan–rescan assessment of vorticity_LV_{A-peak} and vorticity_LV_{A-avg} showed non-significant differences between the scans, good-strong ICCs (vorticity_LV_{A-peak}: 0.91, $P = 0.001$ and vorticity_LV_{A-avg}: 0.89, $P = 0.002$) and CVs of 11%.

Table 4. Scan-rescan comparison of vortex flow variables for the cohort with all subjects (N=12)

	Scan 1	Scan 2	Difference (scan 2 – scan 1)	Pearson correlation coefficient	Intraclass correlation coefficient	Coefficient of variation (%)
	Mean ± SD (min - max) or median [IQR] (min-max)	Mean ± SD (min - max) or median [IQR] (min-max)	Mean ± SD (min -max) or median [IQR] (min-max)		ICC (95% C.I.)	
Early filling						
Vorticity_LV _{E-peak} (ml/s)	4671 ± 992 (2950-6370)	4551 ± 1043 (2930-6200)	-120 ± 1075 (-239-1710)	0.44	0.63 (-0.37-0.90)	15
Vorticity_LV _{E-avg} (ml/s)	2862 ± 636 (1720-3840)	2788 ± 671 (1810-3930)	-74 ± 608 (-1510-1060)	0.57	0.74 (0.06-0.93) ^b	13
Late filling						
Vorticity_LV _{A-peak} (ml/s)	2715 [2502-4142] (2176-5463) ^c	3193 ± 945 (2174-4914)	-10 ± 547 (-1270-840)	0.75 ^b	0.92 (0.73-0.98) ^a	11
Vorticity_LV _{A-avg} (ml/s)	2660 ± 842 (1740-4180)	2599 ± 766 (1730-4050)	-61 ± 484 (-1270-740)	0.82 ^b	0.91 (0.68-0.97) ^a	11

* Subjects with measurements outside the 95% confidence interval of the respective Bland-Altman plots

^a $P < 0.001$, ^b $P < 0.05$, ^c $P < 0.05$ for non-normality (Shapiro-Wilk test). Abbreviations: E=early diastolic filling, A=late diastolic filling

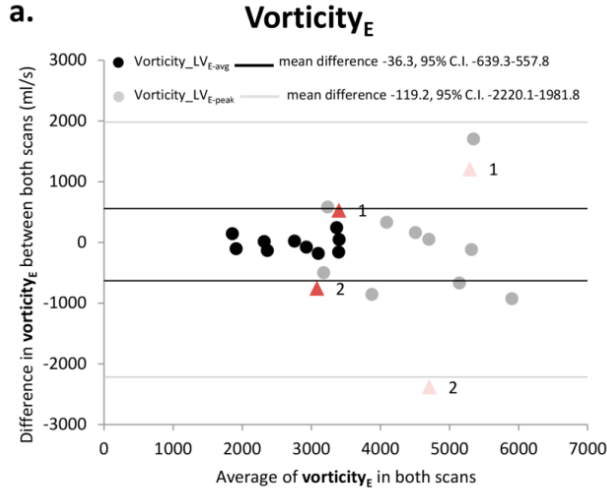
Table 5. Scan-rescan comparison of vortex flow variables for the sub-cohort without Subject 1 and 2 (N=10)

	Scan 1	Scan 2	Difference (scan 2 – scan 1)	Pearson correlation coefficient	Intraclass correlation coefficient	Coefficient of variation (%)
	Mean \pm SD (min -max) or median [IQR] (min-max)	Mean \pm SD (min -max) or median [IQR] (min-max)	Mean \pm SD (min -max) or median [IQR] (min-max)		ICC (95% C.I.)	
Early filling						
Vorticity_LV _{E-peak} (ml/s)	4546 \pm 1008 (2950-6370)	4520 \pm 1004 (2930-6200)	-27 \pm 796 (-940-1710)	0.69 ^b	0.83 (0.27-0.96) ^b	11
Vorticity_LV _{E-avg} (ml/s)	2764 \pm 614 (1720-3560)	2720 \pm 613 (1810-3610)	-44 \pm 277 (-380-480)	0.90 ^a	0.95 (0.80-0.99) ^a	7
Late filling						
Vorticity_LV _{A-peak} (ml/s)	2563 [2468-3628] (2176-5463) ^c	3012 \pm 852 (2174-4586)	-69 \pm 575 (-1270-840)	0.64 ^b	0.91 (0.64-0.98) ^b	11
Vorticity_LV _{A-avg} (ml/s)	2269 [1889-3251] (1740-4180) ^c	2465 \pm 679 (1730-3730)	-75 \pm 511 (-1270-740)	0.82 ^b	0.89 (0.53-0.97) ^b	11

* Subjects with measurements outside the 95% confidence interval of the respective Bland-Altman plots

^a $P < 0.001$, ^b $P < 0.05$, ^c $P < 0.05$ for non-normality (Shapiro-Wilk test). Abbreviations: E=early diastolic filling, A=late diastolic filling

Vorticity over early diastolic filling



Vorticity over late diastolic filling

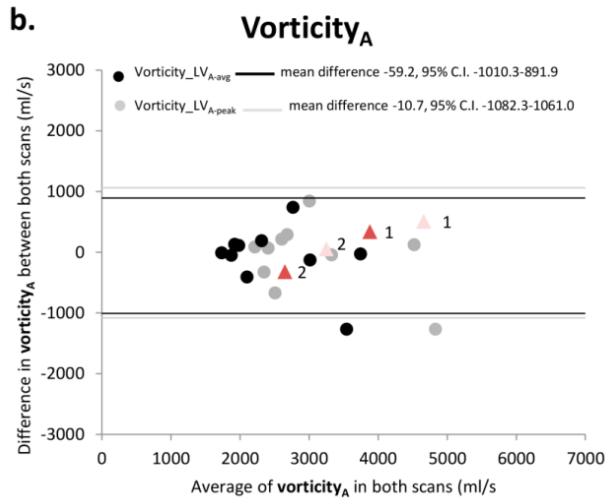


Figure 4. Bland-Altman plots of volumetric vorticity over peak early filling (vorticity_LV_{E-avg} and vorticity_LV_{E-peak}) and late filling (vorticity_LV_{A-avg} and vorticity_LV_{A-peak}). (a) Bland-Altman plot depicting the agreement between vorticity_LV_{E-avg} (black) and vorticity_LV_{E-peak} (grey) in scan 1 and scan 2. Subject 1 and 2 are depicted as red triangles (vorticity_LV_{E-avg} dark red; vorticity_LV_{E-peak} light red). (b) Bland-Altman plot depicting the agreement vorticity_LV_{A-avg} (black) and vorticity_LV_{A-peak} (grey) in scan 1 and scan 2. Subject 1 and 2 are depicted as red triangles (vorticity_LV_{A-avg} dark red; vorticity_LV_{A-peak} light red)

Discussion

In the current study, kinetic energy, viscous energy loss and vorticity inside the left ventricle during diastole are derived from 4D flow MRI and scan–rescan reproducibility of these parameters is tested. Scan–rescan reproducibility is essential for the clinical application of a parameter since it reflects the reliability of a measurement and feasibility of repeated measurement evaluations. The main findings of this study are: (1) internal consistency between kinetic energy and viscous energy loss is strong-excellent in both scans during early and late diastolic filling; (2) In the majority (10 out of 12) of subjects, reproducibility of peak and average kinetic energy and viscous energy loss during early, late and total diastolic filling shows non-significant differences with a good to excellent agreement (by means of ICC) and CVs up to 25%; (3) In the studied parameters, time-averaged measurements over E- and A-filling show stronger reproducibility than peak measurements. (4) For all subjects, EL_{index} shows good reproducibility with a small non-significant difference between the scans, strong agreement and a CV of 9%; (5) Assessment of volumetric vorticity over the left ventricle during early and late diastolic filling shows non-significant differences, good–excellent ICCs and CVs up to 11%.

In the Bland–Altman plots for E-filling parameters, measurements obtained in two subjects (Subject 1 and 2 in *Appendix 2*) showed distinct higher differences between scan and rescan measurements than the measurements of the majority of the cohort. These high differences had an impact on the scan–rescan reproducibility for KE and EL measures. This impact seemed to be largest during early diastolic filling, where reproducibility was much higher for the sub-cohort without Subject 1 and 2. However, during late diastolic filling, reproducibility was similar. There is no obvious explanation for the measurements that showed distinct higher differences between scan and rescan measurement, but this could be related to the technical restrictions of the 4D flow MRI acquisition or to physiological differences between scans, or a combination of both. It is to be expected that physiological differences were small as all subjects are healthy volunteers that were scanned twice under the same circumstances with only a short break between the scans (± 10 min) and heart rate was not significantly different between both scans. Still, subtle physiological differences could result in poor scan–rescan reproducibility for these few cases. *Table A1* in *Appendix 2* shows the HR, LV outflow and CO of all subjects. Subject 1 and 2 present the highest CO differences, however there are other subjects with CO differences within the same range. *Table A2* in *Appendix 2* shows subject specific scan–rescan information from the mitral valve flow curves. Subject 1 and 2 have the highest difference in area under the curve of the E-filling and peak filling rate of the E-filling. This could indicate that differences may be related to technical restrictions of the

acquisition, as the E-filling duration, E peak filling rate and the area-under-the-curve are sensitive to temporal and spatial resolution. These observations are important to take into consideration when evaluating flow energetics and vorticity in a research or clinical setting.

Kinetic energy (KE) over LV diastole

Multiple 4D flow MRI studies showed that patients with LV dysfunction present altered flow patterns through the LV with impaired preservation of inflow KE to the end of diastole and altered KE-time curves (the amount of KE inside the LV during each time step over the total cardiac cycle) [4, 6, 7, 21], even in patients with normal to mild LV remodeling and normal to mildly depressed LV systolic function [7]. These KE changes in the LV could be a valuable diagnostic marker to evaluate diastolic function and might be useful for early detection of deteriorating ventricular function [1, 4–7, 21, 22], which could reduce patient morbidity and mortality [23]. However, there is a lack of studies validating LV KE derived from 4D flow MRI in a scan–rescan setting. Therefore, reliability and reproducibility of KE measurements from 4D flow MRI in a repeated scan setting remains largely unknown. Kanski et al. [24] compared mean KE and peak KE between two scans (with and without respiratory gating) with the aim to evaluate the impact of respiratory gating on KE measurements. They found a strong correlation between the KE measurements in both scans. The current study differs from the study by Kanski et al. [24] in that we used the same protocol for both scans. In the current study, moderate–strong correlation was found between KE measurements in both scans. Absolute values of $KE_{E\text{-peak}}$ and $KE_{A\text{-peak}}$ reported in the current study are in agreement with previous studies [1, 25, 26].

In the current study we showed the reproducibility of the KE measurements assessed with 4D flow MRI with good–strong agreement (by means of ICCs), however substantial CVs up to 23% were also found. Based on the Bland–Altman analysis the variability of $KE_{E\text{-avg}}$ and $KE_{A\text{-avg}}$ was less than the variability of $KE_{E\text{-peak}}$ and $KE_{A\text{-peak}}$ as shown by the smaller limits of agreement. This might be expected, given that the definition of average is computed over multiple time points and therefore evens out the variations more than a single-time measure such as the peak, especially when the definition of the peak also is affected by the temporal resolution of the 4D flow MRI data.

The assessment of intracardiac EL could provide crucial details on the function of the heart apart from the standard MRI parameters and could be used to further unravel the influence of complex surgery for congenital heart defects [1]. To our knowledge, this is the first study assessing scan–rescan reproducibility of in vivo LV EL over diastole assessed by 4D flow MRI. Results of $\text{norm_}\dot{E}_{L-E-\text{peak}}$ in the current study correspond well with that of a different healthy controls cohort of a recent 4D flow MRI study by Elbaz et al. [1]. Also $\text{norm_}\dot{E}_{L-E-\text{avg}}$ values are consistent. Furthermore, both results of $\text{norm_}\dot{E}_{L-A-\text{peak}}$, as well as $\text{norm_}\dot{E}_{L-A-\text{avg}}$ are similar to previously reported numbers [1]. Both $\text{EL}_{\text{total diastole}}$ and $\text{norm_EL}_{\text{total diastole}}$ are slightly higher in our study than in the study by Elbaz et al. [1]. However, results remain in the same range. These differences in results could be explained in part by differences in heart rate between the volunteers of this study and those of the previous study. This is because the total viscous energy loss over diastole is computed over the time period between the first and the last phase of the diastole (Eq. 3) in *Appendix 1*) and heart rate mainly affects the duration of diastole. Still, the EL-time curve over total diastole in the current study (*Figure 1d*) agrees well with reported in vivo [1] and in vitro [2] EL time curves. In this study we demonstrated the reproducibility of the EL parameters with moderate–strong ICCs and substantial CVs of up to 25%. Similar to KE, the Bland–Altman analysis shows that the variability of $\dot{E}_{L-E-\text{avg}}$ and $\dot{E}_{L-A-\text{avg}}$ was less than the variability of $\dot{E}_{L-E-\text{peak}}$ and $\dot{E}_{L-A-\text{peak}}$. The amount of energy lost over diastole relative to the average kinetic energy as measured by means of EL_{index} , shows good reproducibility for all subjects with an ICC of 0.94 ($P < 0.001$) and an CV of 9%. The Bland–Altman plot shows that all subjects are within the same range of differences. This suggests that among tested parameters EL_{index} is the least sensitive to subtle physiological variations or discrepancies affected by technical limitations of the 4D flow MRI data in the healthy subjects, which might have affected the lesser reproducibility of KE and EL in some subjects. This observation could be attributed to the fact that EL_{index} is a dimensionless parameter concerned with the relative changes in EL to KE and not with their absolute changes as in other tested parameters. As such, the reported reproducibility of EL_{index} could also be considered as another reflection of a good internal consistency in this study. Although a similar EL_{index} parameter was reported in a previous study and was shown to be significantly altered in patients with acute myocardial infarction [18], EL_{index} was computed in that study from 2D echo particle image velocimetry and over the complete cardiac cycle as compared to this study’s volumetric measurement from 4D flow MRI and over diastole only. Therefore, it is not possible to perform a direct comparison with the published results of that study.

Vorticity inside the LV during diastolic filling

LV vortex quantification parameters, such as vorticity, could be useful in the assessment of LV and RV diastolic (dys)function [1, 8, 9, 11, 12]. In recent studies, vorticity was shown to be a marker of diastolic dysfunction, both in the LV [9] and the RV [8] of patients with pulmonary hypertension. To our knowledge, no previous study is available on assessing scan–rescan reproducibility of in vivo vorticity_LV over diastole from 4D flow MRI. Fenster et al. [8] assessed vorticity inside the RV using the integral of vorticity magnitude over the volumes and found results in the same order of magnitude as the results in the current study. In a recent paper by Schafer et al. [9] LV vorticity in healthy subjects was assessed. However, it is not clear whether this was computed over the whole LV volume and therefore we cannot compare results to our measurements. The current study showed scan–rescan reproducibility of integral vorticity_LV during E-filling as well as during A-filling with good–excellent ICCs and CVs up to 11%. Based on the Bland–Altman analyses, similar to the KE and EL results, the variability of the average of the vorticity_LV_{E-avg} and vorticity_LV_{A-avg} was less than the variability of the peaks vorticity_LV_{E-peak} and vorticity_LV_{A-peak}. Vorticity_LV_{E-avg} shows less variability than vorticity_LV_{A-avg} but vorticity_LV_{E-peak} shows slightly more variability than vorticity_LV_{A-peak}.

Technical considerations

The post-processing steps that are followed for obtaining these flow energetics and vorticity parameters involve manual segmentation, registration and valve tracking. Manual segmentation on cine short axis images can be performed with excellent reproducibility [27]. In this study, manual segmentation was performed by one observer with over 2 years of experience in MRI and verified by another observer with over 15 years of experience, with validated software [28], which warrants high accuracy. Next, to correct for patient motion related misalignment and minimize errors between the cine short axis and the 4D flow acquisitions, automated image-based 3D rigid registration was performed using the validated Elastix image registration toolbox [17]. Another post-processing step requires retrospective valve tracking and mitral flow velocity mapping for assessing the beginning and ending of diastole. The reproducibility and observer variability of this semi-automated method was shown to be excellent [14, 15].

Limitations

A limitation of this study is the small number of subjects. Furthermore, no patients were scanned in this study as this is difficult to assess in clinical research. In most of our patient studies, 4D flow MRI is part of a clinical MRI evaluation of about 75–90 minutes, sometimes involving the use of contrast for late gadolinium enhancement and sometimes involving a Dobutamine rest/stress protocol. Scan–rescan evaluation in such cases would imply repeating some of these evaluations as well. Furthermore, repeating 4D flow MRI for scan–rescan purposes would imply an additional scan-time of approximately 30 minutes (because of replanning), which makes the total scan-time too long to keep the patient in the same physiological state. Another limitation is that the influence of a different scanning protocol or scanner was not assessed. However, it is important to note that in the current study the aim was to assess scan–rescan reproducibility by using the exact same protocol and the same scanner machine twice. The use of different scanners or scanning protocols could result in altered reproducibility, which should be evaluated in future studies.

Conclusion

In conclusion, left ventricular kinetic energy and viscous energy loss quantification from 4D flow MRI in healthy volunteers shows strong–excellent in-scan consistency. Scan–rescan assessment of left ventricular kinetic energy, viscous energy loss and vorticity shows overall good agreement in the majority of the scanned subjects. Nevertheless, in two out of twelve subjects, considerable variation between the scans was found. Agreement of A-filling measurements is better than E-filling between scans in the studied parameters. Furthermore, time-averaged measurements over early and late filling show better reproducibility compared to peak measurements. Strong reproducibility for all cases is found in the dimensionless index, EL_{index} , that measures the ratio of the amount of viscous energy lost relative to the average kinetic energy over diastole. EL_{index} seems to be less influenced by technical and/or slight physiological differences between scans and may therefore be a useful parameter of energetics for future studies

References

1. Elbaz MS, van der Geest RJ, Calkoen EE, de Roos A, Lelieveldt BP, Roest AA, Westenberg JJ: Assessment of viscous energy loss and the association with three-dimensional vortex ring formation in left ventricular inflow: In vivo evaluation using four-dimensional flow MRI. *Magn Reson Med*. 2017, 77:794-805
2. Pedrizzetti G, Domenichini F: Nature optimizes the swirling flow in the human left ventricle. *Phys Rev Lett* 2005, 95:108101.
3. Kamphuis VP, Westenberg JJM, van der Palen RLF, Blom NA, de Roos A, van der Geest R, Elbaz MSM, Roest AAW: Unravelling cardiovascular disease using four dimensional flow cardiovascular magnetic resonance. *Int J Cardiovasc Imaging* 2017, 33:1069-1081.
4. Eriksson J, Bolger AF, Ebberts T, Carlhall CJ: Four-dimensional blood flow-specific markers of LV dysfunction in dilated cardiomyopathy. *Eur Heart J Cardiovasc Imaging* 2013, 14:417-424.
5. Fredriksson AG, Svalbring E, Eriksson J, Dyverfeldt P, Alehagen U, Engvall J, Ebberts T, Carlhall CJ: 4D flow MRI can detect subtle right ventricular dysfunction in primary left ventricular disease. *J Magn Reson Imaging* 2016, 43:558-565.
6. Kanski M, Arvidsson PM, Toger J, Borgquist R, Heiberg E, Carlsson M, Arheden H: Left ventricular fluid kinetic energy time curves in heart failure from cardiovascular magnetic resonance 4D flow data. *J Cardiovasc Magn Reson* 2015, 17:111.
7. Svalbring E, Fredriksson A, Eriksson J, Dyverfeldt P, Ebberts T, Bolger AF, Engvall J, Carlhall CJ: Altered Diastolic Flow Patterns and Kinetic Energy in Subtle Left Ventricular Remodeling and Dysfunction Detected by 4D Flow MRI. *PLoS One* 2016, 11:e0161391.
8. Fenster BE, Browning J, Schroeder JD, Schafer M, Podgorski CA, Smyser J, Silveira LJ, Buckner JK, Hertzberg JR: Vorticity is a marker of right ventricular diastolic dysfunction. *Am J Physiol Heart Circ Physiol* 2015, 309:H1087-1093.
9. Schafer M, Browning J, Schroeder JD, Shandas R, Kheyfets VO, Buckner JK, Hunter KS, Hertzberg JR, Fenster BE: Vorticity is a marker of diastolic ventricular interdependency in pulmonary hypertension. *Pulm Circ* 2016, 6:46-54.
10. Kheradvar A, Pedrizzetti G: Vortex formation in the heart. In *Vortex formation in the cardiovascular system*. London: Springer; 2012: 19
11. Kheradvar A, Assadi R, Falahatpisheh A, Sengupta PP: Assessment of transmitral vortex formation in patients with diastolic dysfunction. *J Am Soc Echocardiogr* 2012, 25:220-227.
12. Stewart KC, Charonko JC, Niebel CL, Little WC, Vlachos PP: Left ventricular vortex formation is unaffected by diastolic impairment. *Am J Physiol Heart Circ Physiol* 2012, 303:H1255-1262.
13. Kamphuis VP, Roest AAW, Westenberg JJM, Elbaz MSM: Biventricular vortex ring formation corresponds to regions of highest intraventricular viscous energy loss in a Fontan patient: analysis by 4D Flow MRI. *Int J Cardiovasc Imaging* 2017.
14. Kamphuis VP, van der Palen RLF, de Koning PJH, Elbaz MSM, van der Geest RJ, de Roos A, Roest AAW, Westenberg JJM: In-scan and scan-rescan assessment of LV in- and outflow volumes by 4D flow MRI versus 2D planimetry. *J Magn Reson Imaging* 2018, 47:511-522
15. Westenberg JJ, Roes SD, Ajmone Marsan N, Binnendijk NM, Doornbos J, Bax JJ, Reiber JH, de Roos A, van der Geest RJ: Mitral valve and tricuspid valve blood flow: accurate quantification with 3D velocity-encoded MR imaging with retrospective valve tracking. *Radiology* 2008, 249:792-800.
16. Garg P, Westenberg JJM, van den Boogaard PJ, Swoboda PP, Aziz R, Foley JRJ, Fent GJ, Tyl FGJ, Coratella L, ElBaz MSM, et al: Comparison of fast acquisition strategies in whole-heart four-dimensional flow cardiac MR: Two-center, 1.5 Tesla, phantom and in vivo validation study. *J Magn Reson Imaging* 2018, 47: 272-281
17. Klein S, Staring M, Murphy K, Viergever MA, Pluim JP: elastix: a toolbox for intensity-based medical image registration. *IEEE Trans Med Imaging* 2010, 29:196-205.
18. Agati L, Cimino S, Tonti G, Cicogna F, Petronilli V, De Luca L, Iacoboni C, Pedrizzetti G: Quantitative analysis of intraventricular blood flow dynamics by echocardiographic particle image velocimetry in patients with acute myocardial infarction at different stages of left ventricular dysfunction. *Eur Heart J Cardiovasc Imaging* 2014, 15:1203-1212.

19. Hyslop NP, White WH: Estimating precision using duplicate measurements. *J Air Waste Manag Assoc* 2009, 59:1032-1039.
20. Bland JM, Altman DG: Statistical methods for assessing agreement between two methods of clinical measurement. *Lancet* 1986, 1:307-310.
21. Bolger AF, Heiberg E, Karlsson M, Wigstrom L, Engvall J, Sigfridsson A, Ebbers T, Kvitting JP, Carlhall CJ, Wranne B: Transit of blood flow through the human left ventricle mapped by cardiovascular magnetic resonance. *J Cardiovasc Magn Reson* 2007, 9:741-747.
22. Mohiaddin RH: Flow patterns in the dilated ischemic left ventricle studied by MR imaging with velocity vector mapping. *J Magn Reson Imaging* 1995, 5:493-498.
23. Francis GS: Pathophysiology of chronic heart failure. *Am J Med* 2001, 110 Suppl 7A:37S-46S.
24. Kanski M, Toger J, Steding-Ehrenborg K, Xanthis C, Bloch KM, Heiberg E, Carlsson M, Arheden H: Whole-heart four-dimensional flow can be acquired with preserved quality without respiratory gating, facilitating clinical use: a head-to-head comparison. *BMC Med Imaging* 2015, 15:20.
25. Carlsson M, Heiberg E, Toger J, Arheden H: Quantification of left and right ventricular kinetic energy using four-dimensional intracardiac magnetic resonance imaging flow measurements. *Am J Physiol Heart Circ Physiol* 2012, 302:H893-900.
26. Hussaini SF, Rutkowski DR, Roldan-Alzate A, Francois CJ: Left and right ventricular kinetic energy using time-resolved versus time-average ventricular volumes. *J Magn Reson Imaging* 2016.
27. Grothues F, Smith GC, Moon JC, Bellenger NG, Collins P, Klein HU, Pennell DJ: Comparison of interstudy reproducibility of cardiovascular magnetic resonance with two-dimensional echocardiography in normal subjects and in patients with heart failure or left ventricular hypertrophy. *Am J Cardiol* 2002, 90:29-34.
28. van der Geest RJ, Reiber JH: Quantification in cardiac MRI. *J Magn Reson Imaging* 1999, 10:602-608.

Appendix 1

Viscous Energy Loss Computation from 4D flow MRI

Given the acquired velocity field v , the rate of viscous energy loss ($\dot{E}L$) in watt (W) and the total energy loss (EL_{total}) in joule (J) over a given period of time T can be computed from 4D flow MRI using the viscous dissipation function Φ_v in the Newtonian Navier-Stokes energy equations:

$$\Phi_v = \frac{1}{2} \sum_{i=1}^3 \sum_{j=1}^3 \left[\left(\frac{\partial v_i}{\partial x_j} + \frac{\partial v_j}{\partial x_i} \right) - \frac{2}{3} (\nabla \cdot v) \delta_{ij} \right]^2, \begin{cases} \delta_{ij} = 1, \text{ if } i = j \\ \delta_{ij} = 0, \text{ if } i \neq j \end{cases} \quad [\text{s}^{-2}] \quad (\text{Eq.1})$$

Φ_v represents the rate of viscous energy dissipation per unit volume. i, j correspond to the principal velocity directions x, y, z . $\nabla \cdot v$ denotes the divergence of the velocity field. Therefore, the rate of viscous energy loss ($\dot{E}L$) in Watt at an acquired time phase t can be computed as:

$$\dot{E}L_t = \mu \sum_{i=1}^M \Phi_v L_i \quad [\text{watt (W)}] \quad (\text{Eq.2})$$

assuming the blood as a Newtonian fluid, the dynamic viscosity is $\mu = 0.004 \text{ Pa}\cdot\text{s}$, N as the total number of voxels in the given domain of interest (e.g. LV), L_i as the voxel volume.

As a result, the total viscous energy loss (EL) in joules over time period T starting at phase t_{start} and ending at t_{end} can be computed as:

$$EL_T = \sum_{d=t_{start}}^{t_{end}} \dot{E}L_d p_d \quad [\text{joule (J)}] \quad (\text{Eq.3})$$

with p_d the time step (temporal resolution) of the acquired 4D flow MRI.

Vorticity Computation from 4D flow MRI

If u, v, w denote the three velocity field components acquired from 4D flow MRI over the principal velocity directions x, y, z , respectively, the vorticity ($\omega_{i,t}$) at voxel i of an acquired time phase t

$$\omega_{i,t} = \left(\frac{\partial w_{i,t}}{\partial y_{i,t}} - \frac{\partial v_{i,t}}{\partial z_{i,t}}, \frac{\partial u_{i,t}}{\partial z_{i,t}} - \frac{\partial w_{i,t}}{\partial x_{i,t}}, \frac{\partial v_{i,t}}{\partial x_{i,t}} - \frac{\partial u_{i,t}}{\partial y_{i,t}} \right) \quad [1/\text{s}] \quad (\text{Eq.4})$$

Then, Vorticity_LV denoting the integral sum of vorticity over the segmented LV volume at an acquired time phase t in liter (ml) per second (s) can be computed as

$$\text{Vorticity_LV}_t = \sum_{i=1}^M |\omega_{i,t}| L_{i,t} \quad [\text{ml/s}] \quad (\text{Eq.5})$$

With $|\omega_{i,t}|$ as the magnitude of the vorticity vector, M as the total number of voxels in the segmented LV volume and $L_{i,t}$ as the voxel volume.

Appendix 2

Table A1. Subject specific scan-rescan assessment

Subject	HR 1 (bpm)	HR 2 (bpm)	Difference HR (bpm)	LV outflow 1 (ml)	LV outflow 2 (ml)	Difference LV outflow (ml)	CO 1 (l/min)	CO 2 (l/min)	Difference CO (l/min)
1*	67.1	69.6	2.5	104.1	124.9	20.7	6.99	8.7	24.4
2*	53.8	51.6	-2.2	112.9	94.4	-18.5	6.08	4.9	-19.7
3	58.0	51.8	-6.2	110.0	126.4	16.4	6.38	6.6	2.7
4	61.5	59.1	-2.4	81.5	72.4	-9.1	5.01	4.3	-14.7
5	71.9	66.2	-5.7	68.4	66.0	-2.4	4.92	4.4	-11.2
6	50.5	52.9	2.4	100.7	108.6	7.9	5.08	5.7	12.9
7	63.7	60.4	-3.3	104.0	107.8	3.8	6.62	6.5	-1.7
8	57.7	53.1	-4.6	85.4	86.4	1.0	4.93	4.6	-6.9
9	71.1	72.1	1.0	75.3	84.5	9.1	5.35	6.1	13.7
10	68.0	61.3	-6.7	85.0	81.8	-3.2	5.78	5.0	-13.3
11	48.5	58.3	9.8	90.3	88.7	-1.5	4.38	5.2	18.2
12	58.0	62.0	4.0	71.1	76.3	5.2	4.12	4.7	14.7

Differences were calculated as: value scan 2 - value scan 1.

* subjects with marked high differences for the assessment of early filling parameters

Abbreviations: A=late diastolic filling; AUC=area under the curve; CO=cardiac output; E= early diastolic filling; HR=heart rate.

Table A2. Subject specific scan-rescan information from the MV flow curves

E-filling									
Subject	E AUC 1 (ml)	E AUC 2 (ml)	Difference E AUC (ml)	E PFR 1 (ml/s)	E PFR 2 (ml/s)	Difference E PFR (ml/s)	E dur 1 (ms)	E dur 2 (ms)	Difference E dur (ms)
1*	78.6	94.8	16.2	522.8	738.8	216.0	332	292	-40
2*	84.3	71.3	-13.0	567.4	388.4	-179.1	323	413	90
3	85.7	96.4	10.7	744.5	734.7	-9.9	309	270	-39
4	68.5	61.4	-7.1	551.4	537.9	-13.5	316	263	-53
5	52.6	46.8	-5.8	343.6	362.2	18.6	348	297	-51
6	83.9	84.6	0.7	500.2	545.2	45.0	378	328	-50
7	79.3	87.5	8.2	683.6	647.7	-35.8	314	351	37
8	72.2	71.6	-0.6	592.5	543.6	-48.9	384	350	-34
9	59.4	66.8	7.4	506.1	563.6	57.4	272	300	28
10	58.7	58.9	0.2	367.5	376.7	9.2	322	373	51
11	64.5	60.9	-3.6	398.4	363.9	-34.4	349	343	-6
12	52.8	47.4	-5.4	380.3	314.4	-65.9	330	313	-17
A-filling									
Subject	A AUC 1 (ml)	A AUC 2 (ml)	Difference AUC A (ml)	A PFR 1 (ml/s)	A PFR 2 (ml/s)	Difference A PFR (ml/s)	A dur 1 (ms)	A dur 2 (ms)	Difference A dur (ms)
1*	28.1	29.3	1.18	342.1	357.7	15.5	166	175	9
2*	19.1	14.1	-4.95	243.5	159.6	-83.9	144	188	44
3	32.8	28.0	-4.80	409.5	347.0	-62.5	172	194	22
4	15.3	12.4	-2.93	161.8	158.0	-3.8	190	131	-59
5	16.7	15.0	-1.67	187.0	176.3	-10.7	174	208	34
6	13.6	22.0	8.36	137.4	231.3	93.8	189	197	8
7	32.3	29.6	-2.74	409.2	374.7	-34.5	157	160	3
8	17.5	17.5	0.08	221.1	217.1	-4.0	175	176	1
9	18.3	19.6	1.30	243.7	245.0	1.3	136	137	1
10	17.6	14.4	-3.26	185.3	173.6	-11.8	162	170	8
11	17.5	14.4	-3.12	181.8	172.3	-9.5	209	205	-4
12	8.5	12.9	4.43	114.5	164.0	49.5	165	187	22

Differences were calculated as: value scan 2 - value scan 1.

* subjects with marked high differences for the assessment of early filling parameters

Abbreviations: A=late diastolic filling; AUC=area under the curve; CO=cardiac output; dur= duration; E= early diastolic filling; HR=heart rate; PRF=peak filling rate.

Chapter 10

Disproportionate intraventricular viscous energy loss in Fontan patients: analysis by 4D flow MRI

Vivian P Kamphuis*, Mohammed SM Elbaz*, Pieter J van den Boogaard, Lucia JM Kroft, Rob J van der Geest, Albert de Roos, Willem A Helbing, Nico A Blom, Jos JM Westenberg, Arno AW Roest

* equal contribution

European Heart Journal – Cardiovascular imaging 2018 doi: 10.1093/ehjci/jeu096. [Epub ahead of print]

Abstract

Objective

To noninvasively assess intraventricular viscous energy loss (EL) and proportionality to kinetic energy (KE) in Fontan patients using 4D flow magnetic resonance imaging (MRI) and compare to healthy controls.

Methods

Thirty Fontan patients and 15 controls underwent 4D flow MRI. Ventricular EL was computed and normalized by end-diastolic volume (EDV). EL over the cardiac cycle (EL_{cycle}) relative to the average kinetic energy (KE_{cycle}) was quantified using a dimensionless index, EL_{index} ($EL_{\text{cycle}}/KE_{\text{cycle}}$).

Results

Viscous energy loss was significantly elevated in Fontan patients compared to controls ($EL_{\text{cycle}}/\text{EDV}$: 3.7 vs. 2.6 J/m³, $P=0.001$). Fontan patients with inflow of blood entering a ventricle, which leaves that ventricle through a ventricular septal defect to the aorta, defined as discordant inflow-to-outflow showed significantly higher EL compared to patients with inflow of blood into the same ventricle from which the blood is ejected into the aorta, defined as concordant inflow-to-outflow ($EL_{\text{cycle}}/\text{EDV}$: 6.8 vs. 3.2 J/m³, $P=0.001$). EL was not significantly different in Fontan patients with a systemic left versus a systemic right ventricle ($EL_{\text{cycle}}/\text{EDV}$: 3.5 vs. 3.6 J/m³, $P=0.91$). EL_{index} was significantly elevated in Fontan patients compared to controls (EL_{index} : 0.4 vs. 0.2, $P<0.001$). Highest EL_{index} was found in Fontan patients with discordant inflow-to-outflow compared to concordant inflow-to-outflow (0.5 vs. 0.3, $P=0.01$).

Conclusion

Fontan patients show disproportionate intraventricular viscous energy loss relative to kinetic energy. Intraventricular viscous energy loss is elevated in these patients compared to healthy controls, and highest viscous energy loss is found in patients with discordant inflow to outflow.

Introduction

In patients with complex congenital intracardiac deformations, in whom a biventricular circulation cannot be created, the Fontan procedure is a palliative approach in which the systemic venous return is directed to the pulmonary arteries without passing through a ventricle [1]. The Fontan procedure results in normalisation of the arterial saturation and abolishment of the volume overload, however at the cost of increased systemic venous pressure and decreased cardiac output (CO) [2]. Furthermore, the intracardiac anatomy is not restored which leads to alterations in intracardiac hemodynamics [3]. These patients require lifelong follow-up and the main cause of mortality is circulatory failure [4]. The reasons behind such failure are not fully understood [5], and little is known about the influence of disturbed intracardiac flow patterns on cardiac efficiency and its role in the pathophysiological mechanisms leading to declining circulatory function. Accurate visualization and quantification of intracardiac hemodynamics might help in understanding this decline and may aid in early detection of deterioration of ventricular function.

4D flow MRI is a novel technique that is used to assess *in vivo* blood flow patterns and to quantify hemodynamic markers from blood flow velocity [6]. This technique was recently used to show decreased diastolic intraventricular kinetic energy (KE) in Fontan patients [7]. Also, increased viscous energy loss (EL), the KE that is lost due to frictional forces between blood and surrounding structures and induced by blood viscosity, was reported in corrected atrioventricular septal defect (AVSD) patients [8]. In the healthy left ventricle (LV), the amount of EL is proportional to the KE that is produced [9]. The EL/KE ratio can be defined by the dimensionless EL_{index} [10, 11].

We hypothesize that the various underlying intracardiac deformations of Fontan patients promote inefficient flow-structure interactions that would increase EL disproportionate to the KE produced, reflected by an altered EL_{index} . To our knowledge, *in vivo* EL or EL_{index} has not been reported in Fontan patients. Therefore, the purpose of this study is to noninvasively assess intraventricular EL and EL_{index} in Fontan patients using 4D flow MRI and to compare these results to EL and EL_{index} in the LV of healthy volunteers.

Methods

Study population

Of the 30 Fontan patients who were prospectively included in this study, 7 patients underwent MRI with 4D Flow as part of standard care and 23 were part of a multicentre study that was approved by the Medical Ethical Committee of the Erasmus Medical Center Rotterdam, with local approval of the Medical Ethical Committee of the Leiden University Medical Center, The Netherlands. Informed consent was obtained from all prospectively included participants. Regarding the retrospective data: at the time of the study, no ethical approval was required for anonymised studies with patient data that was collected as part of standard care in the Netherlands. Maximum oxygen uptake ($\text{VO}_2 \text{ max}$), derived from cardiopulmonary exercise tests (CPET) on a upright bicycle ergometer was included when CPET was done within 6 months of the MRI (N=22) [12]. Fifteen controls with a similar age and without a history of cardiac disease were included for comparison. These volunteers were part of a group of 30 healthy volunteers of whom KE and EL were reported previously in comparison to corrected AVSD patients [13].

Fontan patient grouping

First, intraventricular EL results in the total Fontan patient group (11 patients with a systemic LV, 13 patients with a systemic right ventricle [RV] and 6 “biventricular” patients, as shown in *supplementary Table A1*) were compared to the LV energy loss of the controls since the systemic RV of the Fontan patients more closely resembles loading conditions of the systemic LV as compared to the loading conditions of the subpulmonary RV of the controls. Furthermore, systemic loading conditions of the RV sustaining the systemic circulation in Fontan patients induces marked changes in RV function, partly resembling LV contraction patterns [14].

Then, patients were grouped into two groups for comparison to each other by: 1) concordance or discordance of the inflow into the ventricle versus the outflow to the aorta; 2) systemic LV versus systemic RV. Concordant inflow-to-outflow was defined as inflow of blood into the same ventricle from which the blood is ejected into the aorta, as is the case in a patient with tricuspid atresia with a normal ventriculo-arterial connection. Discordant inflow-to-outflow was defined as inflow of all (or part of) the blood entering a ventricle, which leaves that ventricle through a ventricular septal defect to the aorta, for example in double inlet left ventricle with the aorta arising from a hypoplastic RV.

Cardiovascular MRI acquisition

For the Fontan patients, whole-heart 4D flow MRI was obtained on a 3T scanner (Ingenia, Philips Healthcare, Best, the Netherlands) in 4-chamber orientation, with 3D volume covering the whole heart. Maximal amplitude was 45 mT/m for each axis, slew rate of 200 T/m/s and a combination of FlexCoverage Posterior coil in the table top with a dStream Torso coil, providing up to 32 coil elements for signal reception. Velocity-encoding of 150 cm/s in all three directions was used in a standard four-point encoding scheme, spatial resolution $3.0 \times 3.0 \times 3.0 \text{ mm}^3$ or better, flip angle 10° , echo time (TE) 3.7 ms, repetition time (TR) 7.7–10 ms, true temporal resolution 30–40 ms, sensitivity encoding factor 2 in anterior-posterior direction and echo planar imaging readout with a factor 5. Concomitant gradient correction and phase offset correction was performed using standard available scanner software. Retrospective gating was used with 30 phases reconstructed to represent one cardiac cycle and free breathing was allowed without motion suppression. It has been shown that whole-heart 4D flow MRI can be acquired with preserved accuracy without respiratory gating [15]. Typical acquisition time of the 4D flow MRI scan was approximately 8 minutes.

Cine two-dimensional left 2-chamber, 4-chamber, coronal and sagittal aorta views and transversal images were acquired, using steady-state free-precession sequences with TE/TR 1.5/3.0, 350 mm field-of-view, 45° flip angle, acquisition resolution $1.9 \times 2.0 \times 8.0 \text{ mm}^3$. Retrospective gating was used with 30 phases reconstructed to represent one cardiac cycle. Free breathing was allowed without motion suppression; three signal averages were taken to minimize effects of breathing motion.

Volunteers underwent whole-heart 4D flow MRI on the same 3T scanner with a similar scan protocol except for the acquired spatial resolution of $2.3 \times 2.3 \times 4.2 \text{ mm}^3$ [13]. To test the influence of different spatial resolutions on EL and KE, an additional test was performed in two healthy volunteers under the same scan conditions except for the spatial resolution, applying the resolution used in the Fontan patients (resolution 1: $3.0 \times 3.0 \times 3.0 \text{ mm}^3$) and volunteers (resolution 2: $2.3 \times 2.3 \times 4.2 \text{ mm}^3$) (*supplementary Table A2 and supplementary Figure A1*).

Data preparation

Image analysis was performed by one observer (VPK) with >3 years of cardiac MRI experience and verified by a radiologist (LJMK) with >20 years of cardiac MRI experience. Endocardial borders were manually traced in all slices and phases in the transversal images and ventricular volume was calculated at the end-diastolic and end-systolic phases using in-house developed *MASS* software (*Figure 1*). Papillary muscles were disregarded and

assumed to be included in the ventricular volume. Remaining parts of the septum in “biventricular patients” were not included in the ventricular volume. Stroke volume (SV) was calculated as ventricular end-diastolic volume (EDV) – end-systolic volume. Cardiac output was computed as $SV \times \text{heart Rate (HR)}$. Ventricular shape was assessed by the sphericity index as short-axis to long-axis ratio in the cine four-chamber view. Time points of systolic and diastolic phases, E/A ratio and regurgitation fraction were derived from ventricular inflow and outflow profiles from retrospective valve tracking [16].

Segmentation of the ventricular cavity in the 4D flow MRI acquisition, required for the energy analysis, was obtained by transforming the available time-varying segmentation of cine transversal acquisition to the 4D flow MRI data. To account for potential patient-motion-related misalignment between these acquisitions, automated image-based 3D rigid registration by mutual information was performed using the phase with maximal depiction of the ventricular cavity in both scans with the Elastix image registration toolbox [17]. Intraventricular KE and EL were obtained by one investigator (MSME) with >6 years MRI experience using in-house developed MATLAB-based software (MathWorks Inc., version R2013b).

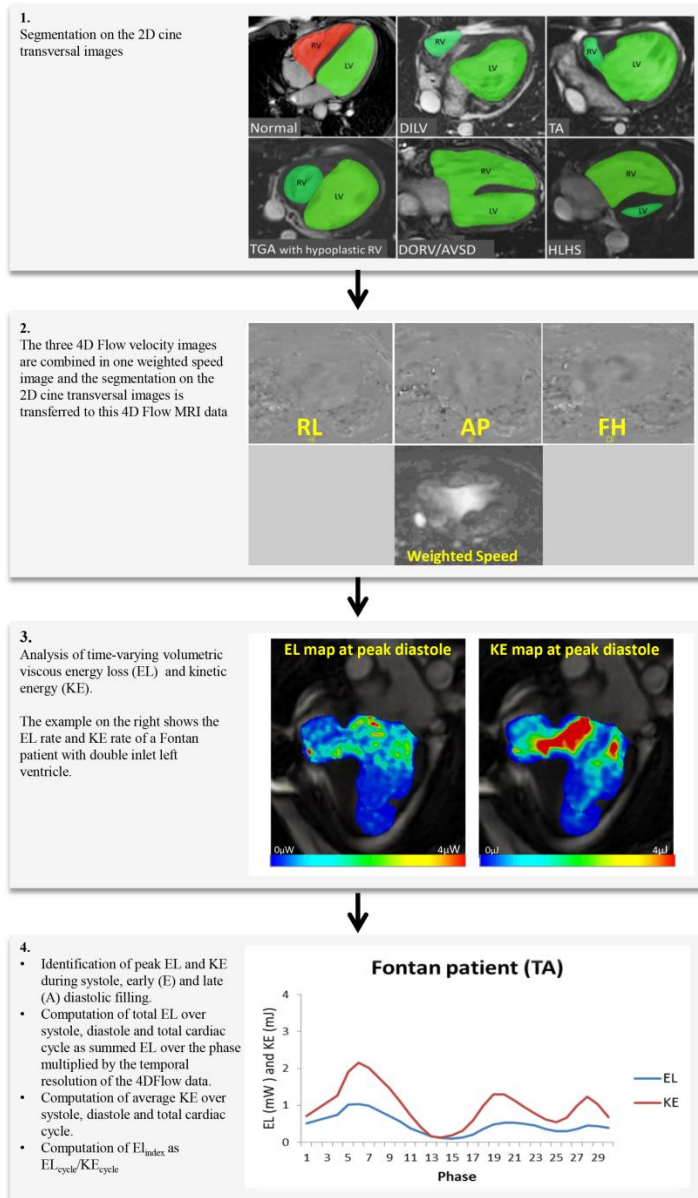


Figure 1. Kinetic energy (KE) and viscous energy loss (EL) analysis. 1) segmentation on the 2D cine transversal images; 2) segmentation on the 4D flow data; 3) analysis of time-varying volumetric KE and EL and 4) identification of the peaks and averages. DILV=double inlet left ventricle; TA=tricuspid atresia; TGA=transposition of the great arteries; RV=right ventricle; DORV=double outlet right ventricle; AVSD=complete atrioventricular septal defect; HLHS=hypoplastic left heart syndrome.

Computation of intraventricular energetics

Intraventricular EL was computed from 4D flow MRI using the dissipation terms from the Navier-Stokes energy equations assuming blood as a Newtonian fluid [8], as shown in the supplementary methods. The peak viscous energy loss rate ($\dot{E}L$, in watt (W)) during systole ($\dot{E}L_{\text{peak-systole}}$), early (E) diastolic filling ($\dot{E}L_{E\text{-peak}}$) and late (A) diastolic filling ($\dot{E}L_{A\text{-peak}}$) were assessed. Furthermore, summed EL over the total cardiac cycle (EL_{cycle}), systole (EL_{systole}) and diastole (EL_{diastole}) in Joule (J) were computed. In this study, we normalized EL parameters by EDV and SV to account for heterogeneity in ventricular volume and flow. EL parameters normalized by EDV are reported as $\dot{E}L_{\text{peak-systole}}/\text{EDV}$, $\dot{E}L_{E\text{-peak}}/\text{EDV}$ and $\dot{E}L_{A\text{-peak}}/\text{EDV}$ in W/m^3 and as $EL_{\text{cycle}}/\text{EDV}$, $EL_{\text{systole}}/\text{EDV}$ and $EL_{\text{diastole}}/\text{EDV}$ in J/m^3 .

The amount of intraventricular KE was computed as $\frac{1}{2}mv^2$, with (m) as the mass representing the voxel volume multiplied by the density of blood (1.025g/ml) and (v) as the 3-directional velocity from 4D flow MRI. For each acquired time-phase, volumetric KE was then computed by integrating the computed KE over the segmented 3D ventricular volume. In order to quantify KE, the time-averaged KE and peak KE in Joule (J) over the total cardiac cycle (KE_{cycle}), over systole (KE_{systole} , $KE_{\text{peak-systole}}$), over diastole (KE_{diastole}), peak early diastolic filling ($KE_{E\text{-peak}}$) and peak late diastolic filling ($KE_{A\text{-peak}}$) were assessed. To allow comparison of our results with a previous study reporting peak KE values normalized by SV [7, 8], KE values in the current study were also normalized by SV (reported as $KE_{\text{cycle}}/\text{SV}$, $KE_{\text{systole}}/\text{SV}$, $KE_{\text{peak-systole}}/\text{SV}$, $KE_{\text{diastole}}/\text{SV}$, $KE_{E\text{-peak}}/\text{SV}$, $KE_{A\text{-peak}}/\text{SV}$), in mJ/ml .

In healthy hearts the amount of EL is proportional to the amount of KE [9]. To assess whether changes in EL levels in Fontan patients are a proportional consequence of changes in KE we computed an energy loss index (EL_{index}) indicating the amount of EL indexed to the average KE produced over the cardiac cycle. EL_{index} is a dimensionless index that was used in an earlier 2D echo particle image velocimetry study by Agati et al. [10]. The diastolic EL_{index} and its reproducibility from 4D flow MRI was recently shown in healthy subjects [11]. In the current study, EL_{index} was computed as $EL_{\text{cycle}}/KE_{\text{cycle}}$. With EL_{cycle} as the summed volumetric EL (in Joule) lost during the total cardiac cycle and KE_{cycle} as the average volumetric KE (in Joule) during the total cardiac cycle. In this study we defined “disproportionate” as a disturbance in the EL_{index} compared to controls i.e. altered proportionality/fraction of total EL that is lost relative to KE produced over the cardiac cycle (measured by EL_{index}) compared to values found in the studied healthy controls.

Statistical Analysis

Data analysis was performed using SPSS Statistics (version 23.0 IBM SPSS, Chicago, IL). Variables were tested for normal distribution using the Shapiro-Wilk test. Continuous data is reported as mean \pm standard deviation (SD) or as median with inter-quartile range (IQR) in case of non-normality of the data. Comparison of variables amongst different groups was performed using the unpaired Student's t-test or, in case of non-normality, the Mann-Whitney U-test. Normal limits were derived from the 95% confidence interval (CI) of the healthy control group. To test the association of EL_{index} and EL and conventional markers of functional status (such as E/A ratio, AV regurgitation fraction and VO_2 max) in the studied Fontan patients, the correlation was tested by the Spearman correlation coefficient (ρ). A P -value <0.05 was considered statistically significant.

Results

Characteristics of the patients and controls are shown in *Table 1*. Of the Fontan patients 28/30 have an extracardiac conduit, 2 have a lateral tunnel. Characteristics of the patient subgroups are also shown in *Table 1* and *supplementary table A1*. As shown in *supplementary Table A2* and *supplementary Figure A1*, the influence of spatial resolutions on EL and KE is: 1-4% on EL_{cycle} , 3-4% on KE_{cycle} and 3-8% on EL_{index} .

Viscous energy loss in Fontan patients versus controls

EL and EL_{index} results for the whole Fontan group versus the controls are reported in *Table 2*. During systole, $EL_{systole}/EDV$ as well as $\dot{E}L_{peak-systole}/EDV$ were significantly higher in Fontan patients. During diastole $EL_{diastole}/EDV$ was not significantly different in Fontan patients versus controls. However, $\dot{E}L_{E-peak}/EDV$ was significantly lower in Fontan patients, while $\dot{E}L_{A-peak}/EDV$ was significantly higher in Fontan patients. Without normalization, EL results for the whole Fontan group versus the controls are similar to the results normalized by EDV, however, $\dot{E}L_{E-peak}$ was not significantly different in Fontan patients versus controls (*supplementary Table A3*). Also, when normalizing by SV, EL results remain similar (*supplementary Table A4*).

Table 1. Characteristics of patients and controls

Total study group			
	Fontan patients (N=30)	Controls (N=15)	<i>P</i> -value
Age (years)	14 [11-18]	14 ± 5	0.42
Male (%)	10/30 (33%)	5/15 (33%)	1.00*
HR (bpm)	81.4 ± 17.0	78.9 ± 11.7	0.62
SV (mL)	63.6 [55.8-77.4]	73.2 ± 18.8	0.32
CO (L/min)	5.5 ± 2.0	5.7 ± 1.3	0.78
EDV (mL)	131.2 [108.2-171.1]	119.7 ± 35.8	0.08
EF (%)	48.4 ± 7.7	61.8 ± 4.2	<0.001
E/A ratio	1.2 [1.0-1.6]	1.9 [1.8-2.2]	<0.001
Regurgitation (%)	6.5 [4.8-10.0]	1.0 [0.0-2.0]	<0.001
VO ₂ max (mL/kg/min)	31.0 ± 7.6	n/a	n/a
Fontan subgroups			
	Concordant in- to outflow (N=21)	Discordant in- to outflow (N=9)	<i>P</i> -value
Age (years)	13 [11-17]	15 [15-18]	0.08
Male (%)	8/21 (38%)	2/9 (22%)	0.70*
HR (bpm)	85.9 ± 14.2	70.9 ± 19.2	0.02
SV (mL)	63.0 ± 16.7	84.1 ± 39.0	0.05
CO (L/min)	5.3 ± 1.4	6.0 ± 3.0	0.39
EDV (mL)	132.9 ± 36.0	169.8 ± 70.7	0.07
EF (%)	48.1 ± 8.4	49.2 ± 5.9	0.73
E/A ratio	1.1 ± 0.3	2.0 ± 0.8	<0.001
Regurgitation (%)	8.6 ± 6.8	8.1 ± 3.2	0.83
VO ₂ max (mL/kg/min)	30.4 ± 8.4	33.0 ± 3.9	0.52
	Left ventricle (N=11)	Right ventricle (N=13)	<i>P</i> -value
Age (years)	15.6 ± 4.0	13.1 ± 2.8	0.08
Male (%)	1/11 (9%)	7/13 (54%)	0.15*
HR (bpm)	74.6 ± 18.1	88.2 ± 14.4	0.05
SV (mL)	61.8 ± 17.2	62.3 ± 16.8	0.94
CO (L/min)	4.6 ± 1.8	5.4 ± 1.2	0.25
EDV (mL)	125.7 ± 39.8	137.0 ± 34.3	0.47
EF (%)	50.2 ± 7.0	45.9 ± 8.5	0.20
E/A ratio	1.5 ± 0.9	1.2 ± 0.3	0.21
Regurgitation (%)	6.3 ± 3.5	10.7 ± 7.8	0.10
VO ₂ max (mL/kg/min)	30.7 ± 8.0	31.1 ± 9.2	0.91

*assessed with the Chi-square test

HR=heart rate; SV=stroke volume; CO=cardiac output; EDV=end-diastolic volume; EF=ejection fraction; VO₂max=maximum oxygen uptake from cardiopulmonary exercise test.

Table 2. Quantitative analysis of viscous energy loss normalized by EDV

Total study group			
	Fontan patients (N=30)	Controls (N=15)	P-value
EL _{systole} /EDV (J/m ³)	2.1 [1.3-2.6]	0.9 ± 0.2	<0.001
EL _{peak-systole} /EDV (W/m ³)	9.8 [4.6-15.3]	5.4 ± 1.5	0.003
EL _{diastole} /EDV (J/m ³)	1.7 [1.3-2.1]	1.7 ± 0.3	0.87
EL _{E-peak} /EDV (W/m ³)	6.8 [4.6-8.8]	10.1 ± 3.0	0.01
EL _{A-peak} /EDV (W/m ³) ^a	5.0 [3.3-7.9]	3.2 ± 1.7	0.003
EL _{cycle} /EDV (J/m ³)	3.7 [2.8-5.0]	2.6 ± 0.4	0.001
EL _{index}	0.4 [0.3-0.5]	0.2 ± 0.04	<0.001
Fontan subgroups			
	Concordant in-to-outflow (N=21)	Discordant in-to-outflow (N=9)	P-value
EL _{systole} /EDV (J/m ³)	1.6 [1.1-2.2]	3.0 [2.2-7.3]	0.001
EL _{peak-systole} /EDV (W/m ³)	7.9 [4.4-11.3]	17.3 [10.9-42.6]	0.002
EL _{diastole} /EDV (J/m ³)	1.7 [1.2-1.9]	2.4 ± 0.8	0.03
EL _{E-peak} /EDV (W/m ³)	6.3 [4.3-8.5]	8.5 ± 3.1	0.16
EL _{A-peak} /EDV (W/m ³) ^a	6.4 ± 3.2	4.3 ± 1.7	0.09
EL _{cycle} /EDV (J/m ³)	3.2 [2.6-3.9]	6.8 ± 3.5	0.001
EL _{index}	0.3 [0.3-0.4]	0.5 ± 0.2	0.01
	Left ventricle (N=11)	Right ventricle (N=13)	P-value
EL _{systole} /EDV (J/m ³)	1.7 [1.2-4.5]	1.9 ± 0.9	0.53
EL _{peak-systole} /EDV (W/m ³)	10.1 [4.6-17.3]	8.6 [4.2-12.9]	0.39
EL _{diastole} /EDV (J/m ³)	2.1 ± 1.1	1.7 [1.3-1.9]	0.53
EL _{E-peak} /EDV (W/m ³)	5.1 [4.4-7.7]	7.2 [4.7-8.9]	0.49
EL _{A-peak} /EDV (W/m ³) ^a	4.5 [3.3-6.7]	6.3 ± 3.0	0.53
EL _{cycle} /EDV (J/m ³)	3.5 [2.6-8.7]	3.6 ± 1.0	0.91
EL _{index}	0.4 [0.3-0.7]	0.3 [0.3-0.4]	0.21

^aone patient had no A-wave and was excluded

EL=viscous energy loss; EDV=end-diastolic volume; E-peak=peak early diastole; A-peak=peak late diastole

Non-normalized results are shown in the *supplementary Table A3*, results normalized by stroke volume are shown in *supplementary Table A4*.

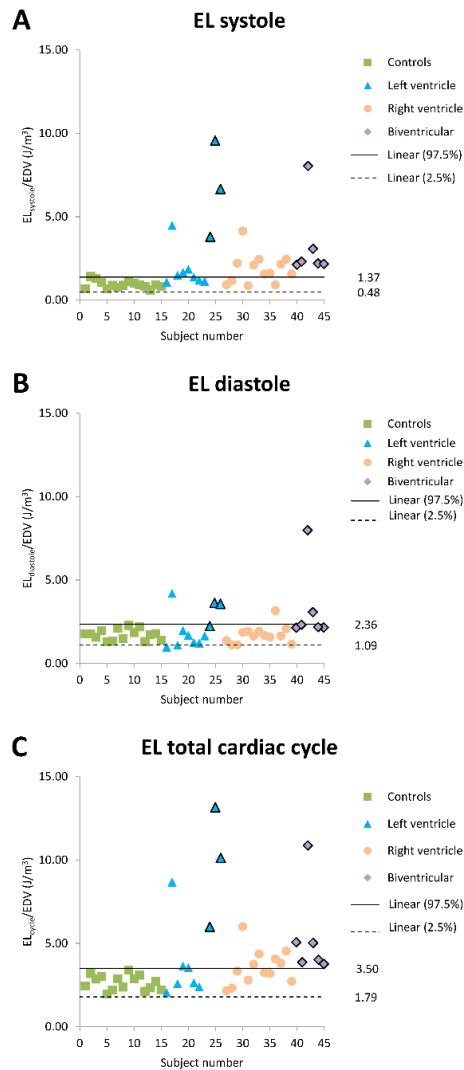


Figure 2. Total viscous energy loss over complete systole (a), complete diastole (b) and complete cardiac cycle (c). The solid line represents the 97.5% (upper limit) and the dashed line represents the 2.5% (lower limit) of the confidence interval of the controls. Patients with discordant inflow-to-outflow are marked with a solid black outline.

Viscous energy loss in Fontan patients with concordant vs. discordant inflow to outflow

EL and EL_{index} results for the Fontan patients with concordant inflow-to-outflow versus Fontan patients with discordant inflow-to-outflow are reported in *Table 2*. During systole,

EL_{systole}/EDV as well as $EL_{\text{peak-systole}}/EDV$ were significantly higher in Fontan patients with discordant inflow-to-outflow. Similarly, EL_{diastole}/EDV was significantly higher in Fontan patients with discordant inflow-to-outflow versus Fontan patients with concordant inflow-to-outflow. $EL_{\text{E-peak}}/EDV$ and $EL_{\text{A-peak}}/EDV$ were not significantly different in Fontan patients with discordant inflow-to-outflow versus Fontan patients with concordant inflow-to-outflow. EL_{cycle}/EDV was significantly higher in Fontan patients with discordant inflow-to-outflow. Also, EL_{index} was significantly higher in Fontan patients with discordant inflow-to-outflow versus Fontan patients with concordant inflow-to-outflow. In *Figure 2*, patients with discordant inflow-to-outflow are shown with a solid black outline. This figure shows that for EL_{systole}/EDV and EL_{cycle}/EDV all patients with discordant inflow-to-outflow were above the 95% CI derived from the controls. The significantly higher EL in patients with discordant inflow to outflow is also indicated in *Figure 3*, where *Figure 3b* shows a cross-section of the EL rate map in a patient with concordant inflow-to-outflow at peak systole and *Figure 3d* shows the EL rate cross-sectional map of a patient with discordant inflow-to-outflow at peak systole. Notably, *Figure 3d* shows the highest EL rate at the level of the ventricular septal defect to the outflow tract. Furthermore, *Figure 4a* and *4c* show cross-sectional EL maps with marked differences in these two patients at peak diastole.

As shown in *Figure 5*, EL_{index} in Fontan patients with discordant inflow-to-outflow (shown with a solid black outline) was consistently above the 95% CI of the controls.

Without normalization, EL results for the Fontan patients with a concordant inflow-to-outflow versus Fontan patients with discordant inflow-to-outflow are similar to the results normalized by EDV. However, the absolute $EL_{\text{E-peak}}$ was significantly higher in Fontan patients with discordant inflow-to-outflow versus patients with concordant inflow to outflow, while there was no significant difference when normalizing by EDV (*supplementary Table A3*). When normalizing by SV, EL results are similar to the EL results normalized by EDV (*supplementary Table A4*).

Viscous energy loss in Fontan patients with a systemic LV or systemic RV

EL and EL_{index} results for the Fontan patients with a systemic LV versus Fontan patients with a systemic RV are reported in *Table 2*. None of the reported parameters, measured over systole, diastole or the total cardiac cycle, were significantly different in Fontan patients with a systemic LV versus Fontan patients with a systemic RV. Results for EL_{systole}/EDV , EL_{diastole}/EDV and EL_{cycle}/EDV in Fontan patients with a systemic LV, systemic RV or biventricular morphology are depicted in *Figure 2* with different colors and shapes. EL_{index} was not significantly different in Fontan patients with a systemic LV versus Fontan patients

with a systemic RV. EL_{index} in Fontan patients with a systemic LV, systemic RV or biventricular morphology is also depicted in *Figure 5*. Without normalization, EL results for the Fontan patients with a systemic LV versus Fontan patients with a systemic RV also showed no significant differences (*supplementary Table A3*). When normalizing by SV EL results remain similar (*supplementary Table A4*).

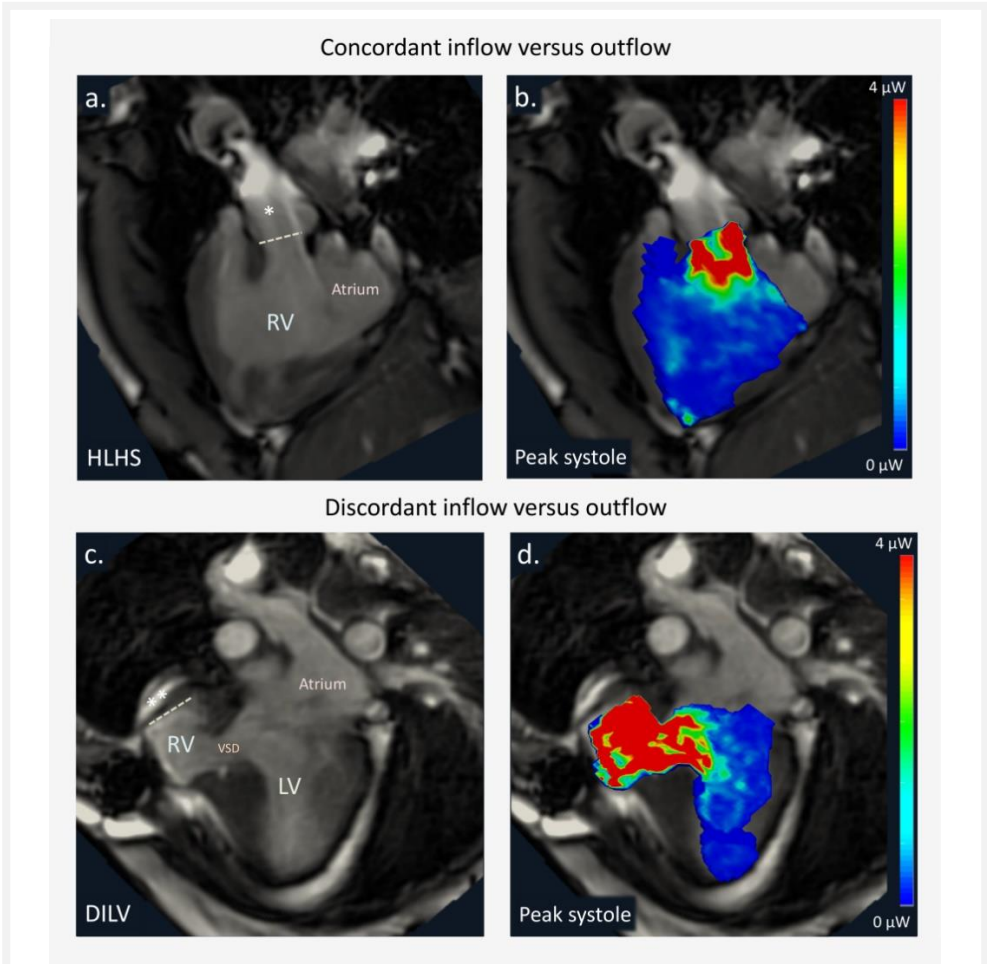
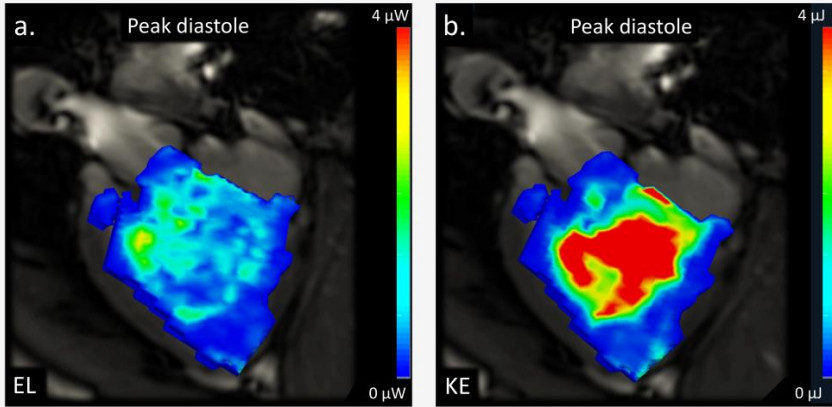


Figure 3. Cross-sectional Map of viscous energy loss (EL) rate in a patient with concordant inflow-to-outflow (a, b) and a patient with discordant inflow-to-outflow (c, d) at peak systole. a) two-chamber view of a patient with hypoplastic left heart syndrome. The dashed line shows the level of the neo-aortic valve to the neo-aorta which is shown by an asterisk (*). b) EL rate of the same patient at peak systole. c) three-chamber view of a patient with double inlet left ventricle. The dashed line shows the level of the aortic valve, the aorta is shown by two asterisks (**). d) EL rate of the same patient at peak systole. LV=left ventricle; RV=right ventricle; HLHS=hypoplastic left heart syndrome; DILV=double inlet left ventricle; VSD=ventricular septal defect

EL and KE maps in a patient with concordant inflow versus outflow (HLHS)



EL and KE maps in a patient with discordant inflow versus outflow (DILV)

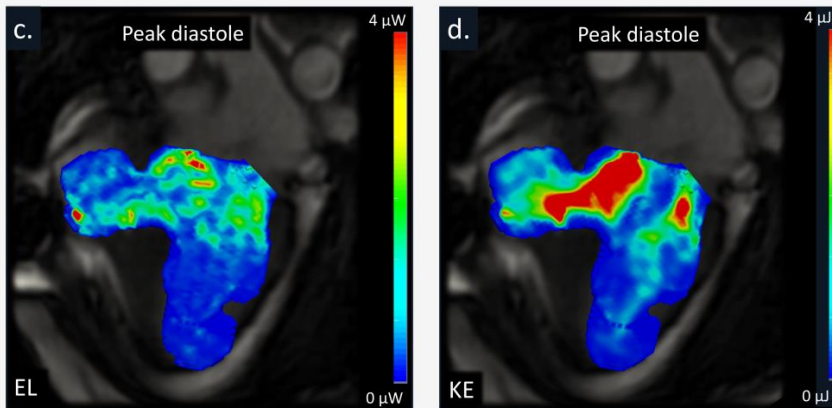
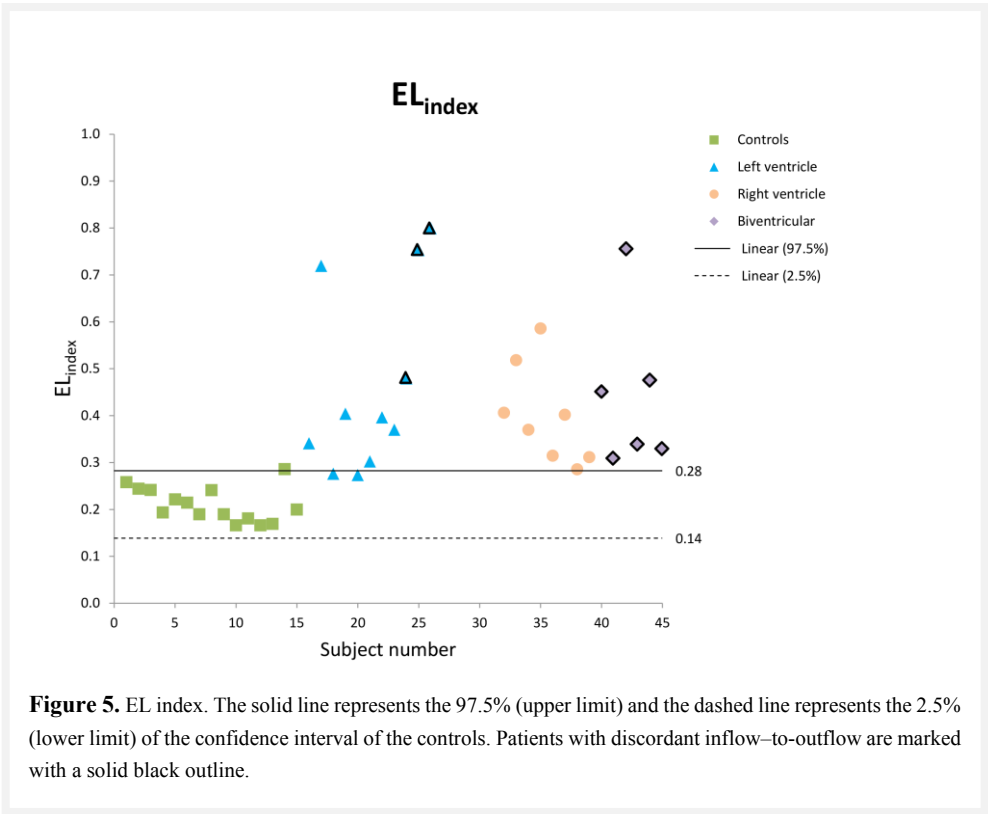


Figure 4. Cross-sectional maps of viscous energy loss (EL) rate and kinetic energy (KE) rate of the same acquired diastolic time-point in a patient with concordant inflow-to-outflow (a, b) and a patient with discordant inflow-to-outflow (c, d) at peak diastole. These maps belong to the same patients presented with systolic EL maps in Figure 4. a) EL rate in a patient with hypoplastic left heart syndrome at peak diastole. b) KE rate in the same patient. c) EL rate in a patient with double inlet left ventricle at peak diastole. d) KE rate in the same patient. EL=viscous energy loss; KE=kinetic energy; HLHS=hypoplastic left heart syndrome; DILV=double inlet left ventricle.



Kinetic energy results

KE results for the whole Fontan group versus controls and the Fontan subgroups, normalized by SV (in mJ/mL) as previously reported [7], are shown in *Table 3*. $KE_{\text{systole}}/\text{SV}$, $KE_{\text{diastole}}/\text{SV}$ and $KE_{\text{cycle}}/\text{SV}$ were not significantly different in Fontan patients compared to controls. Also, $KE_{\text{peak-systole}}/\text{SV}$ and $KE_{A\text{-peak}}/\text{SV}$ were not significantly different in Fontan patients versus controls. However, $KE_{E\text{-peak}}/\text{SV}$ was significantly lower in Fontan patients compared to controls.

Fontan patients with discordant inflow-to-outflow showed significantly higher $KE_{\text{systole}}/\text{SV}$ and $KE_{\text{peak-systole}}/\text{SV}$ compared to patients with concordant inflow-to-outflow. Furthermore, patients with discordant inflow-to-outflow showed significantly lower $KE_{A\text{-peak}}/\text{SV}$ compared to patients with concordant inflow-to-outflow. When comparing Fontan patients with a systemic LV to patients with a systemic RV, none of the reported KE parameters were significantly different.

Table 3. Quantitative analysis of kinetic energy normalized by SV

Total study group			
	Fontan patients (N=30)	Controls (N=15)	P-value
KE _{systole} /SV (mJ/ml)	0.025[0.018-0.034]	0.021±0.006	0.08
KE _{peak-systole} /SV (mJ/ml)	0.047[0.029-0.065]	0.040±0.009	0.17
KE _{diastole} /SV (mJ/ml)	0.018[0.013-0.022]	0.021±0.006	0.16
KE _{E-peak} /SV (mJ/ml)	0.032[0.023-0.039]	0.063±0.017	<0.001
KE _{A-peak} /SV (mJ/ml)	0.021[0.014-0.033] ^a	0.018 [0.010-0.022]	0.08
KE _{cycle} /SV (mJ/ml)	0.023±0.008	0.021±0.005	0.42
Fontan subgroups			
	Concordant in-to-outflow (N=21)	Discordant in-to-outflow (N=9)	P-value
KE _{systole} /SV (mJ/ml)	0.023±0.009	0.042±0.019	0.001
KE _{peak-systole} /SV (mJ/ml)	0.041±0.018	0.074±0.031	0.001
KE _{diastole} /SV (mJ/ml)	0.017[0.013-0.023]	0.017±0.005	0.86
KE _{E-peak} /SV (mJ/ml)	0.031[0.023-0.037]	0.040±0.016	0.30
KE _{A-peak} /SV (mJ/ml)	0.028[0.018-0.036]	0.015±0.006	0.008
KE _{cycle} /SV (mJ/ml)	0.021±0.008	0.026±0.005	0.14
	Left ventricle (N=11)	Right ventricle (N=13)	P-value
KE _{systole} /SV (mJ/ml)	0.023[0.015-0.048]	0.025±0.011	0.87
KE _{peak-systole} /SV (mJ/ml)	0.038[0.028-0.083]	0.046±0.021	0.87
KE _{diastole} /SV (mJ/ml)	0.016±0.005	0.022 [0.011-0.025]	0.17
KE _{E-peak} /SV (mJ/ml)	0.031±0.011	0.032 [0.023-0.039]	0.65
KE _{A-peak} /SV (mJ/ml)	0.024±0.012	0.028 [0.017-0.038]	0.56
KE _{cycle} /SV (mJ/ml)	0.021±0.007	0.024±0.010	0.40

^aone patient had no a-wave and was excluded
KE=kinetic energy; SV=stroke volume; E-peak=peak early diastole; A-peak=peak late diastole

Relation to conventional markers

In the current study, there was no correlation between E/A ratio and EL_{diastole} ($\rho=0.38$, $P=0.06$) in the Fontan patients. Also, there was no relation between EL_{cycle} and AV regurgitation fraction ($\rho=0.002$, $P=0.99$) and no relation between EL_{index} and AV regurgitation fraction ($\rho=0.02$, $P=0.92$). Comparison between EF and EL_{index} showed poor correlation ($\rho=0.25$, $P=0.18$). Shape of the ventricle, measured by the sphericity index, was not related to EL_{cycle} (EL_{cycle} versus systolic sphericity index: $r=0.18$, $P=0.35$; EL_{cycle} versus diastolic sphericity index: $r=0.12$, $P=0.52$) or EL_{index} (EL_{index} versus systolic sphericity index: $r=0.28$, $P=0.14$; EL_{index} versus diastolic sphericity index: $r=0.30$, $P=0.11$). Furthermore, no relation was observed between EL_{cycle} and VO₂ max from CPET ($\rho=0.05$, $P=0.83$) or EL_{index} and VO₂ max ($\rho=0.11$, $P=0.64$).

Discussion

In the current study, intraventricular viscous energy loss was noninvasively assessed with 4D flow MRI in patients with a Fontan circulation. Main findings of the study are: 1) viscous energy loss was significantly elevated in Fontan patients compared to healthy volunteers; 2) Fontan patients with discordant inflow-to-outflow had significantly elevated viscous energy loss compared to Fontan patients with concordant inflow-to-outflow; 3) viscous energy loss was not significantly different between Fontan patients with a systemic left ventricle versus a systemic right ventricle; 4) EL_{index} , the total amount of viscous energy loss proportional to the average amount of kinetic energy produced over the cardiac cycle, was significantly higher in Fontan patients (disproportionate) compared to healthy controls and EL_{index} was significantly higher in Fontan patients with discordant inflow-to-outflow versus Fontan patients with concordant inflow-to-outflow.

Energetics in Fontan patients versus controls

In the healthy heart, intraventricular blood flow is organized in such a way that is thought to preserve KE and facilitate efficient ejection of the blood [18-20]. Interruption of this natural flow arrangement, as seen in cardiac diseases or after valve replacement, is suggested to increase EL, thereby reducing the efficiency of the cardiac pump [20]. The complex intracardiac deformations in Fontan patients may promote inefficient flow-structure interaction that could increase EL and change the proportion of EL indexed to KE. When increased EL is present for years the accumulative effect might contribute to adverse myocardial adaptation or remodelling due to the accumulated myocardial work load. However, little *in vivo* studies describe the influence of disturbed intracardiac flow patterns on cardiac efficiency and its role in the pathophysiological mechanisms leading to declining circulatory function. Knowledge on the impact of altered geometric arrangement on energetics might help in understanding circulatory failure and aid in early detection of deterioration of ventricular function.

Our results showed that systolic and total EL were significantly elevated in Fontan patients compared to controls. The elevated EL was most pronounced during systole, while EL during diastole was comparable between Fontan patients and controls. This shows that the influence of intracardiac deformations on energetics is largest during systole, most likely due to the higher frictional forces between blood and surrounding structures during systole. Importantly, EL_{index} was significantly higher in Fontan patients compared to controls. This elevated index in Fontan patients shows that the amount of energy that is lost due to viscosity-induced frictional forces is disproportionate to the KE produced, which indicates that the

changes in EL are stimulated by the complex interaction between blood flow and the intracardiac deformations and not merely a reflection of proportionate changes in KE produced.

Intraventricular EL results in the Fontan patients were compared to left ventricular EL of the controls. Although a matter of debate, this approach was chosen because inflow from the pulmonary veins and from the (common) atrium and the afterload posed on the sub systemic ventricle by the aorta is different compared to the venous return, the right atrial inflow and the afterload caused by the pulmonary arterial circulation. Subsequently, systemic loading conditions of the RV sustaining the systemic circulation in Fontan patients induces marked changes to RV function, partly resembling LV contraction patterns [14].

In the current study group of relatively young Fontan patients, we found no correlation between EL and other conventional markers of functional status. Currently, it is largely unknown how the heart reacts to increased EL and how this relates to traditional markers of functional status. However, eventually an accumulation of disproportionate EL present for many years might contribute to increased myocardial load and eventually circulatory failure during long-term follow-up.

As stated above, EL in Fontan patients has not been reported before. Sjöberg et al. [7] recently reported a significantly decreased peak diastolic ventricular KE (normalized by SV) by 4D flow MRI in Fontan patients compared to healthy volunteers (0.028 ± 0.010 versus 0.057 ± 0.011 mJ/ml, $P < 0.001$). Sjöberg et al. [7] did not evaluate E and A filling separately. We showed significantly decreased KE at peak E filling compared to controls (0.032 [0.023-0.039] versus 0.063 ± 0.017 mJ/ml, $P < 0.001$). However, in the current study, KE at peak A filling was not significantly different between Fontan patients and controls (0.021 [0.014-0.033] versus 0.018 [0.010-0.022] mJ/ml, $P = 0.08$). Furthermore, similar to Sjöberg et al. [7], we observed no significant difference in KE at peak systole between Fontan patients and healthy controls.

Energetics in Fontan patients with concordant vs. discordant inflow to outflow

Using computational fluid dynamics, it has been shown that the natural LV geometry leads to the most efficient flow organization from filling to ejection and an unnatural asymmetry caused by cardiac disease or valvular abnormalities reduces this efficiency [20]. To evaluate whether EL in Fontan patients depends on disruption of normal geometry, we performed a subgroup analysis of Fontan patients with discordant inflow-to-outflow versus Fontan patients with concordant inflow-to-outflow. Our results show that Fontan patients with

discordant inflow-to-outflow had significantly elevated EL compared to Fontan patients with concordant inflow-to-outflow. Also, EL_{index} , the proportion of EL indexed to KE produced, was significantly different in this patient group. These results are in line with our hypothesis that abnormal flow-structure interaction, for instance because of an abnormal outflow pathway, leads to disproportionate EL. Being dimensionless, EL_{index} could enable standardized quantification of ventricular energetics and comparison between different patients. As such, EL_{index} could be a novel marker indicating the efficiency of flow-structure interaction. Furthermore, the reported results may have clinical implications for surgical strategy and long-term follow-up in these patients.

KE and EL in Fontan patients with a systemic LV or systemic RV

The systemic RV in Fontan patients is less capable of sustaining systemic pressures [21] and Fontan patients with a systemic RV are more prone to heart failure [22]. In the current study, we compared Fontan patients with a systemic LV versus a systemic RV. However, our results did not display any significant differences in EL or EL_{index} between these two groups, which indicates that the systemic ventricle being the LV or RV is of less influence to the intraventricular energetics in the studied patients.

Limitations

A limitation of the current study is the heterogeneous study group with several underlying anatomies. However, this is inherent to studies with Fontan patients. Furthermore, our subgroups are relatively small and not equal in numbers. Still, the results show large significant differences between the groups. Wong et al. [23] recently reported an association between ventricular shape and functional strain markers in patients with hypoplastic left heart syndrome. We did not find an association between ventricular shape (measured by sphericity index) and EL. However, our study group consisted of patients with several underlying anatomies and the 2D sphericity index might not be the optimal reflection of ventricular shape in these complex patients. In the current study, the healthy volunteers were scanned with a slightly different spatial resolution from the patients. To test the influence of such a difference in resolution on EL and KE results, we have performed additional validation in two healthy volunteers scanned twice (once under each resolution). Results of this validation in *supplementary Table A2* and *supplementary Figure A1* show that the different spatial resolutions that were used for the Fontan patients (**resolution 1**: $3.0 \times 3.0 \times 3.0 \text{ mm}^3$) and volunteers (**resolution 2**: $2.3 \times 2.3 \times 4.2 \text{ mm}^3$) resulted in a relative difference of 1-4% on EL_{cycle} , 3-4% on KE_{cycle} and 3-8% on EL_{index} , which are in the same range as scan-rescan differences that were recently published [11]. The difference in EL_{index} between the total

Fontan group versus the volunteers in the current study was 78%. Therefore, the minor difference in spatial resolutions between healthy subjects and patients that were used in this study, only has a minor effect on EL calculation and can be neglected when compared to the difference in EL between healthy subjects and patients. Lastly, it has to be taken into account that 4D flow MRI recordings are averaged over many heartbeats, thus small-scale fluctuations and intermittent acute phenomena, that may have an important effect on energy dissipation, cannot be evaluated by this technique.

Conclusion

In conclusion, Fontan patients show disproportionate intraventricular viscous energy loss relative to produced kinetic energy. Furthermore, intraventricular viscous energy loss in Fontan patients is elevated compared to healthy controls. Highest viscous energy loss is found in patients with discordant inflow-to-outflow. To our knowledge, this is the first study that provides a quantitative *in vivo* assessment of intraventricular viscous energy loss in Fontan patients using 4D flow MRI. Future studies should further investigate the correlation between viscous energy loss and clinical markers of circulatory failure such as decreased VO_2 max during exercise tests and increased NTproBNP and the use of energy loss parameters in early detection or prediction of heart failure.

Supplementary Data

Formulae for the computation of viscous energy loss from 4D flow MRI are provided in supplementary methods. Additional characteristics of the Fontan patients are shown in the *supplementary Table A1*. An additional experiment in two volunteers scanned with different spatial resolutions is shown in *supplementary Table A2* and *supplementary Figure A1*. Non-normalized EL and EL normalized by SV results are also shown in the supplementary data (*Table A3* and *A4*, respectively)

References

1. Fontan F, Baudet E: Surgical repair of tricuspid atresia. *Thorax* 1971, 26:240-248.
2. Gewillig M: The Fontan circulation. *Heart* 2005, 91:839-846.
3. She HL, Roest AA, Calkoen EE, van den Boogaard PJ, van der Geest RJ, Hazekamp MG, de Roos A, Westenberg JJ: Comparative Evaluation of Flow Quantification across the Atrioventricular Valve in Patients with Functional Univentricular Heart after Fontan's Surgery and Healthy Controls: Measurement by 4D Flow Magnetic Resonance Imaging and Streamline Visualization. *Congenit Heart Dis* 2017, 12:40-48.
4. Alsaied T, Bokma JP, Engel ME, Kuijpers JM, Hanke SP, Zuhlke L, Zhang B, Veldtman GR: Factors associated with long-term mortality after Fontan procedures: a systematic review. *Heart* 2017, 103:104-110.
5. Ponikowski P, Voors AA, Anker SD, Bueno H, Cleland JG, Coats AJ, Falk V, Gonzalez-Juanatey JR, Harjola VP, Jankowska EA, et al: 2016 ESC Guidelines for the diagnosis and treatment of acute and chronic heart failure: The Task Force for the diagnosis and treatment of acute and chronic heart failure of the European Society of Cardiology (ESC) Developed with the special contribution of the Heart Failure Association (HFA) of the ESC. *Eur Heart J* 2016, 37:2129-2200.
6. Kamphuis VP, Westenberg JJM, van der Palen RLF, Blom NA, de Roos A, van der Geest R, Elbaz MSM, Roest AAW: Unravelling cardiovascular disease using four dimensional flow cardiovascular magnetic resonance. *Int J Cardiovasc Imaging* 2017, 33:1069-1081.
7. Sjöberg P, Heiberg E, Wingren P, Ramgren Johansson J, Malm T, Arheden H, Liuba P, Carlsson M: Decreased Diastolic Ventricular Kinetic Energy in Young Patients with Fontan Circulation Demonstrated by Four-Dimensional Cardiac Magnetic Resonance Imaging. *Pediatr Cardiol* 2017, 38:669-680.
8. Elbaz MS, van der Geest RJ, Calkoen EE, de Roos A, Lelieveldt BP, Roest AA, Westenberg JJ: Assessment of viscous energy loss and the association with three-dimensional vortex ring formation in left ventricular inflow: In vivo evaluation using four-dimensional flow MRI. *Magn Reson Med* 2017, 77:794-805.
9. Akins CW, Travis B, Yoganathan AP: Energy loss for evaluating heart valve performance. *J Thorac Cardiovasc Surg* 2008, 136:820-833.
10. Agati L, Cimino S, Tonti G, Cicogna F, Petronilli V, De Luca L, Iacoboni C, Pedrizzetti G: Quantitative analysis of intraventricular blood flow dynamics by echocardiographic particle image velocimetry in patients with acute myocardial infarction at different stages of left ventricular dysfunction. *Eur Heart J Cardiovasc Imaging* 2014, 15:1203-1212.
11. Kamphuis VP, Westenberg JJM, van der Palen RLF, van den Boogaard PJ, van der Geest RJ, de Roos A, Blom NA, Roest AAW, Elbaz MSM: Scan-rescan reproducibility of diastolic left ventricular kinetic energy, viscous energy loss and vorticity assessment using 4D flow MRI: analysis in healthy subjects. *Int J Cardiovasc Imaging* 2018, 34: 905-920.
12. Ten Harkel AD, Takken T, Van Osch-Gevers M, Helbing WA: Normal values for cardiopulmonary exercise testing in children. *Eur J Cardiovasc Prev Rehabil* 2011, 18:48-54.
13. Calkoen EE, Roest AA, Kroft LJ, van der Geest RJ, Jongbloed MR, van den Boogaard PJ, Blom NA, Hazekamp MG, de Roos A, Westenberg JJ: Characterization and improved quantification of left ventricular inflow using streamline visualization with 4DFlow MRI in healthy controls and patients after atrioventricular septal defect correction. *J Magn Reson Imaging* 2015, 41:1512-1520.
14. Petersen E, Helle-Valle T, Edvardsen T, Lindberg H, Smith HJ, Smevik B, Smiseth OA, Andersen K: Contraction pattern of the systemic right ventricle shift from longitudinal to circumferential shortening and absent global ventricular torsion. *J Am Coll Cardiol* 2007, 49:2450-2456.
15. Kanski M, Toger J, Steding-Ehrenborg K, Xanthis C, Bloch KM, Heiberg E, Carlsson M, Arheden H: Whole-heart four-dimensional flow can be acquired with preserved quality without respiratory gating, facilitating clinical use: a head-to-head comparison. *BMC Med Imaging* 2015, 15:20.
16. Kamphuis VP, van der Palen RLF, de Koning PJH, Elbaz MSM, van der Geest RJ, de Roos A, Roest AAW, Westenberg JJM: In-scan and scan-rescan assessment of LV in- and outflow volumes by 4D flow MRI versus 2D planimetry. *J Magn Reson Imaging* 2018, 47:511-522.
17. Klein S, Staring M, Murphy K, Viergever MA, Pluim JP: elastix: a toolbox for intensity-based medical image registration. *IEEE Trans Med Imaging* 2010, 29:196-205.

18. Bellhouse BJ: Fluid mechanics of a model mitral valve and left ventricle. *Cardiovasc Res* 1972, 6:199-210.
19. Kilner PJ, Yang GZ, Wilkes AJ, Mohiaddin RH, Firmin DN, Yacoub MH: Asymmetric redirection of flow through the heart. *Nature* 2000, 404:759-761.
20. Pedrizzetti G, Domenichini F: Nature optimizes the swirling flow in the human left ventricle. *Phys Rev Lett* 2005, 95:108101.
21. Sano T, Ogawa M, Taniguchi K, Matsuda H, Nakajima T, Arisawa J, Shimazaki Y, Nakano S, Kawashima Y: Assessment of ventricular contractile state and function in patients with univentricular heart. *Circulation* 1989, 79:1247-1256.
22. Khairy P, Fernandes SM, Mayer JE, Jr., Friedman JK, Walsh EP, Lock JE, Landzberg MJ: Long-term survival, modes of death, and predictors of mortality in patients with Fontan surgery. *Circulation* 2008, 117:85-92.
23. Wong J, Lamata P, Rathod RH, Bertaud S, Dedieu N, Bellsham-Revell H, Pushparajah K, Razavi R, Hussain T, Schaeffter T, et al: Right ventricular morphology and function following stage I palliation with a modified Blalock-Taussig shunt versus a right ventricle-to-pulmonary artery conduit. *Eur J Cardiothorac Surg* 2017, 51:50-57.

Supplementary data

Supplementary methods

Viscous Energy Loss Computation from 4D flow MRI

Viscous energy loss corresponds to the kinetic energy that is irreversibly converted/lost to thermal energy due to frictional forces induced in the fluid through fluid viscosity and the no-slip condition. Viscous energy loss is computed using the viscous dissipation function Φ_v which represents the work done by the viscous stresses (i.e. frictional forces) on a fluid particle. That is, Φ_v quantifies the rate of viscosity-induced energy dissipation per unit volume. Viscous stresses induced by frictional forces in the fluid, stimulating viscous energy dissipation, can be computed in terms of the viscous stress tensor (a tensor that quantifies the rate of fluid deformation due to viscosity and boundary slip condition). From the Navier-Stokes energy balance equations of incompressible Newtonian fluid, it can be derived that the loss of kinetic energy (to heat) due to viscosity-induced frictional/stress forces on a fluid particle can be computed in terms of the dissipation function Φ_v and the dynamic viscosity μ as follows (1,2):

Given the acquired velocity field v , the rate of viscous energy loss (\dot{EL}) in watt (W) and the total energy loss in joule (J) over a given period of time T can be computed from 4D flow MRI using the viscous dissipation function Φ_v in the Newtonian Navier-Stokes energy equations:

$$\Phi_v = \frac{1}{2} \sum_{i=1}^3 \sum_{j=1}^3 \left[\left(\frac{\partial v_i}{\partial x_j} + \frac{\partial v_j}{\partial x_i} \right) - \frac{2}{3} (\nabla \cdot v) \delta_{ij} \right]^2, \begin{cases} \delta_{ij} = 1, \text{ if } i = j \\ \delta_{ij} = 0, \text{ if } i \neq j \end{cases} \text{ [s}^{-2}\text{]} \quad [\text{Eq.1}]$$

Φ_v represents the rate of viscous energy dissipation per unit volume. i, j correspond to the principal velocity directions x, y, z . $\nabla \cdot v$ denotes the divergence of the velocity field. Therefore, the rate of viscous energy loss (\dot{EL}) in Watt at an acquired time phase t can be computed as:

$$\dot{EL}_t = \mu \sum_{i=1}^M \Phi_v L_i \text{ [watt (W)]} \quad [\text{Eq.2}]$$

assuming the blood as a Newtonian fluid, the dynamic viscosity is $\mu=0.004$ Pa·s, N as the total number of voxels in the given domain of interest (e.g. LV), L_i as the voxel volume.

As a result, the total viscous energy loss (EL) in joules over time period T starting at phase t_{start} and ending at t_{end} can be computed as:

$$\mathbf{EL}_T = \sum_{d=t_{\text{start}}}^{t_{\text{end}}} \mathbf{EL}_d \mathbf{p}_d \text{ [joule (J)]} \quad [\text{Eq.3}]$$

with p_d the time step (temporal resolution) of the acquired 4D flow MRI.

For more details on the derivation of the viscous dissipation function and viscous energy loss, readers are referred to (2)

References belonging to the supplementary data

1. Elbaz MS, van der Geest RJ, Calkoen EE, de Roos A, Lelieveldt BP, Roest AA, et al. Assessment of viscous energy loss and the association with three-dimensional vortex ring formation in left ventricular inflow: In vivo evaluation using four-dimensional flow MRI. *Magn Reson Med*. 2017;77(2):794-805.
2. Canuto C, Quarteroni A, Hussaini MY, Zang TA. Fundamentals of Fluid Dynamics. In: Canuto C, Hussaini MY, Quarteroni A, Zang TA, editor. *Spectral Methods - Evolution to Complex Geometries and Applications to Fluid Dynamics*. Berlin Heidelberg: Springer-Verlag 2007.

Table A1. Individual subject characteristics

Subject	Diagnosis	Ventricular morphology	Concordant/discordant inflow to outflow	Type of Fontan	Fenestration (at time of MRI)	NYHA class
1	HLHS	Right	Concordant	Extacardiac	no	I
2	cAVSD, DORV	Biventricular	Discordant	Lateral tunnel	Yes	II
3	TGA, VSD, PS, hypoplastic LV	Biventricular	Discordant	Extacardiac	No	I
4	TA	Left	Concordant	Extacardiac	No	I
5	HLHS	Right	Concordant	Extacardiac	No	I
6	DILV, with aorta from RV	Left	Discordant	Extacardiac	No	I
7	HLHS	Right	Concordant	Extacardiac	No	I
8	TGA, VSD, hypoplastic RV	Left	Discordant	Extacardiac	No	I
9	HLHS	Right	Concordant	Extacardiac	No	I
10	TA	Left	Concordant	Extacardiac	No	I
11	DILV, with aorta from RV	Left	Discordant	Extacardiac	No	I
12	HLHS	Right	Concordant	Extacardiac	No	I
13	TA	Left	Concordant	Extacardiac	No	I
14	DORV	Right	Concordant	Extacardiac	No	I
15	Unbalanced AVSD, hypoplastic LV	Biventricular	Discordant	Extacardiac	No	I
16	ccTGA, VSD, PS, straddling TV	Biventricular	Discordant	Extacardiac	No	I
17	ccTGA, VSD, PS, straddling TV	Biventricular	Discordant	Extacardiac	No	I
18	HLHS	Right	Concordant	Extacardiac	No	I
19	HLHS	Right	Concordant	Extacardiac	No	I
20	PA	Left	Concordant	Extacardiac	No	II
21	TA	Left	Concordant	Lateral tunnel	No	I
22	DORV, PS	Right	Concordant	Extacardiac	No	I
23	TGA, multiple VSDs, PA	Biventricular	Discordant	Extacardiac	No	II
24	HLHS	Right	Concordant	Extacardiac	No	I
25	HLHS	Right	Concordant	Extacardiac	No	I
26	TA	Left	Concordant	Extacardiac	No	I
27	HLHS	Right	Concordant	Extacardiac	No	I
28	PA	Left	Concordant	Extacardiac	No	I
29	TA	Left	Concordant	Extacardiac	No	I
30	HLHS	Right	Concordant	Extacardiac	No	I

Abbreviations: NYHA = New York Heart Association; cAVSD = complete atrioventricular septal defect; ccTGA = congenitally corrected transposition of the great arteries; DILV = double inlet left ventricle; DORV = double outlet right ventricle; LV = left ventricle; HLHS = hypoplastic left heart syndrome; VSD = ventricular septal defect; PA = pulmonary atresia; PS = pulmonary stenosis; RV = right ventricle; TGA = transposition of the great arteries; TV=tricuspid valve

Table A2. Spatial resolution test in additional healthy volunteers

Subject 1				
Age (y)	49			
Gender	Male			
EDV (mL)	154.9			
SV (mL)	84.7			
CO (L/min)	5.6			
	Spatial resolution 1*	Spatial resolution 2*	Absolute difference	Relative difference (%)
EL _{systole} (mJ)	0.22	0.23	0.02	8
EL _{peak-systole} (mW)	1.01	1.13	0.12	11
EL _{diastole} (mJ)	0.37	0.23	-0.13	-36
EL _{E-peak} (mW)	1.25	1.31	0.06	5
EL _{A-peak} (mW)	1.05	0.80	-0.25	-24
EL _{cycle} (mJ)	0.59	0.57	-0.02	-4
KE _{systole} (mJ)	1.32	1.40	0.08	6
KE _{peak-systole} (mJ)	2.49	2.81	0.32	13
KE _{diastole} (mJ)	1.18	1.21	0.04	3
KE _{E-peak} (mJ)	3.09	4.07	0.98	32
KE _{A-peak} (mJ)	2.34	2.15	-0.18	-8
KE _{cycle} (mJ)	1.23	1.28	0.05	4
EL _{index}	0.48	0.44	-0.04	-8
Subject 2				
Age	29			
Gender	Male			
EDV	236.5			
SV	107.8			
CO (L/min)	6.4			
	Spatial resolution 1*	Spatial resolution 2*	Absolute difference	Relative difference (%)
EL _{systole} (mJ)	0.42	0.40	-0.02	-4
EL _{peak-systole} (mW)	1.47	1.38	-0.09	-6
EL _{diastole} (mJ)	0.49	0.50	0.01	2
EL _{E-peak} (mW)	1.61	1.62	0.00	0
EL _{A-peak} (mW)	0.85	0.86	0.01	1
EL _{cycle} (mJ)	0.91	0.90	-0.01	-1
KE _{systole} (mJ)	2.52	2.39	-0.13	-5
KE _{peak-systole} (mJ)	4.82	4.38	-0.44	-9
KE _{diastole} (mJ)	2.04	2.00	-0.04	-2
KE _{E-peak} (mJ)	5.56	5.24	-0.32	-6
KE _{A-peak} (mJ)	2.52	2.52	0.01	0
KE _{cycle} (mJ)	2.23	2.15	-0.08	-3
EL _{index}	0.41	0.42	0.01	3
* Spatial resolution 1 = $3.0 \times 3.0 \times 3.0 \text{ mm}^3$, spatial resolution 2 = $2.3 \times 2.3 \times 4.2 \text{ mm}^3$				

Abbreviations: EDV = end-diastolic volume; SV = stroke volume; CO = cardiac output; EL = viscous energy loss; E-peak = peak early diastole; A-peak = peak late diastole; KE = kinetic energy

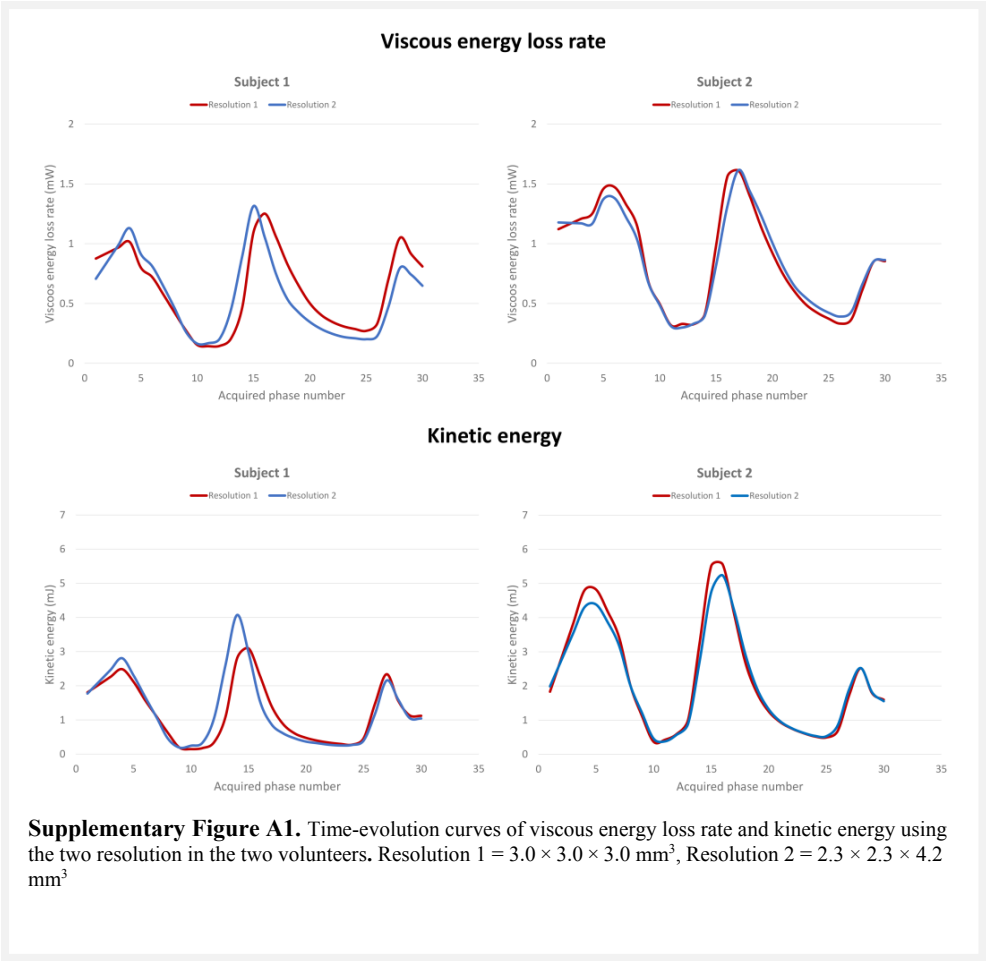


Table A3. Quantitative analysis of non-normalized viscous energy loss

Total study group			
	Fontan patients (N=30)	Controls (N=15)	P-value
EL _{systole} (mJ)	0.3 [0.2-0.4]	0.1±0.0	<0.001
EL _{peak-systole} (mW)	1.5 [0.6-2.3]	0.6±0.2	0.001
EL _{diastole} (mJ)	0.2 [0.2-0.3]	0.2±0.1	0.09
EL _{E-peak} (mW)	1.0 [0.6-1.3]	1.2±0.4	0.23
EL _{A-peak} (mW) ^a	0.8±0.4	0.4±0.2	<0.001
EL _{cycle} (mJ)	0.5 [0.4-0.7]	0.3±0.1	<0.001
Fontan subgroups			
	Concordant in- to outflow (N=21)	Discordant in- to outflow (N=9)	P-value
EL _{systole} (mJ)	0.2±0.1	0.6±0.3	<0.001
EL _{peak-systole} (mW)	1.1±0.6	2.5 [2.1-4.1]	<0.001
EL _{diastole} (mJ)	0.2±0.1	0.3 [0.3-0.4]	0.002
EL _{E-peak} (mW)	0.9 [0.6-1.2]	1.3 [0.9-1.6]	0.04
EL _{A-peak} (mW) ^a	0.8±0.4	0.7±0.4	0.60
EL _{cycle} (mJ)	0.5±0.2	1.0±0.4	<0.001
	Left ventricle (N=11)	Right ventricle (N=13)	
EL _{systole} (mJ)	0.2 [0.2-0.6]	0.2±0.1	0.61
EL _{peak-systole} (mW)	1.1 [0.7-3.0]	1.2±0.7	0.65
EL _{diastole} (mJ)	0.3±0.1	0.2±0.1	0.44
EL _{E-peak} (mW)	0.8±0.3	1.0±0.5	0.17
EL _{A-peak} (mW) ^a	0.6 [0.4-0.8]	0.8±0.4	0.33
EL _{cycle} (mJ)	0.6±0.4	0.5±0.1	0.20

^aone patient had no A-wave and was excluded

Abbreviations: EL = viscous energy loss; E-peak = peak early diastole; A-peak = peak late diastole

Table A4. Quantitative analysis of viscous energy loss normalized by stroke volume

Total study group			
	Fontan patients (N=30)	Controls (N=15)	<i>P</i> -value
EL _{systole} /SV (J/m ³)	4.3 [2.7-5.9]	1.5±0.4	<0.001
EL _{peak-systole} /SV (W/m ³)	18.6 [11.6-29.7]	8.6±2.2	<0.001
EL _{diastole} /SV (J/m ³)	3.7 [3.0-4.7]	2.8±0.6	0.002
EL _{E-peak} /SV (W/m ³)	13.4 [9.6-18.6]	16.2±4.6	0.30
EL _{A-peak} /SV (W/m ³) ^a	10.8 [7.2-16.3] ^a	5.1 [3.1-6.5]	<0.001
EL _{cycle} /SV (J/m ³)	8.1 [6.0-10.7]	4.3±0.7	<0.001
Fontan subgroups			
	Concordant in- to outflow (N=21)	Discordant in- to outflow (N=9)	<i>P</i> -value
EL _{systole} /SV (J/m ³)	3.8±1.7	8.8±5.4	<0.001
EL _{peak-systole} /SV (W/m ³)	17.9 [8.2-26.3]	48.8±35.4	0.003
EL _{diastole} /SV (J/m ³)	3.4 [2.7-3.9]	5.0±1.7	0.02
EL _{E-peak} /SV (W/m ³)	13.0 [9.1-16.8]	17.3±6.0	0.14
EL _{A-peak} /SV (W/m ³) ^a	13.4 [7.6-16.9] ^a	8.5±2.4	0.05
EL _{cycle} /SV (J/m ³)	7.5±2.7	13.8±6.7	0.001
	Left ventricle (N=11)	Right ventricle (N=13)	<i>P</i> -value
EL _{systole} /SV (J/m ³)	3.2 [2.6-8.7]	4.1±1.7	0.87
EL _{peak-systole} /SV (W/m ³)	18.5[11.2-40.4]	19.9±12.1	0.73
EL _{diastole} /SV (J/m ³)	4.3±2.2	3.6[3.1-3.9]	0.96
EL _{E-peak} /SV (W/m ³)	10.5[9.3-18.0]	13.9[10.7-18.5]	0.39
EL _{A-peak} /SV (W/m ³) ^a	11.0±5.6	15.8[7.6-17.3]	0.36
EL _{cycle} /SV (J/m ³)	6.2[5.0-14.3]	7.9±2.3	0.91

^aone patient had no a-wave and was excluded

Abbreviations: SV = stroke volume; E-peak = peak early diastole; A-peak = peak late diastole; EL = viscous energy loss

Chapter 11

Intraventricular vorticity is associated with viscous energy loss and kinetic energy from 4D flow MRI in healthy subjects and Fontan patients

Vivian P Kamphuis, Arno AW Roest, Pieter J van den Boogaard, Lucia JM Kroft, Hildo J. Lamb, Willem A Helbing, Nico A Blom, Jos JM Westenberg, Mohammed SM Elbaz

Submitted

Abstract

Objective

The aims of this study were to use 4D flow MRI to directly assess 1) the association of *in vivo* left ventricular (LV) vorticity with kinetic energy (KE) and viscous energy loss (EL) over the cardiac cycle in healthy subjects; 2) intraventricular vorticity in Fontan patients and the relation to KE and EL over the cardiac cycle and 3) the relation between ejection fraction (EF) with vorticity, EL and KE in the studied cohort.

Methods

15 healthy subjects and 30 Fontan patients underwent whole-heart 4D flow MRI. Ventricular vorticity, KE and EL were computed over systole (vorticity_vol_{avg systole}, KE_{avg systole}, EL_{avg systole}) and diastole (vorticity_vol_{avg diastole}, KE_{avg diastole}, EL_{avg diastole}). The association between vorticity_vol and KE and EL was tested by Spearman correlation. Furthermore, Fontan patients were grouped by EF as within or below the 95% confidence interval derived from the healthy subjects.

Results

In healthy subjects, vorticity_vol showed strong-excellent correlation with KE (systole: $\rho=0.96$, $P<0.001$; diastole: $\rho=0.90$, $P<0.001$) and good-strong correlation with EL (systole: $\rho=0.85$, $P<0.001$; diastole: $\rho=0.84$, $P<0.001$). Fontan patients showed significantly higher vorticity_vol compared to healthy subjects (vorticity_vol_{avg systole}: 3141.7 [2285.9-3875.8] vs 1738.6 [1338.2-2414.7] mL/s, $P<0.001$; vorticity_vol_{avg diastole}: 3078.0 [2042.0-3655.0] vs 2109.3 [1586.3-2818.1] mL/s, $P=0.002$). Still, in Fontan patients vorticity_vol also showed good-strong correlation with KE (systole: $\rho=0.91$, $P<0.001$; diastole: $\rho=0.85$, $P<0.001$) and EL (systole: $\rho=0.82$, $P<0.001$; diastole: $\rho=0.89$, $P<0.001$). Notably, Fontan patients with an EF within the 95% confidence interval derived from the healthy subjects showed significantly higher vorticity_vol_{avg systole} and EL_{avg systole}, but significantly decreased KE_{avg diastole}, compared to the healthy subjects.

Conclusions

There is a good-excellent correlation between 4D flow MRI-derived vorticity, kinetic energy and viscous energy loss in healthy subjects and Fontan patients. Fontan patients show higher vorticity compared to healthy subjects. Though, despite the higher levels, volumetric vorticity in Fontan patients show a persistent good-strong correlation with kinetic energy and viscous energy loss.

Background

In the healthy left ventricle (LV), both *in vivo* and *in vitro* studies have confirmed the formation of vortical flow patterns within the ventricular blood flow [1-3]. Nevertheless, it remains unclear how such vortical flow impacts or associates with cardiac (patho)physiology. Earlier *in vivo* studies have postulated a role of vortical flow in maintaining kinetic energy (KE) in a manner that minimizes energy loss (EL) to reduce the mechanical energy needed to direct inflow towards the outflow tract during the subsequent systole [2, 3]. These observations suggest that vortical flow affects both intracardiac flow and ventricular function. Nevertheless, such speculated association between vortical flow with KE and EL has not been directly verified *in vivo* over the intrinsically three-dimensional time-varying intraventricular flow over the cardiac cycle neither in healthy subjects nor patients. Furthermore, the association of vortical flow, KE and EL to conventional measures of ventricular function such as ejection fraction (EF) remains unclear.

Four-dimensional (4D) flow magnetic resonance imaging (MRI) provides the three-directional, three-dimensional time-varying flow field that enables *in vivo* time-varying volumetric measurements of intraventricular KE, EL and vorticity (curl of velocity-a measure of vortical flow strength) over the entire cardiac cycle [4-6]. Therefore, 4D flow MRI could enable direct quantitative verification of the postulated association between vortical flow (by means of vorticity), KE and EL in a volumetric time-varying manner in the entire intraventricular flow and over the cardiac cycle in healthy subjects and patients.

In patients with a Fontan circulation, a palliative procedure for patients in whom a biventricular circulation cannot be created [7], the abnormal underlying ventricular anatomy could impact intraventricular hemodynamics resulting in complex altered flow patterns [8-13]. Even though survival after the Fontan operation has increased drastically in the past decades, Fontan patients are still prone to circulatory failure [14]. Studying the association of vorticity with EL and KE in Fontan patients could potentially help improve our understanding of the complex hemodynamics interplay in patients with abnormal ventricular anatomy as compared to healthy subjects. Hence, might eventually aid in the early detection of deterioration of ventricular function.

The aims of this study were to use 4D flow MRI to directly assess 1) the association of *in vivo* LV vorticity with KE and EL over the cardiac cycle in healthy subjects; 2) intraventricular vorticity in Fontan patients and the relation to KE and EL over the cardiac cycle and 3) the relation between EF (by MRI) with vorticity, EL and KE in the studied cohort.

Methods

Study population

A total of 45 subjects were included in this study: Fifteen healthy subjects were part of a total group of 30 healthy subjects of whom the KE and EL were reported previously in comparison to corrected atrioventricular septal defect patients [4]. Also, 30 Fontan patients were included in this study: 7 Fontan patients underwent a CMR scan with 4D flow MRI as part of standard care and 23 were prospectively included as part of a multicenter study that was approved by the Medical Ethical Committee of the Erasmus Medical Center in Rotterdam (MEC-2014-326, NL48188.078.14), with local approval of the Medical Ethical Committee of the Leiden University Medical Center, Leiden, The Netherlands. Informed consent was obtained from all prospectively included participants. Regarding the retrospective data: at the time of the study: in the Netherlands, no ethical approval was required for anonymized studies with patient data that was collected as part of standard care.

Cardiovascular magnetic resonance acquisition

For the Fontan patients, whole-heart 4D flow MRI was obtained on a 3 Tesla scanner (Ingenia, Philips Medical Systems, the Netherlands) with maximal amplitude of 45 mT/m for each axis, slew rate of 200 T/m/s and a combination of FlexCoverage Posterior coil in the table top with a dStream Torso coil, providing up to 32 coil elements for signal reception. Velocity-encoding of 150 cm/s in all three directions was used in a standard four-point encoding scheme, spatial resolution $3.0 \times 3.0 \times 3.0 \text{ mm}^3$ or better, flip angle 10° , echo time (TE) 3.7 ms, repetition time (TR) 7.7-10 ms, true temporal resolution 30-40 ms, sensitivity encoding factor 2 in anterior-posterior direction and echo planar imaging readout with a factor 5. Concomitant gradient correction and phase offset correction was performed using standard available scanner software. Typical acquisition time of the whole-heart 4D flow MRI scan was approximately 8 minutes. Cine two-dimensional left 2-chamber, 4-chamber, coronal and sagittal aorta views and transversal images were acquired, using steady-state free-precession sequences with TE/TR 1.5/3.0, 350 mm field-of-view, 45° flip angle, acquisition resolution $1.9 \times 2.0 \times 8.0 \text{ mm}^3$. Retrospective gating was used with 30 phases reconstructed to represent one cardiac cycle. To allow for a reasonable scanning time, free breathing was allowed without using motion suppression; three signal averages were taken to minimize effects of breathing motion. In the healthy subjects whole-heart 4D flow MRI was obtained on the same 3 Tesla scanner (Ingenia, Philips Medical Systems, the Netherlands). The scan protocol was similar with only a slightly different spatial resolution of $2.3 \times 2.3 \times 4.2 \text{ mm}^3$.

Data preparation

Image analysis was performed by one observer (VPK) with >3 years of experience in CMR and verified by a radiologist (LJMK) with >20 years of experience in CMR. The ventricular volume was calculated at the end-diastolic and end-systolic phases using in-house developed *MASS* software by manually tracing the endocardial border in all slices and phases in the transversal images. Papillary muscles were disregarded and assumed to be included in the ventricular volume. In patients who had two ventricles functioning as the systemic ventricle (mentioned as “biventricular” patients), remaining parts of the septum were not included in the ventricular volume. Stroke volume (SV) was calculated as: left ventricular end-diastolic volume (EDV) – left ventricular end-systolic volume (ESV). Cardiac output (CO) was computed as: $SV \times \text{heart Rate (HR)}$. EF was computed as $((EDV - ESV)/EDV) \times 100$. Following previously published methods [15], start and end of the systolic and diastolic phases were determined from the flow-time curves that resulted from retrospective valve tracking assessing the inflow and outflow of the LV in the healthy subjects and the systemic ventricle in Fontan patients. Segmentation of the ventricular cavity in the 4D flow MRI acquisition, which is required for the energy and vorticity analyses, was obtained following previously published workflow [5]. In brief, the available time-varying segmentation of multi-slice cine transversal anatomical acquisition was transformed to the 4D flow MRI data using automated registration [4]. That is, to account for potential patient-motion related misalignment between the two acquisitions, automated image-based 3D rigid registration by mutual information was performed using the phase with the maximal depiction of the ventricular cavity in both scans with the Elastix image registration toolbox [16]. Analysis of vorticity, EL and KE in the segmented ventricular volumes was done by one investigator (MSME) with >6 years of experience in CMR using an in-house developed MATLAB-based software (MathWorks Inc., version R2013b).

Computation of intraventricular vorticity from 4D flow MRI

Following previously published work [5], for each acquired time-phase, voxel-wise vorticity magnitude (1/s) was first computed. If u, v, w denoted the three velocity field components acquired from 4D flow MRI over the principal velocity directions x, y, z , respectively, the vorticity ($\omega_{i,t}$) at voxel i of an acquired time phase t is:

$$\omega_{i,t} = \left(\frac{\partial w_{i,t}}{\partial y_{i,t}} - \frac{\partial v_{i,t}}{\partial z_{i,t}}, \frac{\partial u_{i,t}}{\partial z_{i,t}} - \frac{\partial w_{i,t}}{\partial x_{i,t}}, \frac{\partial v_{i,t}}{\partial x_{i,t}} - \frac{\partial u_{i,t}}{\partial y_{i,t}} \right) [1/s]$$

Then, the instantaneous integral vorticity magnitude was computed as the cumulative sum of voxel-wise vorticity and multiplied by voxel volume to give the integral in [milliliter.1/second] i.e. [ml/s] with the following formula:

$$\text{Vorticity}_t = \sum_{i=1}^M |\omega_{i,t}| L_{i,t} [\text{mL/s}].$$

With $|\omega_{i,t}|$ as the magnitude of the vorticity vector, M as the total number of voxels in the segmented ventricular volume and $L_{i,t}$ as the voxel volume. Note that the computed vorticity integral parameter is a scalar quantity and therefore does not take the vorticity direction into account. We will refer to this vorticity integral over the ventricular volume as vorticity_vol throughout the text, to differentiate it from voxel-wise vorticity. In order to quantify intraventricular vorticity, the time-average vorticity_vol over systole and diastole (vorticity_vol_{avg systole}, vorticity_vol_{avg diastole}, respectively) was computed. All vorticity parameters were reported as absolute values (mL/s), normalized by EDV (1/s) and normalized by SV (1/s).

Association of vorticity with intraventricular KE and EL from 4D flow MRI

The relation between intraventricular vorticity_vol versus EL and KE during systole and diastole was tested. Following recently published methods [5], we have computed EL from 4D flow MRI using the dissipation terms from the Navier-Stokes energy equations, assuming blood as a Newtonian fluid. Average EL over systole (EL_{avg systole}) and diastole (EL_{avg diastole}) were computed. EL parameters were reported as absolute values (mW), normalized by EDV (mW/mL) and normalized by SV (mW/mL). The amount of intraventricular KE was computed as $\frac{1}{2} mv^2$, with (m) as the mass representing the voxel volume multiplied by the density of blood (1.025 g/ml) and (v) as the 3-directional velocity from 4D flow MRI. For each acquired time-phase, volumetric KE was then computed by integrating (by cumulative sum) the computed KE over the segmented 3D ventricular volume. In order to quantify KE, the time-average kinetic energy over systole (KE_{avg systole}) and diastole (KE_{avg diastole}) were computed.

Relation of ejection fraction with vorticity_vol, KE and EL

To measure the relation between EF versus vorticity_vol, KE and EL, the subjects were grouped based on their EF. First, the normal range of EF was derived from the 95% confidence interval (CI) of the 15 healthy subjects. Then, the Fontan patients were subdivided in patients with EF within the 95% CI of healthy subjects and patients with EF below the lower limit of the 95% CI of healthy subjects.

Statistical Analysis

Data analysis was performed using SPSS Statistics (version 23.0 IBM SPSS, Chicago, IL). Continuous data is reported as median with inter-quartile range (IQR). Comparison of variables amongst different groups was performed using the Mann-Whitney U-test. Correlations between vorticity_vol and KE or EL parameters were tested by the Spearman correlation coefficient (ρ). Correlation was classified as follows: >0.95 : excellent; $0.95-0.85$: strong; $0.85-0.70$: good; $0.70-0.5$: moderate; <0.5 : poor. The Kruskal-Wallis H test (between groups) was used to test whether the differences between the healthy subjects and the Fontan patients with preserved EF and reduced EF were significant. When significant, individual comparisons were made using the Mann-Whitney U-test with Bonferroni correction, resulting in a significance level set at $P<0.017$.

Results

Characteristics of the healthy subjects and Fontan patients are shown in *Table 1*. Median age of the healthy subjects was 14 [11-18] years, median age of the Fontan group was 14 [10-16] years. There were no significant differences in SV or EDV between the healthy subjects and the Fontan patients (SV: 72.4 [55.1-88.7] versus 63.6 [55.8-77.4] mL, $P=0.32$; EDV: 114.0 [90.8-147.2] versus 131.2 [108.2-171.1] mL, $P=0.08$, respectively). There was a significant difference in EF between the healthy subjects and the Fontan patients (62.1 [58.2-65.6] versus 49.2 [43.7-53.6] %, $P<0.001$). The Fontan group consisted of 11 patients with a systemic LV, 13 patients with a systemic right ventricle and 6 "biventricular" patients.

Table 1. Characteristics of healthy subjects and Fontan patients

	Fontan patients (N=30)	Healthy subjects (N=15)	P-value
	Median [IQR]	Median [IQR]	
Age (years)	14 [11-18]	14 [10-16]	0.42
Male (%)	10/30 (33%)	5/15 (33%)	1.00*
BSA (m ²)†	1.4 [1.2-1.6]	1.4 [1.2-1.6]	0.86
HR (bpm)	83.5 [67.8-96.0]	77.0 [68.0-90.0]	0.53
SV (mL)	63.6 [55.8-77.4]	72.4 [55.1-88.7]	0.32
CO (l/min)	5.3 [4.0-6.7]	5.2 [4.5-6.8]	0.44
EDV (mL)	131.2 [108.2-171.1]	114.0 [90.8-147.2]	0.08
EF (%)	49.2 [43.7-53.6]	62.1 [58.2-65.6]	<0.001

*assessed with the Chi-square test

† according to the Mosteller Method: BSA (m²) = square root of (height (cm) × weight (kg)/3600)

Abbreviations: IQR = interquartile range; HR = heart rate; SV = stroke volume; CO = cardiac output; EDV = end-diastolic volume; EF = ejection fraction

Association of LV vorticity_vol with KE and EL in healthy subjects

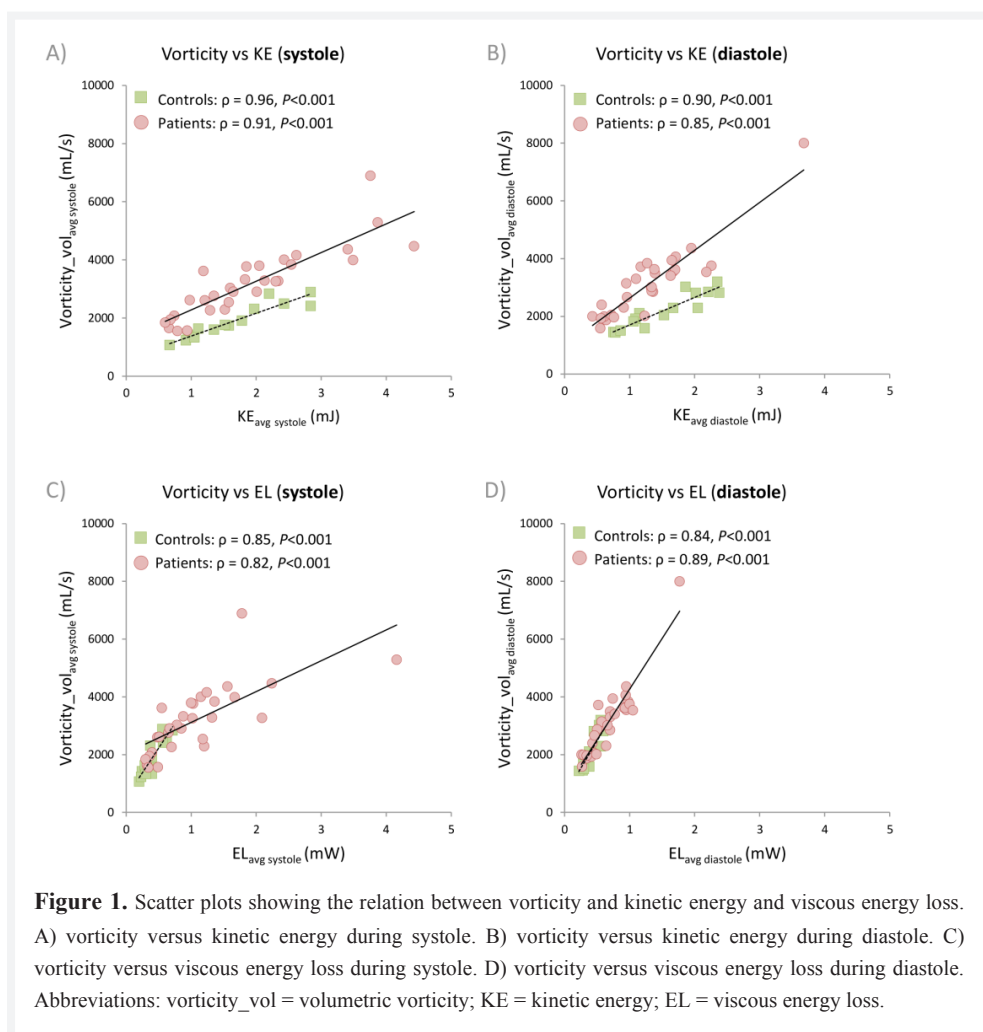
Table 2 shows vorticity_vol analysis in the LV of healthy subjects. In these healthy subjects, average non-normalized vorticity_vol was significantly higher during diastole than during systole (2109.3 [1586.3-2818.1] versus 1738.6 [1338.2-2414.7] mL/s, $P=0.001$). Figure 1 shows scatter plots of the association between vorticity_vol versus KE and EL in healthy subjects. In healthy subjects, vorticity_vol showed significant excellent correlation with KE during systole ($\rho=0.96$, $P<0.001$) and significant strong correlation during diastole ($\rho=0.90$, $P<0.001$); vorticity_vol showed significant strong correlation with EL during systole ($\rho=0.85$, $P<0.001$) and significant good correlation during diastole ($\rho=0.84$, $P<0.001$).

Table 2. Quantitative analysis of vorticity_vol

	Fontan patients (N=30)	Healthy subjects (N=15)	P-value
	Median [IQR]	Median [IQR]	
<i>Systole</i>			
Vorticity_vol _{avg systole} (mL/s)	3141.7 [2285.9-3875.8]	1738.6 [1338.2-2414.7]	<0.001
Vorticity_vol _{avg systole} /SV (1/s)	45.9 [38.2-53.7]	24.9 [21.6-28.1]	<0.001
Vorticity_vol _{avg systole} /EDV (1/s)	21.4 [18.6-25.3]	16.1 [13.6-18.0]	<0.001
<i>Diastole</i>			
Vorticity_vol _{avg diastole} (mL/s)	3078.0 [2042.0-3655.0]	2109.3 [1586.3-2818.1]	0.002
Vorticity_vol _{avg diastole} /SV (1/s)	42.3 [37.4-50.5]	30.6 [26.1-32.8]	<0.001
Vorticity_vol _{avg diastole} /EDV (1/s)	22.3 [17.7-25.0]	19.1 [16.3-20.1]	0.025
Abbreviations: IQR = interquartile range; SV = stroke volume; EDV = end-diastolic volume			

Intraventricular vorticity_vol in Fontan patients

The results of the vorticity_vol analysis in Fontan patients are shown in Table 2. Non-normalized vorticity_vol was not significantly different during diastole compared to systole (3078.0 [2042.0-3655.0] versus 3141.7 [2285.9-3875.8] mL/s, $P=0.63$). Compared to healthy subjects, the average vorticity was significantly higher in Fontan patients during systole (vorticity_vol_{avg systole}: 3141.7 [2285.9-3875.8] versus 1738.6 [1338.2-2414.7] mL/s, $P<0.001$), as well as during diastole (vorticity_vol_{avg diastole}: 3078.0 [2042.0-3655.0] versus 2109.3 [1586.3-2818.1] mL/s, $P=0.002$). Normalization by SV or EDV gave similar results. Figure 1 shows scatter plots of vorticity_vol versus KE and EL in Fontan patients. Vorticity_vol showed strong correlation with KE during systole ($\rho=0.91$, $P<0.001$) and diastole ($\rho=0.85$, $P<0.001$) and vorticity_vol showed good correlation with EL during systole ($\rho=0.82$, $P<0.001$) and strong correlation during diastole ($\rho=0.89$, $P<0.001$).



Association between vorticity_vol, KE, EL and EF

Figure 2 shows a plot of EF in healthy subjects and Fontan patients with limits of the 95% CI derived from the healthy subjects. The 95% CI of EF driven from healthy subjects in this study was 54-70%. Based on the EF of healthy subjects, the Fontan patients were subdivided in patients with EF within the 95% CI of the healthy subjects (n=7) and patients with EF below the lower limit of the 95% CI of the healthy subjects (n=23). Of note, none of the patients had EF above the upper limit of the 95% CI of the healthy subjects.

Table 3 shows results of the quantitative measurements for the healthy subjects and the two Fontan patient groups. Notably, patients with EF within the 95% CI of the healthy subjects showed significantly higher $v_{avg\ systole}$ and $EL_{avg\ systole}$ than the healthy subjects, independent from the normalization method. Furthermore, $KE_{avg\ diastole}/EDV$ is significantly lower in patients with EF within the 95% CI of the healthy subjects compared to healthy subjects, independent from the normalization method. Comparison of patients with EF within the 95% CI of the healthy subjects versus patients with EF below the 95% CI of the healthy subjects showed significantly higher $v_{avg\ diastole}/SV$ for the latter (46.6 [41.0-53.0] versus 36.6 [28.9-39.7, $P=0.001$]). None of the other differences were statistically significant.

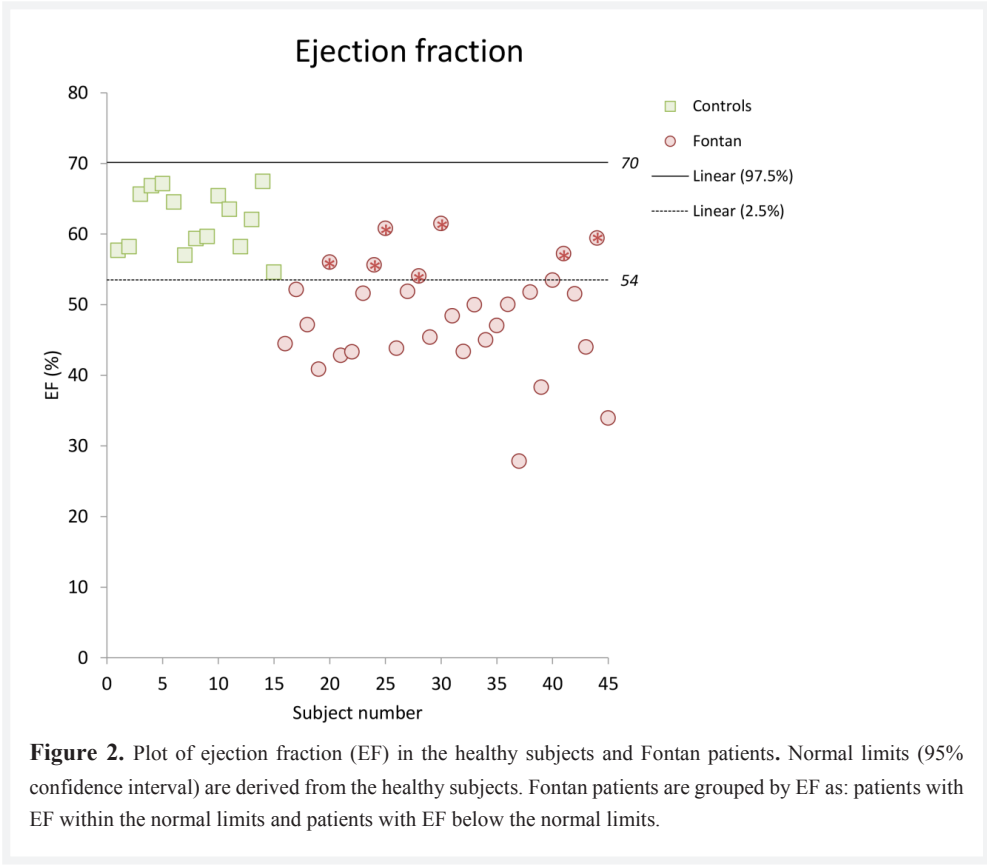


Table 3. 4D flow MRI-derived vorticity, KE and EL versus 2D CMR-derived EF

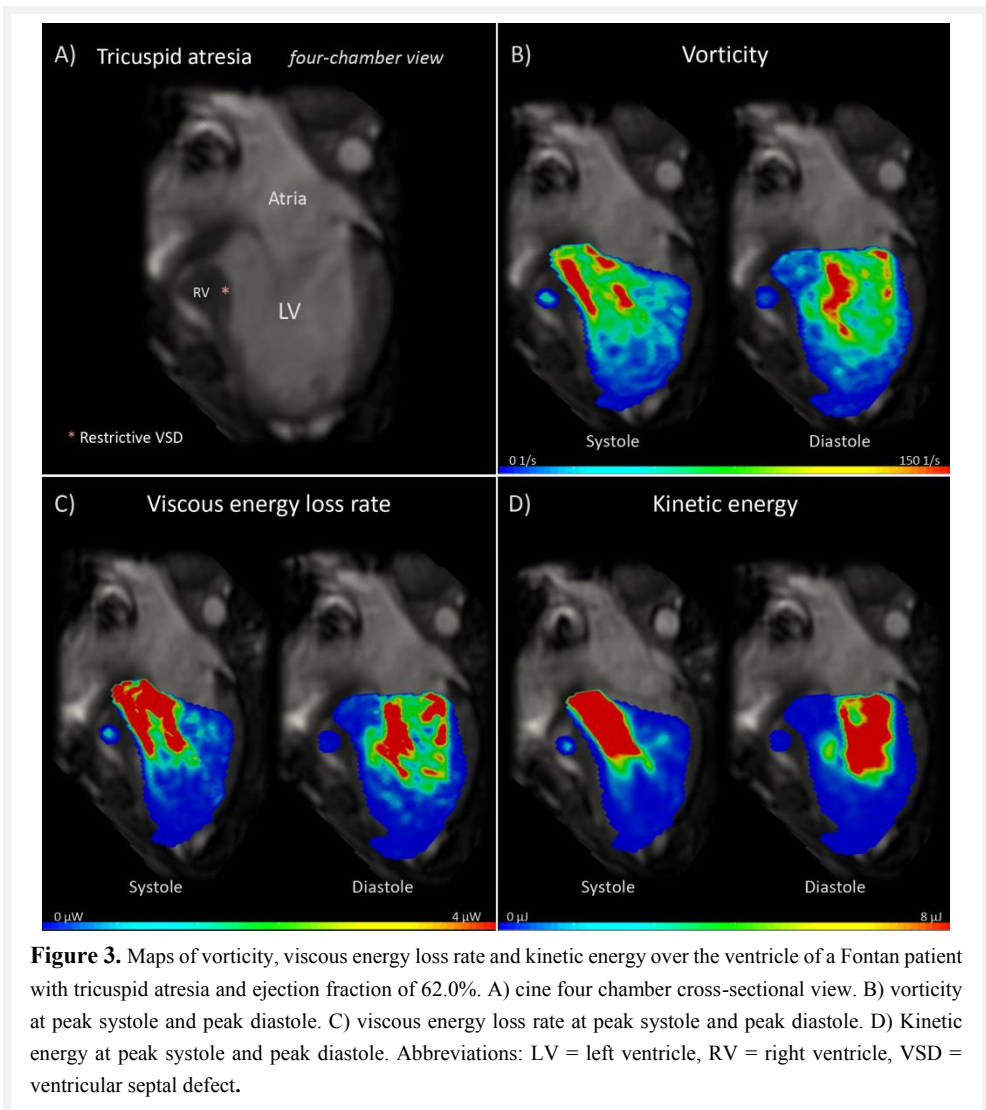
Healthy subjects	Patients in the 95% CI range of EF	Patients below 95% CI of EF	P-value	P-value	P-value	P-value
N=15	N=7	N=23	between all groups*	between controls and patients in the normal range	between controls and patients below 95%CI	between patients in the normal range and patients below 95%CI
Subject characteristics						
Age (years)	14 [10-16]	11 [10-15]	0.14	0.63	0.22	0.05
BSA (m ²)	1.4 [1.2-1.6]	1.3 [1.1-1.3]	0.03	0.08	0.33	0.008**
HR (bpm)	77.0	73.0	0.84	0.54	0.30	0.29
SV (mL)	[68.0-90.0]	[68.0-82.0]				
	72.4	58.2	0.43	0.21	0.52	0.44
	[55.1-88.7]	[52.8-69.3]				
EDV (mL)	114.0	103.4	0.008	0.63	0.016**	0.007**
	[90.8-147.2]	[95.0-123.6]				
Vorticity						
Vorticity_vol _{volsystole} /SV (1/s)	24.9	40.6	<0.001	0.003**	<0.001**	0.04
	[21.6-28.1]	[30.0-43.7]				
Vorticity_vol _{volsystole} /EDV (1/s)	16.1	21.9	<0.001	0.005**	<0.001**	0.92
	[13.6-18.0]	[16.8-26.6]				
Vorticity_vol _{voldiastole} /SV (1/s)	30.6	36.6	<0.001	0.11	<0.001**	0.001**
	[26.1-32.8]	[28.9-39.7]				
Vorticity_vol _{voldiastole} /EDV (1/s)	19.1	20.3	0.05	0.33	0.018	0.31
	[16.3-20.1]	[16.2-24.1]				
Kinetic energy						
KE _{volsystole} /SV (mJ/mL)	0.021	0.023	0.11	0.78	0.04	0.31
	[0.018-0.025]	[0.012-0.029]				
KE _{volsystole} /EDV (mJ/mL)	0.012	0.012	0.94	1.00	0.77	0.85
	[0.011-0.016]	[0.007-0.017]				
KE _{voldiastole} /SV (mJ/mL)	0.021	0.013	0.03	0.011**	0.52	0.02
	[0.015-0.025]	[0.009-0.016]				
KE _{voldiastole} /EDV (mJ/mL)	0.012	0.007	0.006	0.004**	0.013**	0.21
	[0.009-0.016]	[0.005-0.010]				
Viscous energy loss						
EL _{volsystole} /SV (mW/mL)	0.005	0.013	<0.001	0.003**	<0.001**	1.00
	[0.004-0.006]	[0.004-0.023]				
EL _{volsystole} /EDV (mW/mL)	0.003	0.007	0.001	0.004**	<0.001**	0.34
	[0.003-0.004]	[0.003-0.013]				
EL _{voldiastole} /SV (mW/mL)	0.006	0.008	0.001	0.27	<0.001**	0.10
	[0.004-0.008]	[0.004-0.010]				
EL _{voldiastole} /EDV (mW/mL)	0.003	0.004	0.16	0.54	0.05	0.67
	[0.003-0.005]	[0.003-0.006]				

*assessed with the Kruskal-Wallis H test

† according to the Mosteller Method: BSA (m²) = square root of (height (cm) × weight (kg)/3600)

** P<0.017 significant based on Bonferroni correction

Two Fontan patients with EF within the 95% CI of the healthy subjects are depicted in *Figure 3* and *Figure 4*. In *Figure 3*, maps of vorticity, viscous energy loss rate and KE over the ventricle of a Fontan patient with tricuspid atresia and EF of 62.0% are shown. *Figure 4* shows maps of vorticity, viscous energy loss rate and KE over the ventricle of a Fontan patient with an unbalanced atrioventricular septal defect and EF of 61.5%. Despite similar EF, these patients show different vorticity, viscous energy loss rate and KE maps.



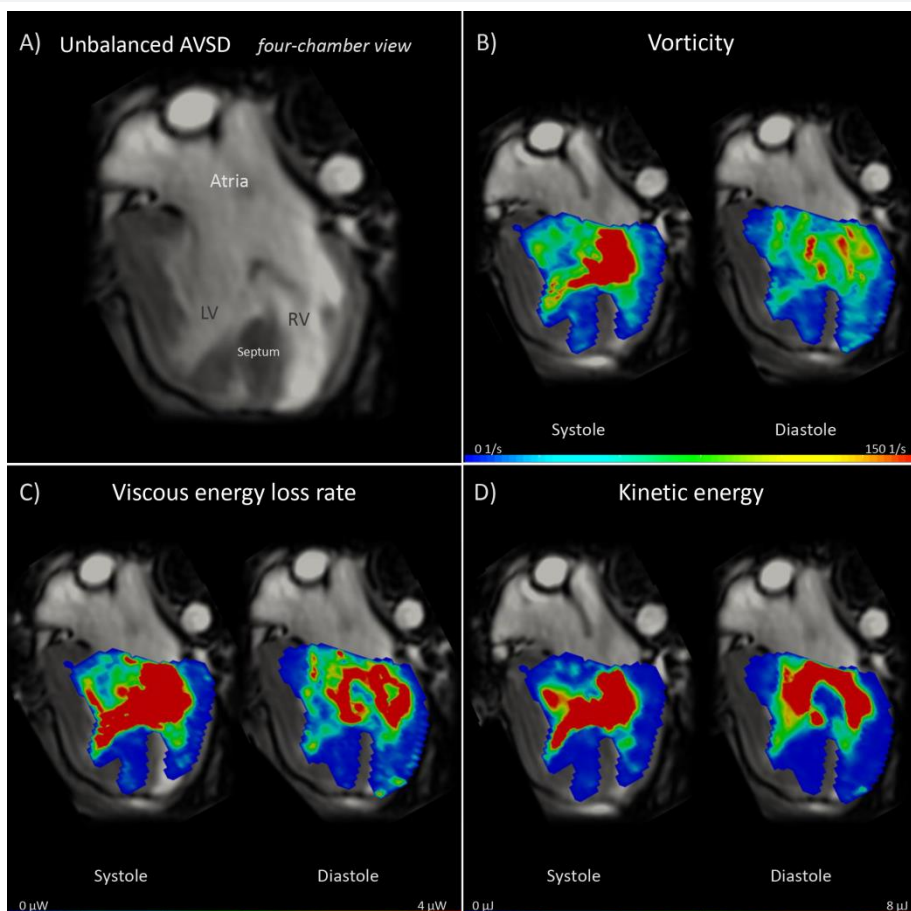


Figure 4. Maps of vorticity, viscous energy loss rate and kinetic energy over the ventricle of a Fontan patient with an unbalanced atrioventricular septal defect and ejection fraction of 61.5%. A) cine four chamber cross-sectional view. B) vorticity at peak systole and peak diastole. C) viscous energy loss rate at peak systole and peak diastole. D) Kinetic energy at peak systole and peak diastole. Abbreviations: LV = left ventricle, RV = right ventricle.

Discussion

In the current study, association of *in vivo* 4D flow MRI-derived intraventricular vorticity, KE and EL was assessed in healthy subjects and Fontan patients. Furthermore, the relation between vorticity, KE and EL and EF (as a measure of global ventricular function), was tested. Main findings of the study were: 1) in healthy subjects, volumetric vorticity (vorticity integral over the ventricular volume) showed strong-excellent correlation with KE and good-strong correlation with EL; 2) Fontan patients showed significantly higher volumetric

vorticity compared to healthy subjects; 3) Despite the higher levels, volumetric vorticity in Fontan patients showed a persistent good-strong correlation with KE and EL. 4) Patients with an EF within the 95% CI derived from the healthy subjects presented significantly increased systolic vorticity and EL and decreased diastolic KE compared to the studied healthy subjects.

LV volumetric vorticity in healthy subjects and relation to KE and EL

Earlier studies have shown that during diastole, a recirculating vortical flow pattern is formed while during systole a half-looped redirection of flow occurs from mitral inflow towards the LV outflow tract [2, 3]. These studies have hypothesized a role of such vortical flow formation in storing KE and minimizing energy loss to facilitate efficient ejection of flow in the systemic circulation [2, 3]. Alterations in this normal flow formation caused by cardiac diseases could lead to increased EL, which could eventually lead to reduced ventricular function [3]. Measuring the relation between vortical flow, KE and EL could provide insight into the (patho)physiological mechanisms of flow energy preservation. The hypothesized association between vortical flow and EL was confirmed in part from a CFD study showing an association between disturbed vortex ring flow patterns and increased energy loss during diastole [3]. This result was recently confirmed *in vivo* [4]. Nevertheless, these studies have only focused on the relation between EL and vortex ring structure (representing only a part of the total vortical flow pattern) at an instance of diastole (around peak diastole- time around full vortex ring formation) but neither on the entire intraventricular vortical flow within the ventricle nor over the entire cardiac cycle. Importantly, to our knowledge, the relation between volumetric vorticity, KE and EL has not been verified *in vivo* from 4D flow MRI in healthy subjects or patients over the cardiac cycle.

Our results showed that volumetric ventricular vorticity (vorticity_vol) in healthy subjects is positively correlated with KE during both systole and diastole. The current study shows that in healthy subjects non-normalized vorticity_vol during diastole was significantly higher than during systole, which indicates that the vortical flow pattern during diastolic filling has a larger contribution to vorticity than the half-looped redirection of flow during systole. As such, our results provide quantitative confirmation and extends the previous postulation on the role of vortical flow in optimizing energetics in the healthy LV to systole and diastole [2]. Such results might emphasize the role of normal vortical flow patterns in optimizing the overall hemodynamic energetics in the ventricle and might help to understand the impact of interventions on intracardiac flow patterns. Hence, might eventually aid in early detection of patients prone to ventricular deterioration.

Intraventricular vorticity_vol in Fontan patients and relation to KE and EL

Intraventricular vorticity from 4D flow MRI has been shown in the LV of patients with chronic obstructive pulmonary disease [17] and the right ventricle (RV) of patients with pulmonary hypertension [18-20] and tetralogy of Fallot [21]. However, intraventricular vorticity in Fontan patients has not been shown. It has been reported that the abnormal ventricular anatomy in these patients causes alterations in 4D flow MRI-derived KE profiles [13]. The current study shows that intraventricular vorticity in Fontan patients is higher than LV vorticity in healthy subjects. Similar to the healthy subjects, our findings showed that in Fontan patients vorticity_vol presented good-strong correlation with KE and EL. This is an important finding, as it shows that despite the inherent heterogeneity of the underlying ventricular anatomy in Fontan patients studied herein, the pronounced association between vorticity, EL and KE still persisted. Our results also suggest that patients with complex vortical flow patterns, e.g. due to structural abnormalities, could be more prone to excessive loss of flow energetics which might contribute on the long term to a decline in cardiac function. This knowledge can be important for all heart diseases, congenital and acquired, leading to cardiac dysfunction as it may help to a better understanding of the contribution of hemodynamic flow patterns to overall disease progression. However, future studies are needed to study the impact of the reported association between vortical flow, KE and EL in different disease progression stages and to reveal whether a better treatment of cardiac function would associate to a restoration of vortical flow and associated energetic levels to a more normal state compared to that of the healthy heart.

In this study, the normal range of EF was derived from the 95% confidence interval of the studied healthy subjects (54-70 %) to allow for a better agreement between the age and gender distribution in the studied healthy subjects with the studied Fontan group, using the same imaging protocol. Nevertheless, this lower limit of 54% is similar to the published normal lower limit of EF in children aged 8-17 years (54% in male subjects, 55% in female subjects) [22]. The current study shows that Fontan patients with EF within the 95% confidence interval still have significantly increased systolic vorticity_vol and EL, but decreased diastolic KE compared to the healthy subjects.

We may speculate that this might mean that hemodynamic alterations by means of vorticity and EL are related to deterioration of ventricular function during long-term follow-up even before changes in conventional function measurements such as EF become apparent. These observations, imply that vorticity could be a sensitive marker to subtle ventricular hemodynamic changes as compared to the more global functional parameters such as EF.

Nevertheless, further studies with larger number of patients, different patient cohorts, multiple 4D flow MRI scans and longer follow-up are needed to further confirm such a link.

Study limitations

This study has some limitations. A limitation is that the Fontan patients form a heterogeneous group with several underlying anatomies, which implies that our findings are only a generalization for all Fontan patients. Nevertheless, our found strong correlations in these patients despite such heterogeneity may further emphasize the soundness of our results. Furthermore, 4D flow MRI data was obtained during free breathing without using motion suppression. However, it has previously been reported that KE and vortex volume quantification from 4D flow MRI can be acquired with preserved accuracy without respiratory gating [23]. Furthermore, spatial resolution was slightly different between healthy subjects and patients. Nevertheless, the reported correlation of vorticity with KE, EL were reported separately for healthy subjects group and the Fontan patient group and similar correlations with the same trend were found over both groups, which could further emphasize the reliability of our results.

Conclusions

Volumetric vorticity correlates well with volumetric viscous energy loss and kinetic energy from 4D flow MRI during both systole and diastole in the left ventricle of healthy subjects. Fontan patients present significantly increased levels of intraventricular vorticity compared to healthy subjects. Despite the higher levels, volumetric vorticity in Fontan patients showed a persistent correlation with kinetic energy and viscous energy loss. Therefore, our *in vivo* results may confirm the previously speculated role of intraventricular vorticity in optimizing kinetic energy and energy loss levels in the ventricle. Notably, Fontan patients with an ejection fraction within the 95% CI of healthy subjects still showed significantly increased levels of systolic vorticity and viscous energy loss and significantly decreased levels of diastolic kinetic energy versus healthy subjects. Further studies with larger number of patients are needed to further understand the impact of such results on cardiac function.

References

1. Elbaz MS, Calkoen EE, Westenberg JJ, Lelieveldt BP, Roest AA, van der Geest RJ: Vortex flow during early and late left ventricular filling in normal subjects: quantitative characterization using retrospectively-gated 4D flow cardiovascular magnetic resonance and three-dimensional vortex core analysis. *J Cardiovasc Magn Reson* 2014, 16:78.
2. Kilner PJ, Yang GZ, Wilkes AJ, Mohiaddin RH, Firmin DN, Yacoub MH: Asymmetric redirection of flow through the heart. *Nature* 2000, 404:759-761.
3. Pedrizzetti G, Domenichini F: Nature optimizes the swirling flow in the human left ventricle. *Phys Rev Lett* 2005, 95:108101.
4. Elbaz MS, van der Geest RJ, Calkoen EE, de Roos A, Lelieveldt BP, Roest AA, Westenberg JJ: Assessment of viscous energy loss and the association with three-dimensional vortex ring formation in left ventricular inflow: In vivo evaluation using four-dimensional flow MRI. *Magn Reson Med* 2017, 77:794-805.
5. Kamphuis VP, Westenberg JJM, van der Palen RLF, van den Boogaard PJ, van der Geest RJ, de Roos A, Blom NA, Roest AAW, Elbaz MSM: Scan-rescan reproducibility of diastolic left ventricular kinetic energy, viscous energy loss and vorticity assessment using 4D flow MRI: analysis in healthy subjects. *Int J Cardiovasc Imaging* 2018, 34: 905-920.
6. Kheradvar AP, G: Vortex formation in the heart. In *Vortex formation in the cardiovascular system*. London: Springer; 2012: 19
7. Fontan F, Baudet E: Surgical repair of tricuspid atresia. *Thorax* 1971, 26:240-248.
8. Kamphuis VP, Roest AAW, Westenberg JJM, Elbaz MSM: Biventricular vortex ring formation corresponds to regions of highest intraventricular viscous energy loss in a Fontan patient: analysis by 4D Flow MRI. *Int J Cardiovasc Imaging* 2018, 34:441-442.
9. Lampropoulos K, Budts W, Van de Bruaene A, Troost E, van Melle JP: Visualization of the intracavitary blood flow in systemic ventricles of Fontan patients by contrast echocardiography using particle image velocimetry. *Cardiovasc Ultrasound* 2012, 10:5.
10. Markl M, Geiger J, Kilner PJ, Foll D, Stiller B, Beyersdorf F, Arnold R, Frydrychowicz A: Time-resolved three-dimensional magnetic resonance velocity mapping of cardiovascular flow paths in volunteers and patients with Fontan circulation. *Eur J Cardiothorac Surg* 2011, 39:206-212.
11. She HL, Roest AA, Calkoen EE, van den Boogaard PJ, van der Geest RJ, Hazekamp MG, de Roos A, Westenberg JJ: Comparative Evaluation of Flow Quantification across the Atrioventricular Valve in Patients with Functional Univentricular Heart after Fontan's Surgery and Healthy Controls: Measurement by 4D Flow Magnetic Resonance Imaging and Streamline Visualization. *Congenit Heart Dis* 2017, 12:40-48.
12. Sundareswaran KS, Haggerty CM, de Zelicourt D, Dasi LP, Pekkan K, Frakes DH, Powell AJ, Kanter KR, Fogel MA, Yoganathan AP: Visualization of flow structures in Fontan patients using 3-dimensional phase contrast magnetic resonance imaging. *J Thorac Cardiovasc Surg* 2012, 143:1108-1116.
13. Sjöberg P, Heiberg E, Wingren P, Ramgren Johansson J, Malm T, Arheden H, Liuba P, Carlsson M: Decreased Diastolic Ventricular Kinetic Energy in Young Patients with Fontan Circulation Demonstrated by Four-Dimensional Cardiac Magnetic Resonance Imaging. *Pediatr Cardiol* 2017, 38:669-680.
14. Alsaied T, Bokma JP, Engel ME, Kuijpers JM, Hanke SP, Zuhlke L, Zhang B, Veldtman GR: Factors associated with long-term mortality after Fontan procedures: a systematic review. *Heart* 2017, 103:104-110.
15. Kamphuis VP, van der Palen RLF, de Koning PJH, Elbaz MSM, van der Geest RJ, de Roos A, Roest AAW, Westenberg JJM: In-scan and scan-rescan assessment of LV in- and outflow volumes by 4D flow MRI versus 2D planimetry. *J Magn Reson Imaging* 2018, 47:511-522.
16. Klein S, Staring M, Murphy K, Viergever MA, Pluim JP: elastix: a toolbox for intensity-based medical image registration. *IEEE Trans Med Imaging* 2010, 29:196-205.
17. Schafer M, Humphries S, Stenmark KR, Kheifets VO, Buckner JK, Hunter KS, Fenster BE: 4D-flow cardiac magnetic resonance-derived vorticity is sensitive marker of left ventricular diastolic dysfunction in patients with mild-to-moderate chronic obstructive pulmonary disease. *Eur Heart J Cardiovasc Imaging* 2018, 19:415-424.

18. Browning JR, Hertzberg JR, Schroeder JD, Fenster BE: 4D Flow Assessment of Vorticity in Right Ventricular Diastolic Dysfunction. *Bioengineering (Basel)* 2017, 4.
19. Fenster BE, Browning J, Schroeder JD, Schafer M, Podgorski CA, Smyser J, Silveira LJ, Buckner JK, Hertzberg JR: Vorticity is a marker of right ventricular diastolic dysfunction. *Am J Physiol Heart Circ Physiol* 2015, 309:H1087-1093.
20. Schafer M, Browning J, Schroeder JD, Shandas R, Kheyfets VO, Buckner JK, Hunter KS, Hertzberg JR, Fenster BE: Vorticity is a marker of diastolic ventricular interdependency in pulmonary hypertension. *Pulm Circ* 2016, 6:46-54.
21. Hirtler D, Garcia J, Barker AJ, Geiger J: Assessment of intracardiac flow and vorticity in the right heart of patients after repair of tetralogy of Fallot by flow-sensitive 4D MRI. *Eur Radiol* 2016.
22. Kawel-Boehm N, Maceira A, Valsangiacomo-Buechel ER, Vogel-Claussen J, Turkbey EB, Williams R, Plein S, Tee M, Eng J, Bluemke DA: Normal values for cardiovascular magnetic resonance in adults and children. *J Cardiovasc Magn Reson* 2015, 17:29.
23. Kanski M, Toger J, Steding-Ehrenborg K, Xanthis C, Bloch KM, Heiberg E, Carlsson M, Arheden H: Whole-heart four-dimensional flow can be acquired with preserved quality without respiratory gating, facilitating clinical use: a head-to-head comparison. *BMC Med Imaging* 2015, 15:20.

Chapter 12

Dobutamine-induced increase in intracardiac kinetic energy,
energy loss and vorticity is inversely related to VO_2 max in
Fontan patients

Vivian P Kamphuis, Mohammed SM Elbaz, Pieter J van den Boogaard, Lucia JM Kroft,
Hildo J Lamb, Mark G Hazekamp, Monique RM Jongbloed, Nico A Blom, Willem A
Helbing, Arno AW Roest*, Jos JM Westenberg*

*Shared last authorship

Submitted for publication

Abstract

Objective

The objective of this study was to assess the effect of pharmacologic stress on intraventricular kinetic energy (KE), viscous energy loss (EL) and vorticity from 4D flow magnetic resonance imaging (MRI) in Fontan patients and to study the relation between stress response and exercise capacity.

Methods

Ten Fontan patients underwent whole-heart 4D flow MRI before and during 7.5 µg/kg/min Dobutamine infusion and cardiopulmonary exercise testing (CPET) on the same day. Average ventricular KE, EL and vorticity were computed over systole, diastole and the total cardiac cycle (vorticity_vol_{avg cycle}, KE_{avg cycle}, EL_{avg cycle}). The relation to peak oxygen uptake (VO₂ max) from CPET was tested by Pearson's correlation.

Results

Dobutamine stress caused a significant 88% increase in KE (KE_{avg cycle}: 1.8 ± 0.5 vs 3.3 ± 0.9 mJ, $P < 0.001$), a significant 108% increase in EL (EL_{avg cycle}: 0.9 ± 0.4 vs 1.9 ± 0.9 mW, $P < 0.001$) and a significant 27% increase in vorticity (vorticity_vol_{avg cycle}: 3440.7 ± 899.1 vs 4394.4 ± 1321.6 mL/s, $P = 0.002$). All were negatively correlated to VO₂ max (KE_{avg cycle}: $r = -0.83$, $P = 0.003$; EL_{avg cycle}: $r = -0.80$, $P = 0.006$; vorticity_vol_{avg cycle}: $r = -0.64$, $P = 0.047$).

Conclusion

In conclusion, 4D flow MRI-derived intraventricular kinetic energy, viscous energy loss and vorticity in Fontan patients increase during pharmacologic stress and show a negative correlation with exercise capacity measured by VO₂ max.

Introduction

The Fontan procedure is a palliative surgical procedure for patients with complex congenital intracardiac deformations in whom a biventricular circulation cannot be created [1]. Survival of patients after the procedure has increased drastically over the past decades [2, 3] but still, these patients exhibit diminished exercise capacity, which is related to a worse functional health status [4-6]. Several factors have been identified that play a role in the reduced exercise capacity in these patients, such as an inadequate ventricular response to exercise, reduced pulmonary function, muscle weakness and energy loss in the Fontan tunnel [7-11]. Four-dimensional (4D) flow magnetic resonance imaging (MRI) enables comprehensive assessment of *in vivo* blood flow patterns and quantification of hemodynamic parameters from blood flow velocity such as kinetic energy (KE), viscous energy loss (EL, the KE that is lost due to viscosity-induced frictional forces) and vorticity [12].

Recently, altered flow patterns, levels of KE and vortex formation in the intraventricular blood flow pattern were observed in Fontan patients [13-15]. Furthermore, reduced exercise capacity was linked to 4D flow MRI-derived EL in the total cavopulmonary connection of Fontan patients [11]. However, currently the link between altered intracardiac hemodynamics during stress and exercise capacity remains unknown. We hypothesize that Dobutamine stress impacts these intracardiac hemodynamic parameters and that this may be linked to decreased exercise capacity in Fontan patients.

Therefore, the purpose of this study was 1) to noninvasively assess the influence of pharmacologic stress on KE, EL and vorticity measured by 4D flow MRI in intraventricular blood flow in Fontan patients and 2) to study the relation between the hemodynamic stress response in terms of KE, EL and vorticity and exercise capacity assessed by maximum oxygen uptake ($\text{VO}_2 \text{ max}$) from cardiopulmonary exercise tests (CPET).

Methods

Study population

Twenty-six Fontan patients were prospectively evaluated in this study at the Leiden University Medical Center (LUMC) as part of a multicenter study that was approved by the Medical Ethical Committee of the Erasmus Medical Center in Rotterdam (MEC-2014-326, NL48188.078.14), with local approval of the Medical Ethical Committee of the LUMC, The Netherlands. Informed consent was obtained from all of these participants. All patients underwent cardiopulmonary exercise testing (CPET) and an MRI scan on the same day.

Patients were included in the current study when the Dobutamine stress MRI scan with 4D flow MRI at rest and stress was fully completed: which was the case in 10/26 (38%) patients. Reasons for not finishing the complete scan were: 10 (38%) patients refused stress testing, in 4 (15%) patients stress testing could only be completed without 4D flow MRI and in 2 (8%) patients Dobutamine infusion had to be stopped because of ventricular extra systoles.

Cardiopulmonary exercising testing

Cardiopulmonary exercising testing was performed on an upright bicycle ergometer (GE Healthcare). Starting wattage and workload increase per minute were defined by the attending physician. Patients were encouraged to exercise until exhaustion. VO_2 max was derived from the CPET following previously published methods [16].

Cardiovascular magnetic resonance acquisition and image analysis

A complete MRI scan including whole-heart 4D flow MRI was obtained on a 3.0 Tesla scanner (Ingenia, Philips Healthcare, the Netherlands) during rest and with Dobutamine 7.5 $\mu\text{g}/\text{kg}/\text{min}$. Details on MRI acquisition are provided in *Appendix I*. Dobutamine infusion was reduced to 5 $\mu\text{g}/\text{kg}/\text{min}$ or stopped in case of a $>50\%$ increase in HR, systolic, or diastolic blood pressure; a $<20\%$ decrease HR, systolic, or diastolic blood pressure or when rhythm disorders occurred. The test was stopped when the patient experienced discomfort. Image analysis was performed using in-house developed *MASS* software by one observer (VPK) with three years of experience in cardiac MRI and verified by a radiologist (LJMK) with over 20 years of experience in cardiac MRI. Aliasing of 4D flow velocity images was visually checked in the source images (all three velocity components) and unwrapped using a sliding velocity scaling in *MASS* software. Ventricular volume was segmented in all slices and phases in the cine transversal images (papillary muscles were included in the ventricular volume; remaining parts of the septum in “biventricular” patients were not included in the ventricular volume). Segmented volumes were then used to compute stroke volume (SV) as: end-diastolic volume (EDV) – end-systolic volume. Cardiac output (CO) was computed as $\text{SV} \times \text{heart rate}(\text{HR})$. To assess the shape of the ventricle the sphericity index was calculated as the short to long axis ratio: ventricular width / ventricular height at end-systole and end-diastole in the 2D cine transversal images. Time points of systolic and diastolic phases were derived from the flow-time curves that resulted from retrospective valve tracking assessing the inflow and outflow of the systemic ventricle in Fontan patients, following previously published methods [17]. Segmentation of the ventricular cavity in the 4D flow MRI acquisition, that is required for the energy and vorticity analysis, was obtained by transforming the available time-varying segmentation of multi-slice cine transversal

anatomical acquisition to the 4D flow MRI data [18]. To account for potential patient-motion related misalignment between the two acquisitions, automated image-based 3D rigid registration by mutual information was performed using the phase with maximal depiction of the ventricular cavity in both scans with the Elastix image registration toolbox [19].

Computation of KE, EL and vorticity in the 4D flow MRI data

The amount of intraventricular KE was computed as $\frac{1}{2}mv^2$, with m as the mass representing the voxel volume multiplied by the density of blood (1.025 g/mL) and v as the magnitude of the 3-directional velocity vector assessed from 4D flow MRI. For each acquired time-phase, volumetric KE was then computed by integrating (by cumulative sum) the computed KE over the segmented 3D ventricular volume. The KE was quantified by the time-average kinetic energy over systole ($KE_{\text{avg systole}}$), diastole ($KE_{\text{avg diastole}}$) and the complete cardiac cycle ($KE_{\text{avg cycle}}$), all expressed in milliJoule (mJ) [20]. EL was computed from 4D flow MRI using the dissipation terms from the Navier-Stokes energy equations, following recently published methods [18, 20], assuming blood as a Newtonian fluid. Average EL in milliWatt (mW) was computed over systole ($EL_{\text{avg systole}}$), diastole ($EL_{\text{avg diastole}}$) and the complete cardiac cycle ($EL_{\text{avg cycle}}$). Furthermore, voxel-wise vorticity magnitude (in 1/s) was computed for each acquired time-phase and then integrated over the total ventricular volume [20]. To differentiate from voxel-wise vorticity, we will refer to this integrated volumetric vorticity as vorticity_vol (in mL/s). This vorticity_vol is a scalar quantity and does not take the vorticity direction into account. In order to quantify the integral vorticity_vol, the time-averaged vorticity over systole and diastole and the total cardiac cycle ($\text{vorticity_vol}_{\text{avg systole}}$, $\text{vorticity_vol}_{\text{avg diastole}}$, $\text{vorticity_vol}_{\text{avg cycle}}$ respectively) was assessed. All EL, KE and vorticity parameters at rest and stress were also given normalized by SV.

Statistical Analysis

Data analysis was performed using SPSS Statistics (version 23.0 IBM SPSS, Chicago, IL). Variables were tested for normal distribution using the Shapiro-Wilk test. Continuous data is reported as mean \pm standard deviation (SD) or median [inter-quartile range (IQR)], in case of non-normality of the data. The absolute differences between rest and stress measurements (stress measurement – rest measurement) were assessed and significance was tested with the paired samples t-test or the Wilcoxon signed-rank test in case of non-normality of the data. Furthermore, the relative differences (as a percentage) between rest and stress measurements $[(\text{stress measurement} - \text{rest measurement})/\text{rest measurement} \times 100]$ were calculated. Correlation between measurements was tested with the Pearson correlation coefficient or the Spearman's rank correlation coefficient in case of non-normality of the data. Correlation was

classified as follows: >0.95: excellent; 0.95–0.85: strong; 0.85–0.70: good; 0.70–0.5: moderate; <0.5: poor. A *P*-value <0.05 was considered statistically significant.

Results

Characteristics of the Fontan patients are shown in *Table 1*. Heart rate (HR) increased from 83.4 ± 18.9 bpm to 110.9 ± 20.0 bpm between the rest and Dobutamine stress scans ($P<0.001$). SV increased from 80.8 ± 29.4 to 92.0 ± 33.9 mL between the rest and Dobutamine stress scans ($P=0.004$). Cardiac output (CO) increased from 6.4 ± 1.3 L/min to 9.7 ± 2.2 L/m ($P<0.001$). In one patient, Dobutamine infusion was decreased to 5 µg/kg/min because of a >50% increase in systolic blood pressure from baseline.

Table 1. Patient characteristics

	Rest	Dobutamine stress	Difference	Difference (%)	<i>P</i> -value
	Mean \pm SD	Mean \pm SD	<i>Stress-Rest</i> Mean \pm SD	<i>(Stress-rest)/rest</i> * 100% Mean \pm SD	
Group characteristics					
Age (years)	16.5 \pm 3.8	n/a	n/a	n/a	n/a
Male (%)	4/10 (40)	n/a	n/a	n/a	n/a
VO ₂ max*	30.2 \pm 8.6	n/a	n/a	n/a	n/a
HR (bpm)	83.4 \pm 18.9	110.9 \pm 20.0	27.5 \pm 8.2	35 \pm 12	<0.001
EDV (mL)	164.4 \pm 43.9	156.8 \pm 46.0	-7.6 \pm 13.9	-5 \pm 8	0.12
ESV (mL)	83.6 \pm 23.7	64.8 \pm 20.9	-18.8 \pm 8.8	-23 \pm 11	<0.001
SV (mL)	80.8 \pm 29.4	92.0 \pm 33.9	11.1 \pm 9.2	14 \pm 10	0.004
EF (%)	49.1 \pm 8.5	58.6 \pm 8.1	9.5 \pm 3.2	20 \pm 8	<0.001
CO (L/min)	6.4 \pm 1.3	9.7 \pm 2.2	3.3 \pm 1.3	52 \pm 17	<0.001
Systolic blood pressure (mmHg)	121.2 \pm 15.2	150.6 \pm 19.3	29.4 \pm 12.1	25 \pm 11	<0.001
Diastolic blood pressure (mmHg)	62.7 \pm 10.0	70.3 \pm 6.0	7.6 \pm 9.5	14 \pm 19	0.03
Sphericity index systole	1.1 \pm 0.3	1.2 \pm 0.4	0.1 \pm 0.2	7 \pm 25	0.44
Sphericity index diastole	1.0 \pm 0.1	1.1 \pm 0.2	0.05 \pm 0.2	6 \pm 19	0.41
Subject specific characteristics					
Subject number	Underlying anatomy	Ventricular morphology	Type of Fontan		
1	Unbalanced AVSD, hypoplastic LV	Biventricular	Extracardiac		
2	TGA, VSD, PS, hypoplastic LV	Biventricular	Extracardiac		
3	ccTGA, VSD, PS, straddling TV	Biventricular	Extracardiac		
4	PA	Left	Extracardiac		
5	TA	Left	Lateral tunnel		
6	TA	Left	Extracardiac		
7	PA	Left	Extracardiac		
8	DILV, with aorta from RV	Left	Extracardiac		
9	HLHS	Right	Extracardiac		
10	TGA, VSD, PS, hypoplastic LV	Right	Extracardiac		

*from cardiopulmonary exercise testing.

HR = heart rate; EDV = end diastolic volume; ESV = end systolic volume; SV = stroke volume; CO = cardiac output; EF = ejection fraction; VO₂ max = maximal oxygen uptake; AVSD=atrioventricular septal defect; LV=left ventricle, TGA=transposition of the great arteries; VSD=ventricular septal defect; PS=pulmonary stenosis; TV=tricuspid valve; PA=pulmonary atresia; TA=tricuspid atresia; DILV=double inlet right ventricle; RV=right ventricle; HLHS=hypoplastic left heart syndrome

Table 2. Quantitative analysis of energetics and vorticity at rest and stress

	Rest	Dobutamine stress	Difference	Difference (%)	P-value
	Mean \pm SD	Mean \pm SD	<i>Stress-Rest</i> Mean \pm SD	<i>(Stress-rest)/rest</i> * 100% Mean \pm SD	
Non-normalized					
KE _{avg systole} (mJ)	2.4 \pm 1.1	5.1 \pm 1.8	2.7 \pm 1.2	126 \pm 61	<0.001
KE _{avg diastole} (mJ)	1.4 \pm 0.3	2.2 \pm 0.7	0.8 \pm 0.7	61 \pm 57	0.007
KE _{avg cycle} (mJ)	1.8 \pm 0.5	3.3 \pm 0.9	1.5 \pm 0.8	88 \pm 52	<0.001
EL _{avg systole} (mW)	1.2 \pm 0.8	3.1 \pm 1.8	1.8 \pm 1.1	155 \pm 61	0.001
EL _{avg diastole} (mW)	0.7 \pm 0.2	1.2 \pm 0.5	0.5 \pm 0.4	71 \pm 66	0.007
EL _{avg cycle} (mW)	0.9 \pm 0.4	1.9 \pm 0.9	1.0 \pm 0.6	108 \pm 49	<0.001
Vorticity_vol _{avg systole} (mL/s)	3591.6 \pm 1147.8	4927.7 \pm 1625.6	1336.1 \pm 725.7	37 \pm 17	<0.001
Vorticity_vol _{avg diastole} (mL/s)	3371.2 \pm 769.7	4085.7 \pm 1215.7	714.5 \pm 815.5	21 \pm 25	0.02
Vorticity_vol _{avg cycle} (mL/s)	3440.7 \pm 899.1	4394.4 \pm 1321.6	953.7 \pm 683.8	27 \pm 19	0.002
Normalized by stroke volume					
KE _{avg systole/SV} (mJ/mL)	0.029 \pm 0.009	0.057 \pm 0.018	0.028 \pm 0.013	98 \pm 46	<0.001
KE _{avg diastole/SV} (mJ/mL)	0.019 \pm 0.006	0.025 \pm 0.007	0.006 \pm 0.008	40 \pm 44	0.03
KE _{avg cycle/SV} (mJ/mL)	0.023 \pm 0.005	0.037 \pm 0.009	0.014 \pm 0.008	64 \pm 40	<0.001
EL _{avg systole/SV} (mW/mL)	0.015 \pm 0.008	0.035 \pm 0.019	0.019 \pm 0.012	124 \pm 51	0.001
EL _{avg diastole/SV} (mW/mL)	0.009 \pm 0.003	0.013 \pm 0.004	0.004 \pm 0.004	48 \pm 50	0.01
EL _{avg cycle/SV} (mW/mL)	0.012 \pm 0.004	0.021 \pm 0.009	0.010 \pm 0.005	81 \pm 36	<0.001
Vorticity_vol _{avg systole/SV} (1/s)	45.4 \pm 10.3	55.1 \pm 15.5	9.7 \pm 5.9	20 \pm 10	0.001
Vorticity_vol _{avg diastole/SV} (1/s)	43.8 \pm 10.4	45.5 \pm 9.1	1.7 \pm 7.1	6 \pm 17	0.46
Vorticity_vol _{avg cycle/SV} (1/s)	44.1 \pm 9.7	49.1 \pm 11.1	4.9 \pm 4.4	11 \pm 11	0.006
SD = standard deviation; KE = kinetic energy; SV = stroke volume; EL = viscous energy loss; e-peak = peak early diastole; a-peak = peak late diastole					

Intraventricular KE, EL and vorticity_vol at rest and stress

Table 2 shows the non-normalized results of KE, EL and vorticity_vol at rest and Dobutamine stress. KE_{avg systole} significantly increased by 126 \pm 61% during the Dobutamine stress scan (2.4 \pm 1.1 vs 5.1 \pm 1.8 mJ, P <0.001). KE_{avg diastole} significantly increased by 61 \pm 57% during the stress scan (1.4 \pm 0.3 vs 2.2 \pm 0.7 mJ, P =0.007). Average KE significantly increased by 88 \pm 52% during the complete cardiac cycle (KE_{avg cycle}: 1.8 \pm 0.5 vs 3.3 \pm 0.9 mJ, P <0.001). With Dobutamine stress, EL significantly increased by 155 \pm 61% when calculated over systole (EL_{avg systole}: 1.2 \pm 0.8 vs 3.1 \pm 1.8 mW, P =0.001), and 71 \pm 66% over diastole (EL_{avg diastole}: 0.7 \pm 0.2 vs 1.2 \pm 0.5 mW, P =0.007). Average EL significantly increased by 108 \pm 49% when calculated over the complete cardiac cycle (EL_{avg cycle}: 0.9 \pm 0.4 vs 1.9 \pm 0.9 mW, P <0.001). Vorticity_vol_{avg systole} significantly increased by 37 \pm 17%

during the Dobutamine stress scan (3591.6 ± 1147.8 vs 4927.7 ± 1625.6 mL/s, $P < 0.001$). Vorticity_vol_{avg diastole} significantly increased by $21 \pm 25\%$ during the stress scan (3371.2 ± 769.7 vs 4085.7 ± 1215.7 mL/s, $P = 0.02$). Average vorticity_vol significantly increased by $27 \pm 19\%$ when calculated over the complete cardiac cycle (vorticity_vol_{avg cycle}: 3440.7 ± 899.1 vs 4394.4 ± 1321.6 mL/s, $P = 0.002$). *Figure 1* shows an example of the intracardiac hemodynamics during stress in one patient. Boxplots of the absolute differences for the total group and the individual changes between rest and stress values of KE, EL and vorticity_vol are shown in *Figure 2*.

Results of KE, EL and vorticity_vol at rest and Dobutamine stress normalized by SV are also shown in *Table 2*. Normalized by stroke volume, KE and EL values still showed a significant increase during systole and diastole and over the total cycle, similar to the non-normalized values. Only vorticity_vol_{avg diastole}/SV did not change significantly (43.8 ± 10.4 vs 45.5 ± 9.1 1/s, $P = 0.46$).

Relation between difference HR, stroke volume from 2D planimetry and KE, EL and vorticity

The difference in HR between rest and stress was not associated with the difference in KE, EL or vorticity_vol (KE_{avg cycle}: $r = -0.27$, $P = 0.45$; EL_{avg cycle}: $r = 0.01$, $P = 0.97$; vorticity_vol_{avg cycle}: $r = -0.26$, $P = 0.48$). The increase in SV between rest and stress was significantly associated with the difference in vorticity_vol_{avg cycle} (vorticity_vol_{avg cycle}: 0.72 , $P = 0.02$), but not with the difference in KE or EL (KE_{avg cycle}: $r = -0.46$, $P = 0.19$; EL_{avg cycle}: $r = 0.48$, $P = 0.16$).

Relation to VO₂ max from cardiopulmonary exercise testing

Figure 3 shows the scatter plot between VO₂ max from CPET and the relative rest-stress difference in KE, EL and vorticity. This plot shows a significant good inverse correlation between VO₂ max from CPET and relative KE_{avg cycle} rest-stress difference ($r = -0.83$, $P = 0.003$). Furthermore, there is a significant good inverse correlation between VO₂ max from CPET and relative EL_{avg cycle} rest-stress difference ($r = -0.80$, $P = 0.006$). VO₂ max from CPET and relative vorticity_vol_{avg cycle} rest-stress difference show a significant moderate inverse correlation ($r = -0.64$, $P = 0.047$). In the two patients with normal VO₂ max [16] the relative rest-stress difference in vorticity_vol was 0.3-15%, the relative rest-stress difference in KE 20-42% and in EL 30- 59%. The patient with the lowest VO₂ max showed a 55% increase in vorticity_vol, but a 166% increase in KE and a 195% increase in EL during stress. Overall, decreased VO₂ max is related to increases in vorticity_vol, KE and EL rest-stress differences, though both relative rest-stress differences in KE and EL showed a three-fold stronger increase than relative difference in vorticity_vol.

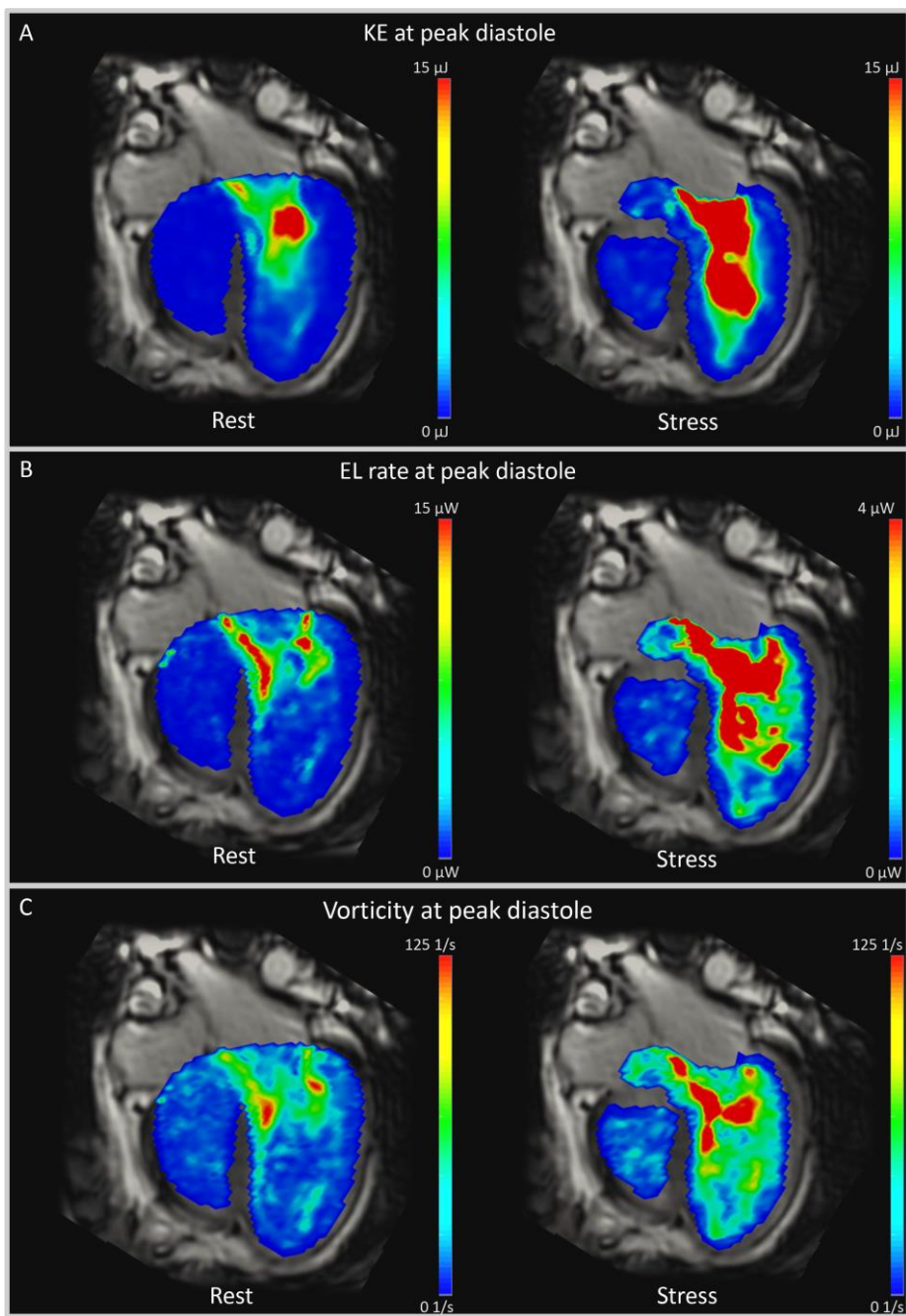


Figure 1. Intracardiac hemodynamics at rest and dobutamine stress in a 19 year old female patient with pulmonary atresia at peak diastolic filling. A) shows the intraventricular kinetic energy (KE) at rest and stress. B) shows the intraventricular viscous energy loss (EL) rate at rest and stress. C) shows the intraventricular vorticity at rest and stress.

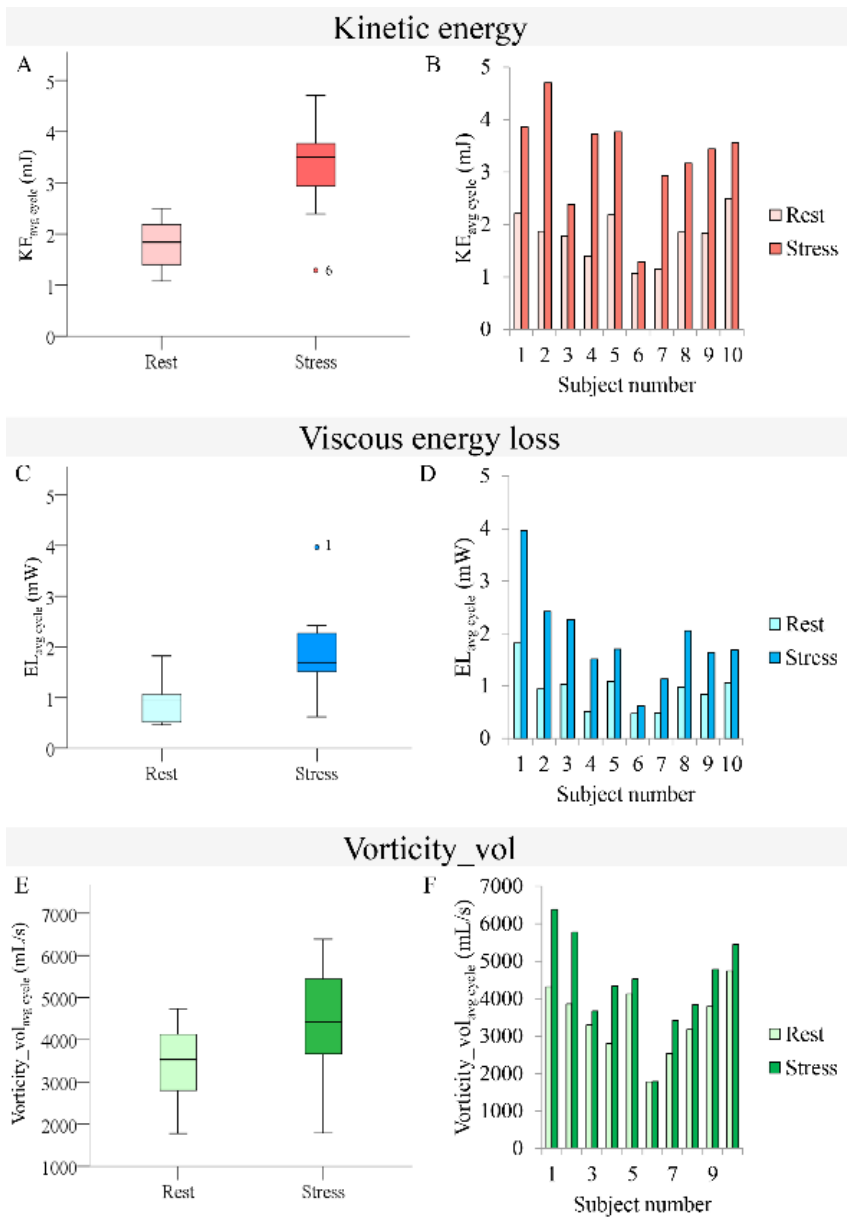


Figure 2. Relative difference in intraventricular kinetic energy (KE), viscous energy loss (EL) and vorticity (vorticity_vol) over the total cardiac cycle between rest and stress. A) Difference in kinetic energy in the total group in rest and stress; B) Difference in kinetic energy per subjects in rest and stress; C) Difference in viscous energy loss in the total group in rest and stress; D) Difference in viscous energy loss per subjects in rest and stress; E) Difference in vorticity in the total group in rest and stress; F) Difference in vorticity per subjects in rest and stress.

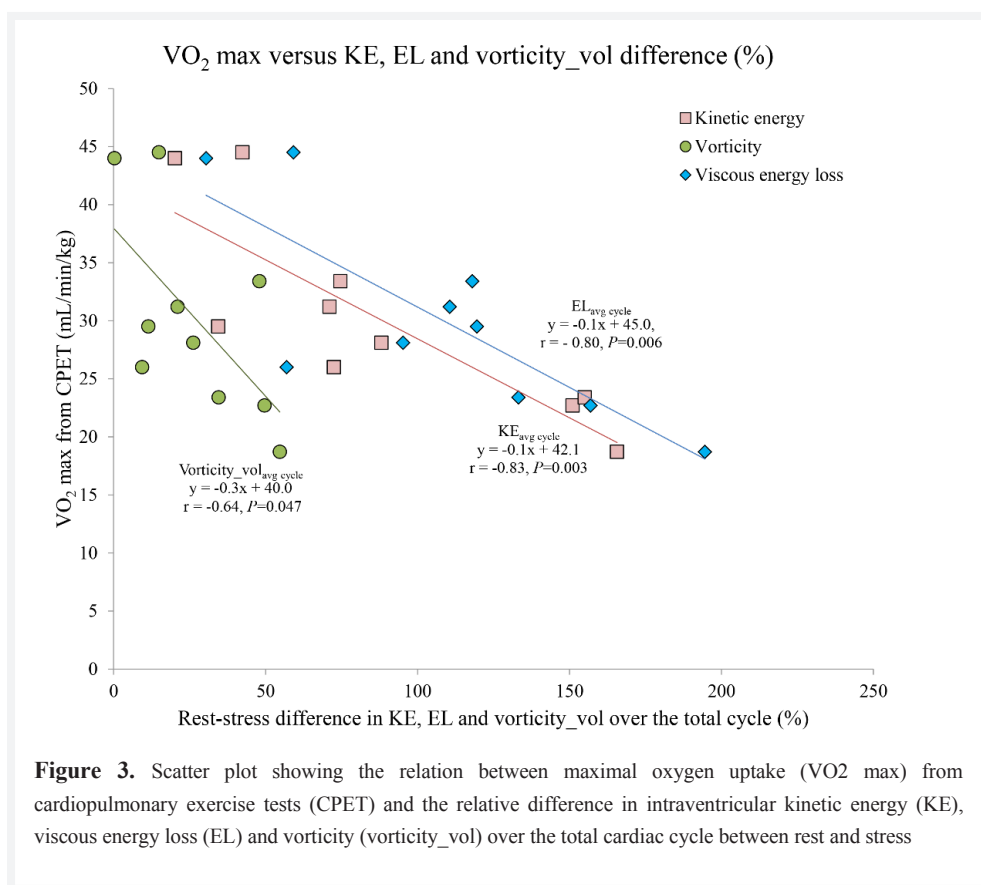


Figure 3. Scatter plot showing the relation between maximal oxygen uptake (VO₂ max) from cardiopulmonary exercise tests (CPET) and the relative difference in intraventricular kinetic energy (KE), viscous energy loss (EL) and vorticity (vorticity_vol) over the total cardiac cycle between rest and stress

Discussion

In the current study, the effect of pharmacologic stress on intraventricular KE, EL and vorticity, derived from 4D flow MRI, was evaluated in Fontan patients and the relation was tested between stress response on these markers and exercise capacity, measured by VO₂ max from cardiopulmonary exercise testing. Main findings of the study are: 1) intraventricular KE, EL and vorticity_vol increased during pharmacologic stress; 2) the increase in KE and EL under stress was 3-4 times higher than the increase in vorticity_vol; 3) VO₂ max from CPET showed a significant negative correlation with the relative rest-stress differences in KE, EL and vorticity_vol, however, at identical VO₂ max value, both relative rest-stress differences in KE and EL showed a three-fold stronger increase than relative difference in vorticity_vol.

In the normal left ventricle at rest, blood flow follows the path that is most efficient for optimal ejection of flow in the systemic circulation. The shape of the healthy left ventricle and normal mitral valve contributes to the formation of a recirculating flow pattern during diastole, forming a confined region of vortical flow that conserves momentum by storing KE, while during systole the flow follows a rather semi-circular path towards the aortic outflow tract [21, 22]. During stress the complex dynamic flow patterns in the heart might change in order to achieve redirection of momentum through the curved paths of flow [23]. However, the effect of pharmacologic stress on 4D flow MRI-derived intraventricular flow patterns and KE, EL and vorticity in the healthy left ventricle, has not been published.

Fontan patients have various structural ventricular and valvular anomalies and the ventricle that sustains the systemic circulation can be the left ventricle or the right ventricle. Furthermore, in some patients, diastolic inflow of blood occurs in the same ventricle as it is ejected from (i.e., as is the case in a patient with tricuspid atresia with a normal ventriculo-arterial connection) while in other patients, inflowing blood has to pass through a ventricular septal defect first to reach the aorta (i.e., as is the case in patients with in double inlet left ventricle with the aorta arising from a hypoplastic RV). The abnormal intracardiac anatomy in Fontan patients causes differences in intraventricular flow patterns, which can be assessed and studied by 4D flow MRI [15]. In a similar way, altered flow patterns have been visualized and quantified in patients with a corrected atrioventricular septal defect [24] in which altered vortex formation was associated with increased EL obtained by 4D flow MRI [18]. Furthermore, in a patient with a Fontan circulation with a complete atrioventricular septal defect and a double outlet right ventricle with pulmonary stenosis, abnormal intracardiac structures have been linked to regions of vortex formation and increased EL [13]. In Fontan patients decreased diastolic KE was reported [14]. However, all these published studies focused on patients in rest and the response in 4D flow MRI-derived hemodynamic parameters such as KE, EL and vorticity after stress has not been evaluated earlier.

Our study showed that Dobutamine-induced stress resulted in a significant increase in KE, EL and vorticity_vol. Notably, in the current study the Dobutamine stress-induced increase in KE and EL is 3-4 times higher than the increase in vorticity_vol (KE_{avg cycle} increase 88%; EL_{avg cycle} increase 108%, vorticity_vol_{avg cycle} increase 27%). The difference in increase in KE and EL compared to vorticity_vol could partly be explained by the abnormal underlying anatomy of the Fontan patients. Increased KE results in higher EL, which is possibly enhanced by more flow-structure interaction. However, the increase in vorticity_vol is not in the same order of magnitude. Vorticity in the ventricular flow might have a favorable effect (i.e., conservation of momentum by KE storage and redirection of flow during diastole which

takes place in a confined region of vortical flow distal to the mitral valve) [21, 22]. However, vorticity may also have an adverse effect on the intracardiac blood flow when optimal flow redirection may be perturbed by flow separation and vortex shedding distal to abnormal intracardiac structures in the flow field [25-27]). In this study, we are not able to discriminate between favorable and adverse effects of vorticity but in either case, the KE contributes to vortex formation but does not show a linear relation with vorticity under stress. The relation between vortex formation and flow velocity (i.e. kinetic energy) has been studied before: Gharib et al. [28] described that the volume and circulation of a vortex ring that is formed from inflow through a circular nozzle into a large unconstrained volume will both increase with increasing inflow velocity, but only up to a critical point where optimal vortex formation has been achieved and both volume and vorticity of the main vortex will remain approximately constant. However, secondary, vortices may start to appear that will contribute to the total summed vorticity. Furthermore, in our study the shape of the ventricle measured by the sphericity index and EDV remained similar during rest and stress. This could support the hypothesis that the size of the vortical flow region during diastole is restricted in growth and unable to expand at the same rate as the KE increase during stress. In addition, the increase of vortex shedding distal to intracardiac structures may be limited in magnitude as well when ventricular size and shape do not change during stress.

Survival after the Fontan procedure has increased drastically over the past decades [2, 3]. Still, patients with a Fontan circulation exhibit diminished exercise capacity, related to worse functional health status [4-6]. Several factors have been identified that play a role in the reduced exercise capacity in these patients [7-11]. However, the only previous study that related exercise capacity to 4D flow MRI-derived EL was aimed at the total cavopulmonary connection of Fontan patients [11] and not at intraventricular flow dynamics. In the current study, an increase in the relative rest-stress difference in KE, EL and vorticity_vol was inversely correlated with VO₂ max, though notably relative rest-stress differences in KE and EL showed a three-fold stronger increase than relative difference in vorticity_vol. This is in line with our previous speculation that, in patients with lower exercise capacity, storage capacity of KE inside the confined vortical flow region is limited and therefore, does not follow the increase of total KE. This also results in more viscous dissipation of KE. Furthermore, the abnormal intraventricular anatomy could play a role in this relation as well. Nevertheless, our findings provide evidence that intracardiac hemodynamics may play a role in exercise capacity in Fontan patients.

Our results showed no association between the difference in HR and the difference in KE, EL or vorticity. However, HR increase during low-dose Dobutamine stress is limited to a

30% increase. From this study, we cannot determine whether this relation would be similar when HR increase is higher. Also, we showed that SV difference is directly related to vorticity difference, but not to the difference in KE or EL, as the increase in these parameters is much stronger than the increase in vorticity.

A limitation of the current study is the limited sample size. However, our results are still highly statistically significant. Furthermore, we did not include an evaluation of turbulent kinetic energy, which could be relevant in Fontan patients, as turbulent flow may be present due to the structural intraventricular abnormalities. Also, since there is no data available on the normal 4D flow MRI-derived hemodynamic stress response we were not able to compare these results in Fontan patients to healthy controls. Additionally, 4D flow MRI is a time-resolved imaging modality that only represents time-averaged blood flow acquired over multiple heart cycles. Consequently, this limits the evaluation to coherent vortical flow only, while incoherent unstable flow, especially during stress-induced increased cardiac workload, cannot be estimated, although the effect may not be negligible.

Conclusion

In conclusion, intraventricular kinetic energy, viscous energy loss and vorticity values derived from 4D flow MRI increased during pharmacologic stress, with a three to four times higher increase in KE and EL compared to the vorticity increase. The increase in KE, EL and vorticity showed a negative correlation with exercise capacity measured by VO_2 max from cardiopulmonary exercise testing and at identical VO_2 max value, both relative rest-stress differences in KE and EL showed a three-fold stronger increase than the relative differences in vorticity.

References

- Fontan F, Baudet E: Surgical repair of tricuspid atresia. *Thorax* 1971, 26:240-248.
- Chin AJ, Whitehead KK, Watrous RL: Insights after 40 years of the fontan operation. *World J Pediatr Congenit Heart Surg* 2010, 1:328-343.
- Gersony WM: Fontan operation after 3 decades: what we have learned. *Circulation* 2008, 117:13-15.
- Robbers-Visser D, Kapusta L, van Osch-Gevers L, Strengers JL, Boersma E, de Rijke YB, Boomsma F, Bogers AJ, Helbing WA: Clinical outcome 5 to 18 years after the Fontan operation performed on children younger than 5 years. *J Thorac Cardiovasc Surg* 2009, 138:89-95.
- Hock J, Reiner B, Neidenbach RC, Oberhoffer R, Hager A, Ewert P, Muller J: Functional outcome in contemporary children with total cavopulmonary connection - Health-related physical fitness, exercise capacity and health-related quality of life. *Int J Cardiol* 2018, 255:50-54.
- Atz AM, Zak V, Mahony L, Uzark K, D'Agincourt N, Goldberg DJ, Williams RV, Breitbart RE, Colan SD, Burns KM, et al: Longitudinal Outcomes of Patients With Single Ventricle After the Fontan Procedure. *J Am Coll Cardiol* 2017, 69:2735-2744.
- Bossers SS, Helbing WA, Duppen N, Kuipers IM, Schokking M, Hazekamp MG, Bogers AJ, Ten Harkel AD, Takken T: Exercise capacity in children after total cavopulmonary connection: lateral tunnel versus extracardiac conduit technique. *J Thorac Cardiovasc Surg* 2014, 148:1490-1497.
- Bossers SS, Kapusta L, Kuipers IM, van Iperen G, Moelker A, Kroft LJ, Romeih S, de Rijke Y, Ten Harkel AD, Helbing WA: Ventricular function and cardiac reserve in contemporary Fontan patients. *Int J Cardiol* 2015, 196:73-80.
- Matthews IL, Fredriksen PM, Bjornstad PG, Thaulow E, Gronn M: Reduced pulmonary function in children with the Fontan circulation affects their exercise capacity. *Cardiol Young* 2006, 16:261-267.
- Greutmann M, Le TL, Tobler D, Biaggi P, Oechslin EN, Silversides CK, Granton JT: Generalised muscle weakness in young adults with congenital heart disease. *Heart* 2011, 97:1164-1168.
- Khiabani RH, Whitehead KK, Han D, Restrepo M, Tang E, Bethel J, Paridon SM, Fogel MA, Yoganathan AP: Exercise capacity in single-ventricle patients after Fontan correlates with haemodynamic energy loss in TCPC. *Heart* 2015, 101:139-143.
- Kamphuis VP, Westenberg JJM, van der Palen RLF, Blom NA, de Roos A, van der Geest R, Elbaz MSM, Roest AAW: Unravelling cardiovascular disease using four dimensional flow cardiovascular magnetic resonance. *Int J Cardiovasc Imaging* 2017, 33:1069-1081.
- Kamphuis VP, Roest AAW, Westenberg JJM, Elbaz MSM: Biventricular vortex ring formation corresponds to regions of highest intraventricular viscous energy loss in a Fontan patient: analysis by 4D Flow MRI. *Int J Cardiovasc Imaging* 2017, 34: 441-44
- Sjoberg P, Heiberg E, Wingren P, Ramgren Johansson J, Malm T, Arheden H, Liuba P, Carlsson M: Decreased Diastolic Ventricular Kinetic Energy in Young Patients with Fontan Circulation Demonstrated by Four-Dimensional Cardiac Magnetic Resonance Imaging. *Pediatr Cardiol* 2017, 38:669-680.
- She HL, Roest AA, Calkoen EE, van den Boogaard PJ, van der Geest RJ, Hazekamp MG, de Roos A, Westenberg JJ: Comparative Evaluation of Flow Quantification across the Atrioventricular Valve in Patients with Functional Univentricular Heart after Fontan's Surgery and Healthy Controls: Measurement by 4D Flow Magnetic Resonance Imaging and Streamline Visualization. *Congenit Heart Dis* 2017, 12:40-48.
- Ten Harkel AD, Takken T, Van Osch-Gevers M, Helbing WA: Normal values for cardiopulmonary exercise testing in children. *Eur J Cardiovasc Prev Rehabil* 2011, 18:48-54.
- Kamphuis VP, van der Palen RLF, de Koning PJH, Elbaz MSM, van der Geest RJ, de Roos A, Roest AAW, Westenberg JJM: In-scan and scan-rescan assessment of LV in- and outflow volumes by 4D flow MRI versus 2D planimetry. *J Magn Reson Imaging* 2018, 47: 511-522.
- Elbaz MS, van der Geest RJ, Calkoen EE, de Roos A, Lelieveldt BP, Roest AA, Westenberg JJ: Assessment of viscous energy loss and the association with three-dimensional vortex ring formation in left ventricular inflow: In vivo evaluation using four-dimensional flow MRI. *Magn Reson Med* 2017, 77:794-805.
- Klein S, Staring M, Murphy K, Viergever MA, Pluim JP: elastix: a toolbox for intensity-based medical image registration. *IEEE Trans Med Imaging* 2010, 29:196-205.

20. Kamphuis VP, Westenberg JJM, van der Palen RLF, van den Boogaard PJ, van der Geest RJ, de Roos A, Blom NA, Roest AAW, Elbaz MSM: Scan-rescan reproducibility of diastolic left ventricular kinetic energy, viscous energy loss and vorticity assessment using 4D flow MRI: analysis in healthy subjects. *Int J Cardiovasc Imaging* 2018, 34:905-92.
21. Pedrizzetti G, Domenichini F: Nature optimizes the swirling flow in the human left ventricle. *Phys Rev Lett* 2005, 95:108101.
22. Kilner PJ, Yang GZ, Wilkes AJ, Mohiaddin RH, Firmin DN, Yacoub MH: Asymmetric redirection of flow through the heart. *Nature* 2000, 404:759-761.
23. Kilner PJ, Henein MY, Gibson DG: Our tortuous heart in dynamic mode--an echocardiographic study of mitral flow and movement in exercising subjects. *Heart Vessels* 1997, 12:103-110.
24. Calkoen EE, Elbaz MS, Westenberg JJ, Kroft LJ, Hazekamp MG, Roest AA, van der Geest RJ: Altered left ventricular vortex ring formation by 4-dimensional flow magnetic resonance imaging after repair of atrioventricular septal defects. *J Thorac Cardiovasc Surg* 2015, 150:1233-1240 e1231.
25. Paterson AR: *A first course in fluid dynamics*. Cambridge university press 1983.
26. Domenichini F, Pedrizzetti G, Baccani, B: Three-dimensional filling flow into a model left ventricle. *Journal of Fluid Mechanics* 2005:179-198.
27. Paul I, Prakash KA, Vengadesan S: Onset of laminar separation and vortex shedding in flow past unconfined elliptic cylinders. *Physics of Fluids* 2014.
28. Gharib M, Rambod E, Shariff K: A universal time scale for vortex ring formation. *Journal of Fluid Mechanics* 1998, 360:121-140.

Appendix 1

MRI acquisition information

A complete MRI scan including whole-heart 4D flow MRI was obtained on a 3.0 Tesla scanner (Ingenia, Philips Healthcare, the Netherlands) with maximal amplitude of 45 mT/m for each axis and slew rate of 200 T/m/s. A combination of FlexCoverage Posterior coil in the table top with a dStream Torso coil, providing up to 32 coil elements was used for signal reception. Velocity-encoding of 150 cm/s in all three directions was used in a standard four-point encoding scheme, spatial resolution $3.0 \times 3.0 \times 3.0 \text{ mm}^3$ or better, flip angle 10° , echo time (TE) 3.7 ms, repetition time (TR) 7.7-10 ms, true temporal resolution 30-40 ms, sensitivity encoding factor 2 in anterior-posterior direction and echo planar imaging readout with a factor 5. Concomitant gradient correction and phase offset correction was performed using standard available scanner software. Typical acquisition time of the whole-heart 4D flow MRI scan was approximately 8 minutes. Cine two-dimensional left 2-chamber, 4-chamber, coronal and sagittal aorta views and transversal images were acquired, using steady-state free-precession sequences with TE/TR 1.5/3.0, 350 mm field-of-view, 45° flip angle, acquisition resolution $1.9 \times 2.0 \times 8.0 \text{ mm}^3$. Retrospective gating was used with 30 phases reconstructed to represent one cardiac cycle. Free breathing was allowed without using motion suppression; three signal averages were taken to minimize effects of breathing motion.

Chapter 13

General discussion

In this thesis the multidimensional electrical and hemodynamic aspects of congenital and acquired heart diseases were assessed by electrocardiography (**Part I**) and magnetic resonance imaging (**Part II** and **Part III**). Studies were performed with techniques that provide comprehensive insights in cardiac diseases that could help patient management and might aid in the detection of patients prone to cardiac deterioration.

Electrocardiographic variables reflecting cardiac function

The first part of this thesis focuses on electrocardiographic variables reflecting cardiac function. The electrocardiogram (ECG) changes dynamically during growth and in congenital cardiology many diseases include the right side of the heart. Furthermore, several patient groups with (corrected) congenital heart diseases are prone to arrhythmias and have an increased risk of sudden cardiac death. Therefore, in **Chapter 2**, characteristics of the 12-lead electrocardiogram in patients with right-sided congenital heart diseases and its relation to prognosis are reviewed. Detection of alterations in the ECG could be helpful in patient follow-up, however the standard 12-lead ECG does not allow for straightforward three-dimensional (3D) visualization and quantification of the electrical currents from the heart, which could increase the prognostic value of the ECG. In contrast to the one-dimensional scalar representation of the 12-lead ECG, vectorcardiography (VCG) gives insight in the time-resolved multi-dimensional nature of the heart's electrical forces.

In **Chapter 3** diagnostic validity could not be established, however, the normal values of the pediatric VCG provided in this chapter could be valuable in the serial follow-up of children with congenital heart diseases, such as an ostium secundum atrial septal defect (ASDII), which was the focus of **Chapter 4**. In **Chapter 4** electrical remodeling after percutaneous ASDII closure in pediatric and adult patients is shown. The results show that successful percutaneous atrial septal defect closure is followed by a decrease in heart rate, P-wave amplitude, PQ duration, QRS duration and QTc in both children and adults. These changes mostly occur acutely after device closure except for QRS duration and QTc interval in both children and adults and for PQ duration in adults. Most of these electrocardiographic changes remained limited. The changes in the vectorcardiographic spatial QRS-T angle reflect increasing concordance of the electrocardiogram, which can be interpreted as partly normalization of the electrical properties of the heart. The ventricular gradient showed changes which are a result of action potential duration dynamics after ASDII closure. Further studies with larger and more homogeneous patient groups are needed to evaluate the preferential direction of these ventricular gradient changes.

While **Chapter 4** focuses on the VCG in RV volume overload, the focus of **Chapter 5** is to show the usefulness of the VG in electrocardiographic detection of RV pressure overload in patients with pulmonary hypertension. The results show that a combination of the electrocardiographic Butler-Leggett score [1] and vectorcardiographic VG allow for detection of increased pulmonary artery pressure. Future studies should evaluate the use of the VG in other patient groups with right ventricular pressure overload.

4D flow MRI-derived cardiac flow and function: validation and clinical utility

The second part of this thesis focuses on the validation and clinical utility of four-dimensional (4D) flow magnetic resonance imaging (MRI)-derived cardiac flow and function. The normal shape and function of the left ventricle (LV) and mitral valve induce complex organized intracardiac flow patterns that lead to the most efficient ejection of blood in the systemic circulation [2, 3]. The visualization of these complex 3D flow patterns in the normal LV and the consequences of cardiac diseases causing interruption of this natural blood flow organization remains challenging. Recently, 4D flow MRI (3 spatial dimensions + time) emerged as a unique method for non-invasive *in vivo* visualization and quantification of the dynamic flow patterns in the heart and great vessels. **Chapter 6** provides an overview of the current role of 4D flow MRI in unraveling cardiovascular disease. Knowledge of normal and abnormal intracardiac flow patterns can increase our understanding of normal physiology and may help unravel the complex pathophysiological mechanisms leading to cardiovascular disease. 4D flow MRI shows promise as a diagnostic tool and could aid in management of cardiovascular disease and timing of surgical intervention. However, dedicated studies are still warranted to show the clinical value of 4D flow MRI.

Currently, the main application of 4D flow MRI is valvular flow quantification. 4D flow MRI-derived streamline visualization (curves tangent to the velocity direction at a particular point in time) combined with retrospective valve tracking provides a validated method that allows for direct quantification of flow over all four valves and regurgitation in a single acquisition [4-8]. Consequently, 4D flow MRI has several advantages over two-dimensional (2D) phase contrast MRI, which is the current clinical standard. Firstly, 4D flow MRI allows for quantification of blood flow volumes over all four valves in a single acquisition. Furthermore, measurement planes can be placed in every phase, adjusted to the flow direction and velocity distribution. Multiple studies have already shown that 4D flow MRI is more accurate than 2D phase contrast MRI in healthy volunteers and patients with acquired and congenital heart diseases [4-8]. Especially in patients with complex, dynamic regurgitant jets such as in corrected atrioventricular septal defect patients, the possibility of placing

adjustable measurement planes can be crucial for accurate quantification of regurgitation fraction [7].

In **Chapter 6** an example of the potential clinical use of 4D flow MRI with retrospective valve tracking is shown in a patient with Ebstein's anomaly. In these patients, reliable blood flow quantification is invaluable for assessment of diseases progress and timing of intervention. Still, the main limiting factor of 4D flow MRI in the clinical routine remains the long acquisition time and time-consuming post-processing. Current advances in acquisition and post-processing are aimed on broader implementation of 4D flow MRI in the clinical routine [9].

Validation is the first step in implementing a relatively new tool and good scan-rescan reproducibility of measurements is necessary when multiple scan are acquired during follow-up. **Chapter 7** shows that LV in- and outflow assessment by 4D flow MRI with retrospective valve tracking and particle tracing has good in-scan consistency and strong scan-rescan reproducibility, which indicates that both 4D flow MRI methods are reliable and can be used clinically. However, manual tracking of the valve and adjustment of the measurement plane in retrospective valve tracking is a time-consuming process, which hinders clinical applicability.

Therefore, **Chapter 8** focuses on the comparison between manual valve tracking versus automated valve tracking. Automated valve tracking reduces analysis time and improves reliability of valvular flow quantification compared to manual valve tracking. Moreover, automated valve tracking results in regurgitation reclassification, which is important for patient management and can be an independent predictor of adverse events. Compared to manual valve tracking, automated valve tracking results in significantly smaller net forward volume differences between the valves in all studied patient groups, except in the corrected atrioventricular septal defect patients. This higher net forward flow difference for automated valve tracking, that is not in line with the other findings, could be related to the fact that automated tracking does not allow for plane alignment perpendicular to the flow direction, which has been shown to increase accuracy for manual valve tracking in these patients [7]. Future studies should investigate the possibility of better plane alignment in automated valve tracking.

4D flow MRI-derived novel determinants of intraventricular hemodynamics

The third part of this thesis describes novel 4D flow MRI-derived elements of intraventricular hemodynamics. An unique feature of 4D flow MRI is that it allows for quantification of

hemodynamic markers from the blood flow such as kinetic energy (KE), viscous energy loss (EL) and vorticity (also described in **Chapter 6**). These novel markers are currently used in a research setting only and therefore the assessment of accuracy of these measurement is critical before clinical implementation can take place. Accordingly, **Chapter 9** focuses on the scan-rescan reproducibility of left ventricular KE, EL and vorticity in healthy volunteers. First of all, this study shows strong internal consistency between KE and EL in all scans. Furthermore, scan-rescan reproducibility of KE, EL and vorticity is good to excellent in the majority (10 out of 12) of subjects. In two subjects scan-rescan differences are much higher compared to the other 10 subjects. Although there is no obvious explanation, these higher differences could be related to technical limitations and show the importance of technical accuracy when assessing these hemodynamic markers. In the normal left ventricle, the amount of EL is proportional to the KE that is produced [10]. The ratio between EL and KE can be defined by the dimensionless index, EL_{index} [11]. The EL_{index} was first introduced in an echo particle image velocimetry study [11], but had not been shown in 4D flow MRI studies earlier. Notably, our results show good reproducibility of the EL_{index} in all subjects. The high reproducibility of the 4D flow MRI-derived EL_{index} indicates that it could be a useful marker of energy status that should be further explored in patient groups with acquired and congenital heart diseases.

Fontan patients form an important patient group in congenital cardiology with significant morbidity and mortality. Because of their heterogeneous underlying anatomy including differences in systemic ventricular morphology (i.e. right or left ventricle) and inflow-to-outflow pathways 4D flow MRI is ideally suited to assess the complex intracardiac flow patterns in these patients. In some patients blood flow can directly go from inflow in a ventricle to outflow in the aorta from the same ventricle (in our studies defined as concordant inflow-to-outflow). While in other patients, blood that enters a ventricle first has to go through a ventricular septal defect and the other ventricle to subsequently be ejected in the aorta (in our studies defined as discordant inflow-to-outflow). It is conceivable that the abnormal underlying anatomy and inflow-to-outflow pathway impact hemodynamic markers.

Therefore, in **Chapter 10** intraventricular EL is assessed in Fontan patients and compared to healthy controls. Both 4D flow MRI-derived EL and EL_{index} are significantly increased in Fontan patients compared to healthy controls. Moreover, highest EL is found in patients with discordant inflow-to-outflow compared to patients with concordant inflow-to-outflow. In these patients with discordant inflow-to-outflow eventually increased EL could lead to cardiac deterioration, however larger study groups are needed to further evaluate this finding

and the clinical/surgical implications. No difference is found between patients with a systemic LV as compared to patients with a systemic RV, even though it is known that the systemic RV in Fontan patients is less capable of sustaining systemic pressures [12] and these patients are more susceptible to heart failure [13]. However, numbers in this study are limited and larger groups of patients with a systemic LV or systemic RV are needed to assess the possible difference.

Importantly, Fontan patients are still prone to heart failure and require regular follow-up, even though survival after this procedure has increased drastically over the past decades [14-16]. The role of intraventricular hemodynamics in the development of heart failure remains incompletely understood. As shown in **Chapter 10**, Fontan patients exhibit increased EL and EL_{index} which could eventually lead to deterioration of cardiac function when present for many years. However to further study to role of EL as a marker of cardiac deterioration patients with multiple 4D flow MRI scans and follow-up data are needed. Future studies could repeat the 4D flow MRI scan and link the differences between the 4D flow MRI parameters to alterations in clinical status.

The results reported in **Chapter 10** encouraged further assessment of the complex interplay of intraventricular hemodynamics in healthy subjects and Fontan patient and further evaluation of the underlying mechanisms of increased EL in these patients. In **Chapter 11** the association between intraventricular EL, KE and vorticity in healthy subjects and Fontan patients is assessed. In healthy subjects intraventricular vorticity correlates well with EL and KE. In Fontan patients intraventricular vorticity was significantly increased compared to healthy subjects, but vorticity still correlated well with EL and KE. These results may confirm the suspected role of intraventricular vorticity in optimizing kinetic energy and energy loss levels. Moreover, Fontan patients with an ejection fraction within the 95% confidence interval of the healthy subjects showed significantly increased levels of systolic vorticity and EL but significantly decreased levels of diastolic kinetic energy versus healthy subjects. We could speculate that these results show that 4D flow MRI-derived hemodynamic markers are sensitive to ventricular abnormalities, preceding global functional impairment reflected in ejection fraction. However, further studies are needed to assess the impact of altered hemodynamic markers on cardiac function.

Decreased exercise capacity is related to a worse functional health status in Fontan patients [15, 17, 18] and has been linked to increased energy loss in the Fontan tunnel [19]. The previous chapters (**Chapter 10** and **11**) only focused on intraventricular hemodynamics at rest. **Chapter 12** describes the influence of pharmacological stress on 4D flow MRI-derived EL, KE and vorticity and their relation to VO_2 max from cardiopulmonary exercise tests.

Pharmacological (Dobutamine) stress resulted in an increase in EL, KE and vorticity, however the increase in EL and KE was 3-4 fold stronger than the increase in vorticity.

Chapter 11 described the linear relation between vorticity and KE and EL. However, the results in **Chapter 12** showed that during stress this relation was disturbed (as shown by the difference in rest-stress increase in EL, KE and vorticity). This could be attributed to the fact that the compact region of vortical flow was unable to expand at the same rate as KE because ventricular size and shape did not change during stress or because the compact region of vortical flow already reached its optimal size [20]. It is still unknown from these results if the vorticity in the ventricular blood flow has a favorable or an adverse effect during stress. This question requires computation of the direction of the vortical flow, which is currently challenging. Importantly, the Dobutamine stress-induced increase in KE, EL and vorticity inversely related to VO_2 max in these Fontan patients, though rest-stress differences in KE and EL showed a three-fold stronger increase than relative difference in vorticity. This could show that in patients with low VO_2 max, the region of vortical flow is unable to expand at the same rate as KE and EL. All in all, these findings unveil that the intracardiac interplay between hemodynamics and energetics may play a role in exercise capacity in Fontan patients.

Conclusions and future perspectives

This thesis is part of the multicenter study titled: '*COBRA³: Congenital heart defects: Bridging the gap between Growth, Maturation, Regeneration, Adaptation, late Attrition and Ageing*' and provides insight in the impact of congenital and acquired heart diseases on electrophysiology and hemodynamics in the heart, that could help understand the often complex pathophysiological mechanisms involved in cardiovascular diseases and might aid in the early detection of patients prone to cardiovascular deterioration.

The first part of this thesis (**Chapter 2, 3, 4 and 5**) shows the value of the electrocardiogram and vectorcardiogram in the assessment of patients with right-sided acquired and congenital heart defects. The 3D vectorcardiographic VG and SA could be valuable in the assessment of patients with right ventricular volume or pressure overload. These vectorcardiographic parameters could easily be added to the standard automated ECG assessment in the current clinical routine. However, further studies are needed to assess the clinical use of these parameters.

The second part of this thesis (**Chapter 6, 7 and 8**) shows significant steps towards clinical utility of 4D flow MRI. Valvular flow quantification with 4D flow MRI, especially in

combination with automated valve tracking, has great potential as a future clinical standard. In future research, automated valve tracking should be refined, especially by adding the possibility of better plane alignment.

The third part of this thesis (**Chapter 10, 11 and 12**) provides important insights in intraventricular hemodynamics in Fontan patients at rest and stress. In time to come, knowledge on intraventricular hemodynamics could aid in determining follow-up frequency and the ideal timing of initiation of heart failure management, perhaps even on an individual patient's level. Moreover, these findings can create a platform for further research in the field of intraventricular hemodynamics in healthy subjects and different patient groups with acquired and congenital heart diseases.

References

1. Butler PM, Leggett SI, Howe CM, Freye CJ, Hindman NB, Wagner GS: Identification of electrocardiographic criteria for diagnosis of right ventricular hypertrophy due to mitral stenosis. *Am J Cardiol* 1986, 57:639-643.
2. Kilner PJ, Yang GZ, Wilkes AJ, Mohiaddin RH, Firmin DN, Yacoub MH: Asymmetric redirection of flow through the heart. *Nature* 2000, 404:759-761.
3. Pedrizzetti G, Domenichini F: Nature optimizes the swirling flow in the human left ventricle. *Phys Rev Lett* 2005, 95:108101.
4. Roes SD, Hammer S, van der Geest RJ, Marsan NA, Bax JJ, Lamb HJ, Reiber JH, de Roos A, Westenberg JJ: Flow assessment through four heart valves simultaneously using 3-dimensional 3-directional velocity-encoded magnetic resonance imaging with retrospective valve tracking in healthy volunteers and patients with valvular regurgitation. *Invest Radiol* 2009, 44:669-675.
5. Westenberg JJ, Doornbos J, Versteegh MI, Bax JJ, van der Geest RJ, de Roos A, Dion RA, Reiber JH: Accurate quantitation of regurgitant volume with MRI in patients selected for mitral valve repair. *Eur J Cardiothorac Surg* 2005, 27:462-466; discussion 467.
6. Westenberg JJ, Roes SD, Ajmone Marsan N, Binnendijk NM, Doornbos J, Bax JJ, Reiber JH, de Roos A, van der Geest RJ: Mitral valve and tricuspid valve blood flow: accurate quantification with 3D velocity-encoded MR imaging with retrospective valve tracking. *Radiology* 2008, 249:792-800.
7. Calkoen EE, Westenberg JJ, Kroft LJ, Blom NA, Hazekamp MG, Rijlaarsdam ME, Jongbloed MR, de Roos A, Roest AA: Characterization and quantification of dynamic eccentric regurgitation of the left atrioventricular valve after atrioventricular septal defect correction with 4D Flow cardiovascular magnetic resonance and retrospective valve tracking. *J Cardiovasc Magn Reson* 2015, 17:18.
8. She HL, Roest AA, Calkoen EE, van den Boogaard PJ, van der Geest RJ, Hazekamp MG, de Roos A, Westenberg JJ: Comparative Evaluation of Flow Quantification across the Atrioventricular Valve in Patients with Functional Univentricular Heart after Fontan's Surgery and Healthy Controls: Measurement by 4D Flow Magnetic Resonance Imaging and Streamline Visualization. *Congenit Heart Dis* 2017, 12:40-48.
9. Dyverfeldt P, Bissell M, Barker AJ, Bolger AF, Carlhall CJ, Ebbers T, Francios CJ, Frydrychowicz A, Geiger J, Giese D, et al: 4D flow cardiovascular magnetic resonance consensus statement. *J Cardiovasc Magn Reson* 2015, 17:72.
10. Akins CW, Travis B, Yoganathan AP: Energy loss for evaluating heart valve performance. *J Thorac Cardiovasc Surg* 2008, 136:820-833.
11. Agati L, Cimino S, Tonti G, Cicogna F, Petronilli V, De Luca L, Iacoboni C, Pedrizzetti G: Quantitative analysis of intraventricular blood flow dynamics by echocardiographic particle image velocimetry in patients with acute myocardial infarction at different stages of left ventricular dysfunction. *Eur Heart J Cardiovasc Imaging* 2014, 15:1203-1212.
12. Sano T, Ogawa M, Taniguchi K, Matsuda H, Nakajima T, Arisawa J, Shimazaki Y, Nakano S, Kawashima Y: Assessment of ventricular contractile state and function in patients with univentricular heart. *Circulation* 1989, 79:1247-1256.
13. Khairy P, Fernandes SM, Mayer JE, Jr., Triedman JK, Walsh EP, Lock JE, Landzberg MJ: Long-term survival, modes of death, and predictors of mortality in patients with Fontan surgery. *Circulation* 2008, 117:85-92.
14. Gersony WM: Fontan operation after 3 decades: what we have learned. *Circulation* 2008, 117:13-15.
15. Robbers-Visser D, Kapusta L, van Osch-Gevers L, Strengers JL, Boersma E, de Rijke YB, Boomsma F, Bogers AJ, Helbing WA: Clinical outcome 5 to 18 years after the Fontan operation performed on children younger than 5 years. *J Thorac Cardiovasc Surg* 2009, 138:89-95.
16. Alsaied T, Bokma JP, Engel ME, Kuijpers JM, Hanke SP, Zuhlke L, Zhang B, Veldtman GR: Factors associated with long-term mortality after Fontan procedures: a systematic review. *Heart* 2017, 103:104-110.

17. Hock J, Reiner B, Neidenbach RC, Oberhoffer R, Hager A, Ewert P, Muller J: Functional outcome in contemporary children with total cavopulmonary connection - Health-related physical fitness, exercise capacity and health-related quality of life. *Int J Cardiol* 2018, 255:50-54.
18. Atz AM, Zak V, Mahony L, Uzark K, D'Agincourt N, Goldberg DJ, Williams RV, Breitbart RE, Colan SD, Burns KM, et al: Longitudinal Outcomes of Patients With Single Ventricle After the Fontan Procedure. *J Am Coll Cardiol* 2017, 69:2735-2744.
19. Khiabani RH, Whitehead KK, Han D, Restrepo M, Tang E, Bethel J, Paridon SM, Fogel MA, Yoganathan AP: Exercise capacity in single-ventricle patients after Fontan correlates with haemodynamic energy loss in TCPC. *Heart* 2015, 101:139-143.
20. Gharib M, Rambod E, Kheradvar A, Sahn DJ, Dabiri JO: Optimal vortex formation as an index of cardiac health. *Proc Natl Acad Sci U S A* 2006, 103:6305-6308.

Chapter 14

Dutch summary (Nederlandse samenvatting)

In dit proefschrift worden de multidimensionale elektrische en hemodynamische aspecten van congenitale en verworven hartzieken geëvalueerd met elektrocardiografie (**Deel I**) en beeldvorming met magnetische resonantie (MRI, **Deel II** en **Deel III**). Hiermee werden studies uitgevoerd om uitgebreide kennis te vergaren over cardiale ziekten, wat zou kunnen helpen bij de behandeling van patiënten met congenitale en verworven hartzieken en bij de detectie van patiënten die risico lopen op achteruitgang van de hartfunctie.

Deel 1: Elektrocardiografische variabelen die cardiale functie weerspiegelen

Het eerste deel van dit proefschrift richt zich op elektrocardiografische variabelen die de hartfunctie kunnen weerspiegelen. In **Hoofdstuk 2** worden de kenmerken van het elektrocardiogram (ECG) bij patiënten met rechtszijdige aangeboren hartafwijkingen besproken. Uit dit review blijkt dat het detecteren van veranderingen in het ECG nuttig kan zijn bij de follow-up van patiënten met (rechtszijdige) hartziekten. Echter, het standaard 12-afleidingen ECG biedt enkel een eendimensionale scalaire weergave van de elektrische stromen in het hart, terwijl het vectorcardiogram (VCG) inzicht geeft in de tijd gerelateerde multidimensionale aard van de elektrische krachten van het hart. **Hoofdstuk 3** biedt normaalwaarden van het pediatrische VCG. Deze normaalwaarden zouden waardevol kunnen zijn bij de seriële follow-up van kinderen met aangeboren hartaandoeningen, zoals een type II atriumseptumdefect (ASDII), wat de focus is van **Hoofdstuk 4**. In **Hoofdstuk 4** worden de elektrische veranderingen na percutane ASDII-sluiting bij pediatrische en volwassen patiënten weergegeven. De meeste ECG en VCG-veranderingen vonden direct na sluiting van het ASDII plaats, behalve de QRS duur en het QTc interval bij zowel kinderen als volwassenen en de PQ duur bij volwassenen. De veranderingen in de vectorcardiografische ruimtelijke QRS-T hoek weerspiegelen toenemende concordantie van het elektrocardiogram, wat kan worden geïnterpreteerd als een gedeeltelijke normalisatie van de elektrische eigenschappen van het hart. Ook de vectorcardiografische ventriculaire gradiënt (VG) liet veranderingen zien die het resultaat zijn van veranderingen in de duur van de actiepotentiaal na ASDII-sluiting. Terwijl **Hoofdstuk 4** zich met name richt op het VCG bij volume overbelasting van het rechter ventrikel (RV), ligt de focus van **Hoofdstuk 5** op de bruikbaarheid van het VCG bij electrocardiografische detectie van RV druk overbelasting bij patiënten met pulmonale hypertensie. De resultaten laten zien dat een combinatie van het ECG en VCG kan bijdragen bij de detectie van RV druk overbelasting.

Deel II: 4D flow MRI-afgeleide cardiale flow en functie: validatie en klinische bruikbaarheid

Het tweede deel van dit proefschrift richt zich op de validatie en klinische bruikbaarheid van vierdimensionale (4D) flow MRI-gerelateerde cardiale flow en functie. **Hoofdstuk 6** geeft een overzicht van de huidige rol van 4D flow MRI bij het onderzoeken van hart- en vaatziekten. Dit literatuuroverzicht laat zien dat 4D flow MRI (3 ruimtelijke dimensies + tijd) een unieke methode is voor niet-invasieve *in vivo* visualisatie en kwantificatie van de dynamische bloedstroompatronen in het hart en grote bloedvaten. Kennis van normale en abnormale intra-cardiale bloedstroompatronen kan ons inzicht in de normale fysiologie vergroten en kan helpen bij het ontrafelen van de complexe pathofysiologische mechanismen die leiden tot hart- en vaatziekten. 4D flow MRI is veelbelovend als diagnostisch hulpmiddel en kan helpen bij de follow-up van patiënten met hart- en vaatziekten en de timing van chirurgische ingrepen. Gerichte onderzoeken zijn echter nog steeds nodig om de klinische waarde van 4D flow MRI aan te tonen.

Kwantificatie van bloedstroomvolume over de hartkleppen in het hart is momenteel de belangrijkste toepassing van 4D flow MRI. Hierbij heeft 4D flow MRI meerdere voordelen ten opzichte van tweedimensionale (2D) “phase-contrast MRI”, wat de huidige klinische standaard is. Ten eerste maakt 4D flow MRI het mogelijk om de bloedstroom volumes over alle vier de kleppen in één enkele acquisitie te kwantificeren. Bovendien kunnen meetvlakken in elke fase worden geplaatst en aangepast aan de stroomrichting en snelheid van de bloedstroom. Vooral bij patiënten met complexe, dynamische regurgitatie-“jets”, zoals bij patiënten met een gecorrigeerd atrioventriculair septumdefect, kan de mogelijkheid van het plaatsen van dynamische meetvlakken cruciaal zijn voor nauwkeurige kwantificering van bloedstroomvolumes en regurgitatiefracties. Validatie is de eerste stap bij het implementeren van een relatief nieuwe methode en goede reproduceerbaarheid van metingen tussen scans is belangrijk, met name wanneer meerdere scans worden verkregen tijdens de follow-up. **Hoofdstuk 7** laat zien dat bepaling van het in- en uitstroomvolume uit het linker ventrikel (LV) betrouwbaar gedaan kan worden met 4D flow MRI met goede reproduceerbaarheid van metingen tussen twee scans. Het handmatig volgen van de klep en het aanpassen van het meetvlak is echter een tijdrovend proces, wat de klinische toepasbaarheid belemmert. Daarom wordt in **Hoofdstuk 8** een automatische methode geïntroduceerd voor het kwantificeren van de bloedstroomvolumes over de kleppen. Deze automatische methode vermindert de analysetijd en verbetert de betrouwbaarheid van de metingen in vergelijking met het handmatig volgen van de klepbewegingen. Bovendien resulteert het geautomatiseerd volgen van de kleppen in een andere classificering van de regurgitatiefractie, wat een grote impact kan hebben op de behandeling van patiënten.

Deel III: 4D flow MRI-afgeleide determinanten van intraventriculaire hemodynamica

Het derde deel van dit proefschrift beschrijft nieuwe, van 4D flow MRI-afgeleide, elementen van intraventriculaire hemodynamica. Een uniek kenmerk van 4D flow MRI is dat het de kwantificatie van hemodynamische markers zoals kinetische energie (KE), viskeus energieverlies (EL) en vorticititeit mogelijk maakt (zie ook **Hoofdstuk 6**). Deze nieuwe markers worden momenteel alleen gebruikt voor onderzoeksdoeleinden en daarom is het bepalen van de nauwkeurigheid van deze metingen van groot belang voordat deze klinisch geïmplementeerd kunnen worden. **Hoofdstuk 9** richt zich daarom op de reproduceerbaarheid (tussen twee scans) van KE, EL en vorticititeit in de LV van gezonde vrijwilligers. Allereerst laat deze studie een sterk verband zien tussen KE en EL in alle scans. Daarnaast is de reproduceerbaarheid van KE, EL en vorticititeit bij de meerderheid (10 van de 12) van de proefpersonen goed tot uitstekend. Bij twee proefpersonen zijn de verschillen tussen twee scans veel groter in vergelijking met de andere tien. Deze grotere verschillen zouden gerelateerd kunnen zijn aan technische beperkingen en laten daarmee zien hoe belangrijk technische nauwkeurigheid is bij het beoordelen van deze hemodynamische markers. In de normale LV is de hoeveelheid EL evenredig aan de KE die wordt geproduceerd. De verhouding tussen EL en KE kan worden gedefinieerd met een dimensieloze index: EL_{index} . Opmerkelijk is dat onze resultaten laten zien dat de EL_{index} bij alle proefpersonen goed reproduceerbaar is. De hoge reproduceerbaarheid van de 4D flow MRI-afgeleide EL_{index} geeft aan dat dit een bruikbare marker van de energiestatus zou kunnen zijn die verder zou moeten worden onderzocht in patiëntengroepen met verworven en aangeboren hartaandoeningen.

Fontan-patiënten vormen een belangrijke patiëntengroep in de congenitale cardiologie met aanzienlijke morbiditeit en mortaliteit. Vanwege hun heterogene onderliggende anatomie, waaronder verschillen in systemische ventriculaire morfologie (dat wil zeggen rechter of linker ventrikel) en instroom-naar-uitstroomroutes, is 4D flow MRI bij uitstek geschikt om de complexe bloedstroompatronen van deze patiënten te beoordelen. Bij sommige patiënten kan de bloedstroom rechtstreeks van de instroom in een ventrikel naar de uitstroom in de aorta vanuit dezelfde ventrikel gaan (in onze studies gedefinieerd als concordante instroom naar uitstroom). Bij andere patiënten moet bloed dat een ventrikel binnenkomt eerst door een ventriculair septumdefect en het andere ventrikel gaan om vervolgens in de aorta te komen (in onze studies gedefinieerd als discordante instroom naar uitstroom). Het is denkbaar dat de abnormale onderliggende anatomie en de instroom-naar-uitstroomroute invloed hebben op hemodynamische markers. Daarom wordt intraventriculaire EL in **Hoofdstuk 10** beoordeeld bij Fontan-patiënten en vergeleken met gezonde controles. Zowel 4D flow MRI-afgeleide EL en EL_{index} zijn significant verhoogd bij Fontan-patiënten in vergelijking met

gezonde controles. Bovendien wordt de hoogste EL gevonden bij patiënten met een discordante instroom naar uitstroom in vergelijking met patiënten met een concordante instroom naar uitstroom. Bij deze patiënten met een discordante instroom naar uitstroom zou deze verhoogde EL uiteindelijk kunnen leiden tot verslechtering van de hartfunctie, maar grotere onderzoeksgroepen zijn nodig om deze bevinding en de klinische / chirurgische implicaties verder te evalueren.

In **Hoofdstuk 11** wordt de associatie tussen intraventriculaire EL, KE en vorticeit bij gezonde proefpersonen en Fontan-patiënten aangetoond. Bij gezonde proefpersonen correleert intraventriculaire vorticeit goed met EL en KE. Bij Fontan-patiënten was de intraventriculaire vorticeit significant hoger in vergelijking met gezonde personen, maar de vorticeit bleef nog goed correleren met EL en KE. Deze resultaten kunnen de vermoedelijke rol van intraventriculaire vorticeit bij het optimaliseren van kinetische energie en energieverlies niveaus bevestigen. Bovendien vertoonden Fontan-patiënten met een ejectiefractie binnen het 95% -betrouwbaarheidsinterval van de gezonde proefpersonen significant verhoogde niveaus van systolische vorticeit en EL, maar significant verminderde niveaus van diastolische kinetische energie ten opzichte van gezonde proefpersonen. We zouden kunnen speculeren dat deze resultaten aantonen dat 4D flow MRI-afgeleide hemodynamische markers gevoelig zijn voor ventriculaire afwijkingen, voorafgaand aan globale functionele beperkingen weerspiegeld in de ejectiefractie.

Verminderde inspanningscapaciteit is gerelateerd aan een slechtere functionele gezondheidstoestand bij Fontan patiënten. De voorgaande hoofdstukken (**Hoofdstuk 10** en **11**) hadden alleen betrekking op intraventriculaire hemodynamica in rust. **Hoofdstuk 12** beschrijft de invloed van farmacologische stress op 4D flow MRI-afgeleide EL, KE en vorticeit en hun relatie tot VO_2 max (afgeleid uit ergometrie). Farmacologische stress (Dobutamine) resulteerde in een toename van EL, KE en vorticeit, maar de toename in EL en KE was 3-4 keer sterker dan de toename in vorticeit. Het is nog onbekend of deze vorticeit in de ventriculaire bloedstroom een gunstig of een nadelig effect heeft tijdens stress. Belangrijk is dat de door stress geïnduceerde toename in KE, EL en vorticeit omgekeerd evenredig was met VO_2 max in deze Fontan-patiënten, hoewel rest-stress-verschillen in KE en EL een drievoudig grotere toename vertoonden dan het relatieve verschil in vorticeit. Dit zou kunnen aantonen dat bij patiënten met lage VO_2 max het gebied van de vortex niet in hetzelfde tempo kan uitzetten als KE en EL. Al met al laten deze bevindingen zien dat het intracardiaal samenspel tussen hemodynamica (vorticeit) en energetica (KE en EL) mogelijk een rol speelt bij de inspanningscapaciteit van Fontan-patiënten.

Appendices

Co-author affiliations

List of publications

Curriculum Vitae

Dankwoord

Co-author affiliations

- ✚ From the division of Pediatric Cardiology, Department of Pediatrics, Leiden University Medical Center, Leiden, The Netherlands:
Nico A Blom; Arend DJ ten Harkel; Vivian P Kamphuis; Roel LF van der Palen; Daphne Raad; Arno AW Roest
- ✚ From the division of Pediatric Cardiology, Department of Pediatrics, Academic Medical Center, Amsterdam, The Netherlands:
Nico A Blom; Sally-Ann B Clur
- ✚ From the division of Pediatric Cardiology, Department of Pediatrics, Erasmus Medical Center, Rotterdam, The Netherlands
Willem A Helbing
- ✚ From the department of Radiology, Leiden University Medical Center, Leiden, The Netherlands:
Pieter J van den Boogaard; Rob van der Geest; Patrick JH de Koning; Lucia JM Kroft; Hildo J Lamb; Albert de Roos; Jos JM Westenberg
- ✚ From the Department of Radiology, Northwestern University–Feinberg School of Medicine, Chicago, Illinois, USA
Mohammed SM Elbaz
- ✚ From the department of Cardiology, Leiden University Medical Center, Leiden, The Netherlands:
Nina Ajmone Marsan; Jeroen J Bax; Victoria Delgado; Marlieke L Haeck; Monique RM Jongbloed; Arie C Maan; Sum-Che Man; Cees A Swenne; Hubert W Vliegen
- ✚ From the department of Cardiology, Academic Medical Center, Amsterdam, The Netherlands:
Barbara JM Mulder; Martina Nassif; A Suzanne Vink; Rob J de Winter
- ✚ From the department of Cardiology, Duke University, Durham, North Carolina, USA
Galen S Wagner († 2016)
- ✚ From the Department of Cardiothoracic surgery, Leiden University Medical Center, Leiden, The Netherlands
Mark G Hazekamp
- ✚ From Pie Medical Imaging BV, Maastricht, the Netherlands
Jean-Paul Aben
- ✚ From the Department of Health services, University of Washington, Washington, USA
Charles C. Maynard
- ✚ From the Department of Medical Informatics, Erasmus Medical Center, Rotterdam, The Netherlands
Jan A Kors
- ✚ From the Department of Medical Statistics and Bioinformatics, Leiden University Medical Center, Leiden, The Netherlands
Erik W van Zwet

List of publications

- 1) **Kamphuis VP**, Nassif M, Man S, Swenne CA, Kors JA, Vink AS, ten Harkel ADJ, Maan AC, Mulder BJM, de Winter RJ, Blom NA. Electrical remodeling after percutaneous atrial septal defect closure in pediatric and adult patients. *Submitted*
- 2) **Kamphuis VP**, Roest AA, van den Boogaard PJ, Kroft LJ, Lamb HJ, Helbing WA, Blom NA, Westenberg JJ, Elbaz MS. Intra-ventricular vorticity is associated with kinetic energy and viscous energy loss from 4D Flow MRI in healthy subjects and Fontan patients. *Submitted*
- 3) **Kamphuis VP**, Elbaz MSM, van den Boogaard PJ, Kroft LJM, Lamb HJ, Hazekamp MG, Jongbloed MRM, Blom NA, Helbing WA, Roest AAW, Westenberg JJM. Dobutamine-induced increase in intracardiac kinetic energy, energy loss and vorticity is inversely related to VO₂ max in Fontan patients. *Submitted*
- 4) Rijnberg FM, Elbaz MSM, Westenberg JJM, **Kamphuis VP**, Helbing WA, Kroft LJ, Blom NA, Hazekamp MG, Roest AAW. Four-dimensional flow MRI derived blood flow energetics of the inferior vena cava-to-extracardiac conduit junction in Fontan patients. *Eur J Cardiothorac Surg* 2018 (*in press*)
- 5) **Kamphuis VP**, Raad D, Nassif M, Swenne CA, Blom NA, ten Harkel ADJ. Electrocardiographic characteristics before and after correction of right-sided congenital heart defects and its relation to prognosis. *J Electrocardiol* 2018 [*Epub ahead of print*]
- 6) **Kamphuis VP**, Roest AAW, Ajmone Marsan N, Van den Boogaard PJ, Kroft LJM, Aben JP, Bax JJ, de Roos A, Lamb HJ, Westenberg JJM. Automated cardiac valve tracking for flow quantification with four-dimensional flow MRI. *Radiology*. 2018 [*Epub ahead of print*]
- 7) **Kamphuis VP**, Elbaz MS, van den Boogaard PJ, Kroft LJ, van der Geest RJ, de Roos A, Helbing WA, Blom NA, Westenberg JJ, Roest AA. Disproportionate Intraventricular Viscous Energy Loss in Fontan Patients: analysis by 4D Flow MRI. *Eur Heart J Cardiovasc Imaging* 2018 [*Epub ahead of print*]
- 8) **Kamphuis VP**, Westenberg JJ, van den Boogaard PJ, Clur SB, Roest AAW. Direct assessment of tricuspid regurgitation by 4D flow cardiovascular magnetic resonance in a patient with Ebstein's anomaly. *Eur Heart J Cardiovasc Imaging*. 2018 May 1;19(5):587-588.
- 9) **Kamphuis VP**, Blom NA, van Zwet E, Man S, ten Harkel AD, Maan AC, Swenne CA. Normal values of the ventricular gradient and QRS-T angle, derived from the pediatric electrocardiogram. *J Electrocardiol*. 2018 May - Jun;51(3):490-495.
- 10) **Kamphuis VP**, Westenberg JJ, van der Palen RL, van den Boogaard PJ, van der Geest RJ, de Roos A, Blom NA, Roest AA, Elbaz MS. Scan-rescan Reproducibility of Diastolic Left Ventricular Kinetic Energy, Viscous Energy Loss and Vorticity Assessment Using 4D Flow MRI: Analysis in Healthy Subjects. *Int J Cardiovasc Imaging*. 2018 Jun;34(6):905-920.
- 11) **Kamphuis VP**, Roest AA, Westenberg JJ, Elbaz MS. Bi-ventricular Vortex Ring Formation Corresponds to Regions of Highest Intra-ventricular Viscous Energy Loss in a Fontan Patient: Analysis by 4D Flow MRI. *Int J Cardiovasc Imaging*. 2018 Mar;34(3):441-442
- 12) **Kamphuis VP**, van der Palen RL, de Koning PJ, Elbaz MS, van der Geest R, de Roos A, Roest AA, Westenberg JJ. In-scan and Scan-rescan Assessment of LV In- and Outflow Volumes by 4D Flow MRI versus 2D Planimetry. *J Magn Reson Imaging*. 2018 Feb;47(2):511-522
- 13) **Kamphuis VP**, Westenberg JJ, van der Palen RL, Blom NA, de Roos A, van der Geest R, Elbaz MS, Roest AA. Unravelling cardiovascular disease using four dimensional flow cardiovascular magnetic resonance. *Int J Cardiovasc Imaging*. 2017 Jul;33(7):1069-1081
- 14) **Kamphuis VP**, Wagner GS, Pahlm O, Man S, Olson CW, Bacharova L, Swenne CA. Comparison of model-based and expert-rule based assessment of the culprit artery in triage electrocardiograms of patients with angiographically demonstrated acute coronary occlusion. *J Electrocardiol*. 2015 Jul-Aug;48(4):483-9
- 15) **Kamphuis VP**, Zegers MA, Koppen H. Bilateral Heel Numbness due to External Compression during Obstetric Epidural Analgesia. *Case Rep Neurol* 2015;7:15-17
- 16) **Kamphuis VP**, Haeck MLA, Wagner GS, Maan AC, Maynard C, Delgado V, Vliegen HW, Swenne CA. Electrocardiographic Detection of Right Ventricular Pressure Overload in Patients with Suspected Pulmonary Hypertension. *J Electrocardiol*. 2014 Mar-Apr;47(2):175-82
- 17) Olson C, Estes H, **Kamphuis VP**, Carlsen EA, Wagner GS. Chapter 3: spatial methods for the comprehensive understanding of the ECG. In: Wagner GS. Marriott's practical electrocardiography. 12th edition. Lippincott Williams & Wilkins. 2013

Curriculum Vitae

Vivian Paola Kamphuis was born in Willemstad, Curaçao, the Dutch Antilles, on March 10 1990. She completed secondary school at the Sint-Maartenscollege in Voorburg in 2008 (Profile: Nature & Health + Latin and German), after which she started studying Medicine at the University of Leiden, The Netherlands. During medical school she went to Duke University, North Carolina, USA, for a research internship under supervision of dr. Galen Wagner (Department of Cardiology, Duke University) and dr. Cees Swenne (Department of Cardiology, Leiden University Medical Center) to study the electrocardiographic detection of pulmonary hypertension. Later, she did clinical internships in Pediatric Cardiology at Skåne University Hospital in Lund, Sweden and Emma care in Willemstad, Curaçao, the Dutch Antilles and spend 2.5 months in Surinam for her internship obstetrics and gynaecology. She obtained her medical degree on January 31, 2015. Thereafter, she started as a PhD Candidate in Pediatric Cardiology in the multicenter study “*COBRA*³” for the Netherlands Heart Institute, Utrecht, mainly stationed at the Leiden University Medical Center, The Netherlands, under supervision of Prof. Dr. Nico Blom (Department of Pediatric Cardiology, Leiden University Medical Center), Prof. Dr. Wim Helbing (Department of Pediatric Cardiology, Erasmus Medical Center) and Dr. Arno Roest (department of Pediatric Cardiology, Leiden University Medical Center). During her PhD she mainly focused on advanced cardiovascular imaging of patients with acquired and congenital heart disease and she gave many presentations on this topic at national and international conferences. Outside of her medical career, she is also passionate about imaging: her photos have won several awards and during her PhD she also worked as a photographer.

Dankwoord

- ✚ Dit proefschrift is het resultaat van samenwerking tussen de afdelingen kindercardiologie, radiologie en cardiologie. Het was een voerecht om met zoveel enthousiaste en begaafde mensen te mogen samenwerken. Ik wil iedereen hiervoor hartelijk bedanken. Allereerst natuurlijk alle patiënten, proefpersonen en hun ouders: zonder jullie had dit proefschrift niet tot stand kunnen komen. Bedankt voor jullie deelname aan de onderzoeken in dit proefschrift. Daarnaast bedank ik een aantal mensen in het bijzonder:
- ✚ Prof. Dr. N.A. Blom, beste Nico, bedankt voor deze kans en voor de begeleiding. Ik had me geen betere promotor kunnen wensen. Je was altijd laagdrempelig benaderbaar en ik heb veel gehad aan onze wekelijkse gesprekken. Jouw vertrouwen, humor en voortvarendheid hebben me geholpen bij dit project.
- ✚ Prof. Dr. W.A. Helbing, beste Wim, bedankt voor deze kans en het vertrouwen. Ik heb zeer veel geleerd van dit grote multicenter project.
- ✚ Dr. A.A.W. Roest, beste Arno, jouw deur stond altijd open en ik heb veel aan je positieve instelling, wetenschappelijk inzicht en doortastendheid gehad. Ik heb altijd met je kunnen lachen en ik zal de gezelligheid tijdens alle congressen missen, al zullen er in de toekomst hopelijk nog veel congressen volgen.
- ✚ Dr. J.J.M. Westenberg, beste Jos, bedankt voor je begeleiding en voor het vertrouwen dat je me altijd hebt gegeven. Jouw openheid, oprechtheid en toewijding voor onderzoek inspireren mij. Je stond altijd voor me klaar, dit heb ik erg gewaardeerd.
- ✚ Dr. A.D.J. ten Harkel, beste Derk Jan, bedankt voor al jouw hulp bij de Cobra studie. Het was fijn dat je er altijd voor mij was als ik vragen had, bedankt hiervoor.
- ✚ Dr. Mohammed S.M. Elbaz, thank you for your supervision, motivation and enthusiasm. We spend hours discussing our studies, but we always brought it to a good end.
- ✚ Dr. C.A. Swenne, beste Cees, bedankt dat je altijd in mij geloofd hebt. Het begon allemaal door jou: jij enthousiasmeerde me voor onderzoek en hier ben ik je zeer dankbaar voor. Bedankt voor je tomeloze enthousiasme, positiviteit en geduld, ook als we het allebei eigenlijk niet meer zagen zitten om bijvoorbeeld duizenden ECG's te checken. Bedankt voor alles.
- ✚ Dr. G.S. Wagner, dear Galen, you truly inspired me with your passion for research, cardiology and life in general. You were a true mentor and one of the reasons I started pursuing a PhD. It is such a pity that you are not here anymore, but I know you would have been so proud of me.
- ✚ De echografisten van de kindercardiologie: Gwen, Stephanie, Francisca en Lisette. Bedankt voor alle echo's die jullie hebben gemaakt voor de Cobra studie. Cova, thank you for analyzing so many echocardiograms, I could not have done all that without you.
- ✚ De dames van de prikpost (H3), bedankt voor jullie medewerking als er een patiënt op de poli was die in aanmerking kwam voor de Cobra studie.
- ✚ De afdeling Radiologie, bedankt voor de hulp bij het scannen en de analyse van de MRI scans. Met name Pieter, bedankt voor alle avonden waarop we samen patiënten scanden.
- ✚ Functieafdeling Cardiologie, bedankt voor jullie hulp met de 24-uurs Holters en fietstesten. Soms belde ik jullie heel vaak maar gelukkig was dit nooit een probleem en was het bij jullie altijd gezellig. Arie en Sum-Che, bedankt dat jullie mij altijd hielpen bij ECG conversies en Matlab berekeningen.
- ✚ Afdeling Bos (kindercardiologie), met name de physician assistants: Margot, Kathy en Elsmere, bedankt voor jullie hulp bij de inclusie van patiënten. Wat leuk dat ik ook na mijn semi-arts stage nog contact met jullie kon blijven houden. Elsmere, later als research nurse was je natuurlijk helemaal onmisbaar in het LUMC en UMCU, bedankt daarvoor.
- ✚ Alle (kinder) cardiologen die betrokken waren bij de studie, bedankt voor jullie hulp bij het includeren van patiënten in de Cobra studie.
- ✚ Al mijn lieve kamergenoten van het oude en nieuwe hok en de rest van de kindergeneeskunde onderzoekers: Sabine, Cor Jan, Danny, Ilona, Henriëtte, Janneke, Lisanne, Isabelle, Ineke, Elsmere, Lisette, Emma, Sophie, Berbera, Hilda, Hylke, Tessa en Marieke, bedankt voor alle mooie momenten. In het bijzonder mijn meest recente kamergenoten: Janneke, Lisanne, Isabelle en Henriëtte, wat hebben we veel met elkaar gedeeld en ook al was de kamer soms wat vol, ik had jullie nooit willen missen. Roel, ook al deed je een iets ander traject, jij kan hier natuurlijk ook niet ontbreken. We begonnen

- ongeveer tegelijk met onderzoek en stonden vaak voor dezelfde onderzoeksperikelen. Bedankt voor de steun die ik aan je heb gehad.
- ✚ De andere onderzoekers in de Cobra studie: Marie, Guido, Dennis, Eva en Jelle, bedankt voor alle gezelligheid en steun die we aan elkaar hadden tijdens en na alle besprekingen. Ik heb veel van jullie geleerd over celkleuringen en proefdieronderzoek, een wereld die compleet nieuw voor mij was. Eva, wij begonnen tegelijk en hebben veel met elkaar gedeeld, bedankt daarvoor.
 - ✚ Martina, wij hebben samen een artikel geschreven waarbij we meer drempels tegenkwamen dan we aanvankelijk dachten. Toch hebben we doorgezet en het samen tot een mooi einde kunnen brengen. Samenwerken met jou was altijd leuk.
 - ✚ Julia, Eva, Vera, en de rest, bedankt voor alle mooie feestjes, zonder dansen had ik dit nooit kunnen afronden. We hebben allemaal een drukke baan maar zijn gelukkig nooit te moe voor een latin feest.
 - ✚ Simone, Donna, Esra en Marloes, mijn vriendinnen sinds de basisschool en inmiddels allemaal arts, uiteraard mogen jullie niet aan dit lijstje ontbreken. Ik weet dat jullie er altijd voor mij zijn, en andersom. Bedankt voor onze mooie vriendschap.
 - ✚ Natuurlijk ook dank aan mijn andere vrienden en vriendinnen, ook degenen die ik door drukte wat minder vaak kan zien, jullie zijn altijd in mijn hart. Leonie, wij deden bijna alles tegelijk: geneeskunde, Augustinus, het Rapenburg en promoveren. Bedankt voor je steun en vriendschap. Manon en Emmy, bedankt voor de leuke weekendjes weg, wat fijn dat we daar nog tijd voor konden maken.
 - ✚ Mijn schoonouders: lieve Dick en Marjan, bedankt voor jullie steun tijdens deze periode en dat jullie altijd interesse toonden in mijn proefschrift (en heel vaak mijn lunch verzorgden).
 - ✚ Mijn paranimfen: Maribel, allerliefste babysis, bedankt dat je er altijd voor me bent. Als criminoloog/antropoloog heb je veel mensenkennis, die ik soms goed kon gebruiken. Bedankt dat je vandaag naast mij staat. Annemijn, toen we bij elkaar in het co-groepje kwamen waren we direct vriendinnen en dat is nooit veranderd. Enkele weken na onze eerste ontmoeting gingen we al samen op reis. We hebben veel aan elkaar gehad tijdens onze coschappen en promotietijd. Bedankt dat je vandaag naast mij staat.
 - ✚ Mijn familie, met name mijn ouders: lieve papa en mama, bedankt voor jullie onvoorwaardelijke steun en liefde. Zonder jullie had ik dit allemaal nooit kunnen doen. Jullie zijn mijn grote voorbeeld. Ik draag mijn proefschrift aan jullie op. Oma Suus, Wies, Anne, Ivette, Mirte en Arwen, bedankt voor jullie steun en liefde.
 - ✚ Tom, bedankt dat je er altijd voor mij bent in mijn goede en slechte momenten. Jij zorgt dat ik met beide benen op de grond blijf staan. Hoe cliché het ook is: you are my rock.

